SPACE RESEARCH IN POLAND

Report to
COMMITTEE ON SPACE RESEARCH
(COSPAR)
2018

Polish Space Agency and Polish Committee on Space Research Space Research in Poland

Report to COMMITTEE ON SPACE RESEARCH (COSPAR)

ISBN 978-83-945436-1-7 First edition

Gdansk, 2018

Editor: Piotr Bednarski

1

SATELLITE GEODESY

1. SATELLITE GEODESY

Compiled by Mariusz Figurski and Grzegorz Nykiel

Introduction

This part of the Polish National Report on Satellite Geodesy is the report of works on advanced space techniques performed in Poland in a period of a time from 2016 to 2018.

The activity of the Polish institutions in the field of satellite geodesy and navigation are concentrated on the several main tasks:

- global and regional GPS and SLR measurements in the frame of International GNSS Service (IGS), International Laser Ranging Service (ILRS), International Earth Rotation and Reference Systems Service (IERS), European Reference Frame Permanent Network (EPN),
- Polish geodetic permanent networks – ASG-EUPOS, VRSNET, SMARTNET, TPI NETpro,
- modeling of ionosphere and troposphere,
- practical utilization of satellite methods in local geodetic applications,
- geodynamic study,
- metrological control of Global Navigation Satellite System (GNSS) equipment,
- use of gravimetric satellite missions,
- application of GNSS in overland, maritime and air navigation,
- multi-GNSS application in geodetic studies.

These activities were conducted mainly at the following research centers:

- Department of Astronomy and Geodynamics, University of Warmia and Mazury in Olsztyn;
- Department of Satellite Geodesy and Navigation, University of Warmia and Mazury in Olsztyn;
- Department of Planetary Geodesy, Space Research Centre, Polish Academy of Sciences (SRC PAS) in Warsaw;
- Faculty of Mining Surveying and Environmental Engineering, Department of Geomatics, University of Science and Technology – AGH in Cracow;
- Faculty of Civil Engineering and Geodesy, Military University of Technology (MUT);

- Faculty of Civil and Environmental Engineering, Gdansk University of Technology (GUT);
- Faculty of Navigation, Gdynia Maritime University;
- Institute of Geodesy, University of Warmia and Mazury in Olsztyn;
- Institute of Geodesy and Cartography in Warsaw (IGiK);
- Institute of Geodesy and Geodetic Astronomy, Warsaw University of Technology (WUT);
- Institute of Geodesy and Geoinformatics, Wrocław University of Environmental and Life Sciences;
- Naval Academy in Gdynia;
- Maritime University in Szczecin;
- Polish Air Force Academy in Dęblin;
- Civil Aviation Personnel Education Centre of Central and Eastern Europe Silesian University of Technology/ Polish Air Navigation Agency in Warsaw.

This Report was compiled from information reported in a period from 2016 to 2018 by the correspondents from Polish institutions involved in the use of satellite navigation systems.

The bibliography of the related works is given in the references.

Institute of Geodesy and Cartography J. Kryński

Brief review of the activities of the Institute of Geodesy and Cartography in the field of satellite geodesy is included in annual National Reports of Poland to EUREF (Krynski and Rogowski, 2016, 2017). The reports present main geodetic activities at the national level in Poland, concentrated on maintenance of geodetic and gravity control as well as geomagnetic control, continuing operational work of permanent IGS/EPN GNSS stations, GNSS data processing on the regular basis at the WUT and MUT Local Analysis Centres, activities of MUT and WUT EPN Combination Centre, validation of GNSS orbits using SLR, activity within the EUREF-IP Project, works on GNSS for meteorology, monitoring ionosphere and ionospheric storms, advanced methods for satellite positioning, maintaining the ASG-EUPOS network in Poland, modelling precise geoid, the use of data from satellite gravity missions, monitoring gravity changes, geodynamics, activity in satellite laser ranging and their use.

1. SATELLITE GEODESY

Reference systems and frames

One of the traditional products of the Institute of Geodesy and Cartography is the Astronomical Almanch which last years, besides its full version available on the web site of the Instiitute, is made available on-line with a printed complementary part (Krynski and Sekowski, 2016, 2017)

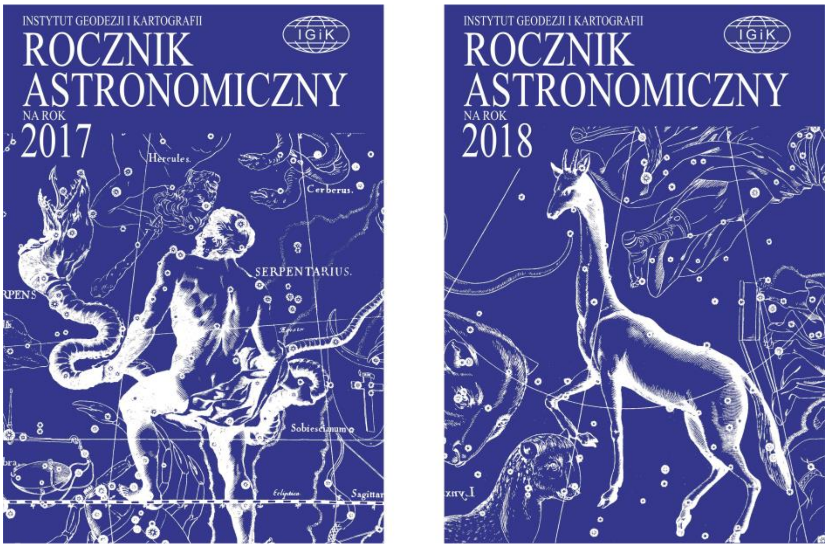

Fig. 1.1. Astronomical Almanc of the Institute of Geodesy and Cartography.

EPOS–PL project – the Polish Earth science infrastructure integrated with the European Plate Observing System Programme (EPOS) (Bosy et al., 2016) – run by the consortium of seven institutions (including the Institute of Geodesy and Cartography), started in 2017 (Bosy et al., 2017). One of the aims of the project is the densification of the GGOS infrastructure in Poland in the framework of EPOS-PL (Sośnica et al., 2017). The Institute of Geodesy and Cartography is responsible for integrating, gathering, and pre-processing gravity data assuring their world-level standard.
The Institute of Geodesy and Cartography is involved in activities concerning gravity reference systems and frames, in particular establishing modern gravity control with the use of the A10 absolute gravimeter (Dykowski et al., 2018; Engfeld et al., 2018) and its maintenance (Dykowski and Krynski, 2017). The installation of the iGrav-027 – the first superconducting gravimeter in Poland, and the only one SG in this part of Europe – completed successfully on April 2016

(Dykowski and Krynski, 2016a; Sekowski et al., 2016; Krynski and Rogowski, 2017) was a very important step towards improving the reliability of maintenance of gravity control in Poland. The iGrav-027 superconducting gravimeter records at Borowa Gora Geodetic-Geophysical Observatory are regularly analysed (Dykowski et al., 2016b, 2017a). The analysis of the iGrav records together with records of collocated seismograph led to very interesting conclusions showing great potential of the gravimetersfor seismic analysis (Dykowski et al., 2017c; Wilde-Piórko et al., 2017).

GNSS Applications

The long time series of weekly and daily solutions for coordinates of a number of permanent GNSS stations was analyzed by the team of the Institute of Geodesy and Cartography, Warsaw, (Krynski et al., 2017a, 2017b). Height changes of the stations in the area of Warsaw metropolitan, obtained from the solutions of short vectors referred to the reference station were determined. in terms of monitoring vertical deformations. They were further used to validate deformations obtained from satellite radar interferometry (Ziółkowski et al., 2016; Żak et al., 2016).

Use of gravimetric satellite missions

The research on the selection of GRACE-based GGMs and a filtering method for estimating mass variations in the Earth system over Poland has been conducted (Godah et al., 2015). It has been shown that in a global scale, both the DDK1 filter and the Gaussian filter with a radius of 700 km substantially reduce the noise in GRACE-based GGMs. Moreover, the results obtained show that the DDK1 filter recovers ~25% more of equivalent water thickness variations signal than the Gaussian filter with a radius of 700 km. This may indicate that the DDK1 filter seems more suitable to reduce the noise contained in RL05 GRACE-based GGMs than other filters investigated. on the other hand, in a local scale, in particular, over the area of Poland, the obtained results revealed that DDK1 and DDK2 filters seem more suitable than the Gaussian filter with a radius of 300 km, 500 km and 700 km as well as DDK3, DDK4, and DDK5 filters, to reduce the noise included in RL05 GRACE-based GGMs over the investigated area. over the area of Poland, the comparison between equivalent water thickness variations obtained from RL05 GRACE-based GGMs and the corresponding ones obtained from the WGHM revealed the superiority of RL05 GRACE-based

1. SATELLITE GEODESY

GGMs developed by the GFZ centre to estimate temporal mass variations in the Earth system over Poland, over other GGM time series investigated.
Quality of the newest 15 global geopotential models developed in 2014-2016 with the use of data from satellite gravity missions was investigated in IGiK. They were evaluated in terms of height anomalies using GNSS/levelling data at ASG-EUPOS stations, and absolute gravity data at 168 stations of national gravity control.
The possibility of using monthly based time series of absolute gravity data for calibration/validation of temporal mass variations derived from satellite observations was discussed. Temporal gravity variations obtained from RL05 GRACE-based GGMs and from GOCE/GRACE-based GGMs were compared with the corresponding ones obtained from the time-series of absolute gravity measurements conducted with the A10-020 gravimeter at the Borowa Gora Geodetic-Geophysical Observatory (Fig. 1.2) (Godah et al., 2016).

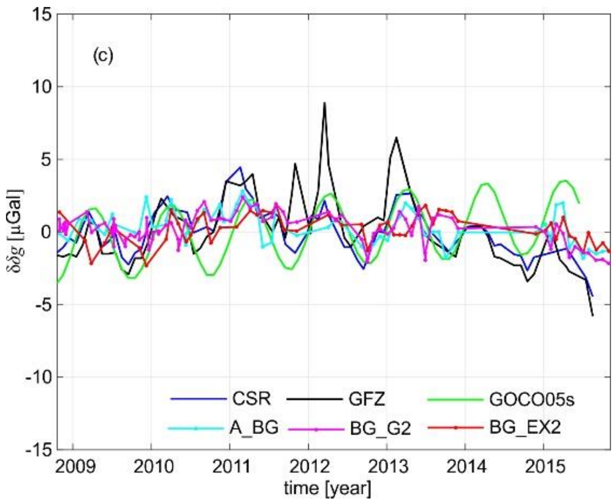

Fig. 1.2. Time series of gravity variations at the Borowa Gora Geodetic-Geophysical Observatory obtained from the CSR and GFZ RL05 GRACE-based GGMs, the GOCO05s and the smoothed/reduced gravity data obtained from the measurements with the A10-020 reduced and smoothed using the local hydrology and the moving average.

The results of the comparison were analysed. They indicate that time series of gravity data from the measurements with the A10-020 gravimeter can be regarded as a valuable tool for the calibration/validation of the long term temporal gravity variations at Borowa Gora Geodetic-Geophysical

Observatory.
The comparison between these GGMs and the Global Land Data Assimilation (GLDAS) hydrological models in terms of equivalent water thickness (Fig. 1.3.) confirms the suitability of GRACE data to study the short term temporal mass variations over Poland (Godah et al., 2017a).

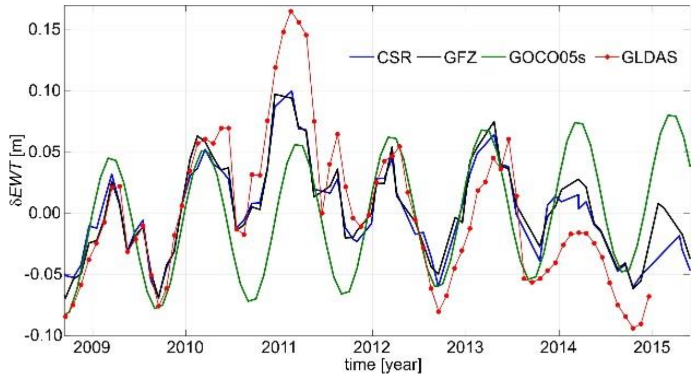

Fig. 1.3. Time series of δEWT at the Borowa Gora Geodetic-Geophysical Observatory obtained from the CSR and GFZ RL05 GRACE-based GGMs, the GOCO05s and GLDAS hydrological models.

Temporal geoid height variations obtained from GGMs developed by GFZ on the basis of GRACE data were calculated for four 3° × 5° subareas in Poland (Fig. 1.4.).
In the subareas investigated variations of geoid height from one epoch to the other can reach 10 mm while differences of geoid height variation between subareas reach 2 mm for the same epoch and 11 mm for different epochs (Fig. 1.5) (Godah et al., 2017b).

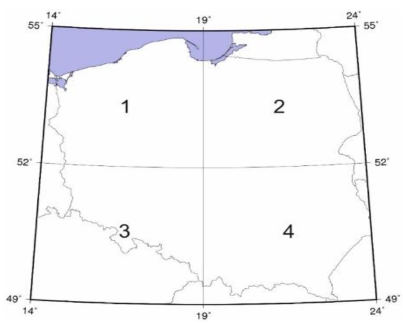

Fig. 1.4. Subareas in Poland for which geoid height variations were investigated.

1. SATELLITE GEODESY

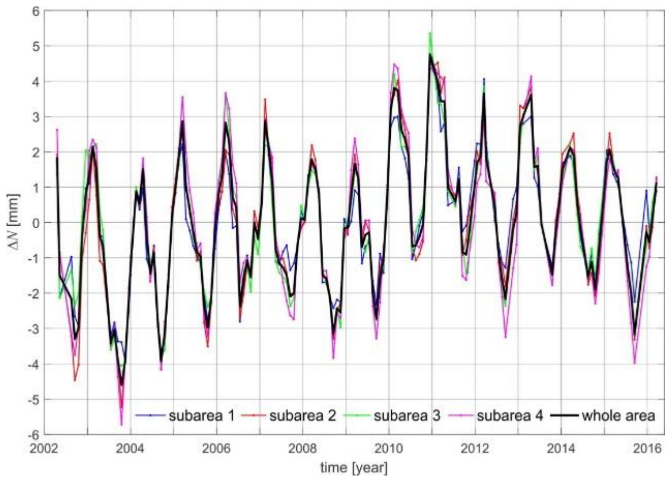

Fig. 1.5. Time series of geoid height variations in subareas investigated.

Application of the PCA/EOF method for the analysis and modelling of temporal variations of geoid heights over Poland was investigated (Godah et al., 2017e). The method has been recommended for modelling temporal variations of geoid heights over the area of Poland as providing slightly better results compared to other methods implemented so far over the area investigated.

Physical height changes in 16 subareas of Central Europe (Fig. 1.6) were estimated with the seasonal decomposition method as well as the PCA/EOF (Principal Component Analysis/Empirical Orthogonal Function) method using GRACE satellite mission data (Godah et al., 2017c)

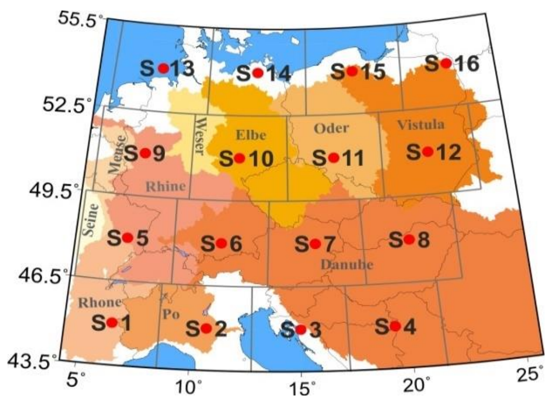

Fig. 1.6. The study area, including sixteen subareas (S1, S2, …, S16) as well as major river basins.

Temporal variations of height anomalies combined with vertical displacements for the period between January 2004 and December 2010 provides physical height changes reaching up to 22.8 mm. Annual periodicity of physical height changes is a dominant one with minimum values observed in spring (February–April) and maximum values in autumn (August–October). Subareas located in the same catchment induce consistent long term/trend components of physical height changes, i.e. the correlation of long term/trend components can reach up to 96.8 %. Models of physical height changes developed using the seasonal decomposition method are slightly better than the corresponding models developed using the PCA/EOF method. They fit quite well (89.5%–96.5% in terms of correlations) to their corresponding values determined from GRACE mission data with standard deviations not exceeding 1.4 mm. Physical height changes estimated using GRACE mission data can play an essential role for the modernization of the vertical reference system over the area investigated. The final interpretation requires complementary studies concerning an understanding of the main sources of these changes, e.g. hydrology in inland areas and sediment and sea level changes in sea areas.

The use of absolute gravity data for the validation of GGMs and for improving quasigeoid heights determined from satellite-only GGMs was investigated (Godah et al., 2017d). Absolute gravity from 161 gravity stations of the modernized Polish gravity control network determined from 2012 to 2014 with the A10-020 absolute gravimeter by the team of the Institute of Geodesy and Cartography, Warsaw, Poland, was used in this investigation. The fit of the chosen GGMs to absolute gravity data was estimated (Fig. 1.7).

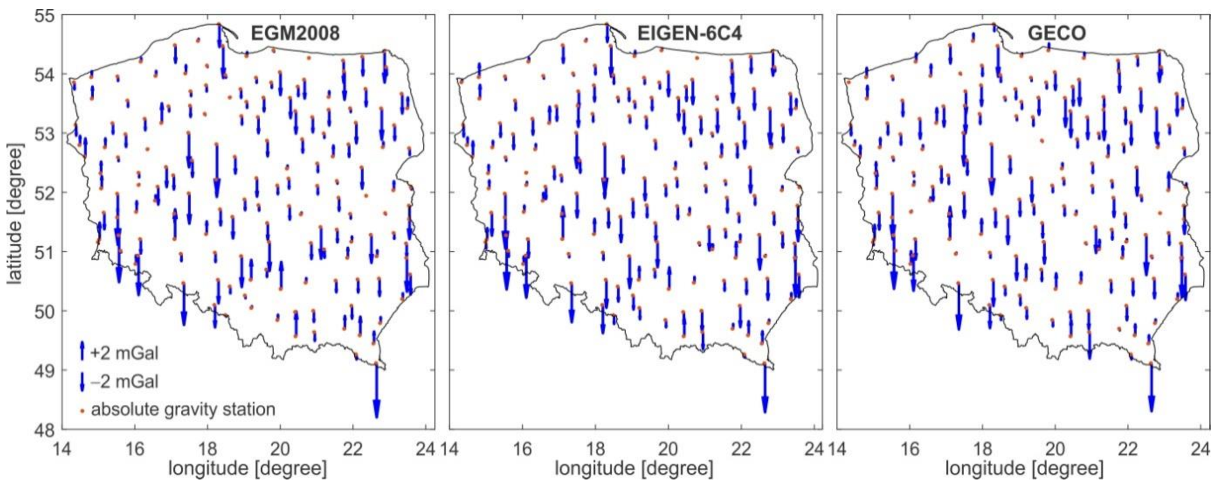

Fig. 1.7. The fit of combined GGMs to absolute gravity data.

Quasigeoid heights determined from the TIM-R05 model were substantially improved when adding absolute gravity data. In terms of standard deviations of quasigeoid heights fit the estimated improvement was at the level of 27%, 45% and 59% when using absolute gravity data of 80 km, 55 km, and 40 km resolution, respectively.

Use of radar satellite data for deformation monitoring

Research on the developing the integrated system of surface deformation monitoring caused by man-made factors, based on Persistent Scatterer Interferometry, measurements from permanent GNSS stations and precise levelling has been continued in IGiK in cooperation with two other institutions (Ziolkowski et al., 2016). Height changes of GNSS stations from the solutions of short vectors and PSI measurements were investigated. Relative deformations in height component between GNSS stations obtained from GNSS (weekly solutions) and PSI (average) data were compared (e.g. Fig. 1.8)

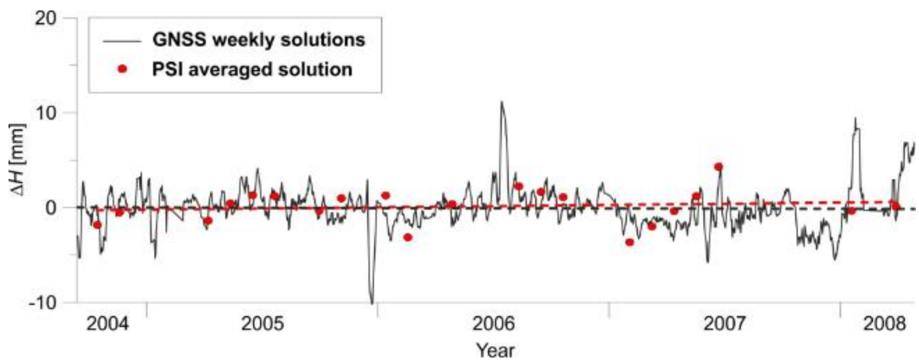

Fig. 1.8. Comparison of relative deformations in height component between Borowa Gora and Jozefoslaw obtained from GNSS (weekly solutions) and PSI (average) data.

It has been shown that the use of mutually complementing observation techniques for monitoring deformations in the investigated area, such as GNSS and PSI, can substantially increase reliability of the interpretation of the results obtained. Common use of both techniques allows in the variations considered as noise observation to extract the signal of height changes that is below the limit of measurement error. Simultaneously, the analysis of results of two completely independent observation techniques leads to the increase of reliability of results obtained using each of these methods (Zak et al., 2016).

Publications:

1. Bosy J., Krynski J., Araszkiewicz A., (2016): *EPOS–PL – the Polish Earth science infrastructure integrated with the EPOS programme*, 17th Czech-Polish Workshop on Recent Geodynamics of the Sudeten and Adjacent Areas, Ramzová, Czech Republic, 20–22 October 2016.
2. Bosy J., Orlecka-Sikora B., Olszewska D., Górka-Kostrubiec B, Lizurek G, Lurka A, Jóźwiak W., Welker E., Werner T., Junosza-Szaniawski R., Araszkiewicz A., Kaplon J., Kryński J., Dykowski P., Czuba W., Janik., Sośnica K., Rohm W., Tymków P., Borkowski A., Hadaś T., Mutke G., Barański A., Szepieniec T., Kocot J., (2017): *EPOS – PL the initiative for European Plate Observation System in Poland, integrated infrastructure and new algorithms*, Symposium of the IAG Subcommission for Europe (EUREF) held in Wroclaw, Poland, 17–19 May 2017 http://www.euref.eu/symposia/2017Wroclaw/04-04-Bosy.pdf.
3. Dykowski P., Kryński J., Sękowski M., (2016a): *Installation and initial results from the iGrav-027 superconducting gravimeter at Borowa Gora Geodetic-Geophysical Observatory*, 18th Geodynamics and Earth Tide Symposium 2016, 5 – 9 June 2016, Trieste, Italy.
4. Dykowski P., Kryński J., Sękowski M., (2016b): *Initial analysis the iGrav-027 superconducting gravimeter records at Borowa Gora Geodetic-Geophysical Observatory*, 1st Joint Commission 2 and IGFS Meeting Symposium GGHS2016 "Gravity, Geoid and Height Systems 2016", 19–23 September 2016, Thessaloniki, Greece.
5. Dykowski P., Kryński J., (2017): *Aspects of establishing a modern gravity control: case study Borowa Gora Observatory*, Symposium of the IAG Subcommission for Europe (EUREF) held in Wroclaw, Poland, 17–19 May 2017 http://www.euref.eu/symposia/2017Wroclaw/p-14-Dykowski.pdf.
6. Dykowski P., Sękowski M., Kryński J., (2017a): *First year of gravity signal records with the iGrav-027 superconducting gravimeter*, IAG-IASPEI Scientific Assembly, Kobe, Japan, 30 July – 4 August 2017.
7. Dykowski P., Grad M., Krankowski A., Krynski J., Olszak T., Polkowski M., Rajner M., Sekowski M., Wilde-Piorko M., (2017c): *Expanding seismic surface waves measurements towards low periods with gravity measurements*, IAG-IASPEI Scientific Assembly, Kobe, Japan, 30 July – 4 August 2017.
8. Dykowski P., Kryński J., Sękowski M., (2018): *The use of the A10-020 absolute gravimeter for the establishment and modernization of national gravity controls in Europe*, Geophysical Research Abstracts, Vol. 20, EGU2018-2025, EGU General Assembly 2018, 8–13 April, Vienna, Austria.
9. Engfeldt A., Lidberg M., Sekowski M., Dykowski P., Krynski J., Ågren J., Olsson P.-A., Bryskhe H., Steffen H., Nielsen J.E. (2018): *RG 2000 – the new gravity reference frame of Sweden*, FIG Congress 2018, 6–11 May 2018, Istanbul, Turkey.
10. Godah W., Szelachowska M., Krynski J., (2015): *On the selection of GRACE-based GGMs and a filtering method for estimating mass variations in the Earth system over Poland*, Geoinformation Issues, Vol. 7, No 1, Warsaw, pp. 5-14.
11. Godah W., Szelachowska M., Krynski J., Dykowski P., (2016): *Analysis of RL05 GRACE-based and GOCE/GRACE-based GGMs using gravity measurements at Borowa Gora Geodetic-*

Geophysical Observatory, ESA Living Planet Symposium 2016 and 6th GOCE User Workshop, 9 – 13 May 2016, Prague, Czech Republic; ESA SP-740, August 2016.

12. Godah W., Szelachowska M., Krynski J., (2017a): *Investigation of geoid height variations and vertical displacements of the Earth surface in the context of the realization of a modern vertical reference system - A case study for Poland*, 1st Joint Commission 2 and IGFS Meeting Symposium GGHS2016 "Gravity, Geoid and Height Systems 2016", 19–23 September 2016, Thessaloniki, Greece, IAG Sypmposia, Springer, Berlin, Heidelberg. https://doi.org/10.1007/1345_2017_15.
13. Godah W., Szelachowska M., Krynski J., (2017b): *On the estimation of physical height changes using GRACE satellite mission data - A case study of Central Europe*, Symposium of the IAG Subcommission for Europe (EUREF) held in Wroclaw, Poland, 17–19 May 2017 http://www.euref.eu/symposia/2017Wroclaw/02-10-Godah.pdf; Geodesy and Cartography, Vol. 66, No 21, pp. 213-228, DOI: 10.1515/geocart-2017-0013.
14. Godah W., Szelachowska M., Krynski J., (2017c): *On the analysis of temporal geoid height variations obtained from GRACE-based GGMs over the area of Poland*, 1st Joint Commission 2 and IGFS Meeting Symposium GGHS2016 "Gravity, Geoid and Height Systems 2016", 19–23 September 2016, Thessaloniki, Greece, Acta Geophysica, 2017, DOI: 10.1007/s11600-017-0064-3.
15. Godah W., Krynski J., Szelachowska M., (2017d): *The use of absolute gravity data for the validation of Global Geopotential Models and for improving quasigeoid heights determined from satellite-only Global Geopotential Models*, Journal of Applied Geophysics, doi:10.1016/j.jappgeo.2018.03.002.
16. Godah W., Szelachowska M., Krynski J., (2017e): *Application of the PCA/EOF method for the analysis and modelling of temporal variations of geoid heights over Poland*, Acta Geodaetica et Geophysica, Vol. 53, Issue 1, pp. 93-105, DOI 10.1007/s40328-017-0206-8
17. Krynski J., Rogowski J.B., (2016): *National Report of Poland to EUREF 2016*, Symposium of the IAG Subcommission for Europe (EUREF) held in San Sebastian, Spain, 25–27 May 2016,
18. Krynski J., Rogowski J.B., (2017): *National Report of Poland to EUREF 2017*, Symposium of the IAG Subcommission for Europe (EUREF) held in Wroclaw, Poland, 17–19 May 2017
19. Kryński J., Sękowski M., (2017): *Rocznik Astronomiczny na rok 2018*, Instytut Geodezji i Kartografii, Warszawa, (ed.) J. Kryński, (90 pp).
20. Krynski J., Zak Ł., Ziolkowski D., Cisak J., Lagiewska M., (2017a): *Estimation of height changes of GNSS stations from the solutions of short vectors and PSI measurements*, Geodesy and Cartography, Vol. 66, No 1, pp. 73-88, DOI: 10.1515/geocart-2017-0008.
21. Krynski J., Zak Ł.,Ziolkowski D., Lagiewska M., Cisak J., (2017b): *Joint estimate of height changes from GNSS solutions of short vectors and PSI measurements using Envisat and TerraSAR-X satellite data*, Symposium of the IAG Subcommission for Europe (EUREF) held in Wroclaw, Poland, 17–19 May 2017
22. Sękowski M., Dykowski P., Kryński J., (2016): *New iGrav superconducting gravimeter station in Central Europe at the Borowa Gora Geodetic-Geophysical Observatory*, Geoinformation Issues, Vol. 8, No 1, Warsaw, pp. 5-17.
23. Sośnica K., Bosy J., Kaplon J., Rohm W., Hadaś T., Sierny J, Kudłacik I., Zajdel R., Kryński J., Dykowski P., Araszkiewicz A., Mutke G., Kotyrba A., Olszewska D., (2017): *Densification of the GGOS infrastructure in Poland in the framework of EPOS-PL*, Symposium of the IAG

Subcommission for Europe (EUREF) held in Wroclaw, Poland, 17–19 May 2017 http://www.euref.eu/symposia/2017Wroclaw/02-10-Godah.pdf.
24. Wilde-Piorko M., Dykowski P., Polkowski M., Olszak T., Grad M., Krynski J., Sekowski M., Krankowski A.,Rajner M., (2017): *Expanding seismic surface waves measurements towards low periods with gravity measurements*, Geoinformation Issues (in print).
25. Ziolkowski D., Lagiewska M., Krynski J., Cisak J., Zak L., Kolodziejczyk M., Uchanski J., Falkowski P., Sadura K., Lukasik S., Godlewski T., (2016): *Deformation studies in Warsaw using Persistent Scatterer Interferometry based on COSMO-SkyMed and ENVISAT data*, ESA Living Planet Symposium 2016 and 6th GOCE User Workshop, 9 – 13 May 2016, Prague, Czech Republic.
26. Żak Ł., Krynski J., Ziółkowski D., Cisak J., Łągiewska M., (2016): *Hight changes of GNSS stations from the solutions of short vectors and PSInSAR measurements*, IAG Commssion 4 Symposium „Positioning and Applications", Wroclaw, Poland, 4-7 September 2016.

Faculty of Civil and Environmental Engineering, Gdansk University of Technology (GUT) M. Figurski, G. Nykiel

Since 2017 at Faculty of Civil and Environmental Engineering of Gdansk University of Technology a new group was formed, whose main goal is to conduct research related to satellite geodesy. Below a brief review of the current studies are presented.

Monitoring of the terrestrial reference frame

The main goal of this task was to launch computational system based on the Bernese GNSS Software Version 5.2 at Gdansk University of Technology. Thanks to that research related to the monitoring of the terrestrial reference frame can be conducted. First results were presented by Figurski and Nykiel (2017) where the impact of ITRS2014/IGS14 on the positions of the reference stations in Europe were investigated. In January 2017 a new realization of the ITRS, ITRF2014 had been introduced. It is characterized by high consistency with the previous ITRF2008 solution. Despite the great consistency of the ITRF solution itself, the introduction of the new satellite and ground antennas phase center calibrations in IGS14 leads to non-negligible differences in station positions. The updated antenna phase center models cause a change in the scale of the network, which we estimated at around 0.7 ppb. Also the translation parameters are changed, for all translation components, while the network orientation remains unchanged. Scale changes cause changes in baselines length between the stations (in most cases we obtained increased length). We also showed that the variable number of fixed reference stations in the GNSS local networks affects only the translation of the frame, and the change of its parameters is correlated with the number of fixed reference stations.

Our analysis confirmed that the differences between ITRF2008 and ITRF2014 are minor. However, changing GNSS antenna calibrations from IGb08 to IGS14 causes changes of stations coordinates up to several millimetres, especially for the vertical component. This effect is mainly due to the introduction of new or updated absolute antenna calibrations. Such changes of coordinates have also impact on the realization of the European Terrestrial Reference Frame (ETRF). In order to present impact of new reference frame and improved antenna models on stability of EPN stations, we show coordinate time series for two stations POTS00DEU (Potsdam, Germany) and DARE00GBR (Daresbury, UK), which antennas have been changed between IGS08.atx and IGS14.atx. At the first station individual calibration was introduced (instead of type mean) and at the second one, the improved type mean calibration was presented. For these stations we estimated coordinates in IGb08 frame with IGS08 antennas calibrations (dotted line in Figure 1.9) from 1928 to 1933 GPS week and in IGS14 frame with IGS14 antennas calibrations (solid line in Figure 1.9) from 1928 to 1937 GPS week. Geocentric coordinates were converted to the local topocentric frame (NEU).

Presented in the paper results are obtained based on the Bernese double difference GNSS processing, which assumes the use of constrained stations and fixed satellite ephemeris to estimate positions in ITRFyy. This becomes a problem where studies about the impact of different phase center calibration on position are carried out. Therefore, further research on this issue should concern the elaboration of the investigated network using PPP method (if obtained accuracy will be on the level of differential method), in which the reference frame is transferred to the points using only satellite ephemeris. Only in this way the quantitative and qualitative influence of the new IGS14 antenna calibration on the implementation of ITRF2008 in Europe can be investigated. However, based on the analysis carried out in this paper, it is clear that the only method that will effectively remove the discontinuities caused by the new antenna calibrations is the third reprocessing of archived GNSS observations.

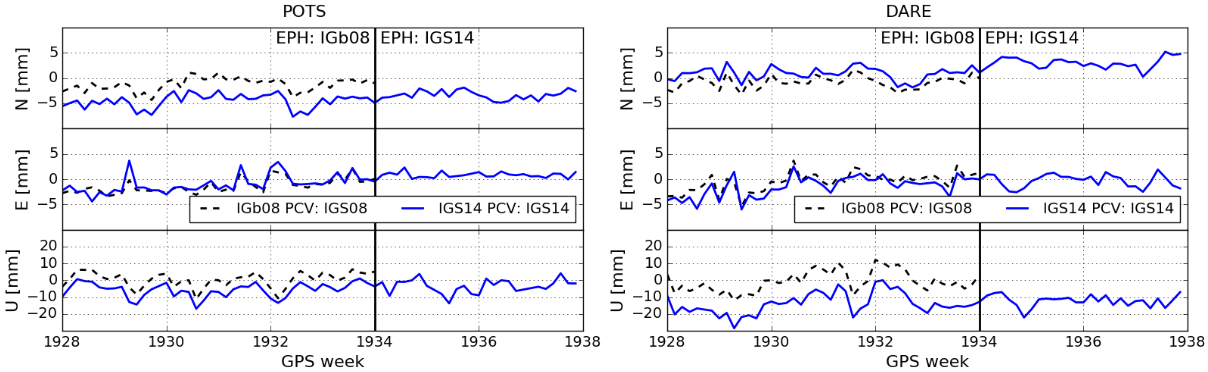

Fig. 1.9. Positioning results (w.r.t. IGb08 EPN cumulative solution at 1934 GPS week) for stations POTS00DEU (Potsdam, Germany) and DARE00GBR (Daresbury, UK).

1. SATELLITE GEODESY

Multi-GNSS

One of the most studies which are on time are these related to the multi-GNSS processing. This also a task in GUT where researches focused on the impact of Galileo observations on multi-GNSS positioning and products are conducted. In one of our paper (Nykiel and Figurski 2017) we presented positioning results obtained with five different combinations of GNSS systems: GPS, Galileo, GPS/Galileo, GPS/GLONASS and GPS/GLONASS/Galileo. In first place we focused on the precision of the position determination. Based on the presented results, we can conclude, that results obtained using Galileo only observation are characterized by the highest standard deviation of the analysed solutions. This is due to the low number of the Galileo satellite. However, even when the constellation is not completed, the differential precise positioning using only Galileo observations can be performed with the horizontal and vertical precision below 1 cm (Figure 1.10). The Galileo observations have significant impact on the multi-GNSS positioning results. Among the analysed solutions, the highest horizontal coordinates precision was obtained when GPS and Galileo observations were performed together. We received the results amounting to 1.95 and 1.96 mm respectively for North and East coordinates. Presented results are even better than the GPS/GLONASS solution. However, this solution gave us better precision in case of Up coordinate, which amounted 5.35 mm (for comparison, GPS_GAL: 5.96 mm). This result is probably caused by the larger number of GLONASS satellites than Galileo, which translates to better geometry of the satellites. However, the GPS_GAL solution enabled us to obtain the lowest bias values for all coordinates.

Besides the positioning results, we also analysed the ambiguities resolution for wide-lane and narrow-lane linear combination (Figure 1.11). After the EOC and the few weeks before that date, the mean ambiguities resolution for the Galileo satellites amounted to 80.85±4.31% and 70.97±5.68%, for WL and NL respectively. In case of multi-GNSS positioning, the best results of ambiguities resolution for GPS and Galileo satellites were obtained for GPS_GAL solution. In that case the mean value of the WL ambiguities resolutions was 79.15±3.45% for GPS and 93.14±2.45% for Galileo. Based on presented studies we conclude that the best results, both in case of position determination and ambiguities resolution, were obtained for GPS/Galileo solution. Presented results are better than the GPS/GLONASS solution (which is used and recommended by the EUREF) and even when all satellites systems were used (GPS/GLONASS/Galileo). In near future the increasing number of Galileo satellites should be expected. Thus, the positioning precision should be even better especially in case of the Up coordinate. In this case, it seems that position determination using GPS/Galileo will be more efficient than GPS/GLONASS or even GPS/GLONASS/Galileo. Especially, if we take into account the computation time of multi-GNSS observations.

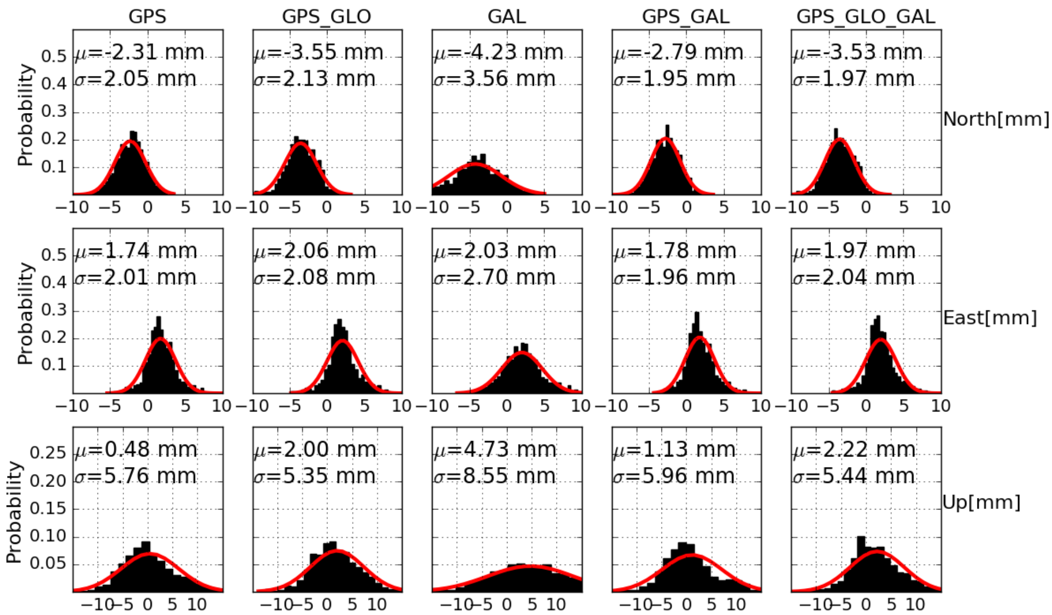

Fig. 1.10. Histograms of the residuals for all analyzed solutions after week 1920. From the top: North, East and Up coordinates.

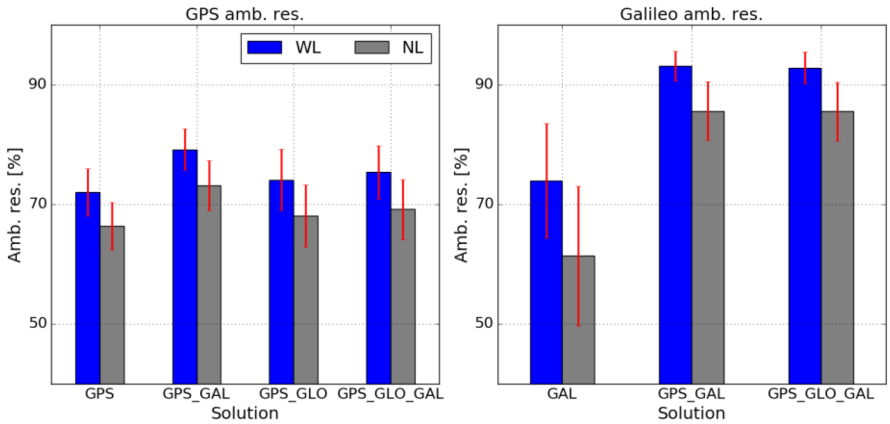

Fig. 1.11. Mean percentage of GPS (left) and Galileo (right) WL (blue) and NL (grey) ambiguities resolutions for tested solutions.

We also presented differences of antenna Phase Center Corrections (PCC) between antenna individual calibration for Galileo E5 frequency and for GPS L2 frequency. We obtained results between -6 and 8 mm. Such big differences show that copying calibration from L2 to E5, as was often done before, can cause significant errors. We also showed preliminary Galileo-only positioning results with E5 frequency antenna calibration. For four tested stations we obtained bias (especially in Up direction) between Galileo solution with individual calibration and with copied from GPS L2. These biases can be caused by the network error propagation, because for other stations of our tested network, as a Galileo E5 calibration we used data from GPS L2. Thus, usage of antenna models for Galileo frequencies seems to make sense only when all station in the network support such calibration. In Fig. 2.3.4 Galileo only positioning results for BRUX station are presented. Two solutions are shown: GAL_14, marked with red line, where individual calibrations were used; and GAL, grey line, where calibration for Galileo E5 were copied from GPS L2. Based on the presented results some bias between solutions is seen, especially in Up coordinate and reached 8.58 mm
(bias for GAL_14: 4.54 mm, GAL:-4.04 mm). Smaller bias, which is about 1 mm, can be seen in North and East direction. It is worth to notice, that use of individual calibration caused only bias change without changing the standard deviations.

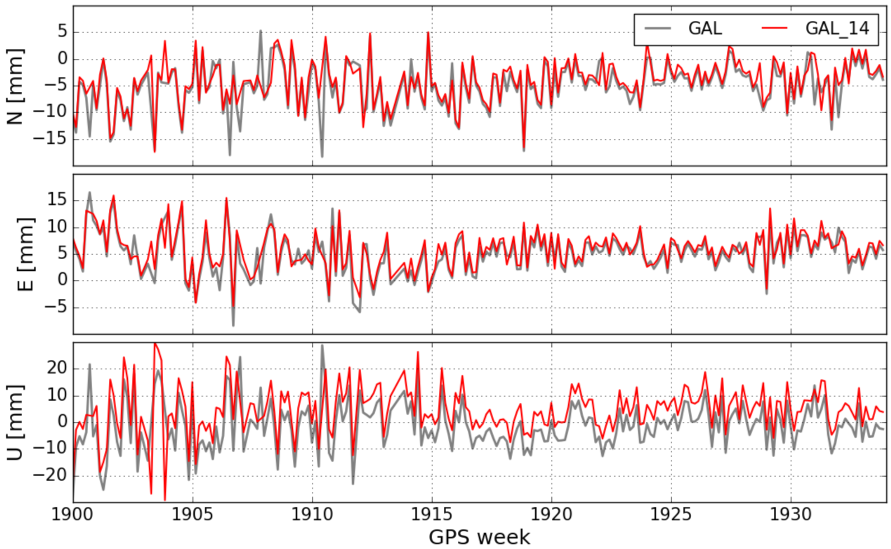

Fig. 1.12. Galileo only positioning results for BRUX station for two solutions: with IGS14 antenna model - GAL_14 (red line); GAL (grey line).

We also investigated impact of Galileo observations on tropospheric parameters (Baldysz et al. 2017). Obtained results showed, that usage of only Galileo-only solution does not provide as precise solutions as in case of e.g. GPS. However, the addition of its observations to observations from the other satellite systems, positively affect final solutions. We analysed five different satellite combinations: GPS-only, Galileo-only, GPS/Galileo, GPS/GLONASS, and GPS/GLONASS/Galileo, for the two periods of time, which covered one year (02.2016– 02.2017) and nearly EOC (10.2016 – 02.2017) time span. Obtained results were compared to the combined, official EPN product. As we expected, not sufficient number of satellites at the beginning of the analysed period, resulted in much higher standard deviation of Galileo results, compared to the other ones (more than 10 mm for most of stations in case of Galileo, and less than 2 mm in case of other combinations). The results quality has improved in nearly EOC period of time (reduction of standard deviation to about 6 mm), however it is still not as high as in case of rest of considered here solutions. It is worth to noticed, that after EOC, addition of Galileo observations to the e.g. GPS caused slightly improvements in obtained ZTD values, which were on the similar level as in case when GLONASS observations were added. Multi GNSS solution is characterized by the highest quality (in term of standard deviation).
Besides the ZTD, we also analysed the results of tropospheric gradients. In case

of only Galileo observations their values, both in case of North and East components, were significantly higher than e.g. GPS gradients, especially before the EOC. However, after EOC, it seems that addition of a Galileo observations to the GPS ones resulted in higher consistency of gradients value (w.r.t. to GPS) than adding a GLONASS observations. Next to the increase of the number

of Galileo satellites, improvement of the Galileo only solutions can be achieved thanks to the new standard of antennas calibrations (IGS14). ZTD bias time series obtained without and with calibrations for Galileo signals, showed a decrease of ZTD bias standard deviation. New antenna calibration have also small, but positive, impact on Galileo gradients.

VLBI support via GNSS techniques

GUT established a cooperation with Centre for Astronomy, Faculty of Physics, Astronomy and Informatics of Nicolaus Copernicus University, whose main aim was to use of GNSS observations to calibrate VLBI observations. The result of this cooperation was publication (Nykiel et al. 2018) where the correlation between integrated water vapor (IWV) and atmospheric opacity (τ_0) are presented, as well as the linear regression coefficients between them. To estimate ZWD, which were converted to IWV, two GNSS processing strategies were used (PPP and DD) with two mapping functions (VMF and GMF). The calculated IWV was compared to the atmospheric opacity derived from the sky-dip method performed by the 32 m radio telescope located in Piwnice/Torun (Poland). The water vapor weighted mean temperature is necessary for both the conversion of ZWD to IWV and for the τ_0 estimation. For this purpose, we used two different methods: the Bevis method (Bevis et al. 1992), which is based on a linear regression between surface temperature and weighted mean temperature, and the Maddalena method (Maddalena and Johnson 2005), which also based on a linear regression, but accounting for the dependency on the frequency of the signal. Based on the studies conducted, it can be stated that IWV derived from GNSS observations may be used to, e.g., calibrate archived observations from radio telescopes or as a verification of obtained τ_0 values. Moreover, when the IWV is estimated in real-time mode, it can be used as a primary source of calibration data, instead of the microwave radiometer or the sky-dip method for the atmospheric opacity measurements. On the other hand, if we have the τ_0 values, they can be a valuable verification of IWV derived from GNSS processing. The coefficients of the linear regression presented in this study confirm that both PPP and DD processing strategy can be applied for above applications (Fig. 1.13).

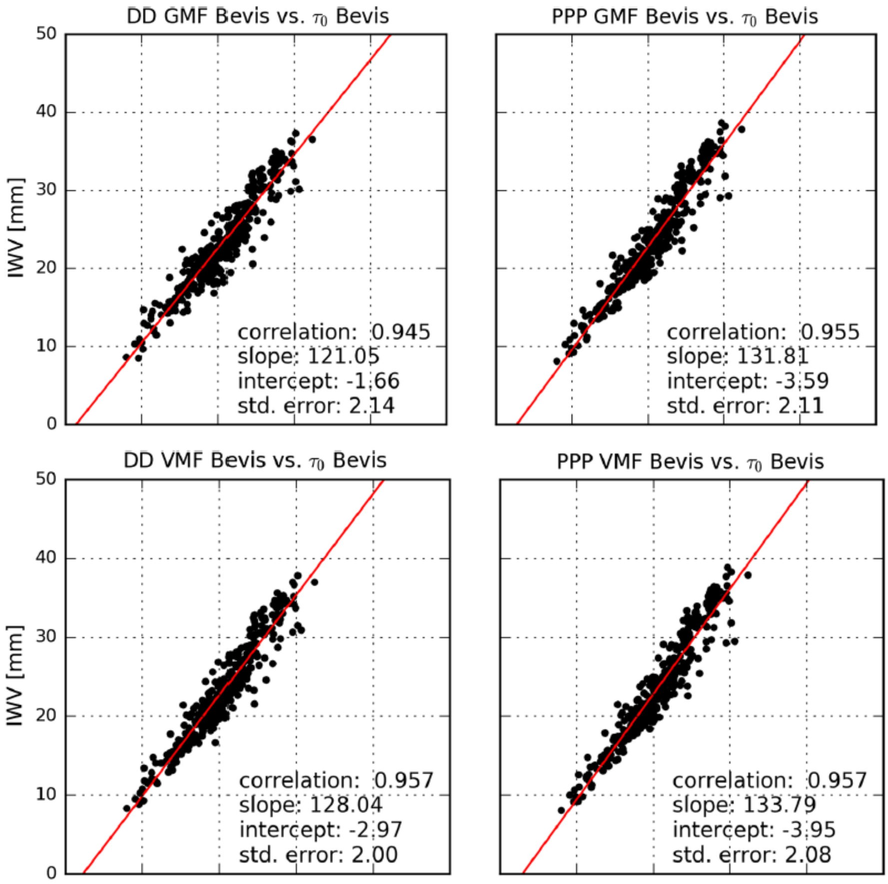

Fig. 1.13. Correlation between IWV and τ_0 derived from GNSS processing.

Detection and characterisation of ionospheric irregularities

Ionospheric studies is the purpose of the cooperation between GUT and Institute of Radio Astronomy of National Academy of Sciences of Ukraine. Studies carried out so far has allowed the develop an original solution for estimation of ionospheric total electron content (TEC) variations (Nykiel et al. 2017).
Traditionally, TEC maps suggest the use of a thin layer model of the ionosphere. Total electron content calculated according to the GNSS receivers' data refers

to the line of sight of a “satellite–receiver” characterized by elevation and azimuth. To display the TEC as a geographical map, current values are projected onto a spherical surface, which simulates the ionosphere in the form of a thin layer. Ambiguity in the choice of a spherical shell’s height is a source of uncertainty in coordinates of ionospheric pierce points (IPPs), whose position relative to different satellites and observation points varies depending on the selected layer height. This leads to the fact that local maps, based on several observed satellites’ data, depend strongly on the choice of the height of the ionospheric layer. In development method we used satellites with elevation angles over 70. Thanks to the differences due to the adopted layer height are much smaller. The maximum obtained differences never exceeded 0.5° and 0.3° in the longitude and latitude directions, respectively. The use of high elevation angle satellites allows us to obtain an ionospheric variation model immediately over the selected area and without the large errors associated with an incorrectly taken layer height. It is quite natural that there is no possibility to use this advantage at high latitudes. A high spatial resolution of the IPPs can be obtained by using the dense regional networks of GNSS stations, such as ASG-EUPOS, SAPOS, etc.

In Figure 2.3.6 representative examples of TEC variation spatial distribution are presented. These maps were obtained using development method. The possibility of build maps of TEC variations with the resolution of tens of kilometres with the temporal rate of tens of seconds is demonstrated. This allows us to analyse the structure and temporal evolution of mesoscale ionospheric irregularities. In accordance with current trends in the development of a four-dimensional (4D) geodesy, the use of the proposed methodology makes it possible to obtain and effectively use a large amount of information organized in the form of time sequences of maps.

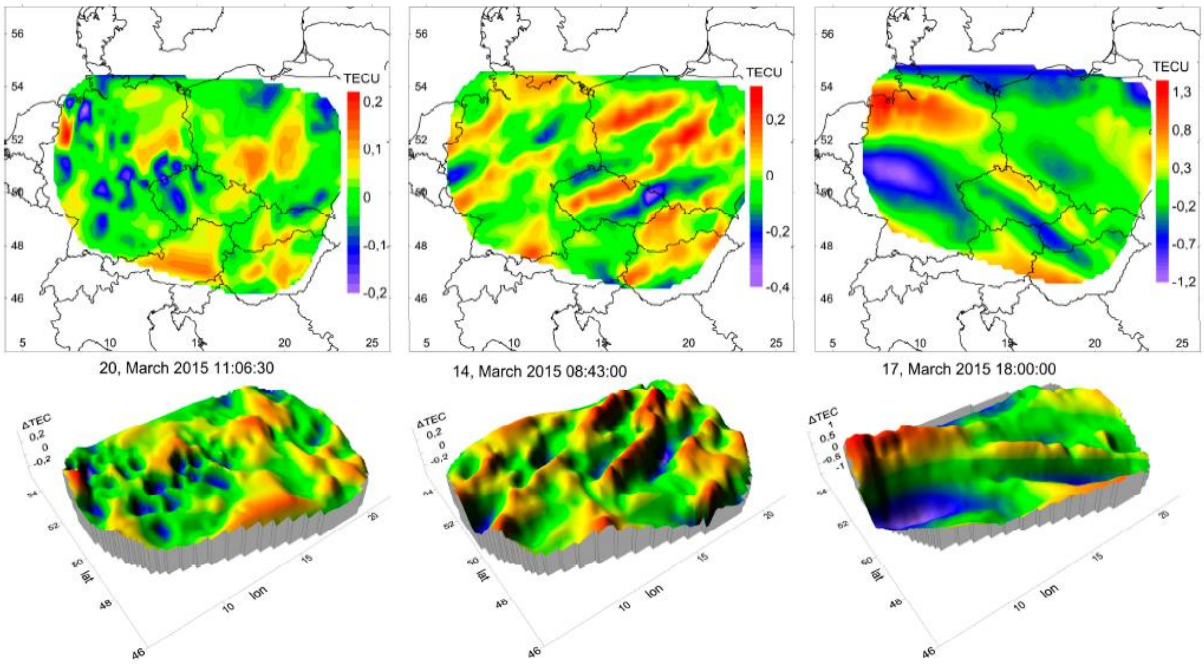

Fig. 1.14. Representative examples of TEC variation spatial distribution.

Long-term GNSS tropospheric products analysis

GNSS is a technique that has started to play important role in research related to the atmosphere. Climate applications of GNSS troposphere products, was area of interest of work conducted at the Military University of Technology and Gdansk University of Technology. Firstly, the possibility of using observations from EUREF Permanent Network (EPN) was investigated. This was done on the basis of zenith tropospheric delay (ZTD) solutions, which were obtained on the basis of GNSS processing strategy adopted for first official reprocessing of EPN (so called 'Repro1' project, 2008). Performed analysis concerned spectral analysis (Lomb scargle periodograms) and estimation of seasonal and long-term changes with using least square estimation (LSE) approach. Also, the Mann-Kendall trend test was conducted in order to confirm the presence of a linear trends estimated with using LSE. Obtained results showed that, 16-year and 18-year ZTD time series from EPN network reflects prevailing weather conditions occurring at given region. The combination of the estimated parameters such as mean ZTD value, annual amplitude value and its phase shift demonstrated climate zones at a given sites. Also estimation of long-term changes showed, that they are specific area over Europe for which occurred only positive or only negative characters of the estimated ZTD linear trend values, which probably was not accidental. Conducted analysis investigated also influence of the length of time series on the estimated linear trend values. By comparing 16-year (01.1998 – 01.2014) and 18-year (01.1996 – 01.2013) ZTD time series from these same stations it was found out that there were differences in estimated linear trend values, which reached up to 0.26 mm/year. Only four stations (out from 30) were characterized by this same value of linear trend, for both shorter and longer period of time. This has become the basis for the assumption, that further climate interpretations should be conducted only in the case of time series from these same period of time.

Obtained results confirmed the usefulness of the regional GNSS network (such as EPN) in research related to the atmosphere sensing. The next step was therefore analysis of the impact of adopted GNSS observations processing strategy on the final troposphere product. Since the first step of studies was based on the processing strategy compatible with Repro1 campaign, the second step concerned comparison of these solutions with solutions obtained according to the Repro2 strategy (more precisely it was official contribution of MUT to the EPN Repro2 project, 2014). These same stations and periods of time were taken into consideration. To preserve the highest possible reliability of the comparison results, we adopted also the same methodology as in case of Repro1 solutions. In term of seasonal signals and mean ZTD values, obtained results from these both reprcessings were similar. There were small differences as to the size of estimated parameters, however they were negligible compared to the values of these parameters. The main discrepancies between these both reprocessings occurred in term of linear trends. Despite the fact, that the distribution of the trends characters were practically the same, the differences occurred in case their values. Generally, linear trend values from Repro2 campaign were smaller than these ones obtained from Repro1 campaign. Only 2 stations had the same value of linear trend obtained on the basis of both reprocessings, 13 stations were characterized by higher linear trend value from Repro2 campaign, and 41 stations were characterized by higher linear trend value from Repro1 campaign (Figure 1.14). For the longer period of time, also the same character of differences were noticed. In this case only 3 stations from Repro2 campaign had higher trend value than corresponding result from Repro1. The rest of stations (25) had these values lower. These results showed that adopted GNSS processing strategy affect long-term analysis. However, due to the fact that these reprocessing differ from each other in terms of software, antenna calibration, elevation mask, mapping functions, ionosphere modelling and applied atmospheric loadings, it was impossible to assess which of these elements were mostly responsible for obtained linear trend value differences.

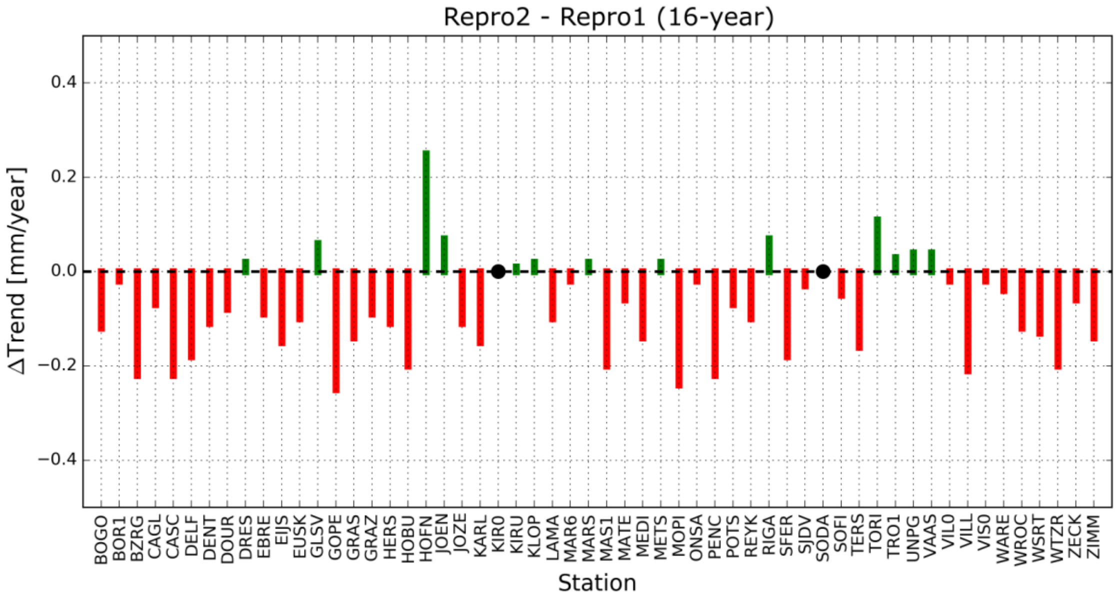

Fig. 1.15. Differences between the values of the 16-year ZTD linear trends obtained from the Repro2 and Repro1 campaigns.

To solve this problem a comprehensive investigation of the influence of adopted GNSS processing strategy on the long-term analysis was performed. Firstly, another eight reprocessings of 20 years of observations collected at 20 EPN stations were conducted. The detailed description of adopted for this purpose calculation schemes are given in Table 1.1.

Table 1.1. GNSS processing strategies used for the purpose of investigation of the influence of adopted GNSS processing strategy on the long-term analysis.

	BSW_PPP_VMF	BSW_PPP_GMF	BSW_DD_VMF	BSW_DD_GMF	GAM_DD_VMF	GAM_DD_STP	GAM_DD_GPT2	GAM_DD_EL20
software	Bernese 5.2	Bernese 5.2	Bernese 5.2	Bernese 5.2	GAMIT 10.50	GAMIT 10.50	GAMIT 10.50	GAMIT 10.50
method	PPP	PPP	DD	DD	DD	DD	DD	DD
data	daily 30-sec GPS observations from 20 EPN stations (since 01.1996 to 01.2016)							
a priori ZHD	VMF1	GPT	VMF1	GPT	VMF1	STP	GPT2	VMF1
Tropo. mapping function	VMF1	GMF	VMF1	GMF	VMF1	Niell	GPT2	VMF1
cut-off angle	5°	5°	5°	5°	5°	5°	5°	20°
High order ionospheric effects	2nd and 3rd order							
Ephemerides	CODE R2 (2013)							
Antenna models	Type mean (IGS08)							
Reference Frame	IGb08							

ZTD solutions obtained on the basis of such approaches were in next step converted to the Integrated Water Vapor (IWV), with using meteorological parameters sourced from ERA-Interim. 20-year GNSS IWV time series were in next step analyzed, with using the same methodology as in case of previous studies. Due to the fact that conversion of ZTD to the IWV is an indirect method, validation of obtained results was also conducted. For this purpose 20-year IWV time series from 20 radio sounding (RS) stations located in the area of GNSS stations were used. The comprehensive comparative analysis concerned such parameters as (i) mean IWV value, (ii) annual amplitude, (iii) semiannual amplitude and (iv) linear trend. Similar as in previous analysis, the biggest discrepancies occurred in case linear trends values. It was found out that the highest consistency between GNSS IWV and RS IWV was achieved, when Precise Point Positioning (PPP) method was applied for observations processing. This was confirmed when both GMF and VMF1 were used. The highest differences between GNSS PPP and RS were found only for these stations which are located at higher altitudes. Figure 2.3.8 represents these results. It case of differential (DD) solutions the highest accuracy was obtain when GPT2 was used for troposphere modelling.

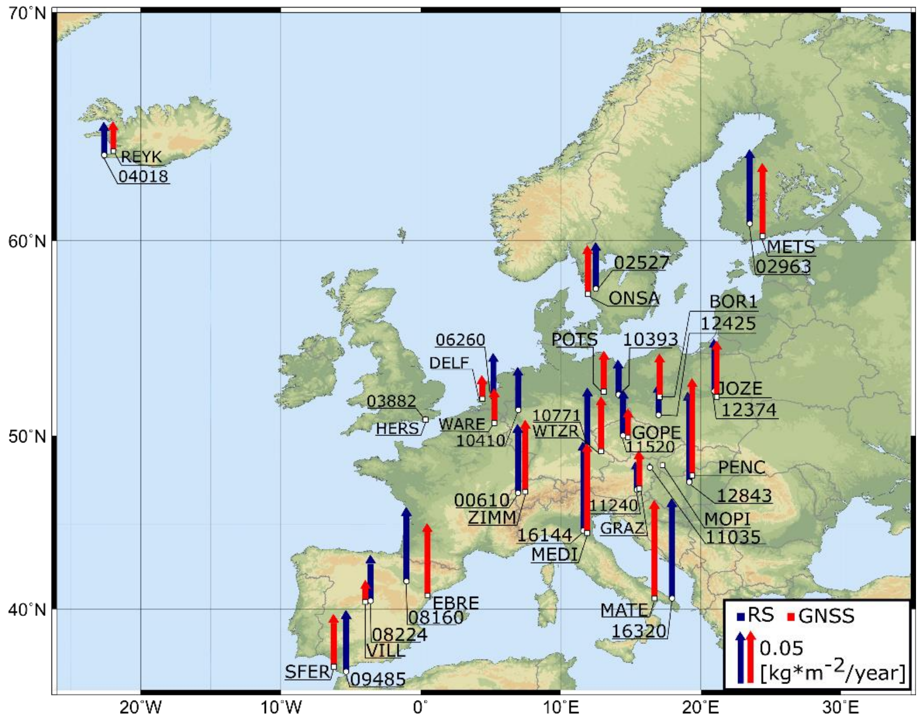

Fig. 1.16. Linear trend value for RS (navy) and GNSS PPP (red) for the 01.1996-01.2016 period of time.

1. SATELLITE GEODESY

METEOPG

Weather portal METEOPG provides weather forecasts from the high resolution version of the HRWRF 3.9.1.1 mesoscale model (High Resolution Weather Research and Forecasting). The portal is a joint venture of the Faculty of Civil and Environmental Engineering at the Gdansk University of Technology and the Academic Computer Centre in Gdansk. In the HRWRF model, optimized parameterization of physics for the Central Europe area has been applied. High resolution geographic data including topography fields, substrate roughness, land use and land cover that were obtained from domestic and foreign databases were also used. High-resolution data collected at the moment allows us to carry out calculations with the use of submerged meshes up to 100 m spatial resolution.
The HRWRF operational model uses three submerged nets with resolutions of 12.5 km, 2.5 km and 0.5 km, respectively. The second grid covers the area of Poland and the third one covers the Pomorskie Voivodeship. Weather forecasting uses data from the global model of the GFS (Global Forecast System) with a resolution of 0.25°, which contains coupled models of atmosphere, soil, ocean and sea ice. The model is run on a daily basis for four main synoptic terms 00, 06, 12, and 18 with a 60 hours forecast time. The portal is still in development and new functionalities will be added in the future. Besides weather forecasting we try to used meteorological data to improve GNSS positioning.

Academic Computer Centre in Gdansk (CI TASK)

All computations related to the GNSS and NWM are performed using supercomputer systems in Academic Computer Centre in Gdansk (CI TASK), which is part of Gdansk University of Technology.
The supercomputer systems at the Compute Center form a specific metacomputing system that consists of:

- Cluster "Tryton" - 3214 processors (Intel® Xeon® Processor E5 v3 @ 2,3 GHz, 12-core), 218 TB total system memory, Mellanox InfiniBand interconnect with FDR 56 Gb/s bandwidth. Total theoretical peak performance: 1,48 PFLOPS.
- Xeon QuadCore based cluster "Galera" - 1344 Intel Xeon QuadCore processors (5376 cores), 25 TB total system memory, 100 TB disk storage. Mellanox InfiniBand interconnect with 20 Gb/s bandwidth.
  Its computing power is exploited in parallel computations and simulations of

condensed matter, large biomolecules and fluid dynamics.
Total theoretical peak performance: 50 TFLOPS.
Linpack performance: 38.17 TFLOPS - 45th on TOP500 (June 2008)

- Itanium 2 based cluster'Holk'
  - 256 Intel Itanium 2 Dual Core with 12 MB L3cache processors, 2,3 TB total system memory, 4 TB disk storage. Mellanox InfiniBand interconnect with 10 Gb/s bandwidth.
    Its computing power is exploited in parallel computations and simulations of condensed matter and large biomolecules.
  - 32 Intel Itanium 2 Dual Core with 12 MB L3cache processors, 128 GB total system memory, 1 TB disk storage, Mellanox InfiniBand interconnect with 10 Gb/s bandwidth, theoretical peak performance 360 Gflop/s. This machine is part of National Cluster of Linux Systems (CLUSTERIX) - a distributed metacluster of a new generation.

  Total theoretical peak performance: 3.2 TFLOPS.
- SGI Altix 3700, 128 Itanium 2, 1.5 GHz processors, 512 GB RAM, 1 TB disk storage . The system has a NUMA architecture with shared memory built around a high-speed NUMAFlex bus and is used as a large-scale computation server (768 GFlops).
- SUN Fire V880, 4 x 64-bit RISC UltraSPARC III processors, 4 GB RAM, 6.4 TB disk storage. The system manages the four Sun StorEdge disk arrays, automated tape library and serves as a local file server for clusters and SGI machines
- SUN Fire V880, 8 x 64-bit RISC UltraSPARC III processors, 8 GB RAM, 3.2 TB disk storage. This machine manages the two Sun StorEdge disk arrays and serves as a network file server for FTP and Usenet services
- SUN Enterprise 5000, 8 x 64-bit RISC UltraSPARC processors, 8 GB RAM, 1 TB disk storage, 8 GFLOPs. Its significant feature is a high-speed GigaPlane bus that can process up to seven transmissions simultaneously. The system manages the SPARCstorage Array and serves as a network file server.
- Managed by IBM Tivoli Storage Manager software archive system, containing Adic Scalar i2000 automated tape library (100 TB) and Sun StorEdge disk array (50 TB).

Publications (since 2017):

1. Baldysz, Z.; Nykiel, G.; Figurski, M.; Araszkiewicz, A. (2018) Assessment of the Impact of GNSS Processing Strategies on the Long-Term Parameters of 20 Years IWV Time Series. *Remote Sens*. 10(4), 496, doi:10.3390/rs10040496

1. SATELLITE GEODESY

2. Nykiel G., Wolak P., Figurski M. (2018) Atmospheric opacity estimation based on IWV derived from GNSS observations for VLBI applications. *GPS Solutions*, 22:9, DOI: 10.1007/s10291-017-0675-9
3. Calka, B., Bielecka, E., and Figurski, M. (2017). Spatial pattern of ASG-EUPOS sites. *Open Geosciences*, 9(1), pp. 613-621. doi:10.1515/geo-2017-0046
4. Zanimonskiy Y.M., Dudnik O.V., Nykiel G., Figurski M. (2017) Investigation of some magnetospheric phenomena of geomagnetic storm on March 17, 2013 based on observations from GNSS and NOAA-15 satellite. *Proceedings of 6th International Radio Electronic Forum (IREF'2017). International Scientific Conference "Radars. Satellite navigation. Radiomonitoring*", Kharkiv, Ukraine, 24-26 October, 2017, pp.196-199
5. Nykiel G, Zanimonskiy YM, Yampolski YM, Figurski M. (2017) Efficient Usage of Dense GNSS Networks in Central Europe for the Visualization and Investigation of Ionospheric TEC Variations. *Sensors*, 17(10):2298, DOI: 10.3390/s17102298
6. Figurski M., Nykiel G. (2017) Investigation of the impact of ITRF2014/IGS14 on the positions of the reference stations in Europe. *Acta Geodyn. Geomater.*, 14, No. 4 (188), 401–410, doi: 10.13168/AGG.2017.0021
7. Nykiel G., Figurski M. (2017) Impact of Galileo Observations on the Position and Ambiguities Estimation of GNSS Reference Stations, *2017 Baltic Geodetic Congress (BGC Geomatics)*, Gdansk, Poland, pp. 225-231, DOI: 10.1109/BGC.Geomatics.2017.11
8. Baldysz Z., Szolucha M., Nykiel G., and Figurski M. (2017) Analysis of the Impact of Galileo Observations on the Tropospheric Delays Estimation, *2017 Baltic Geodetic Congress (BGC Geomatics)*, Gdansk, Poland, pp. 65-71, DOI: 10.1109/BGC.Geomatics.2017.22
9. Bobkowska K., Nykiel, G., Tysiac P. (2017) DMI measurements impact on a position estimation with lack of GNSS signals during Mobile Mapping, *IOP Conf. Series: Journal of Physics: Conf. Series* 870 012010 doi:10.1088/1742-6596/870/1/012010

Department of Civil Engineering and Geodesy, Military University of Technology A. Araszkiewicz

GNSS analysis in the frame of EUREF

MUT is recognized as one of the sixteen EPN Analysis Centre providing final and rapid EPN solution. Currently MUT AC processes data from 142 EPN stations. These stations are distributed homogenously among the Europe (Fig. 2.4.1). Since GPS week 1798 8 stations (ARJ6, JON6, NOR7, OVE6, SVE6, UME6, VIL6, VIS6), since GPS week 1812 3 stations (LEK8, OST6, SKE8) and since GPS week 1940 4 stations (KEV2, KILP, KIV2, MET2) were added to MUT subnetwork. The last update of the processing strategy took place in 2017 (GPS week 1980) and MUT AC uses Gamit/Globk v. 10.61 since then.

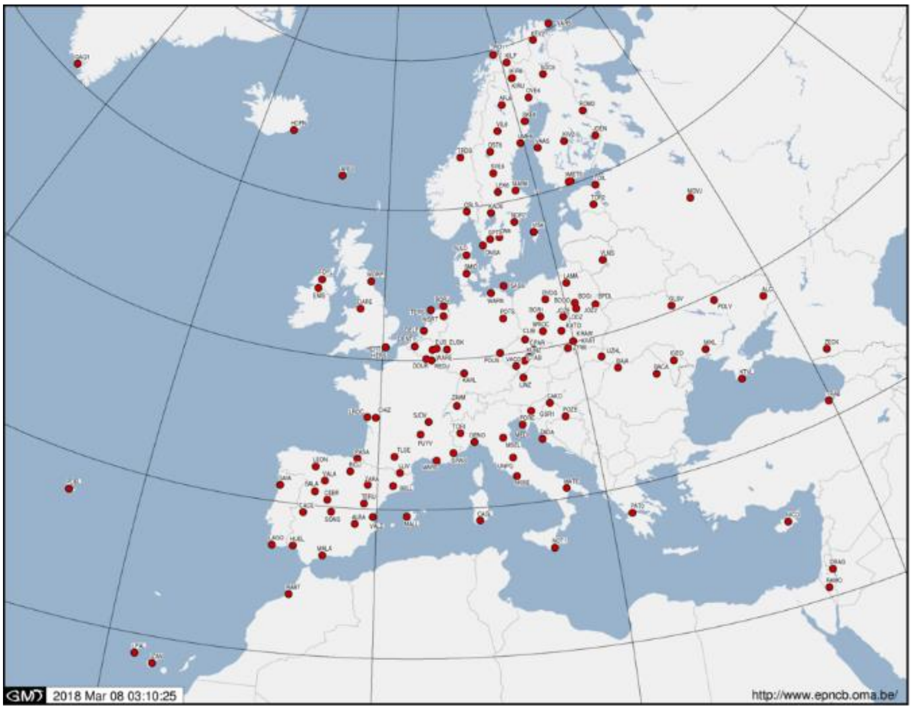

Fig. 1.17. Subnetwork processed by MUT AC (2018, http://www.epncb.oma.be/).

MUT AC also participated in the new latest campaign of EPN Reprocessing project and provided solutions for the entire network. The processing was done for GPS weeks 835-1771 (~18 years) using GAMIT software. In the frame of this project the analysis of the impact of different source of the receiver antenna PCCs (Phase Centre Corrections) were conducted. Research was carried out also on the long-term changes of the GNSS tropospheric delay and its possible use for climate studies.

Routine solutions from all of the EPN AC's are combined by the Analysis Combination Centre (ACC) run by consortium of the Military University of Technology and the Warsaw University of Technology. All combinations are performed with Bernese 5.2. Weekly and daily final positions products are delivered on the basis of 16 individual ACs solutions, while rapid daily and ultra-rapid solutions use input from consecutively 13 and 3 ACs. ACs were encouraged to consider submission of rapid and ultra-rapid solutions to strengthen the reliability of these products. All reports are distributed using EUREF and AC mail system and are available at ftp://epncb.oma.be/pub/product/combin/WWWW. Additionally EPN ACC webpage (http://www.epnacc.wat.edu.pl) presents results of final, rapid and ultra-rapid combinations. For the final ones agreement between ACs solutions for all EPN stations separately for horizontal and vertical components, Helmert transformation parameters of all input solutions wrt the combined one and time series of all stations input residuals wrf to the position resulted from combination. Rapid and ultra-rapid analysis are performed mainly for the purpose of network monitoring. Characteristics of rapid combination can be found at the BKG product center (ftp://igs.bkg.bund.de/EUREF/products/WWWW/eurWWWWDr.sum).

Permanent monitoring of GNSS reference stations

In 2012 MUT launched operationally GNSS permanent networks monitoring service, while in 2015 the system was upgraded. The latest release uses the observations from over 400 permanent stations located in Poland and neighbouring countries. At the moment four GNSS networks are monitored: national ASG-EUPOS and three private: VRSnet.pl, SmartNet Poland and TPI NetPro (Fig. 1.18). Since 2017 MUT began processing of all data in common way and joint adjustment to ensure the consistent and unified reference frame in the frame of EPOS programme. Currently the results of the analyses conducted by MUT (available with approximately 20-hour delay) can be followed on dedicated website.

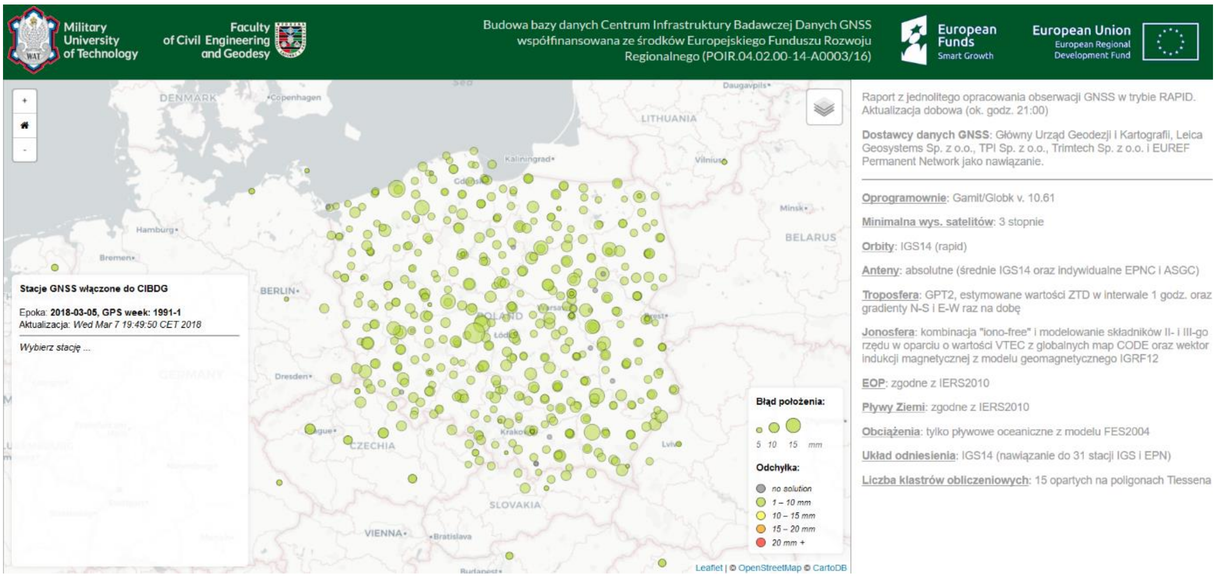

Fig. 1.18. GNSS reference stations monitored by MUT
(2018, http://www.cgs.wat.edu.pl/gnss/mut_gnssr.html).

GNSS and GPS-SLR time series analysis.

The Centre of Applied Geomatics analyses the GPS (from ASG-EUPOS and EPN networks) and SLR time series in terms of reliable velocities estimation. These velocities with their uncertainties are the input data in numerous geodynamical analyses and most of all, determination of kinematic reference frames. The modelling of deterministic part of time series as the sum of trend, seasonal components (annual and semi-annual ones), outliers and offsets with advanced mathematical methods provides the stochastic part of these time series. We then focus on the time series residua and their character. The so-called noise analysis made for the residua tells a lot about possible causes of such a character with pointing on the amplitude and spectral indices of noises. They strictly affect the velocities' uncertainties that can be underestimated by a factor of even 11 when assuming the wrong noise character (Fig. 1.19). The CAG has already made a number of analyses that gave a wide view on the GPS and SLR time series. We modelled the deterministic part of time series with least-squares method as well as wavelet decomposition with Meyer wavelet. The wavelet decomposition has an advantage over LS method, which due to the assumption of fixed amplitudes and phases of seasonal components in time does not work well for such a time-changeable data. The Lomb-Scargle's periodograms made for GPS time series proved the existence of seasonal components with the amplitudes of few millimetres. We use Median Absolute Deviation Criterion for outliers removal and the combination of standard deviation and sequential t-tests (STARS) to deal with offsets. The character of time series is being determined with spectral analyses (SA) and Maximum Likelihood Estimation (MLE). The performed researches showed that the noises in the GPS time series follow the flicker noise model with the amplitudes of few millimetres what is quite consistent with the previously published papers of noise analysis. It clearly demonstrates that the time series residua are self-similar with the hyperbolically decaying autocorrelation function and proven long-range dependencies. The already made analyses proved also the spatial dependencies between GPS stations and pointed on the fact that spatio-temporal filtering of this data is necessary to remove the so-called common mode error (CME). The GPS-SLR co-located stations have been already analysed with wavelet decomposition to model the seasonal changes for both of them and investigate on the time-changeable amplitudes and phases.

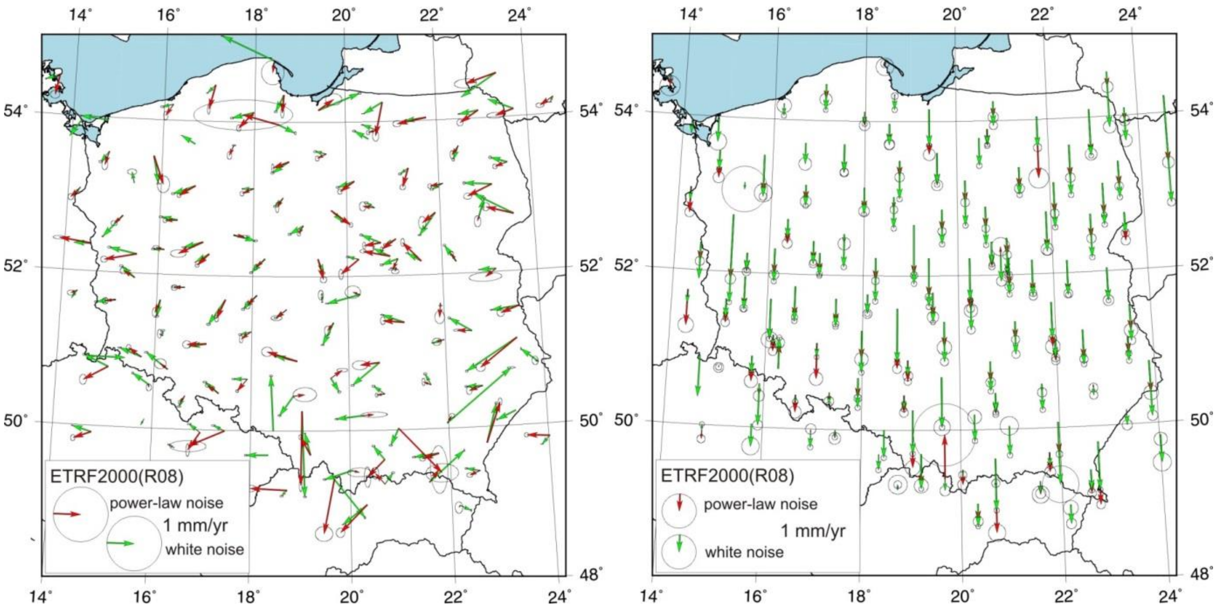

Fig1.19. The permanent stations' velocities for ASG-EUPOS network in the ETRF2000(R08) reference frame. The velocities' uncertainties were showed with different assumptions of noise models and determined with Maximum Likelihood Estimation.

Development of Satellite Observatory of CAG MUT

At the end of 2015 at the Military University of Technology the project "Development of Satellite Observatory of Centre of Applied Geomatics at Military University of Technology" has been completed. It was realized within the Regional Operational Programme of the Mazovian district 2007-2013 and its total value amounted to almost 1 100 000 EUR (funding level – 85%).

The main objective of this project was further development of the CAG MUT Satellite Observatory. This task was done by increasing the technical capabilities of analysing GNSS signals and creating a hardware base for scientific research and industrial applications related to this field. As a result, the CAG MUT research potential has increased significantly and became one of the best equipped laboratories in the region. Moreover, thanks to the implementation of certain solutions, as the purchase of GNSS signal simulator, CAG MUT has become one of the best equipped research centers in Europe. This resulted in an increase in the competitiveness of the solutions developed by CAG MUT, thus allowing chance of participation in various national projects and projects organized by the European Space Agency. In addition CAG MUT has become the ideal

partner for science and research for companies from Mazovia region, who are looking for advanced tools for verification and certification of their products associated with satellite techniques. Additional support of experienced employees of CGS MUT may contribute to the implementation of numerous R&D projects.
During the project advanced technical solutions related to satellite navigation were purchased, such as: GNSS signal simulator, software receiver, high frequency GNSS receiver and microwave radiometer.

EPOS – European Plate Observing System

The GNSS observational infrastructure in Poland is dispersed between scientific institution, governmental centres and private companies. These stations continuously perform GNSS observations and are used to support real-time geodetic measurements. In addition to their intended purpose, they are valuable in the point of view of scientific research in the field of Earth Sciences. In 2017 the project EPOS-PL was launched. This project is co-financed by the European Union from the European Regional Development Fund and is implemented by scientific-industrial consortium (https://epos-pl.eu/). The general objective one of the tasks is to provide GNSS data and products for scientific purpose and ultimately to integrate with GNSS Data & Products TCS developed by WP10 in the frame of EPOS-IP programme. As a part of their plans is to construct the National GNSS Data Repository located at the Military University of Technology and to implement procedures for verification the quality and standards of their data storage.

Publications:

1. Bukala J., Damaziak K., Kroszczynski K., Krzeszowiec M., Malachowski J., *Investigation of parameters influencing the efficiency of small wind turbines*. Journal of Wind Engineering and Industrial Aerodynamics 146:29-38, DOI: 10.1016/j.jweia.2015.06.017
2. Klos A., Bogusz J., Figurski M., Gruszczynski M., *Error analysis for European IGS stations. Studia Geophysica et Geodaetica*, DOI: 10.1007/s11200-015-0828-7
3. Bałdysz, Z., Nykiel, G., Figurski, M., Szafranek, K., and Kroszczyński, K., *Investigation of the 16-year and 18-year ZTD Time Series Derived from GPS Data Processing*. Acta Geophys. 63, 1103-1125, DOI: 10.1515/acgeo-2015-0033
4. Kroszczyński, K., *Angular Distributions of Discrete Mesoscale Mapping Functions* . Acta Geophys. 63, 1126-1149, DOI: 10.1515/acgeo-2015-0035
5. Bogusz J., Kłos A., *On the significance of periodic signals in noise analysis of GPS station coordinates time series*. GPS Solutions, DOI: 10.1007/s10291-015-0478-9

6. Bukała J., Damaziak K., Krzeszowiec M., Karimi H.R., Kroszczynski K., Małachowski J., *Modern small wind turbine design solutions comparison in terms of estimated cost to energy output ratio*. Renewable Energy 11/2015; 83:1166-1173. DOI:10.1016/j.renene.2015.05.047
7. Bogusz J., Kłos A., Figurski M., Kujawa M., *Investigation of long-range dependencies in daily GPS solutions*. Survey Review, DOI: 10.1179/1752270615Y.0000000022
8. Kłos A., Bogusz J., Figurski M., Gruszczyńska M., Gruszczyński M., *Investigation of noises in the weekly time series*. Acta Geodynamica et Geomaterialia, Vol. 12, No. 2(178), xx1–x10, DOI: 10.13168/AGG.2015.0010

9. Figurski M., Araszkiewicz A., Szafranek K., Nykiel G., Podkowa A., *CGSrefmon 2.0 - coordinates stability monitoring system of polish GNSS reference stations*, 15th International Multidisciplinary Scientific GeoConference SGEM 2015, www.sgem.org, SGEM2015 Conference Proceedings, ISBN 978-619-7105-35-3 / ISSN 1314-2704, June 18-24, 2015, Book2 Vol. 2, 145-152 pp, DOI: 10.5593/SGEM2015/B22/S9.018
10. Szafranek K., Araszkiewicz A., Schillak S., Figurski M., Zonik P., *Analysis of the reliability of velocities estimated on the basis of GNSS and SLR observations*, 15th International Multidisciplinary Scientific GeoConference SGEM 2015, www.sgem.org, SGEM2015 Conference Proceedings, ISBN 978-619-7105-35-3 / ISSN 1314-2704, June 18-24, 2015, Book2 Vol. 2, 63-70 pp, DOI: 10.5593/SGEM2015/B22/S9.008
11. Wrona M., *Using GNSS kinematic PPP method for vehicle positioning*, 15th International Multidisciplinary Scientific GeoConference SGEM 2015, www.sgem.org, SGEM2015 Conference Proceedings, ISBN 978-619-7105-34-6 / ISSN 1314-2704, June 18-24, 2015, Book2 Vol. 1, 907-912 pp, DOI: 10.5593/SGEM2015/B21/S8.116
12. Baldysz Z., Nykiel G., Araszkiewicz A., Figurski M. and Szafranek K., *Comparison of GPS tropospheric delays derived from two consecutive EPN reprocessing campaigns from the point of view of climate monitoring*. Atmos. Meas. Tech., 9, 4861-4877, DOI: 10.5194/amt-9-4861-2016, 2016
13. Araszkiewicz A., Figurski M., Jarosiński M., *Erroneous GNSS strain rate patterns and their application to investigate the tectonic credibility of GNSS velocities*. Acta Geophysica. Volume 64, Issue 5, Pages 1412–1429, ISSN (Online) 1895-7455, DOI: 10.1515/acgeo-2016-0057, September 2016
14. Bogusz J., Kłos A., *On the significance of periodic signals in noise analysis of GPS station coordinates time series. GPS Solutions*, Vol. 20, Issue 4, pp 655-664, DOI: 10.1007/s10291-015-0478-9
15. Bogusz, J., Kłos, A., Figurski, M., Kujawa, M. *Investigation of long-range dependencies in the stochastic part of daily GPS solutions*, Survey Review, Vol. 48, Issue 347, pp. 140-147 DOI: 10.1179/1752270615Y.0000000022
16. Kłos, A., Bogusz, J., Figurski, M., Gruszczynski, M. *Error analysis for European IGS stations*, Studia Geophysica et Geodaetica, Vol. 60, Issue 1, pp 17-34, DOI: 10.1007/s11200-015-0828-7
17. Zanimonskiy, Yevgen M., Nykiel, Grzegorz, Paznukhov, Alex V., Figurski, Mariusz, *Modeling of TEC Variations Based on Signals from Near Zenith GNSS Satellite Observed by Dense Regional Network*, Proceedings of the 2016 International Technical Meeting of The Institute of Navigation, Monterey, California, January 2016, pp. 585-590.

18. Nykiel, Grzegorz, Figurski, Mariusz, *Precise Point Positioning Method Based on Wide-lane and Narrow-lane Phase Observations and Between Satellites Single Differencing*. Proceedings of the 2016 International Technical Meeting of The Institute of Navigation, Monterey, California, January 2016, pp. 1055-1066
19. Pacione, R., Araszkiewicz, A., Brockmann, E., and Dousa, J., EPN-Repro2: *A reference GNSS tropospheric data set over Europe*, Atmos. Meas. Tech., Volume 10, Issue 5, 1689-1705, DOI: 10.5194/amt-10-1689-2017.
20. Araszkiewicz A., Völksen C., *The impact of the antenna phase center models on the coordinates in the EUREF Permanent Network*. GPS Solutions, Volume 21, Issue 2, 747-757, doi: 10.1007/s10291-016-0564-7.

Space Research Centre, Polish Academy of Sciences P. Lejba, A. Brzeziński

Activity in Satellite Laser Ranging

On April 26, 2016 SRC Borowiec laser station (BORL) successfully completed quarantine procedure provided by International Laser Ranging Service Analysis Centers
(ILRS ACs) and all results of the station were released to the public area after February 1, 2016. The quarantine bias report obtained from Joint Center for Earth System Technology/Goddard Space Flight Center (JCET/GSFC) NASA confirmed high quality of the observations of LAGEOS-1 and LAGEOS-2 provided by BORL station (Fig. 1.20).

LAGEOS 1 & LAGEOS 2

L1 78113802	PREC EST [mm]	RANGE BIAS [mm]
Mean	3.7	11.0
STD	1.6	15.6
RMS	4.0	18.7
Point	17	17

L2 78113802	PREC EST [mm]	RANGE BIAS [mm]
Mean	2.6	12.0
STD	0.6	11.9
RMS	2.6	16.3
Point	8	8

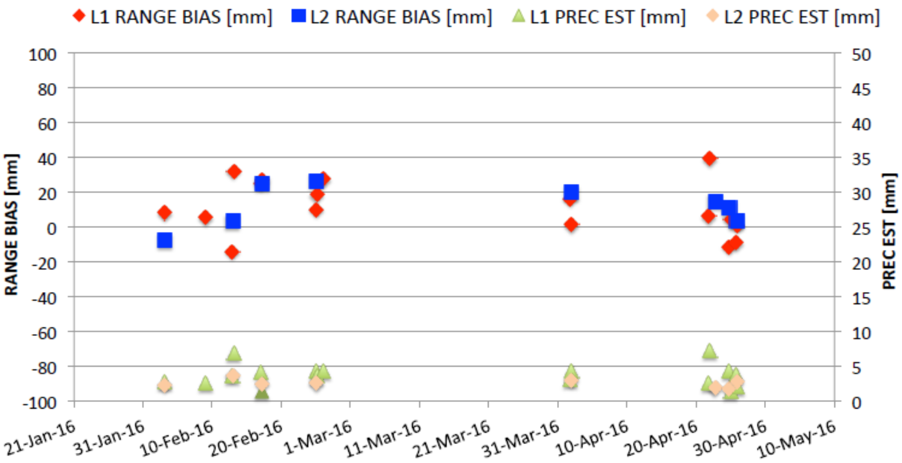

Fig. 1.20. BORL quarantine bias report.

In 2016 BORL station tracked 32 satellites, 21 LEO and 11 MEO. An AVG RMS is from 1.19 to 5.54 cm (700 passes, 664599 single good shots and 10293 normal points). All results were sent to Crustal Dynamics Data Information System (CDDIS) and Eurolas Data Center (EDC) data banks.

Additionally, in 2016 the BORL station launched regular tracking of space debris objects (inactive satellites and rocket bodies) in the frame of Space Debris Study Group (SDSG) of ILRS. A total of 151 space debris passes were performed with the AVG RMS from 1.49 to 75.33 cm (151 passes, 137836 single good shots and 2528 normal points). All results were sent to SDSG data bank. The laser measurements of SRC BORL station supports global research in satellite and space debris rotation determination, which are essential for an improvement of the theory of artificial satellites.

In 2017 the BORL station tracked 36 different objects, cooperative and uncooperative targets, in a total of 838 full passes (Fig.16). 24 of these objects were satellites: 20 LEO and 4 MEO. The average RMS ranged from 1.28 to 6.52 cm (587 passes, 564 367 returns and 9 947 normal points). All the results were

sent to the data banks at NASA's Crustal Dynamics Data Information System (CDDIS) and the Eurolas Data Center (EDC).
The other 12 objects were typical space debris, inactive (defunct) satellites and rocket bodies from the LEO regime. Space debris targets were observed in the frame of Space Debris Study Group (SDSG) of the ILRS (International Laser Ranging Service). A total of 251 space debris passes were performed with the average RMS ranging from 5.18 to 81.60 cm (251 passes, 230 901 returns and 3 529 normal points). All the results were sent to the SDSG data bank.

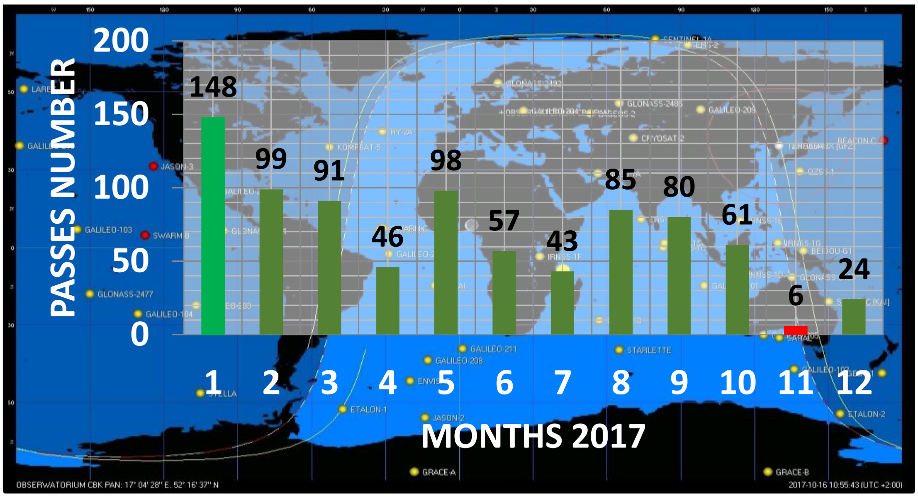

Fig. 1.21. Observational statistics for the BORL station in 2017.

Fig1.21. presents sample results for the Ocean Topography Experiment (TOPEX/Poseidon) satellite. This is a defunct satellite that has been orbiting in an uncontrolled way since 2005. The TOPEX/Poseidon mission is one of the most successful missions prepared by NASA and the CNES (France's Centre National D'études Spatiales). The spacecraft, which was launched on August 10, 1992, is huge (11.5 m x 5.5 m x 6.6 m), has a mass over 2 tons, and an altitude of about 1300 km. The satellite is equipped with an annulus RRA (retroreflector array) with 192 corner cubes. The pass duration over the station is a maximum of 12 minutes.
The main objectives of TOPEX/Poseidon included:

- monitoring of global ocean circulation,
- climate change studies,
- monitoring of the Earth's atmosphere.

On October 9, 2005, control stabilisation was lost and the satellite started to rotate. Currently TOPEX/Poseidon is spinning at about 10 s/rev and is in accelerating mode. As in the case of ENVISAT and JASON-1, the laser observations of TOPEX/Poseidon are used mainly for studies of satellite/space debris spin dynamics.

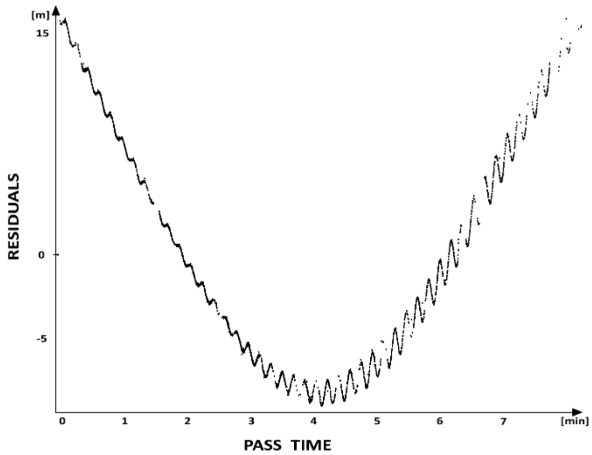

Fig. 1.22. Pass of TOPEX/Poseidon over CBK BORL station on January 27, 2017 at 03:46 UTC (2 614 returns and RMS is 38.37 cm).

In Fig. 1.22. sample results from ENVISAT are shown. This spacecraft, which belongs to the ESA, was launched on March 1, 2002. ENVISAT was assigned for remote sensing and environmental monitoring. It was one of the most successful missions in the ESA's history. Like TOPEX/Poseidon, this spacecraft has been orbiting in an uncontrolled way since 2012. It is particularly huge (26 m x 10 m x 5 m) and massive (over 8 tons).

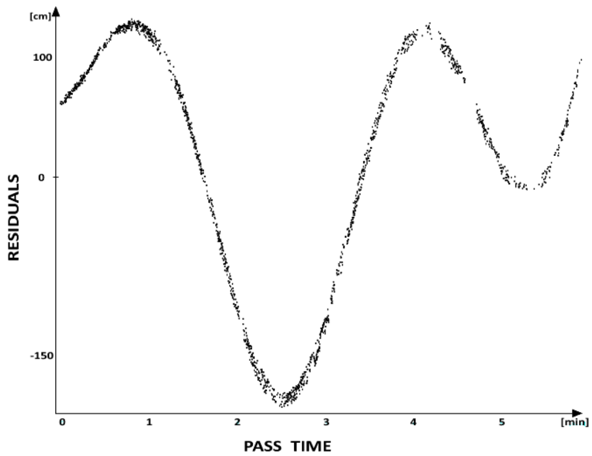

Fig. 1.23. Pass of ENVISAT over CBK BORL station on March 28, 2017 at 19:30 UTC (1759 returns and RMS is 3.61 cm).

Information about the position and behaviour in space of targets like TOPEX/Poseidon and ENVISAT is very important from the point of view of future debris removal missions. We not only need to know exactly where the defunct satellite/space debris is, we also need precise information about its rotation/tumbling and orientation in space as well. Laser measurements made by the CBK BORL station support global research in satellite and space debris rotation determination (TOPEX/Poseidon, ENVISAT, OICETS and others), which are essential for further developing the theory of artificial satellites.

At Borowiec, a second independent laser system is under development. This system is dedicated to the Space Surveillance and Tracking (SST) programme. The new system is situated on an azimuth-elevation mount with a 65 cm Cassegrain telescope (Fig. 2.5.5) equipped with servo drives that provide a tracking accuracy below 1 arcsec, and a 20 cm Maksutov guiding telescope equipped with two fast dedicated optical CMOS cameras. The whole system is controlled by multiplatform steering/tracking software (Fig. 1.25.) and will support space debris/satellite prediction, real-time laser observations, system calibration, ADSB monitoring, data post-processing and other functions. The system will operate 24 hours a day, 7 days a week. Currently, the new telescope mount is in tracking mode.

Fig. 1.24. Second independent satellite laser system developed by CBK (main telescope).

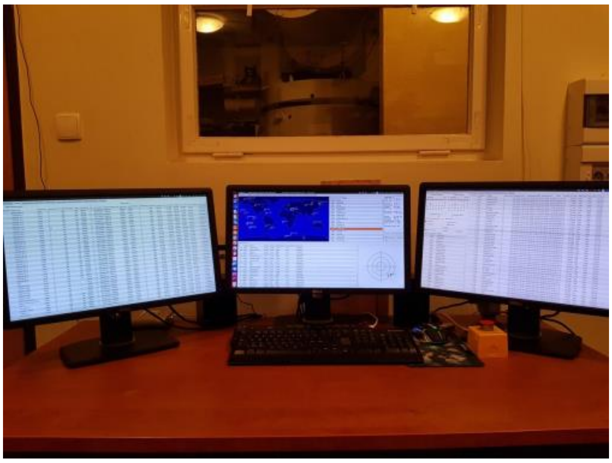

Fig1.25. Second independent satellite laser system developed by CBK (operator room).

1. SATELLITE GEODESY

A geophysical interpretation of polar motion

The global geophysical excitation functions of polar motion do not fully explain the polar motion determined by geodetic techniques. The importance of the atmospheric and oceanic angular momentum signals for the polar motion excitation at monthly (and longer) periods is well established. However, the impact of land hydrosphere mass variations on polar motion excitation is still not as widely known and understood as the role of the atmosphere and ocean.

One common method of assessing the influence of land hydrology on polar motion excitation involves comparing the hydrological excitation function (Hydrological Angular Momentum, HAM) with the observed geodetic excitation functions. The HAM can be estimated either from global models of the land hydrosphere or from variations in the Earth's gravity field. We re-estimate hydrological polar motion excitation functions using: the Gravity Recovery and Climate Experiment (GRACE) gravity fields from the most recent solutions (CSR-RL05 – Center for Space Research, Austin, U.S.A; GFZ-RL05 – Geoforschungs-Zentrum, Potsdam, Germany; JPL-RL05 – Jet Propulsion Laboratory, Pasadena, U.S.A, CNES/GRGS – Centre National d'Etudes Spatiales, Toulouse, France; HUST – Huazhong University of Science and Technology, Wuhan, P.R. China, Tongji-RL02 – Tongji University, Shanghai, P.R. China; WHU-RL01 GNSS Research Center of Wuhan University, P.R. China); the Global Land Data Assimilation System GLDAS and Hydrological Land Surface Discharge Model LSDM hydrological models; and the Coupled Model Intercomparison Project Phase 5 (CMIP5) Miroc5 and MPI-ESM-LR climate models. A hydrological signal in polar motion excitation is estimated as the difference between the observed geodetic excitation functions (Geodetic Angular Momentum, GAM), and the sum of the Atmospheric Angular Momentum (AAM) and Oceanic Angular Momentum (OAM). The study examines the agreement between geodetic residuals (GAO) and different determinations of hydrological excitation functions (HAM).

Our analyses included a comparison of global time series of non-seasonal $\chi1$ and $\chi2$ components of: mean geodetic residuals (Mean GAO), gravimetric excitation functions from GRACE (CSR, JPL, GFZ, HUST, TONGJI, WHU, CNES) and hydrological excitation functions from various models (GLDAS, LSDM, MIROC, MPI). They were conducted for short-term oscillations (periods under 730 days) (Fig. 1.26) and long-term oscillations (periods over 730 days) (Fig. 1.27).

We found a significant correlation between GRACE-based excitation functions and the corresponding geodetic residuals in the non-seasonal part of spectrum.

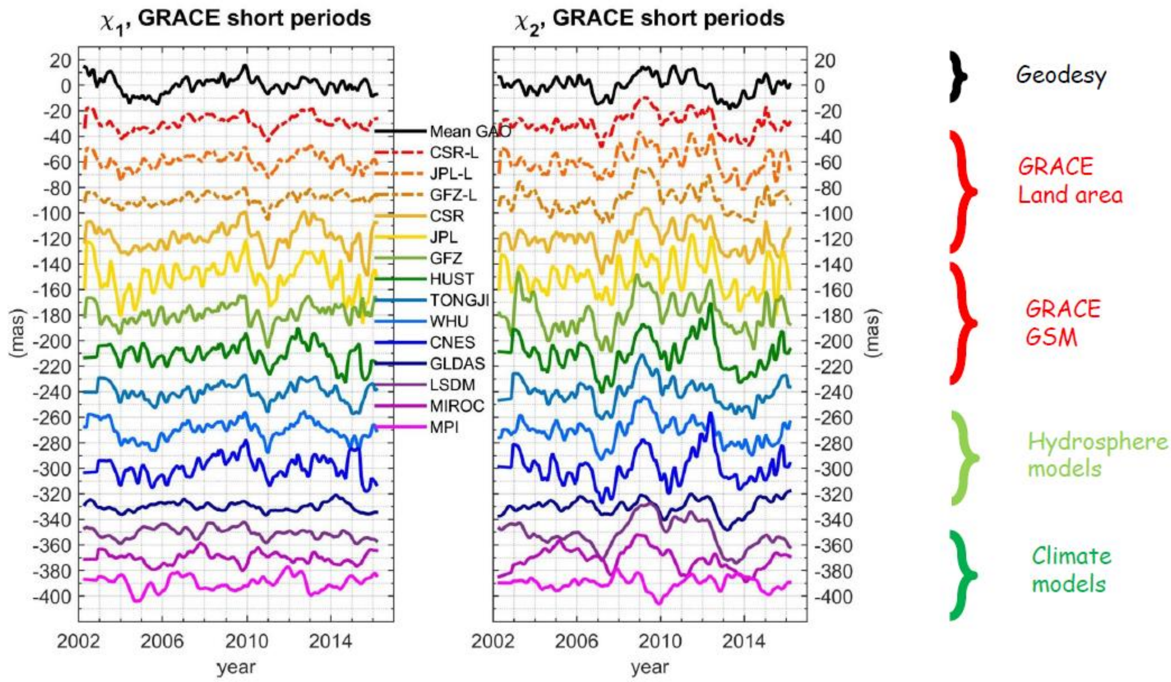

Fig. 1.26. Comparison of short period variations of χ_1 and χ_2 components of mean geodetic residuals (M GAO) with gravimetric (CSR, JPL, GFZ, HUST, TONGJI, WHU, CNES) and hydrological (GLDAS, LSDM, MIROC, MPI) excitation functions. Solid lines show gravimetric excitation computed from the GSM coefficient, dotted lines reflect contributions over the land area only.

1. SATELLITE GEODESY

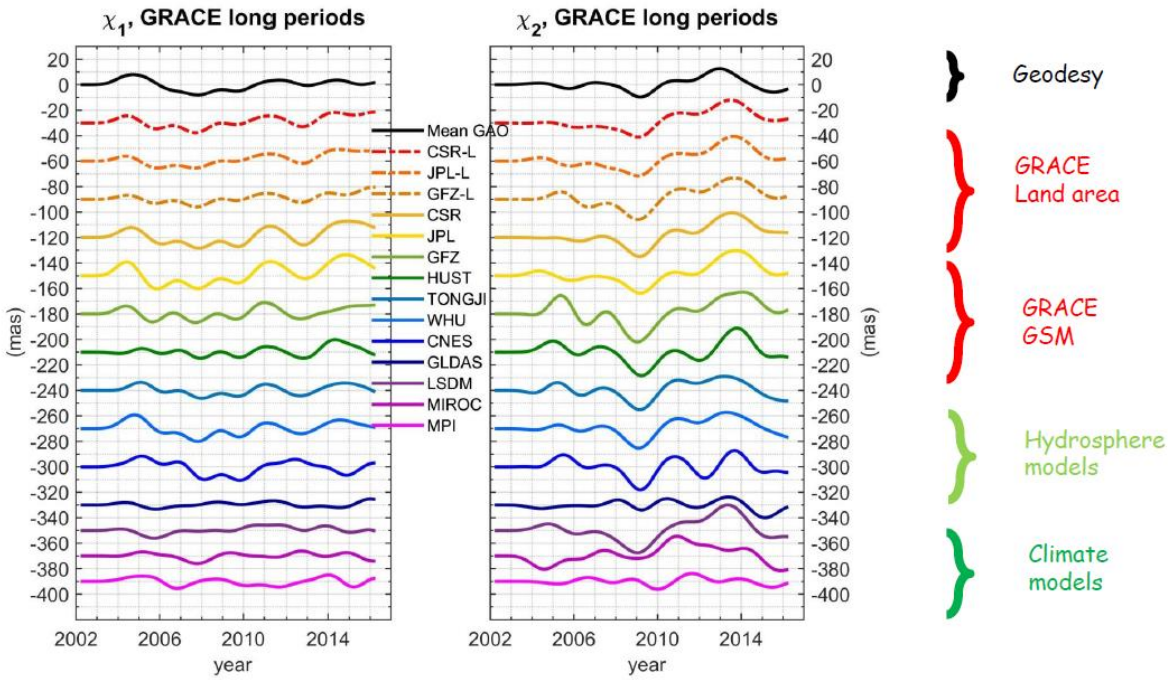

Fig. 1.27. Comparison of short period variations of χ_1 and χ_2 components of mean geodetic residuals (M GAO) with gravimetric (CSR, JPL, GFZ, HUST TONGJI, WHU, CNES) and hydrological (GLDAS, LSDM, MIROC, MPI) excitation functions. Solid lines show gravimetric excitation computed from the GSM coefficient, dotted lines reflect contributions over the land area only.

Determination of High Frequency Earth Rotation Parameters from GPS + Galileo observation data

Within the ESA project 'GNSS-EOP' (ESA EGEP 89.19) under leadership of TU-Vienna, Austria, Department for Geodesy and Geoinformation the potential of recent GNSS observations for the determination of Earth rotation parameters (ERP) at sub-daily periods with the high precision currently achieved has been investigated.

The geodetic ERPs were compared to the so-called geophysical ERPs calculated from consistent AAM and OAM models. Corrections to the IERS sub-daily polar motion + LOD model were derived and the potential of Galileo to contribute significantly to an improved sub-daily tidal ERP-model is discussed. For comparison of geodetic and geophysical excitations 3-hourly atmospheric and oceanic angular momentum (AAM, OAM) data series were established.

The AAM and OAM model was calculated from NASA's GEOS-5 Modern-Era Reanalysis for Research and Applications (MERRA) stream and from a consistent barotropic ocean model. The excitation series were analyzed both in time and spectral domain focusing on signals with periods between 4 and 48 hours.
Figures 1.28, 1.29 show spectra of the ERP parameters comparison with those obtained from the geophysical data spectra, by using the transfer function in spectral domain, computed in the spectrum range from 2 to 70 hours.
The ERP spectra were estimated from two kinds of the GNSS observations, either GPS&GALILEO or GPS &GLONASS. In the case of the polar motion examined are the complex valued components (x – iy). Additionally, bottom panels of the Figures 3 and 4 show the residuals between the spectra estimated from two kinds of the mentioned above GNSS observations for the years 2015-2016.
It is obvious that the polar motion and the LOD spectra computed from the two kinds of the GNSS observations (GPS&Galileo or GPS&GLONASS) show similar features in the diurnal and semi-diurnal band but there are also non-negligible differences visible. By comparing the polar motion spectra obtained from the GPS&Galileo observations in the two study periods, 2014 and 2015-2016, one can see that the first spectra has smaller amplitudes and less variability below 20 hours. In the case of the LOD, spectra analyses show peaks with 12 hours and 8 hours periods in the spectra from both 2015/2016 and 2014 time series. Diagrams of the residuals show that the pole motions spectra obtained from the GPS&GLONASS observations are slightly more variable than those obtained from the GPS&Galileo data while in the case of LOD the spectra obtained from GPS&GLONASS observations are less variable than those computed from the GPS&Galileo data. From the visual inspections of the spectra, it is obvious that the amplitudes of the ERP changes cannot be explained by the effects of the atmospheric and oceanic excitations. Polar motion match the geophysical polar motion spectra in the prograde diurnal band, but elsewhere the geophysical excitation is much smaller than the geodetically obtained signals. The LOD spectrum based on the geodetic observations (GPS&Galileo 2015/2016 and GPS&GLONASS 2014) is too large in all bands to match geophysical signals in LOD.

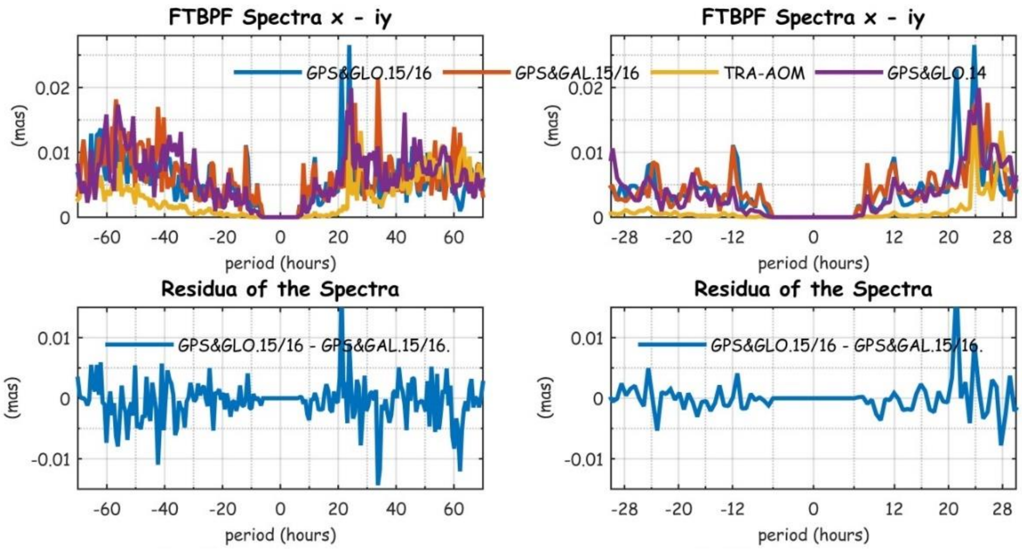

Fig. 1.28. Comparison of polar motion spectra (blue line - GPS&GLONAS 2015/2016, magenta line-GPS&GLONASS 2014, red line GPS&Galileo 2015/2016) with the geophysical polar motion spectra computed from the geophysical excitation (yellow line). Bottom panels shows residua of the polar motion spectra computed using two kinds of the GNSS observations in the period 2015/2016.

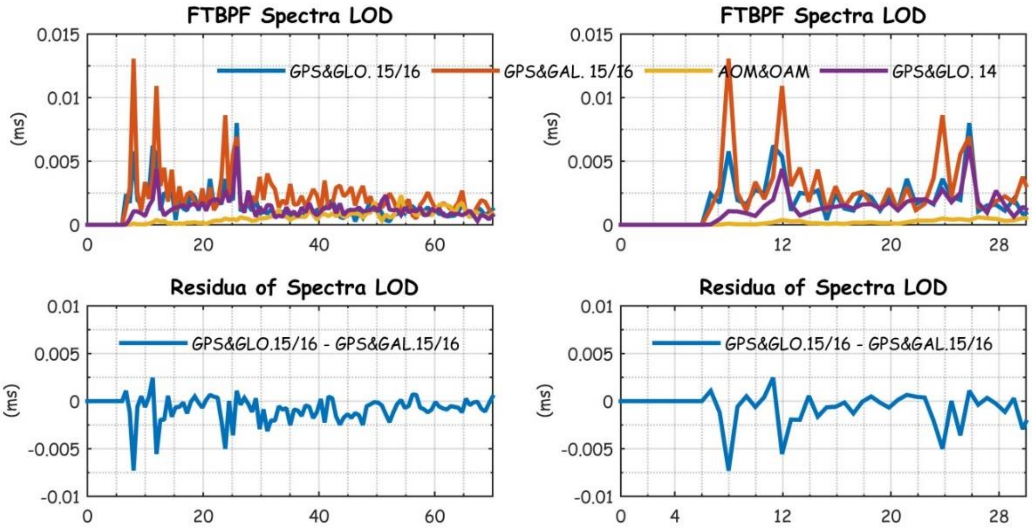

Fig. 1.29. Comparison of the LOD spectra (blue line - GPS&GLONAS 2015/2016, magenta line- GPS&GLONASS 2014, red line GPS&Galileo 2015/2016) with the LOD spectra computed from the geophysical excitation (yellow line). Bottom panels shows residua of the LOD computed using two kinds of the GNSS observations in the period 2015/2016.

Variation in Earth rotation, theoretical modeling and observation

Our research concerned perturbations in Earth rotation caused by the influence of external fluid layers, its atmosphere, oceans and land hydrology. It investigated theoretical issues including data modelling and interpretation methods, and the analysis of the available data derived either from space geodetic observations of the Earth's rotation or from global models of geophysical fluids.

We compared the results of the spectral analysis of the observed free Chandler wobble using two methods: the classic Fourier analysis, and the maximum entropy method. Several tests were performed to check for the influence of Very Long Baseline Interferometry (VLBI) observations on estimations of station coordinates and Earth Orientation Parameters (EOP). Research continued into the use of measurements from the ring laser gyroscope (RLG) in Wettzell, Germany, in combination with geodetic VLBI monitoring of diurnal and subdiurnal signals in the Earth's rotation (Fig. 1.30).

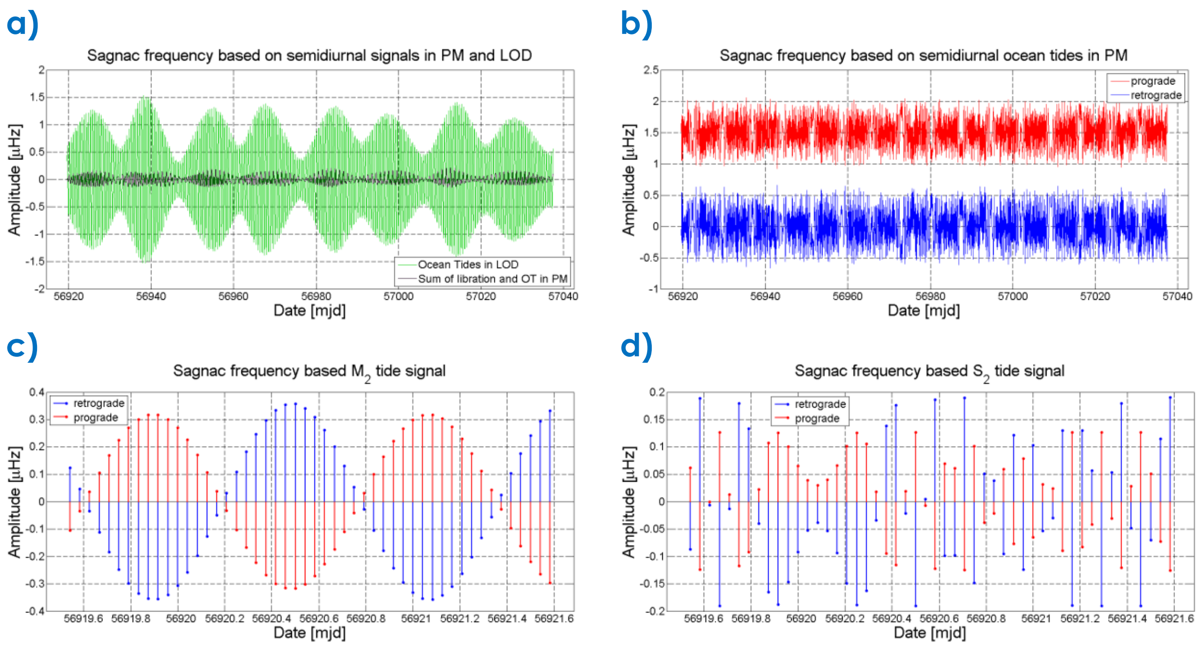

Fig. 1.30. Semidiurnal signals in the Earth's rotation observed by the ring laser gyroscope in Wettzell, Germany. a) is a comparison of the contributions of polar motion (PM) and length-of-day (LOD) variation; b) is a comparison of the contributions from prograde and retrograde ocean tide signals; c) and d) are the same as b) but for the two largest semidiurnal tidal harmonics M_2 and S_2, respectively.

Monitoring of the quality of EGNOS correction data: EGNOS service performance monitoring support (SPMS)

Warsaw is home to one of the EGNOS Ranging and Integrity Monitoring Stations (RIMS), which broadcast embedded correction signals in Europe in order to provide improved GPS performance. CBK PAN's involvement with the EGNOS System also comprises:

- participation in ESA IMAGE/PERFECT Project; and
- participation in GSA SPMS grant.

The CBK PAN is one of the partners in a consortium that performs continuous monitoring of the availability, correctness, continuity and accuracy of the EGNOS-SIS and EGNOS-EDAS corrections, as part of the GSA's SPMS project. Analysis and visualisation of Key Performance Indicators of the EGNOS system, and comparative analysis of the EGNOS corrections, are transmitted directly by satellite (SIS) and distributed via the internet (EDAS).

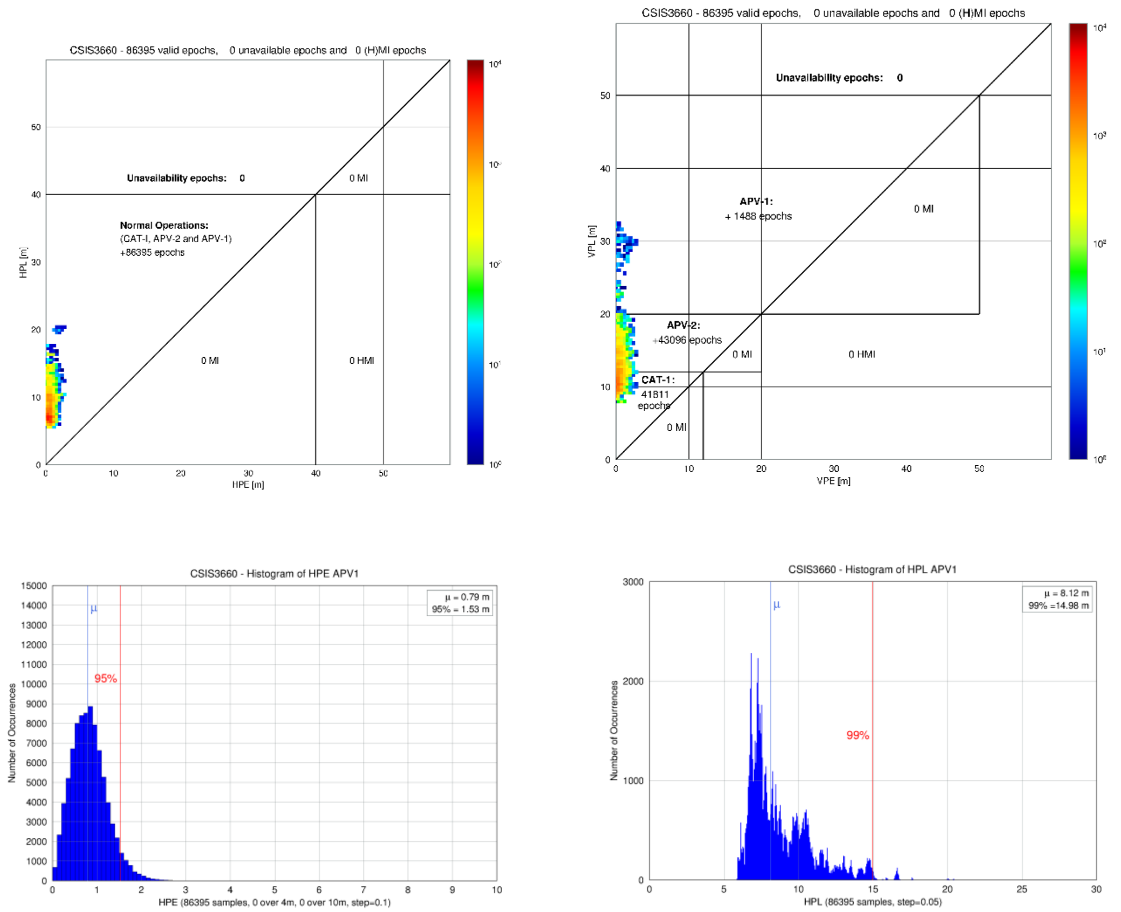

Fig. 1.31. Example of a visual analysis of the EGNOS Signal in Space corrections at the Warsaw.

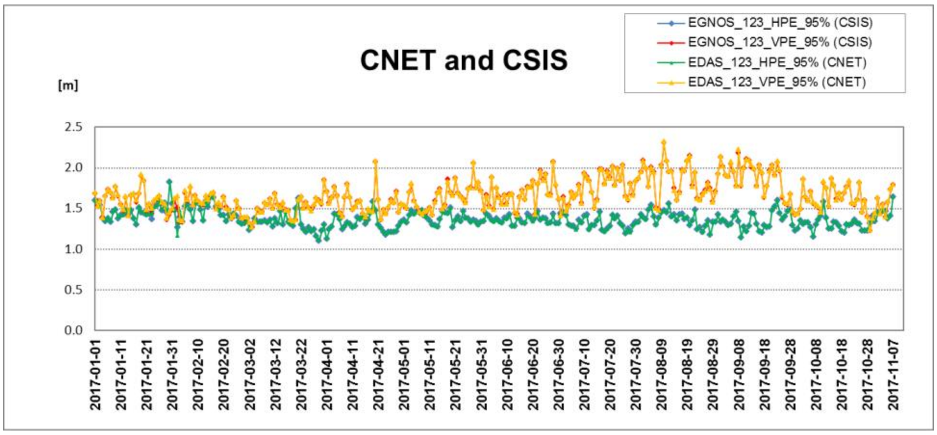

Fig. 1.32. Horizontal and Vertical Position Error in SISNET and EDAS data.

Caesium fountain at the Astrogeodynamical Observatory in Borowiec

At the beginning of December 2016, at the Time and Frequency Laboratory of the CBK PAN in Borowiec, Dr Jerzy Nawrocki and his team of scientists launched the atomic caesium fountain. Less than a year later, at the headquarters of the Poznań Supercomputing and Networking Center (PSNC), a second atomic frequency standard was launched. Both atomic fountains were built with the participation of scientists from the CBK PAN (MA Ing Piotr Dunst and MA Bartłomiej Nagórny) at the National Physical Laboratory in Teddington, near London. The work was carried on under the direction of Dr Krzysztof Szymaniec, an eminent specialist in the field of atomic frequency standards. The Polish atomic caesium fountains will join the group of some of the most accurate atomic clocks in the world, and they are the only such clocks in Poland.
The launch of the second atomic caesium fountain at the PSNC is the result of cooperation between the CBK PAN (Borowiec) and the PSNC. Both atomic frequency standards consist of the same elements and are made using the same technology and the same design. There are three main subsystems to the atomic caesium fountains:

- an optical subsystem,
- a physical subsystem,
- an electronics subsystem with a microwave source.

Each of these subsystems has its own important function, but it is only together

that they are able to achieve the desired effect.
The optical system includes two infrared lasers from Toptica, optical elements and optical fibres. Laser infrared light is used to cool, trap and detect caesium atoms (133Cs). For both detection, and for trapping in a magneto-optical (MOT) trap, the caesium D2 line is used, with a wavelength of 852 nm, i.e., lying in the infrared frequency region. The cooling transition uses the basic state 62S1/2 | F = 4> and the excited state 62P3/2 | F = 5>. Due to the selection rule ΔF = 0; ± 1 transition belongs to closed passages, and transition to the hyperfine level (| F = 3>) of the ground state is prohibited. However, due to the laser's finite spectral width, the atoms sometimes pass to the level of | F = 4> of the excited state. Atoms can go from this state to the level F = 3> of the ground state, as a result of spontaneous emission. This means that they are lost from the cooling transition cycle. The above conditions force the use of an additional laser (a repumper), which pumps atoms back into the cooling passage. The repumper is tuned to the 62S1/2 | F = 3> → 62P3/2 | F = 4> transition. The optics (on the optical table) are used to divide the main laser beam into several beams that perform the required functions (six cooling beams, two detection beams and one beam for optical pumping), and to change the frequency of each of the divided beams using acoustic-optical modulators (AOM). The power of the detection beams is stabilized in an active way using AOMs.
The physical subsystem consists of a vacuum chamber (in which the gas vapour pressure is of the order of ~ 10-9 mbar), a Ramsey resonance cavity, a selection cavity and a tube in which the upward flight of atoms takes place. In the lower part of the vacuum chamber, the cloud of caesium atoms is cooled. This sample of cooled atoms is tossed upwards by the laser light in the vacuum chamber, similar to the way in which a stream of water is ejected in a water fountain. The cloud of atoms passing through Ramsey's resonance cavity during the upward flight and at gravitational collapse is illuminated by microwave radiation. If it has the right frequency, the atoms are stimulated to vibrate. If the microwaves are tuned to the resonant frequency, which excites the most caesium atoms, then we get a model realization of the second (since 1967, the second is defined as a time equal to 9 192 631 770 atomic radiation periods 133Cs).
The third subsystem of the atomic caesium fountain is a series of electronic systems, power supplies and microwave sources. Electronic circuits enable the setting of the appropriate frequencies to send to the AOMs, enable quick switching on and off of the current flowing in the MOT coils and optical pumping

(OP). These electronic circuits and switches are controlled by computer, via the National Instruments card that acquires the data from the detectors. This computer also controls the course of the entire experiment and data recording process.

GalAc

The CBK PAN leads the GalAc project, whose objective is to analyse the feasibility and usefulness of equipping second-generation Galileo spacecraft with accelerometers to improve the accuracy of Precise Orbit Determination (POD) and the Galileo Terrestrial Reference Frame. The project addresses the specific science and technology objectives of the European Global Navigation Satellite System (GNSS) Evolution Program (EGEP), relating to the study and development of innovative GNSS methodologies and technologies, especially algorithms, software and hardware. It is anticipated that GNSS positioning accuracy will reach the level of millimetres, while ground infrastructures can be simpler and more cost-effective. An onboard accelerometer can record direct measurements of nongravitational perturbations (NGP) and spacecraft acceleration due to onboard activity, which are currently unmodeled. As it is unlikely that the number of ground stations will increase, such data may fill the gap. The next step would be the introduction of Inter-Satellite Link technology, which can significantly enhance the orbital solution.

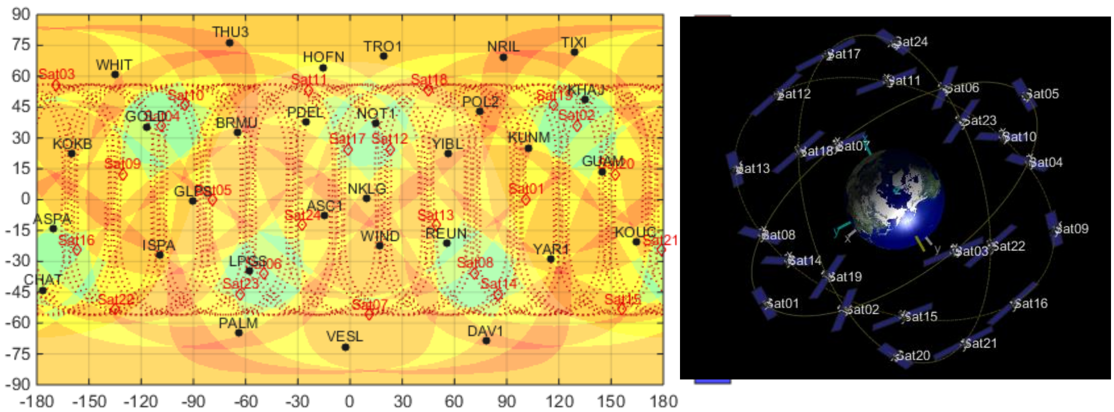

Fig. 1.33. GSTE – Simulated Galileo constellation (coverage and 3d view).

Currently, the project is focused on developing the GSTE software tool (General Simulation and Analysis Tool for Earth-orbiting objects), which combines recent theory, models and data to perform realistic simulations of Galileo satellites in orbit. Particular attention has been paid to the analysis of the nongravitational forces due to solar radiation, and the Earth's visible and thermal radiation. In particular, observed fluxes recorded in the CERES (Clouds and the Earth's Radiant Energy System) database are used to verify existing NGP models and identify areas of potential improvement.

Analysis of the possible improvements in POD is based on a weighted least-squares algorithm (nominally used by many analysis centres) and the extended Kalman filter. The latter is especially useful for nearly-real-time applications (e.g. real-time precise point positioning), thus paving the way for future GNSS data processing.

ESA Contract No: 4000112197/14/NL/MM.

Seismicity of the Fore-Sudetic monocline in the context of tectonic activity in the Świebodzice Depression

Installed in the Geodynamic Laboratory in Książ (GL) at the beginning of this century, long water-tube tiltmeters (WT) provide basic observations for determining the temporal and amplitude of tectonic phenomena. Variations in the tectonic activity of the Ksiaz orogen have been described by us as the function of tectonic activity (FTA). The FTA is an empirical function determined on the basis of measurements carried out with instruments that have a small, linear and well-defined drift, a high sensitivity to orogen deformation, and an extensive measurement base. The above-mentioned conditions are fulfilled by a set of two, perpendicular WTs, with a base that is 65 m wide and 92 m long. Furthermore, instrumental drift (caused mainly by water evaporation from the hydrodynamic system) is linear in approximation, and the sensitivity of the measurement system is nanometric. Given the size of the WT measurement base, which is greater than the area between the rock blocks separated by faults, WT measurements guarantee a high degree of representativeness in the assessment of the momentary tectonic activity of the orogen. They provide kinematic information, i.e. vertical motion and tilting of the foundation.

Measurements obtained with WTs are related to the orogen, and the four WT interferometric gauges are rigidly connected to the base.

A detailed analysis of the deformation process of the Świebodzice Depression revealed that the state of the Książ massif corresponds to the seismicity of the Fore-Sudetic Monocline, according to strictly-defined, temporal and amplitude principles, each of which consists of five precedents.

1. SATELLITE GEODESY

The results of comparative analyses of strong seismic events with the tectonic activity of the Świebodzice Depression orogen leads to the conclusion that strong seismic shocks (magnitude ≥3.6) only occur in particular states of the orogen, described by the FTA and its derivatives. The identification of these principles made it possible to apply temporal and amplitude rules to evaluate the level of seismic hazard in the Fore-Sudetic Monocline.

Publications

1. Birylo, Monika, NASTULA, Jolanta, Kuczynska-Siehien, Joanna; The creation of flood risks model using a combination of satellite and meteorological models - the first step; ACTA GEODYNAMICA ET GEOMATERIALIA, Volume: 12, Issue: 2, Pages: 151-156, DOI: 10.13168/AGG.2015.0018, published 2015
2. Jiang, Z., Czubla, A., NAWROCKI, J., Lewandowski, W., Arias, EF.; Comparing a GPS time link calibration with an optical fibre self-calibration with 200 ps accuracy; METROLOGIA, Volume: 52, Issue: 2, Pages: 384-391, DOI: 10.1088/0026-1394/52/2/384, Published 30 March 2015
3. KACZOROWSKI, Marek, Goluch, Piotr, Kuchmister, Janusz, Cmielewski, Kazimierz, ZDUNEK, Ryszard, Borkowski, Andrzej; Integrated Tectonic Studies: A New Concept Explored in The Geodynamic Laboratory of The Space Research Center in Ksiaz; ACTA GEODYNAMICA ET GEOMATERIALIA, Volume: 12, Issue: 2, Pages: 169-179, published: 2015
4. Morzyński Piotr, Marcin Bober, Dobrosława Bartoszek-Bober, Jerzy NAWROCKI, Przemysław Krehlik, Łukasz Śliwczyński, Marcin Lipiński, Piotr Masłowski,Agata Cygan, Piotr DUNST, Michał Garus, Daniel Lisak, Jerzy Zachorowski, Wojciech Gawlik, Czesław Radzewicz, Roman Ciuryło & Michał Zawada; Absolute measurement of the 1S0−3P0 clock transition in neutral 88Sr over the 330 km-long stabilized fibre optic link, SCIENTIFIC REPORTS, vol. 5, Article number: 17495, DOI: 10.1038/srep17495, Published online: 07 December 2015
5. NASTULA, J., Gross, R.; Chandler wobble parameters from SLR and GRACE; JOURNAL OF GEOPHYSICAL RESEARCH-SOLID EARTH, Volume: 120, Issue: 6, Pages: 4474-4483, DOI: 10.1002/2014JB011825, published: June 2015
6. Cygan, A., Wojtewicz, S., Kowzan, G., Zaborowski, M., Wcislo, P., NAWROCKI, J., Krehlik, P., Sliwczynski, L., Lipinski, M., Maslowski, P., Ciurylo, R., Lisak, D.; Absolute molecular transition frequencies measured by three cavity-enhanced spectroscopy techniques, JOURNAL OF CHEMICAL PHYSICS Volume: 144 Issue: 21 Article Number: 214202, DOI: 10.1063/1.4952651, Published: June 7 2016
7. Olech A., P. Żołądek, M. Wiśniewski, R. Rudawska, M. Bęben, T. Krzyżanowski, M. Myszkiewicz, M. Stolarz, M. Gawroński, M. Gozdalski, T. SUCHODOLSKI, W. Węgrzyk, Z. Tymiński; 2015 Southern Taurid fireballs and asteroids 2005 UR and 2005 TF50, MONTHLY NOTICES OF THE ROYAL ASTRONOMICAL SOCIETY, 10pp, DOI: 10.1093/mnras/stw1261
8. SCHREIBER R., M. Panchenko, J. HANASZ, R. Mutel, I. Christopher; Beaming of intense AKR seen from the Interball-2 spacecraft; J. GEOPHYS. RES. SPACE PHYSICS, 121, DOI:10.1002/2015JA022197

9. Szczerbowski Zbigniew, Marek KACZOROWSKI, Janusz Wiewiórka, Mieczyslaw Jóźwik, Ryszard ZDUNEK, Andrzej Kawalec; Monitoring of Tectonically Active Area of Bochnia, ACTA GEODYN. GEOMATER., Vol. 13, No. 1 (181), 59–67, DOI: 10.13168/AGG.2015.0044, 2016
10. Winska, Malgorzata, NASTULA, Jolanta, KOŁACZEK, Barbara; Assessment of the Global and Regional Land Hydrosphere and Its Impact on the Balance of the Geophysical Excitation Function of Polar Motion, ACTA GEOPHYSICA, Volume: 64, Issue: 1, Pages: 270-292, Published: Febryary 2016
11. Birylo M., Z. Rzepecka, J. Kuczynska-Siehien, J. NASTULA; Analysis of water budget prediction accuracy using ARIMA models; WATER SCIENCE AND TECHNOLOGY, Volume 17, issue 6, DOI: 10.2166/ws.2017.156, 2017
12. Krehlik P., Ł. Buczek, J. Kołodziej, M. Lipiński, Ł. Śliwczyński, J. NAWROCKI, P. NOGAŚ, A. Marecki, E. Pazderski, P. Ablewski, M. Bober, R. Ciuryło, A. Cygan, D. Lisak, P. Masłowski, P. Morzyński, M. Zawada, R. M. Campbell, J. Pieczerak, A. Binczewski, K. Turza; Fibre-optic delivery of time and frequency to VLBI station; Astronomy & Astrophysics, Volume 603, Article Number A48, DOI: 10.1051/0004-6361/201730615, 2017
13. Olech A., P. Żołądek, M. Wiśniewski, Z. Tymiński, M. Stolarz, M. Bęben, D. Dorosz, T. Fajfer, K. Fietkiewicz, M. Gawroński, M. Gozdalski, M. Kałużny, M. Krasnowski, H. Krygiel, T. Krzyżanowski, M. Kwinta, T. Łojek, M. Maciejewski, S. Miernicki, M. Myszkiewicz, P. Nowak, K. Polak, K. Polakowski, J. Laskowski, M. Szlagor, G. Tissler, T. SUCHODOLSKI, W. Węgrzyk, P. Woźniak, P. Zaręba; Enhanced activity of the Southern Taurids in 2005 and 2015; Monthly Notices of the Royal Astronomical Society, Volume 469, Issue 2, p.2077-2088, 10.1093/mnras/stx716, 2017
14. Rzepecka Z., Birylo M., Kuczynska-Siehien J., NASTULA J., Pajak K.; Analysis of groundwater level variations and water balance in the area of the sudety mountains; Acta Geodynamica et Geomaterialia, Volume 14, Issue 3, Pages 313-321, DOI: 10.13168/AGG.2017.0014, 2017
15. Winska Malgorzata, Jolanta NASTULA, David Salstein; Hydrological excitation of polar motion by different variables from the GLDAS models; Journal of Geodesy, 13pp, DOI: 10.1007/s00190-017-1036-8, 2017
16. Wiśniewski M., P. Żołądek, A. Olech, Z. Tyminski, M. Maciejewski, K. Fietkiewicz, R. Rudawska, M. Gozdalski, M.P. Gawroński, T. SUCHODOLSKI, M. Myszkiewicz, M. Stolarz, K. Polakowski; Current status of Polish Fireball Network; Planetary and Space Science, Volume 143, Pages 12-20 (9pp), DOI: 10.1016/j.pss.2017.03.013, 2017
17. Witkowski M., NAGÓRNY B., Munoz-Rodriguez R., Ciurylo R., Zuchowski P.S., Bilicki S., Piotrowski M., Morzynski P., Zawada M.; Dual Hg-Rb magneto-optical trap; OPTICS EXPRESS, Volume: 25, Issue: 4, Pages: 3165-3179, DOI: 10.1364/OE.25.003165, 2017
18. Tercjak M., A. Brzezinski (2017). On the influence of known diurnal and subdiurnal signals in polar motion and UT1 on Ring Laser Gyroscope observations, Pure and Applied Geophysics, DOI 10.1007/s00024-017-1552-8
19. D. Kucharski, G. Kirchner, J. C. Bennett, M. Lachut, K. Sośnica, N. Koshkin, L. Shakun, F. Koidl, M. Steindorfer, P. Wang, C. Fan, X. Han, L. Grunwaldt, M. Wilkinson, J. Rodríguez, G. Bianco, F. Vespe, M. Catalán, K. Salmins, J. R. del Pino, H.-C. Lim, E. Park, C. Moore, P. Lejba, T. Suchodolski, Photon pressure force on space debris TOPEX/Poseidon measured by Satellite Laser Ranging, *Earth and Space Science*, Vol.4, Issue 10, pp. 661-668, October, 2017.

1. SATELLITE GEODESY

20. P. Lejba, T. Suchodolski, P. Michałek, J. Bartoszak,S. Schillak, S. Zapaśnik, First laser measurements to space debris in Poland, *Advances in Space Research*, 2017 (paper accepted for publication), DOI: https://doi.org/10.1016/j.asr.2018.02.033

Institute of Geodesy, University of Warmia and Mazury in Olsztyn (UWM) P. Wielgosz, J. Paziewski, K. Dawidowicz, W. Jarmołowski, A. Krypiak-Gregorczyk, K. Stępniak

Research on Multi-GNSS positioning

This section summarizes recent developments in the GNSS positioning algorithms at the University of Warmia and Mazury in Olsztyn. The discussed results concern mainly development of the methods for integration of multi-constellation signals, methods for mitigation of the ionospheric delay and practical applications of the GNSS positioning techniques to engineering surveying.

Theoretical analysis and practical assessment of the selected models for multi-constellation signals integration were described in (Paziewski and Wielgosz 2017). Following publication (Paziewski and Sieradzki 2017) described theoretical background and performance assessment of instantaneous medium-range GPS+BDS RTK. The papers proved enhancement of the reliability, accuracy and time-to-fix in GNSS positioning induced by application of multi-constellation signals.

The accuracy of the ionospheric corrections in RTK positioning during various ionospheric conditions was analyzed in (Paziewski 2016). This allowed for definition of the desirable accuracy of network ionospheric corrections supporting instantaneous RTK positioning. Moreover the original algorithms for elimination of the influence of the ionospheric disturbances on precise GNSS positioning were developed and evaluated in (Sieradzki and Paziewski 2016). Considering the high-order ionospheric effects in PPP it was proved that modelling of these terms affects the estimated coordinates at the level of a few milimeters in PPP and at negligible level considering medium-range RTK (Banville et al. 2017, Hadas et al. 2017). Furthermore, as it was shown in (Banville et al. 2017), the estimation of high-order effects in the PPP solution lead to the propagation of DCB into the receiver position.

Studies on positioning algorithm development were followed by practical application of the GNSS technology to determination of the displacements of the ground and engineering structures (Paziewski et al. 2017, Malyszko et al

2017, Malyszko et al 2016).

GNSS antenna calibrations and their influence on positioning

It was proven in Dawidowicz and Krzan (2016) that for the GLONASS observations the differences in the calibrations models propagate directly into the position domain, affecting daily and sub-daily results and giving visible variations and oscillations of the coordinates. It was demonstrated, using the Lomb-Scargle spectrum, that there are strong periodic signals in sub-daily results and there are also potential, required further investigation, periodicities in daily results. The mechanism of transferring the differences in the antenna calibration models to the coordinate domain was demonstrated. For this purpose the analysis of the satellite constellation dependent GDOP factors and analysis of differences in mean PCC values were proposed. It has been shown that the detected signals are dependent on differences in the antenna calibration model as well as on GLONASS satellite constellation.
The study Dawidowicz and Krzan (2017) contains the results of empirical analysis of the position components differences obtained in GPS pseudo-kinematic solutions (15 minutes observation windows) using individual and type mean (igs08.atx) antenna calibration models. The position components were derived using Precise Point Positioning (PPP) technique based on the NAPEOS software package. Sub-daily oscillations in time series of obtained solutions were analyzed. It was proven that all antennas of the same type cannot necessarily be represented confidently by a unique type-mean calibration (Fig. 1.34).

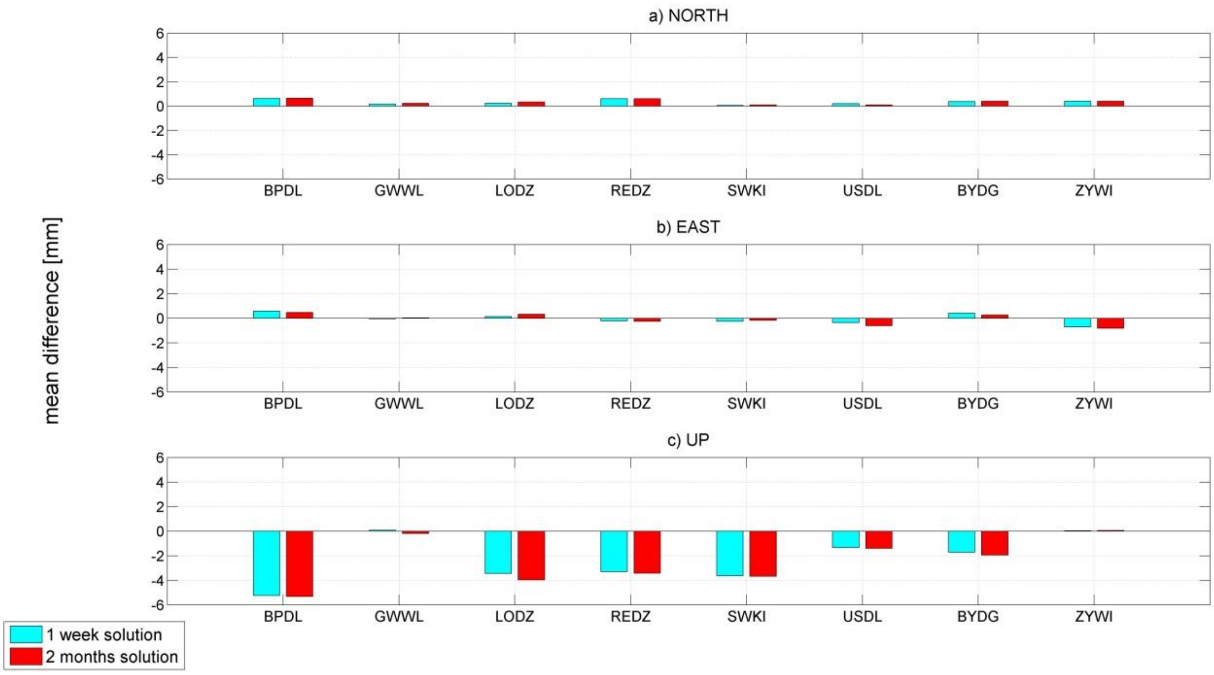

Fig. 1.34. Mean North, East and Up differences caused by the use of different calibration models from sub-daily observation post-processing (TRM55971.00 TZGD antenna case study).

Results of long-term static GNSS observation processing adjustment prove that the often assumed "averaging multipath effect due to extended observation periods" does not actually apply. It is instead visible a bias that falsifies the coordinate estimation. The comparisons between the height difference measured with a geometrical precise leveling and the height difference provided by GNSS clearly verify the impact of the near-field multipath effect. In Dawidowicz and Baryła (2017) it was demonstrated that the way of antennas mounting during observation campaign (distance from nearest antennas) can cause visible changes in pseudo-kinematic precise point positioning results. GNSS measured height differences comparison revealed that bias of up to 3 mm can be noticed in Up component when some object (additional GNSS antenna) was placed in radiating near-field region of measuring antenna.

Application of cross-validation and maximum likelihood in geostatistical methods for geodetic data modeling

The accuracy and unambiguousness of contemporary models of physical phenomena related to the Earth are typical requirements guaranteeing their application in science and practice. Spatial and temporal modeling methods must be therefore based on precise variance and covariance modeling, by parametrized stochastic methods. Variance component estimation (VCE) appears nowadays amongst the most investigated problems in statistics and geostatistics. The Institute of Geodesy of the University of Warmia and Mazury conducts research on stochastic modeling methods with application to Earth gravity field, topography modeling and spatio-temporal modeling of total electron content (TEC) in the ionosphere. The covariance matrices appropriately describing gravity or TEC spatio-temporal behavior obtain their optimal parameters by the application of cross-validation methods (CV) (Krypiak-Gregorczyk et al. 2017) or maximum likelihood modeling (ML) (Jarmołowski 2016 and 2017, Jarmołowski and Łukasiak 2016). The noise variance issue becomes most important and should be especially carefully treated in the investigation of the modeling parameters, as it is related with observational error, data distribution, smoothness and accuracy of the models. The application of precise noise covariance matrix in the least-squares collocation (LSC) of regular gravity and TEC models assures their optimal accuracy in the least-squares sense and increases their potential in the applications.

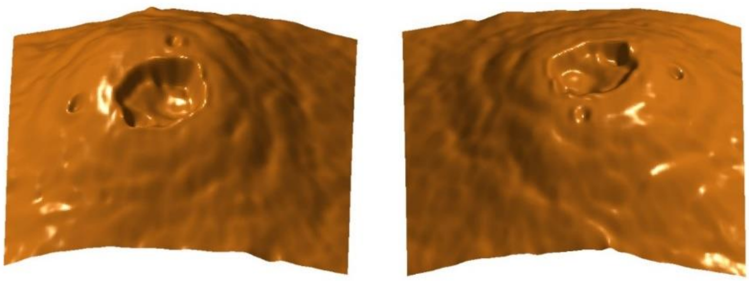

Fig. 1.35. Olympus Mons topography model from MOLA data by LSC method with precise estimation of covariance parameters.

1. SATELLITE GEODESY

Modeling and monitoring of the ionosphere with GNSS data

The Institute of Geodesy of the University of Warmia and Mazury in Olsztyn (IG/UWM) is still developing a new method for accurate regional ionospheric TEC modelling based on un-differenced multi-GNSS carrier phase data. our approach is based on a new methodology of estimating the phase bias of the scaled L1 and L2 carrier phase difference which is a function of the ambiguities, the ionospheric delay, and hardware delays. The tests results show that the carrier phase bias of geometry-free linear combination can be estimated with a very high accuracy, which consequently allows for calculating ionospheric TEC with the uncertainty lower than 1.0 TECU. The estimation of a single parameter of carrier phase bias for each continuous observation arc allows to calculate precise ionospheric delays are calculated at every observational epoch (e.g. 30 s) for each continuous observation arc. The mapping of the vertical TEC at the ionospheric pierce points (IPP) locations are based on single layer model. Then, the different TEC interpolation methods, e.g., thin plate splines (TPS) and least squares collocation (LSC) are applied for accurate ionospheric TEC modeling and providing the vertical regional TEC map. This approach allows for generation TEC maps for Europe with high temporal and spatial resolution. This high accuracy makes the resulting ionosphere model suitable for improving GNSS positioning for high-precision applications. In addition, this high-resolution ionosphere model is used to study the response of this layer to the largest geomagnetic storms in Solar Cycle 24.

Improving tropospheric ZTD estimation with GNSS

Other objective of our research in 2016-2017 was to assess the impact of the latest, advanced methods of GNSS signal tropospheric delay modeling on the estimated stations coordinates, as well as tropospheric parameters for national and regional networks. Thus, we analysed the influence of troposphere modelling on the realization of the ETRS89 (European Terrestrial Reference System) by the reference stations of the Polish national Ground Based Augmentation System (GBAS) network – ASG-EUPOS, and also on the tropospheric parameters which are of interest to meteorology and atmospheric research. In additional. we investigated the influence of the network design strategy on the estimated coordinates of permanent stations and zenith total delay (ZTD) time series. The study shows that the network design has a strong impact on the estimated parameters, especially on the quality and continuity of ZTD estimates. Based on the results of the analysis, we determined the most accurate and homogeneous processing strategy to reprocess ground-based GNSS data not only for geodetic applications, but also for meteorology and climate monitoring applications. It is proved that using the new developed baseline design strategy the reprocessed ZTD time series, as well as time series of station positions are much more continuous and homogeneous in comparison to the standard strategies (Table 1.2).

Table 1.2: Statistics of ZTD estimates and formal errors (sigma) for all three processing variants discussed in the text, computed over 104 common ASG-EUPOS stations. The best values are indicated in bold. Column 2 (resp. 3) gives the number of stations for which the standard deviation of ZTD (resp. sigma) is maximal among the three solutions (e.g. standard deviation of ZTD of the old solution is maximal 62 times out of 104).

Solution	Times Max STD(ZTD)	Times Max STD(sigma)	Rejected data	Used data	Mean STD(ZTD)	Mean STD(sigma)
"light screening": range check on ZTD [0.5 m; 3.0m], on sigma [0 m; 0.1m]						
old	62	81	148	468332	0.0142 m	0.00119 m
new	**11**	**6**	**84**	469534	**0.0129 m**	0.00079 m
obs-max	31	17	109	**471666**	0.0133 m	**0.00067 m**

Water vapour is a key variable of the water cycle and plays a special role in many atmospheric processes controlling weather and the climate. Extreme weather events, such as storms, floods and landslides, heat waves and droughts, are one of the main concern of society. GNSS is one of the very few tools that can be used as atmospheric water vapour sensor and, simultaneously, provide continuous, unbiased, precise and robust atmosphere condition information. Hence, our research aimed also to use GNSS observations from Polish permanent networks to derive values of local atmospheric variables for weather prediction and severe weather monitoring. We analysed the characteristics of water vapour surrounding an extreme weather event using the high-resolution GNSS tropospheric estimates. Zero-differenced Precise Point Positioning (PPP) technique, utilizing precise satellite orbits and clocks, and relative processing mode uses double-difference (DD) observations from a network of stations were used to estimate tropospheric parameters. We compared results from two different scientific software – Bernese GNSS Software v.5.2 and G-Nut. Moreover, in order to validate and assess the quality of the GNSS estimates, IWV obtained based on ERA-Interim reanalysis was compared to GNSS estimates. The results showed good agreement between the estimates from two different software. Validation against data from climate reanalysis confirmed that both approaches provide high-quality tropospheric delays. Also, we observed high agreement in the IWV distributions between GNSS and ERA-Interim. It was also shown that it is possible to observe storm precursors in ZTD time series before the analysed weather events.

Publications:

1. Banville, S., Sieradzki, R., Hoque, M. et al., 2017, On the estimation of higher-order ionospheric effects in precise point positioning, GPS Solut 21: 1817. https://doi.org/10.1007/s10291-017-0655-0
2. Dawidowicz K., Krzan G., (2016), Analysis of PCC model dependent periodic signals in GLONASS position time series using Lomb-Scargle periodogram, Acta Geodynamica et Geomaterialia, 13(3): 299–314. DOI: 10.13168/AGG.2016.0012
3. Dawidowicz K., Krzan G., (2017), Periodic signals in a pseudo-kinematic GPS coordinate time series depending on the antenna phase center model - TRM55971.00 TZGD antenna case study, Survey Review, 49:355, 268-276, DOI: 10.1080/00396265.2016.1166688
4. Dawidowicz K., Baryła R., (2017), GNSS antenna caused near-field interference effect in Precise Point Positioning results, Artificial Satellites, 52(2): 27-40, DOI: 10.1515arsa-2017-0004
5. Golaszewski P., Stępniak K., Wielgosz P., (2017), Zenith Tropospheric Delay Estimates Using Absolute and Relative Approaches to GNSS Data Processing – Preliminary Results, 2017 Baltic Geodetic Congress (BGC Geomatics), Gdansk, 2017, pp. 414-418, DOI: 10.1109/BGC.Geomatics.2017.79.
6. Gołaszewski P., Wielgosz P., Stępniak K., (2017), Intercomparison and validation of GNSS-IWV derived with G-Nut and Bernese software, Proceeding paper: The 10th International Conference "Environmental Engineering", 27-28 April 2017, Vilnius, Lithuania.
7. Hadas, T., Krypiak-Gregorczyk, A., Hernández-Pajares, M., Kaplon, J., Paziewski, J., Wielgosz, P., A. Garcia-Rigo,K. Kazmierski,K. Sosnica,D. Kwasniak,J. Sierny,J. Bosy,M. Pucilowski,R. Szyszko,K. Portasiak,G. Olivares-Pulido,T. Gulyaeva,R. Orus-Perez, 2017, Impact and implementation of higher-order ionospheric effects on precise GNSS applications. Journal of Geophysical Research: Solid Earth, 122. https://doi.org/10.1002/2017JB014750
8. Hernández-Pajares M., Wielgosz P., Paziewski J., Krypiak-Gregorczyk A., Krukowska M., Stępniak K., Kaplon J., Hadas T., Sosnica K., Bosy J., Orus-Perez R., Monte-Moreno E., Yang H., Garcia-Rigo A., Olivares-Pulido G. (2017) Direct MSTID mitigation in precise GPS processing. Radio Sci., 52, 321–337, doi:10.1002/2016RS006159.
9. Jarmołowski W., (2016), Estimation of gravity noise variance and signal covariance parameters in least squares collocation with considering data resolution, Annals of Geophysics, 59/1, S0104

10. Jarmołowski W., Łukasiak J. (2016), A study on along-track and cross-track noise of altimetry data by maximum likelihood: Mars Orbiter Laser Altimetry (MOLA) example., Artificial Satellites (Journal of Planetary Geodesy), 50/4: 143-155.
11. Jarmołowski W., (2017), Fast estimation of covariance parameters in least squares collocation by Fisher scoring with Levenberg-Marquardt optimization. Surveys in Geophysics 38 (4): 701-725
12. Krypiak-Gregorczyk A., Wielgosz P., Borkowski A. (2017) Ionosphere Model for European Region Based on Multi-GNSS Data and TPS Interpolation. Remote Sensing, 9(12):1221. doi:10.3390/rs9121221.
13. Krypiak-Gregorczyk A., Wielgosz P., Jarmołowski W. (2017) A new TEC interpolation method based on the least squares collocation for high accuracy regional ionospheric maps. Measurement Science and Technology 28. doi:10.1088/1361-6501/aa58ae.
14. Krzan G., Dawidowicz K., Stępniak K., Świątek K., (2016), Determining normal heights with the use of Precise Point Positioning, Survey Review, DOI: 10.1080/00396265.2016.1164939.
15. Krzan G., Stępniak K., (2017), Application of the undifferenced GNSS precise positioning in determining coordinates in national reference frames, Artificial Satellites, Vol. 52, No. 3, pp. 49-69.
16. Kuczyńska-Siehień J., Łyszkowicz A., Stępniak K., Krukowska M., (2016), Determination of geopotential value W_0^L at Polish tide gauges from GNSS data and geoid model, Acta Geodaetica et Geophysica,
17. Malyszko L, Paziewski J, Sieradzki R, Kowalska E, Rutkiewicz A, 2017, Detecting Cantilever Beam Vibration with Accelerometers and GNSS. 2017 Baltic Geodetic Congress (BGC Geomatics), Gdansk, 2017, pp. 148-152. doi: 10.1109/BGC.Geomatics.2017.10
18. Paziewski J, 2016, Study on desirable ionospheric corrections accuracy for network-RTK positioning and its impact on time-to-fix and probability of successful single-epoch ambiguity resolution, Advances in Space Research, Vol. 57(4), 1098–1111, DOI 10.1016/j.asr.2015.12.024
19. Paziewski J, Sieradzki R, 2017, Integrated GPS+BDS instantaneous medium baseline RTK positioning: signal analysis, methodology and performance assessment, Advances in Space Research, DOI 10.1016/j.asr.2017.04.016
20. Paziewski J, Sieradzki R, Baryła R, 2017, High-rate GNSS positioning for precise detection of dynamic displacements and deformations: methodology and case study results, In: "Environmental Engineering" 10th International Conference Vilnius Gediminas Technical University Lithuania, 27–28 April 2017 DOI: https://doi.org/10.3846/enviro.2017.224
21. Paziewski J, Wielgosz P, 2017, Investigation of some selected strategies for multi-GNSS instantaneous RTK positioning, Advances in Space Research, Vol. 59(1), 12-23, DOI 10.1016/j.asr.2016.08.034
22. Sieradzki R, Paziewski J, 2016, Study on reliable GNSS positioning with intense TEC fluctuations at high latitude, GPS Solutions, Vol. 20(3), 553–563, DOI 10.1007/s10291-015-0466-0
23. Stepniak K, Baryla R, Paziewski J, Golaszewski P, Wielgosz P, Kurpinski G, Osada E, 2017, Validation of regional geoid models for Poland: Lower Silesia case study, Acta Geodynamica et Geomaterialia, Vol. 14, No. 1 (185), 93–100, DOI: 10.13168/AGG.2016.0031

1. SATELLITE GEODESY

24. Stępniak K., Bock O., Wielgosz P., (2017), Reduction of ZTD outliers through improved GNSS data processing and screening strategies, Atmos. Meas. Tech. Discuss, https://doi.org/10.5194/amt-2017-371.
25. Wielgosz P., Krypiak-Gregorczyk A., Borkowski A. Regional Ionosphere Modeling Based on Multi-GNSS Data and TPS Interpolation. In Proceedings of the Baltic Geodetic Congress (BGC Geomatics), Gdansk, Poland, 22–25 June 2017; pp. 287–291.

Institute of Geodesy and Geoinformatics, Wrocław University of Environmental and Life Sciences K. Sośnica, T. Hadaś, G. Bury, R. Zajdel, K. Kaźmierski

ILRS Associated Analysis Center

The civil and scientific users need intuitive and real-time information about the quality of available multi-GNSS products. In 2013, the multi-GNSS Pilot Project (MGEX) was initiated by the International GNSS Service (IGS) with the major motivation to increase the effort to prepare full integration of new constellations into the IGS common processing routine. Processing of GNSS data for all satellite navigation systems is complicated due to several satellite structural aspects such as varied frequencies of transmitted signals or differences in the shape of satellites' bus and solar panels. Satellite Laser Ranging (SLR) technique can be used as an independent validation tool for the orbit products. Thus, a new Associated Analysis Center of the International Laser Ranging Service at the Wroclaw University of Environmental and Life Sciences (IGG ILRS AAC) has been established providing a service called as multi-GNSS Orbit Validation Visualizer Using SLR (GOVUS) as its main component (Zajdel et al., 2017).
The GOVUS service (www.govus.pl) is addressed to users of multi-Global Navigation Satellite System (multi-GNSS) orbit products and Satellite Laser Ranging (SLR) stations belonging to the International Laser Ranging Service (ILRS), which track GNSS satellites. The main tasks of the developed service are to (1) store archival and current information about the ILRS laser stations and multi-GNSS satellites; (2) store the multi-GNSS microwave orbit validation results using SLR; (3) allow for fast and advanced online analyses on the stored dataset; (4) provide an autonomous computing center; and (5) generate up-to-date dataset and reports. Among all the current providers of multi-GNSS orbits, only the products delivered by the Center for Orbit Determination in Europe (CODE) are currently being validated as a representative example of 5-system orbit

products delivered in the framework of MGEX. CODE multi-GNSS orbit includes particular types of satellites: GPS, GLONASS of type M and K, Galileo of type IOV and FOC, BeiDou-2 of type MEO and IGSO and QZSS (Fig. 2.7.1). The service is divided between separate tools: (1) Plot Analyses; (2) Table List; (3) Station Statistics; (4) Satellite Statistics; (5) Report module; (6) Interactive map; (7) Tools.

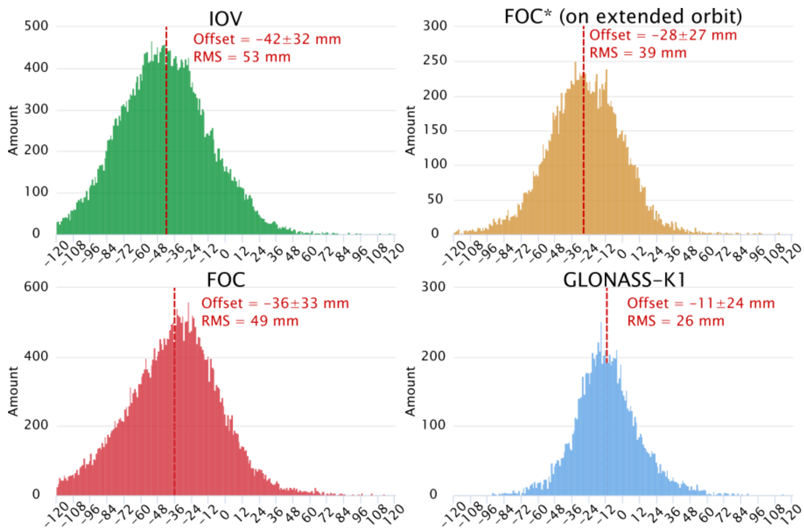

Fig. 1.36. Histograms of SLR residuals for particular satellite types (Zajdel et al., 2017)

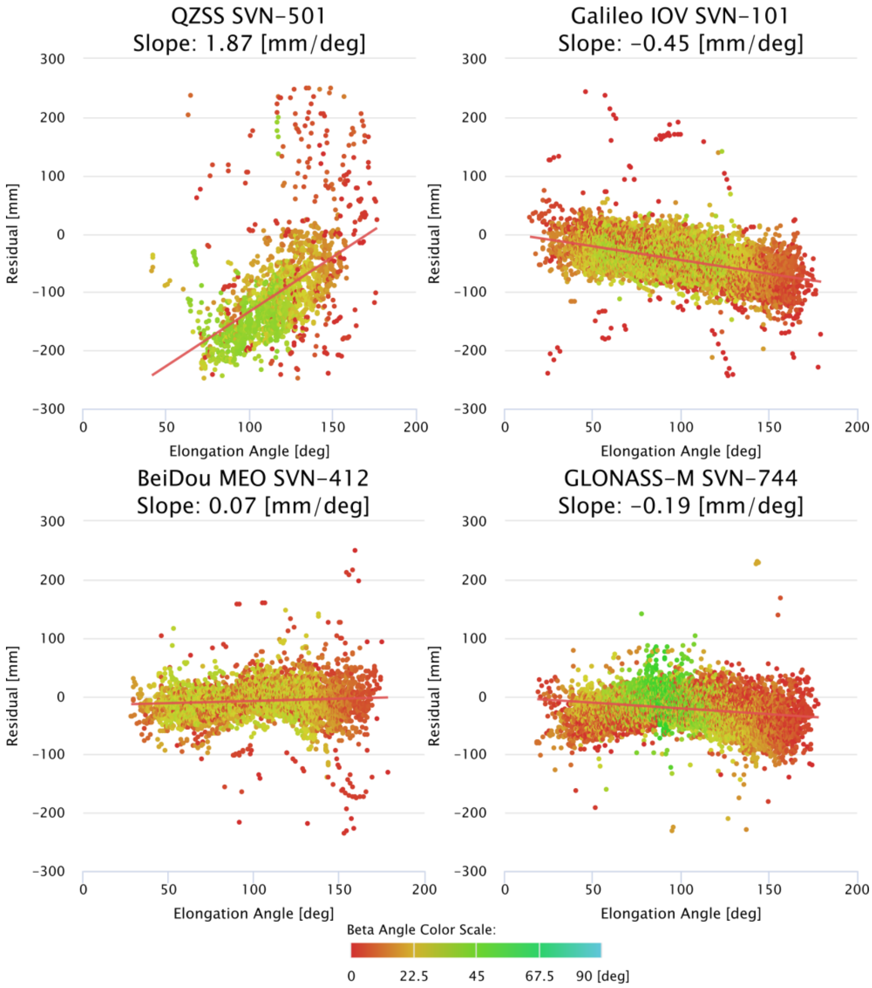

Fig. 1.37. SLR residuals as a function of elongation angle (ε). (period 2015.6-2017.6)

Continuous monitoring and independent validation are advised by both the MGEX and IGS authorities to help in the description of satellites' behavior in space (Fig. 2.7.2). It is important to identify possible issues, such as range biases in the pair of SLR station and the satellite, issues related with orbit determination (e.g. Solar Radiation Pressure mismodeling, access to the metadata with satellite surface properties), satellite systematics in laser measurements (e.g. satellite signature effect, see Sośnica et al., 2018a, 2018b), wrong microwave antenna and laser retroreflector array offsets, all of which limit the consistency between SLR and GNSS, and introduce discrepancies between both space geodetic techniques. GOVUS allows for advanced and comprehensive analyses toward the evaluation of the orbit quality in both SLR and GNSS aspects.

Analyzing Satellite Laser Ranging data to multi-GNSS

The IGG ILRS AAC processes on the regular basis the SLR observations to multi-GNSS constellation. A study presenting the importance of the observation geometry on the estimated orbit parameters of GNSS satellites has been performed. The analyses included the quality assessment of the satellite positions as a function of the number of collected SLR data, the number of observing SLR stations (see Fig. 3), as well as the length of the satellite arc.
The huge number of SLR observations to GNSS satellites allows for the combination of classical SLR observations to Laser Geodynamic Satellites (LAGEOS) with GNSS data. The combination substantially improves the quality of estimated station coordinates, especially for those stations which provide a large number of GNSS observations (see Fig. 1.39).

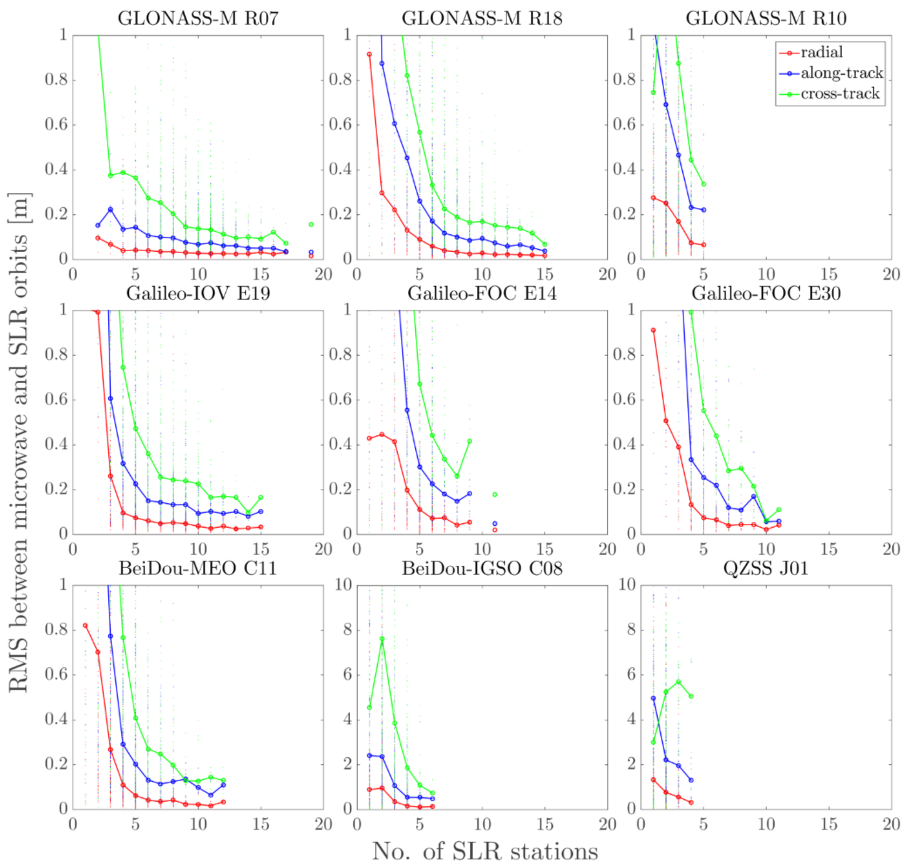

Fig. 1.38. Dependency between the number of SLR tracking stations and the quality of obtained GNSS orbits for the radial, along-track, and cross-track components (Bury et al., 2017)

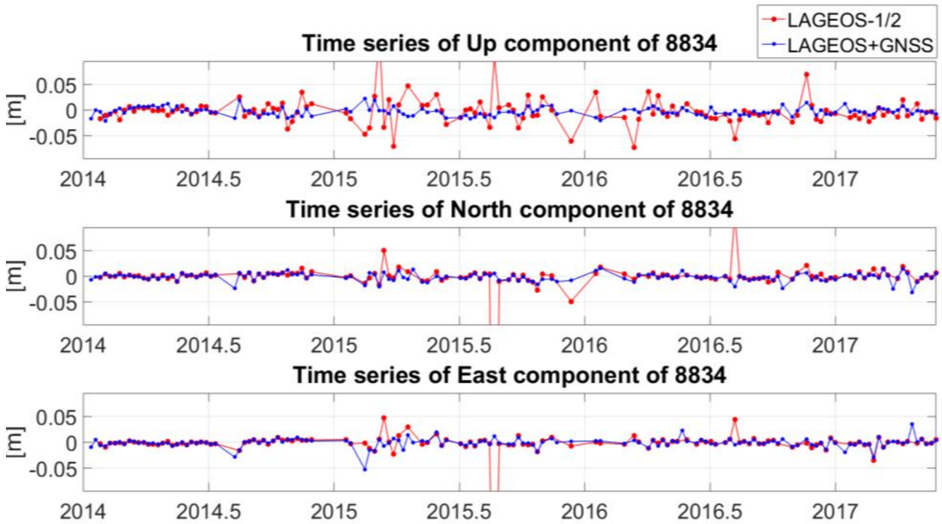

Fig. 1.39. Time series of Wettzell (8834) station coordinates based on SLR tracking of LAGEOS-1/2 satellites and the combined solution using SLR observations to GNSS and LAGEOS-1/2 (Sośnica et al., 2018)

Multi-GNSS positioning in real-time

An original real-time PPP software GNSS-WARP was developed at Wroclaw University of Environmental and Life Sciences (WUELS). The software allows processing GPS, GLONASS, Galileo and BeiDou data in real-time (using corrections from streams), simulated real-time (using recorded orbits and clocks from streams) and postprocessing (with final products) modes, to estimate static and kinematic coordinates. In order to correctly consider all new GNSS system, special inter-system observation weighting has been developed (Kaźmierski et al., 2018a). The best weighting scheme is based on the quality of GNSS orbits and clock products used in real-time positioning (Kaźmierski et al., 2018b).

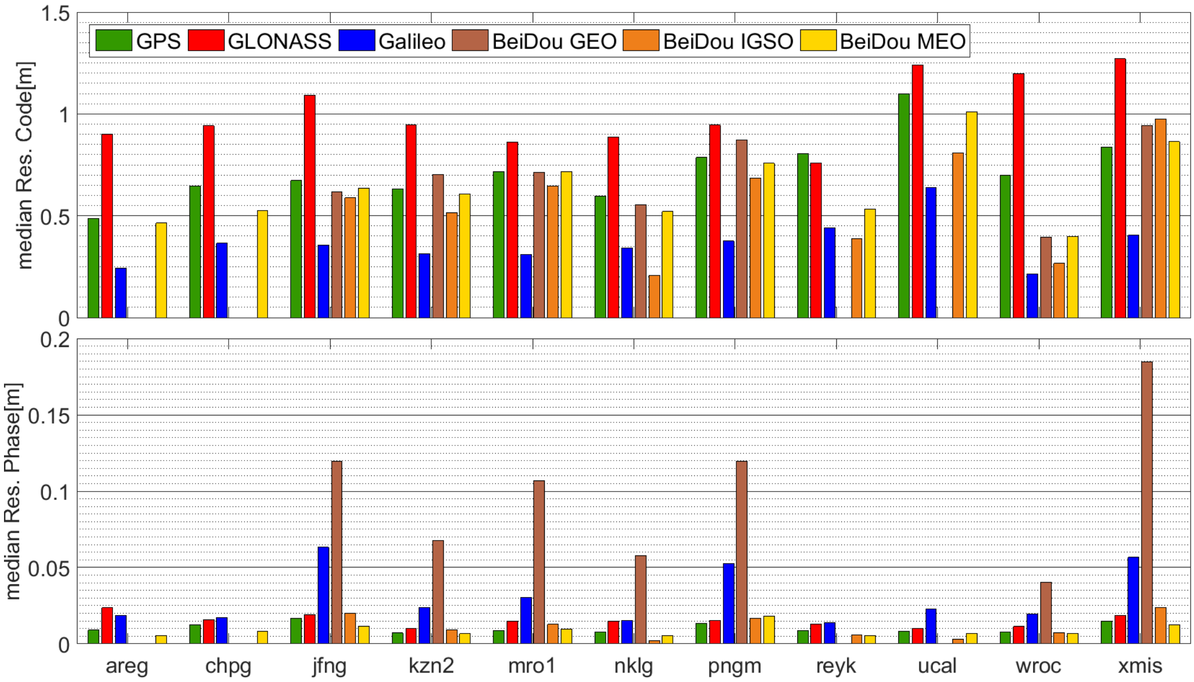

Fig. 1.40. Quality of code pseudorange (top) and carrier phase (bottom) observation residuals of real-time observations for selected multi-GNSS stations using the ionospheric-free linear combination L3.

Troposphere and Ionosphere analysis at WUELS

The GNSS data has been used for studying the events of extreme ionosphere activity (Hernández-Pajares et al., 2017) as well as studying the impact of higher-order ionosphere corrections on the GNSS positions and GNSS orbits (Hadaś et al., 2017; Banville et al., 2017). These activities were performed in the framework of two ESA projects: "Higher Order Ionospheric modelling campaigns for precise GNSS applications – HORION" and "Precise Ionospheric Modelling for Improved GNSS Positioning in Poland".

The optimum stochastic modeling for GNSS tropospheric delay estimation in real-time using a proper weighting has been developed (Hadaś et al., 2017; Ding et al., 2017). A tropospheric delay model has been developed for the EGNOS augmentation system (Kaźmierski et al., 2017). Finally, the least-squares collocation of meteorological and GNSS data was tested for the integration of the tropospheric refractivity and zenith path delays (Wilgan et al., 2017b). The high-resolution numerical weather prediction model was also used to augment real-time PPP (Wilgan et al., 2017a).

Publications:

1. Banville S., Sieradzki R., Hoque M., Węzka K., Hadaś T (2017): On the estimation of higher-order ionospheric effects in precise point positioning. GPS Solutions, Vol. 21 No. 4, Berlin - Heidelberg 2017, pp. 1817-1828. DOI: 10.1007/s10291-017-0655-0
2. Hadaś T., Krypiak-Gregorczyk A., Hernández-Pajares M., Kapłon J., Paziewski J., Wielgosz P., Garcia-Rigo A., Kaźmierski K, Sośnica K., Kwaśniak D., Sierny J., Bosy J., Puciłowski M., Szyszko R., Portasiak K., Olivares-Pulido G., Gulyaeva T., Orus-Perez R. (2017): Impact and Implementation of Higher-Order Ionospheric Effects on Precise GNSS Applications. Journal of Geophysical Research: Solid Earth, Vol. 122 No. 11, Washington, DC, USA 2017, pp. 9420-9436. DOI: 10.1002/2017JB014750
3. Hadaś T., Teferle F. N., Kaźmierski K., Hordyniec P., Bosy J. (2017): Optimum stochastic modeling for GNSS tropospheric delay estimation in real-time. GPS Solutions, Vol. 21 No. 3, Berlin - Heidelberg 2017, pp. 1069-1081. DOI: 10.1007/s10291-016-0595-0
4. Hernández-Pajares M., Wielgosz P., Paziewski J., Krypiak-Gregorczyk A., Krukowska M., Stępniak K., Kapłon J., Hadaś T., Sośnica K., Bosy J., Orus-Perez R., Monte-Moreno E., Yang H., Garcia-Rigo A., Olivares-Pulido G. (2017): Direct MSTID mitigation in precise GPS processing. Radio Science, Vol. 52 No. 3, 2017, pp. 321-337. DOI: 10.1002/2016RS006159
5. Kaźmierski K., Hadaś T., Sośnica K. (2018): Weighting of Multi-GNSS Observations in Real-Time Precise Point Positioning. Remote Sensing, Vol. 10 (1) No. 84, Basel, Switzerland 2018, pp. 1-15. DOI: 10.3390/rs10010084
6. Kaźmierski K., Sośnica K., Hadaś T. (2018): Quality assessment of multi-GNSS orbits and clocks for real-time Precise Point Positioning. GPS Solutions, Vol. online No. 22:11, Berlin - Heidelberg 2018, pp. 1-12. DOI: 10.1007/s10291-017-0678-6
7. Sośnica K., Prange L., Kaźmierski K., Bury G., Drożdżewski M., Zajdel R., Hadaś T. (2018): Validation of Galileo orbits using SLR with a focus on satellites launched into incorrect orbital planes. Journal of Geodesy, Vol. 92 online No. 2, Berlin Heidelberg 2018, pp. 1-18. DOI: 10.1007/s00190-017-1050-x
8. Bury G., Sośnica K. (2017): How many SLR observations and how many station are needed for deriving high-quality multi-GNSS orbits? 2017 ILRS Technical Workshop "Improving ILRS Performance to Meet Future GGOS Requirements", Riga, Latvia, 02-05 October, 2017
9. Sośnica K., Bury G., Zajdel R. (2018): Contribution of multi-GNSS constellation to SLR-derived terrestrial reference frame. Geophysical Research Letters, Vol. online No. , Washington, DC, USA 2018, pp. 1-28. DOI: 10.1002/2017GL076850
10. Tseng T-P., Hwang C., Sośnica K., Kuo C-Y., Liu Y-C., Yeh W-H. (2017): Geocenter motion estimated from GRACE orbits: the impact of F10.7 solar flux. Advances in Space Research, Vol. 59 No. 11, 2017, pp. 2819-2830. DOI: 10.1016/j.asr.2016.02.003
11. Zajdel R., Sośnica K., Bury G. (2017): A New Online Service for the Validation of Multi-GNSS Orbits Using SLR. Remote Sensing, Vol. 9 No. 10 (1049), Basel, Switzerland 2017, pp. 1-22. DOI: 10.3390/rs9101049

12. Kaźmierski K., Santos M., Bosy J. (2017): Tropospheric delay modelling for the EGNOS augmentation system. Survey Review, Vol. 49 No. 357, London, United Kingdon 2017, pp. 399-407. DOI: 10.1080/00396265.2016.1180798
13. Ding W., Teferle F. N., Kaźmierski K., Laurichesse D., Yuan Y. (2017): An evaluation of real-time troposphere estimation based on GNSS precise point positioning. Journal of Geophysical Research: Atmospheres, Vol. 122 No. 5, Washington, DC, USA 2017, pp. 2779-2790. DOI: 10.1002/2016JD025727
14. Wilgan K., Hadaś T., Hordyniec P., Bosy J. (2017): Real-time precise point positioning augmented with high-resolution numerical weather prediction model. GPS Solutions, Vol. 23 No. 3, Berlin - Heidelberg 2017, pp. 1341-1353. DOI: 10.1007/s10291-017-0617-6
15. Wilgan K., Hurter F., Geiger A., Rohm W., Bosy J. (2017) Tropospheric refractivity and zenith path delays from least-squares collocation of meteorological and GNSS data. Journal of Geodesy, Vol. 91 No. 2, Berlin Heidelberg 2017, pp. 117-134. DOI: 10.1007/s00190-016-0942-5

Department of Geodesy and Geodetic Astronomy Warsaw University of Technology (WUT) A. Brzeziński, M. Kruczyk, T. Liwosz, T, Olszak, D. Próchniewicz, M. Rajner, R. Szpunar, J. Walo

Department of Geodesy and Geodetic Astronomy, Faculty of Geodesy and Cartography, Warsaw University of Technology has conducted investigations in the field of satellite geodesy, geodynamics, gravimetry and GNSS meteorology. Summary of the Department activities profile is best described in 2016 paper (Brzeziński *et al.* 2016). Majority of the measurements are conducted at Astro-Geodetic Observatory at Józefosław.

GNSS analysis

Warsaw University of Technology (WUT) has been operating as an EPN Analysis Centre (AC) since 1996. WUT AC regularly processes GNSS data and provides to EUREF final (weekly and daily) and rapid daily solutions of the EPN subnetwork (Liwosz 2015a). At the end of 2017, WUT subnetwork consisted of 118 GNSS stations. WUT AC uses Bernese GNSS Software version 5.2 for GNSS data processing.

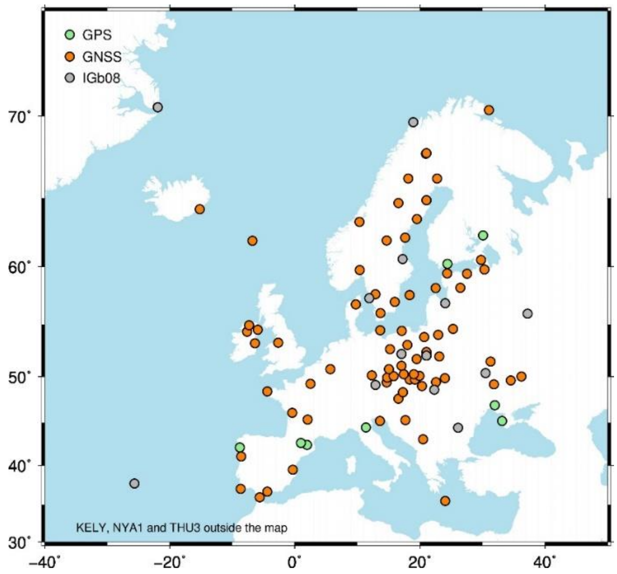

Fig. 1.41. WUT AC EPN network (December 2017), two-system stations in orange, IGb08 reference stations (IGS08 frame definition, also JOZE and JOZ2 at Józefosław)

WUT AC was also analyzing the impact of the non-tidal loading effects on site coordinates in a Polish (Rajner and Liwosz 2017), and in a European regional GPS network (Liwosz 2015b, Liwosz 2017). In the case of European regional network, the non-tidal loading models were applied at the observation level. Modelling the non-tidal loading effect due to the atmosphere improved the mean repeatability of daily time series of the height component by 6.3%, due to oceans by 0.9%, and due to continental water by 2.1%. Modelling all the non-tidal loading effects improved the mean repeatability of the height component by 9.8%. Modelling all the non-tidal effects improved the velocity errors in all components by 7%, and by 23% when in addition also annual and semiannual signals that are present in site coordinate time series were estimated during the velocity estimation.

In 2015, WUT together with Polish Head Office for Geodesy and Cartography (GUGiK) reprocessed 3.7-year GNSS data from Polish national GNSS network and created a new realization of ETRS89 for Poland (Ryczywolski and Liwosz 2015, Liwosz and Ryczywolski, 2016). The new solution was accepted as Class A solution by the EUREF Technical Working Group on the EUREF Symposium 2015 in Leipzig.

Since year 2014, WUT together with the Military University of Technology, Poland, have been operating as the EPN Analysis Combination Centre. Since year 2016 WUT is responsible for the creation of the official EPN (EUREF Permanent Network) combined coordinate solutions. The EUREF combined coordinate solutions are based on GNSS solutions generated by the 16 EPN Analysis Centres (AC). In the beginning of 2016, WUT prepared new reports on final weekly and daily combinations and created new scripts for checking the correctness of station information given in AC SINEX files. At the end of 2016, a methodology for creating weekly combined EPN solutions was changed. Up to and including week 1924, the weekly combined solutions were created directly from the AC weekly solutions (Liwosz and Araszkiewicz 2017). Since week 1925 (November 27–December 4, 2016), the daily AC solutions are used for that purpose; at first the daily AC solutions are combined for each day of the week, and then the seven daily combined solutions are stacked into a weekly solution. It was verified that the new approach allows to more consistently handle position outliers (for both AC and combined daily solutions), and helps to mitigate possible inconsistencies between AC solutions which could be observed when combining on a weekly level.

Advanced methods for satellite positioning

a) Stochastic modeling of GNSS observations

Research on stochastic modeling of GNSS observations was carried out at the Warsaw University of Technology (WUT). It was focused on development the stochastic model for instantaneous Network RTK positioning, called the Network-Based Stochastic Model (NBSM) (Prochniewicz *et al.*, 2016). The NBSM is a weighted model which used a network correction variance estimations as an accuracy characteristic of ionospheric and geometric residual errors. This model uses correction term variances estimated directly in the network solution, together with estimations of the corrections themselves. Such a solution enables the capturing of current residual error values on the basis of observations from a single epoch without using observations from the monitoring station, which is the essential difference compared to the existing models. This approach predisposes the NBSM for application in instantaneous Network RTK positioning. Figure 2 illustrates the schema of the Network RTK performance model composed of three groups of algorithms: network solution, network correction and positioning model. Color red denotes a new elements of this model which were added by NBSM.

The test results of proposed stochastic model were carried out for the instantaneous Network RTK performance. Comparison weighted positioning model based on NBSM with the ionosphere-fixed troposphere-fixed model, which is the standard model for the Network RTK shows that both the ambiguity integer estimation and the validation are characterized by a significantly higher success rate. Application of the NBSM reduced also the rover positioning errors down to the level of 15-30 % (Prochniewicz et al. 2016).

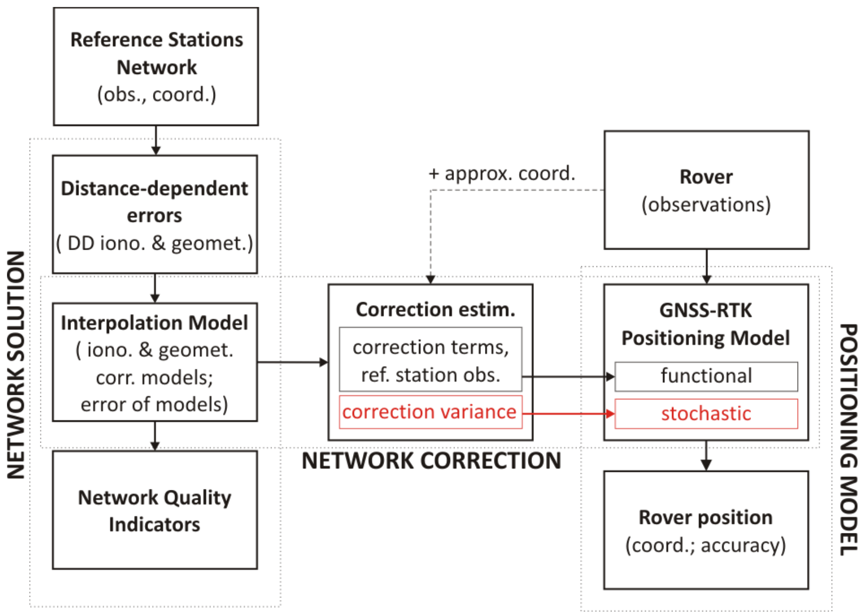

Fig. 1.42. Network RTK positioning model based on NBSM

b) Reliability of GNSS Network RTK positioning

These studies were focused on developing a new approach to the estimation of Network RTK positioning reliability using network solution quality indicators. They are parameters which describe the impact of dispersive (ionospheric) and non-dispersive (geometric) errors on rover positioning. In the Network RTK positioning model, this impact is largely reduced by the application of network corrections. This is the reason why these indicators mostly reflect the accuracy of the determination of these corrections. The existing network solution quality indicators do not provide the possibility of practical interpretation of their indications, understood as the usefulness of quality indexes to indicate the epochs or the time periods, for which the expected reliability of precise positioning solution is low. Their quantitative interpretation is also much more difficult due to the fact that there are no precisely defined critical values for these parameters.

In our study we were developed a new method of estimating Network RTK positioning reliability with the use of two quality indicators: solution accuracy and solution availability (Prochniewicz et al. 2017). These indexes utilize the existing parameters describing the reliability of the ambiguity resolution for the carrier-phase observations and the fixed solution error estimation and they are based on the Network-Based Stochastic Model (NBSM) (Prochniewicz et al. 2016) which takes into account the residual ionospheric and geometric errors. These parameters depend solely on the variance-covariance observation matrix and the design matrices and they do not require current observations from the user's receiver which predestines them for use as external parameters describing the possible reliability of the Network RTK solution and greatly facilitates their application.

The proposed indicators were determined for the test field composed of a part of the regional ASG-EUPOS reference stations network and compared with the results of the instantaneous Network RTK positioning model solution. The indications of the new indexes were also compared to the existing parameters currently used to estimate the reliability of network positioning. Figure 3 presents solution availability index for test network derived as hourly Ambiguity Success Rate (ASR) indicator with the confidence level of 95 %. The analysis of the ASR clearly shows the period for which the correct ambiguity resolution proved to be difficult and ineffective in practice. The lowest ASR (below 50%) was obtained for 17-18 UTC period when only 5 satellites were observed; improvement satellite geometry at about 18 UTC caused a sudden increase the ASR value to about 95%. For the analysed test field, the adoption of the alarm value at 90% already provides the opportunity to correctly identify the periods in which the solution availability is significantly reduced. Figure 2.8.4 presents the solution accuracy index with the assumption of correct ambiguity resolution. The chart shows estimated fixed solution positioning error for each epoch (confidence level 1σ, black) and the actual (real) values of the positioning errors, calculated based on the comparison of the determined position with the known reference values (gray). The analysis of this index for the test baseline shows that proposed method allows to effective identification of the periods for which positioning reliability was reduced.

Functional correlation of the estimated correction term errors in the NBSM for the given epoch with the distance to reference stations enables the determination of the spatial distribution of the ASR index and position error for the specific epoch. Maps of solution availability (ASR) and solution accuracy (positioning error) indexes can be an important information tool in the measurements planning and performance process, enabling the indirect estimations of the accuracy and reliability of the positioning.
The comparison of the indications of availability and accuracy indices with the commonly applied indices (I95, RIM, RIU) for instantaneous Network RTK positioning shows that the proposed indices are much more effective and their interpretation enables a much easier identification of the periods for which the reliability of performance may be reduced. A large advantage of these parameters is also the fact that they do not only depend on the residual errors, as is the case with the existing indexes, but also on the number of satellites, applied method of ambiguity estimation and the observation measurement noise. This enables taking into account all the parameters affecting the quality of the positioning model solution.

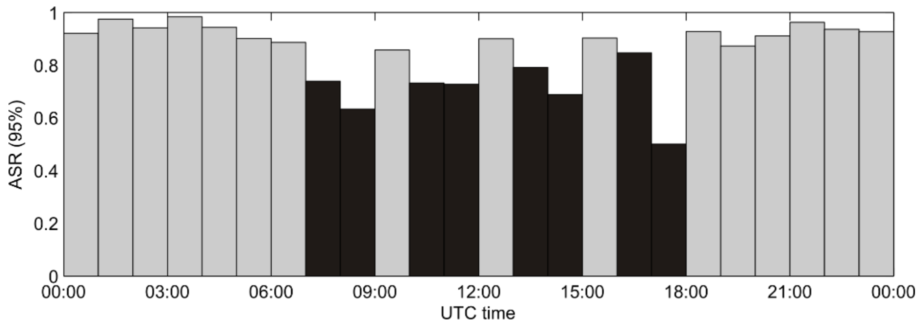

Fig. 1.43. Ambiguity resolution success rate for test baseline - hourly solution availability (95%) index.

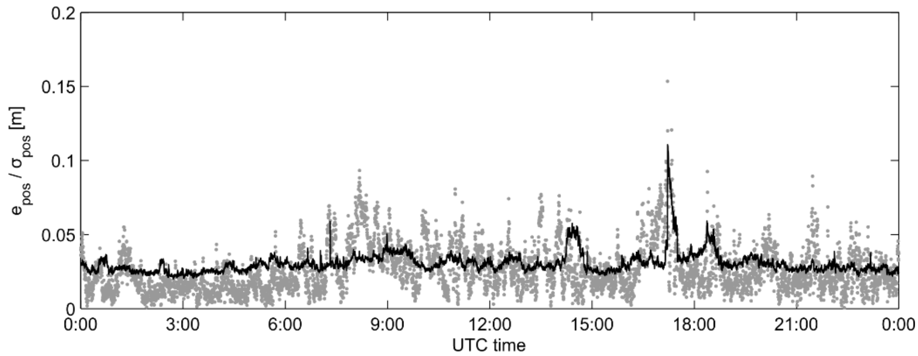

Fig. 1.44. Positioning accuracy of the fixed solution for the test baseline – instantaneous values of the accuracy index: black—estimated errors (1σ), gray—actual errors.

c) Satellite gravimetric missions – utilization and validation of temporal models

Geophysical grids, derived from "Heterogeneous gravity data combination for Earth interior and geophysical exploration research" project (GOCE+) as the components of the Eötvös tensor, gridded with a resolution of 0.2° per 0.2° were used to computation of the sensitivity using a 3D lithospheric model divided into: topography/bathymetry, sediments and location of the Moho boundary. To define tesseroids as mathematical model of the lithosphere we need to set two parameters: density and depth for each layer separately. Altitudes for topography/bathymetry were derived from ETOPO1 model, sediments depths from EuCRUST-07 model, and Moho boundary from Grad and Tiira (2009) seismic map. For high latitudes, we noted the largest changes for the gradients towards the poles, with particular values of 689.07 mE (mili-eotvos) and 1138.19 mE for V_{XX} and V_{ZZ} gradients, respectively. We obtained extreme values for the location of the deep and shallow areas of the crust (Alps, North-Eastern Poland and areas of seas) equal to -3 E and +1.5 E, respectively. Most of the gradients showed strong correlation with anomalies of crustal density of -2.5 E for V_{ZZ} and +1.5 E for V_{YY} in the extreme cases. We have shown that changes in lithosphere density and depth by 50 kg/m^3 and 10 km entail changes in gradient values by 15% for density and 10% for depths. (Lenczuk et al. 2018).

In the aspect of satellite GRACE mission product validation analysis of the temporal models obtained from three processing centers have been done. Analysis included comparing the values of gravitational disturbances, obtained from temporal GRACE monthly solutions with the values determined by gravimetric absolute measurements by FG-5 apparatus. The comparison covered the full range of time solutions for the years 2003-2016 and all repeated gravimetric measurements at the points of geodynamic and the fundamental gravimetric networks in Poland. The most interesting results were obtained for quasi-permanent time series of gravimetric observations in Jozefosław (Szabo 2018) and rarely repeated absolute g determinations on the Lamkówko Observatory of the University of Warmia and Mazury in Olsztyn.

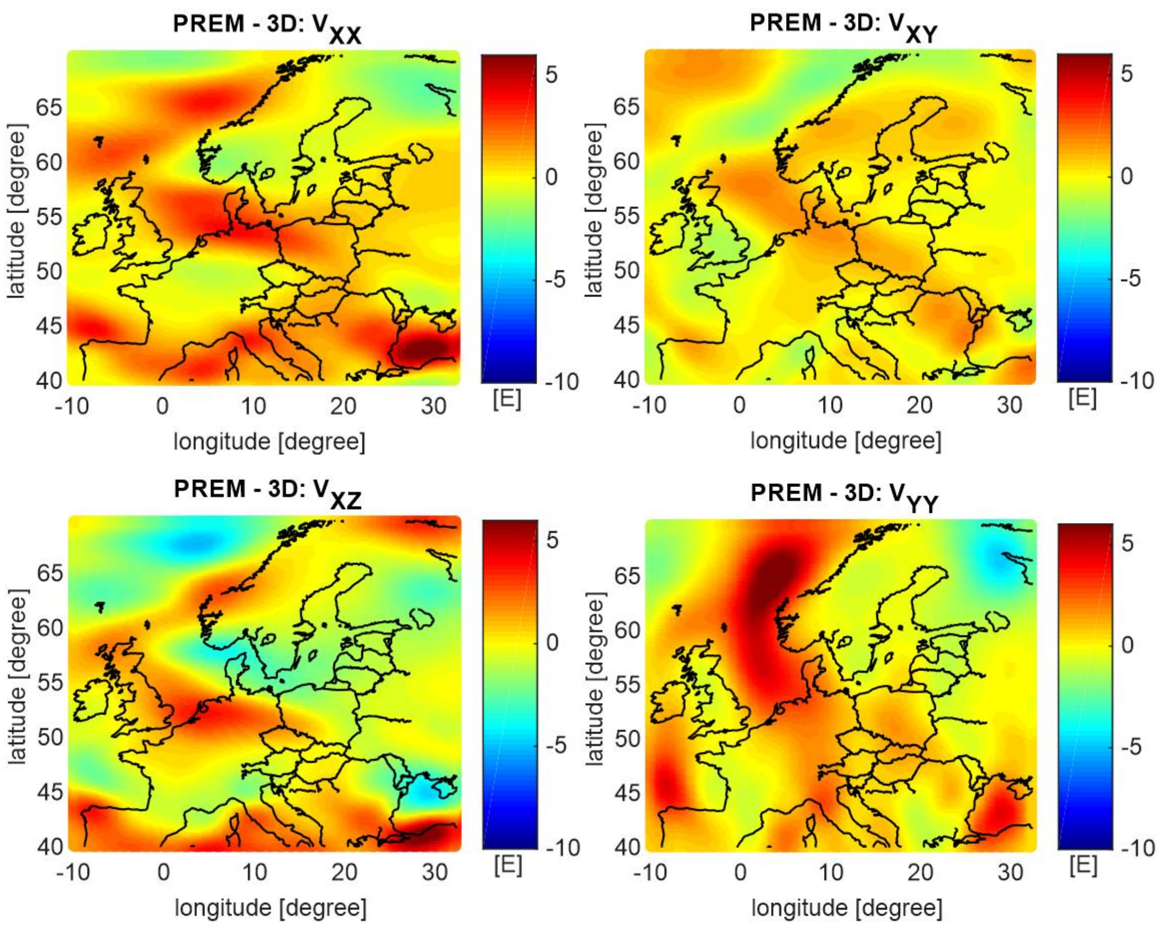

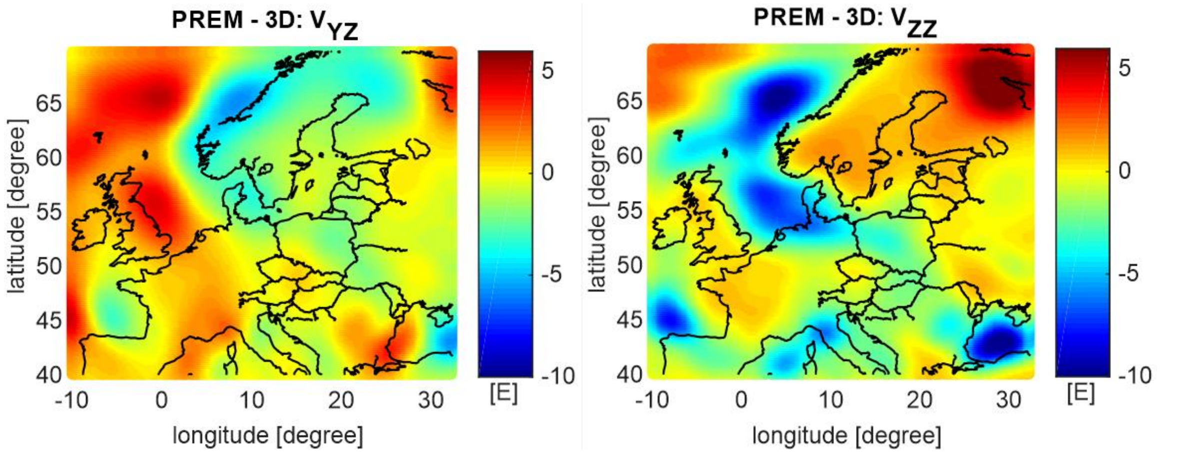

Fig. 1.45. Differences in the second potential derivatives for the studied area obtained from the GOCE mission data reduced by the topographic effect, sediments and Moho boundary depth between the density values from the PREM model and the 3D lithosphere model. Values presented in the LNOF frame from altitude 255 km, expressed in [E] (eotvos).

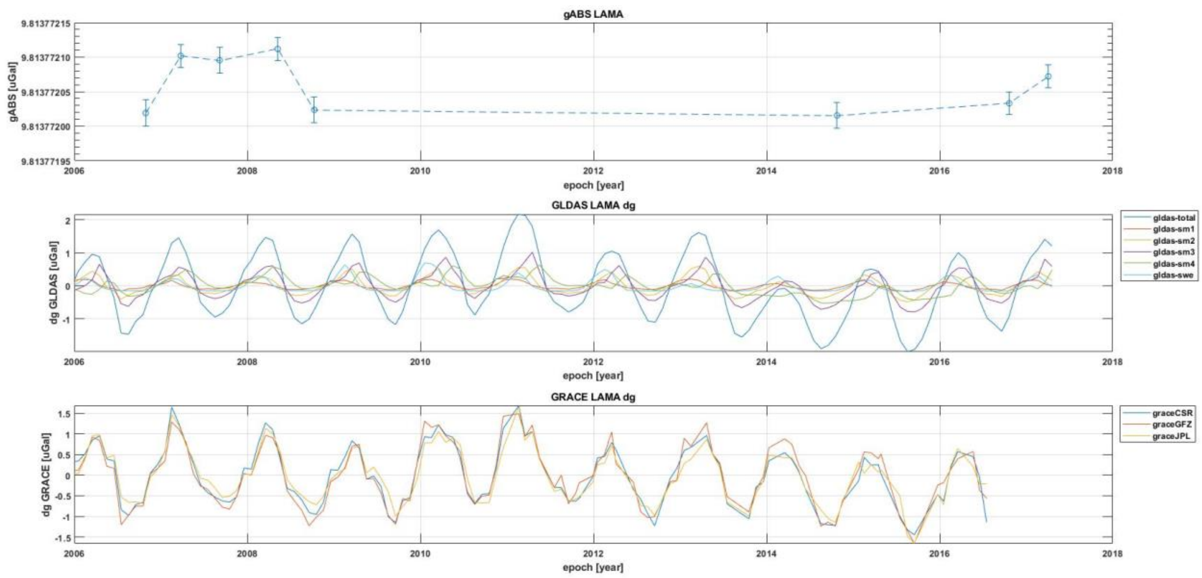

Fig. 1.46. Absolute gravity values and influences of global hydrology in gravity at Lamkówko Observatory.

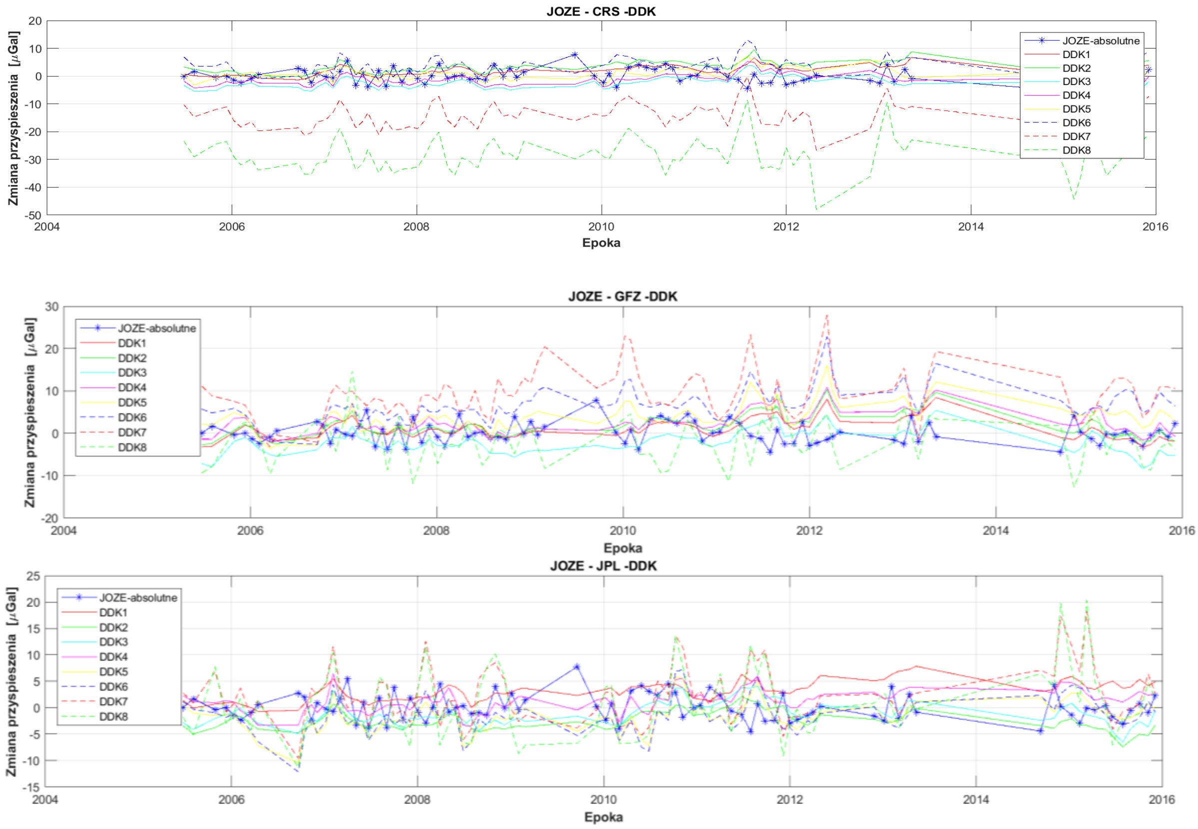

Fig. 1.47. Absolute gravity changes observed by absolute gravimeter and obtained from different DDK filters for GRACE monthly solutions.

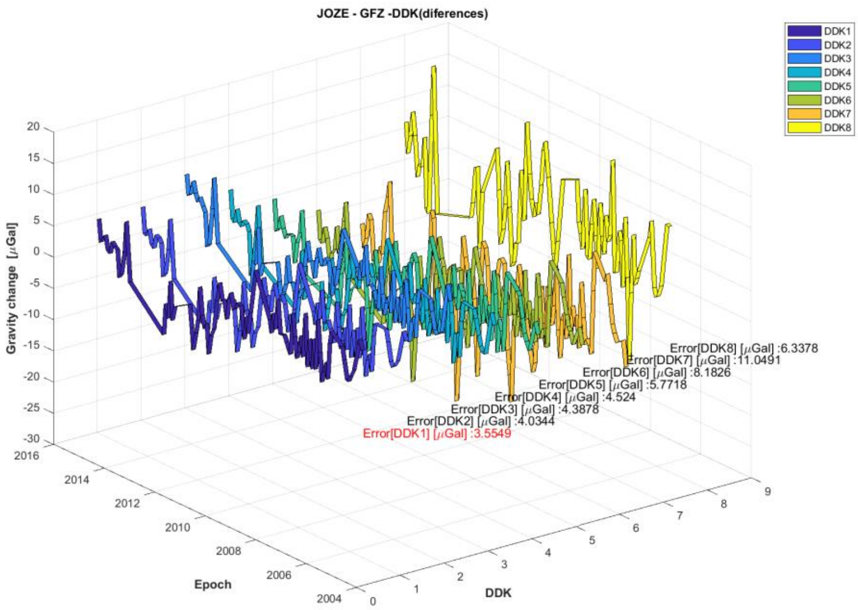

Fig. 1.48. Absolute gravity changes observed by absolute gravimeter and obtained from different DDK filters for GRACE monthly solutions.

GNSS Meteorology

Department continued investigations of IPW (integrated precipitable water i.e. columnar water vapour) as climatologic and aerologic parameter.
Long time series of integrated precipitable water (calculated from tropospheric delay estimates by IGS in PPP mode) averaged daily can serve as change climate indicators. (Kruczyk 2015a). The seasonal model of IPW change has been adjusted to the multi-year series by the least square method. In case of Józefosław 15 year series yields IPW trend of +0.25 mm/year (Fig. 2.8.9). It is probably a signal of global climate change (Brzeziński *et al.* 2016).

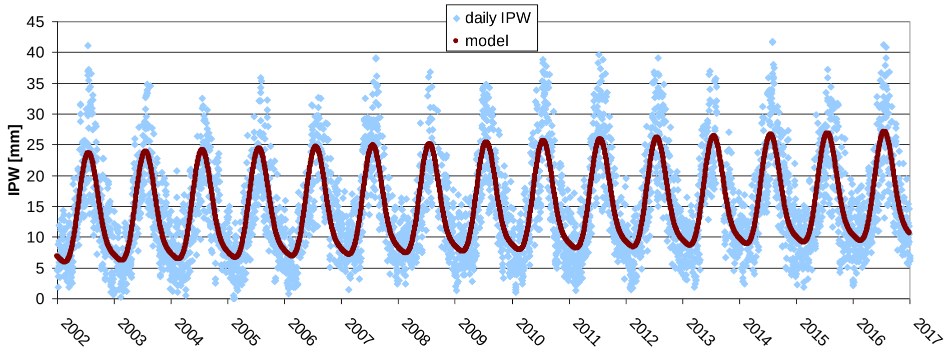

Fig. 1.49. IPW for JOZE (Józefosław, Poland) and model with 2 oscillations (annual and semi-annual) applied to 2003-2016 period, IGS tropospheric solution.

The next field of research is to asses areological techniques of water vapour retrieval both in Central Europe (Kruczyk *et al.* 2017) and in polar regions. Three independent techniques to obtain integrated precipitable water (GPS solution, radio sounding and CIMEL sunphotometer) have been tested in case of dedicated GPS measurements by Polish Polar Station in Hornsund Fjord at four points in Greenland (Kruczyk and Liwosz 2015, Kruczyk, 2015b). CIMEL sunphotometer IPW and IPW values derived from standard solutions of IGS and EPN (combined solution) show relatively good agreement but also some biases of 2–7 %. IPW bias shows seasonal dependence (especially in case of Thule) what signals some systematic deficiencies in solar photometry as IPW retrieval technique (Fig. 2.8.10). Probable cause to this phenomenon is a change of optical filter characteristics in sunphotometer working in extreme polar conditions. Averaged IPW difference for RAOB (radio sounding observation) – GPS is relatively small and show no dependence on temperature. The attempt to compare areological techniques (CIMEL and RAOB) brings similar temperature – IPW difference dependence.

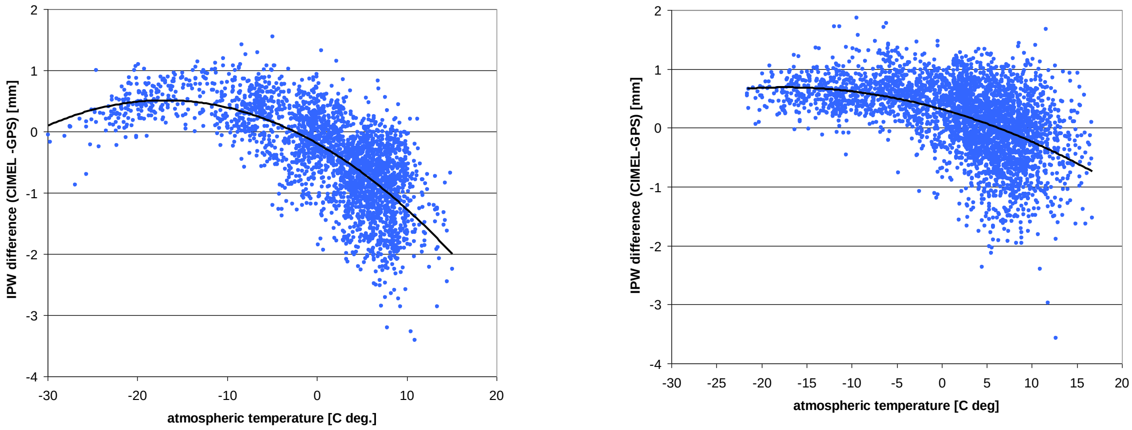

Fig. 1.50. IPW difference (CIMEL-GPS) for Thule-THU2 for 2009–2011 and Ittoqqortoormiit - Scoresbysund (SCOR), Greenland, for 2012–2014 as a function of atmospheric temperature, IGS tropospheric solution.

Geodynamics and Earth Rotation

Tidal gravity measurements conducted at the Astro-Geodetic Observatory at Józefosław near Warsaw with the use of a LaCoste&Romberg Earth Tide no. 26 gravimeter have been used investigate the determination of the FCN parameters from gravity records covering a period of more than three years. (Rajner and Brzeziński 2017)

The Free Core Nutation (FCN) is an important eigenmode which affects both Earth rotation and body tide. The FCN parameters, the resonance period and the quality factor are important for understanding the dynamics of the Earth at nearly diurnal periods. Those parameters are usually estimated either from the Very Long Baseline Interferometry (VLBI) observations of nutation or like in this project tidal gravity measurements. From the resonant enhancements of gravimetric factors and phases of diurnal tidal gravity waves, we could infer the FCN period to be equal to 430 sidereal days. This result is in very good agreement with previous gravimetric and VLBI nutation results, confirming the discrepancy in the dynamic flattening of the outer liquid core from its theoretical value based on the hydrostatic equilibrium assumption. The estimated FCN quality factor ($Q \approx 1300$) is considerably smaller than the VLBI nutation result, which confirms that the local gravity measurements are more sensitive than VLBI global analyses to site-dependent phenomena (such as atmospheric and indirect ocean tidal effects). Also the importance of gravimetric corrections in the FCN analysis, including numerical tests and simulations has been investigated. This allowed to estimate the uncertainty of FCN parameters due to improper or incomplete set of environmental corrections. Authors took also into account the impact of gravimetric factor errors and tidal wave selection on estimated FCN parameters. Paper demonstrated that despite relatively noisy measurements due to unfavorable gravimeter location, authors were able to obtain very good results in case when proper correction and tidal wave selection were applied.

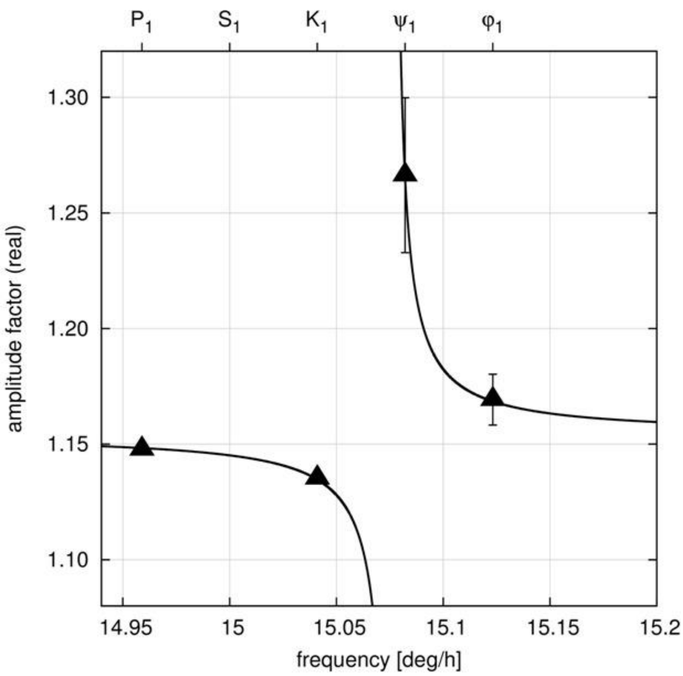

Fig. 1.51. FCN parameters from tidal gravimetric observations.

Another important research in the field of geodynamics include investigation of the loading effects by land hydrology on GNSS positions (Zygmunt et al. 2016) and in view of total water equivalent estimated form GRACE data (Liwosz and Rajner, 2017). Our Department works also on how to use laser ring measurements for Earth rotation parameters determination (Tercjak and Brzeziński 2017).

1. SATELLITE GEODESY

Publications:

1. Brzeziński A., Barlik M., Andrasik E., Izdebski W., Kruczyk M., Liwosz T., Olszak T, Pachuta A., Pieniak M., Próchniewicz D., Rajner M., Szpunar R., Tercjak M., Walo J. (2016) Geodetic and geodynamic studies at Department of Geodesy and Geodetic Astronomy WUT. Reports on Geodesy and Geoinformatics, vol. 100, 2016, pp. 165-200, DOI:10.1515/rgg-2016-0013
2. Bruyninx, C., A. Araszkiewicz, E. Brockmann, A. Kenyeres, T. Liwosz, R. Pacione, W. Söhne, G. Stangl, K. Szafranek, C. Völksen (2017) EUREF Permanent Network in IGS Technical Report 2016 Editors: A. Villiger, R. Dach Astronomical Institute, University of Bern pp. 95-104
3. Kruczyk M. (2015a) Long Series of GNSS Integrated Precipitable Water as a Climate Change Indicator. Reports on Geodesy and Geoinformatics, Vol 99 (2015) pp. 1-18; DOI:10.2478/rgg-2015-0008
4. Kruczyk. M., (2015b) Comparison of Techniques for Integrated Precipitable Water Measurement in Polar Region. Geoinformation Issues Vol. 7, No 1(7) /2015 pp 15-29
5. Kruczyk, M., Liwosz, T. (2015) Integrated precipitable water vapour measurements at Polish Polar Station Hornsund from GPS observations verified by aerological techniques. Reports on Geodesy and Geoinformatics, Vol 98 (2015) 1-17; DOI: 10.2478/rgg-2015-0001
6. Kruczyk, M., T. Liwosz, A. Pietruczuk (2017) Integrated Precipitable Water from GPS Observations and Cimel Sunphotometer Measurements at CGO Belsk. Reports on Geodesy and Geoinformatics, Vol 103, Issue 1 (2017) DOI: 10.1515/rgg-2017-0005
7. Lenczuk, A., M. Barlik, T. Olszak, J. Bogusz (2018) Modelling of the lithosphere's density and thickness for reduction of the GOCE gravity gradients: case study of Central Europe. Pure and Applied Geophysics, 2018 (in review)
8. Liwosz, T. (2015a) Report of the WUT Analysis Centre. EPN Local Analysis Centres Workshop, 14-15 October, Bern, Switzerland (report available at: http://www.epncb.oma.be/_neweventslinks/workshops/EPNLACWS_2015/pdf/report_of_the_WUT_analysis_centre.pdf)
9. Liwosz, T. (2015b) The impact of non-tidal loading effects on regional GPS solutions. Poster presented at 26th General Assembly of the International Union of Geodesy and Geophysics, Prague, Czech Republic, Abstract number IUGG-5094
10. Liwosz, T. (2017) The impact of non-tidal loading effects on site coordinates and a reference frame realization in a regional GPS network. Scientific Works vol. 56, The Warsaw University of Technology Publishing House, ISBN 978-83-7814-695-7, pp. 123, in Polish.
11. Liwosz, T., A. Araszkiewicz (2017) EPN Analysis Coordinator Status Report. EUREF Symposium, Wrocław, Poland, May 17–19.
12. Liwosz, T., M. Ryczywolski (2016) Verification of the Polish geodetic reference frame by means of a new solution based on permanent GNSS data from the years 2011–2014. Reports on Geodesy and Geoinformatics, 102 (1), 52–66, doi:https://doi.org/10.1515/rgg- 2016-0027.
13. Próchniewicz, D., R. Szpunar & J. Walo (2017) A new study of describing the reliability of GNSS Network RTK positioning with the use of quality indicators. Measurement Science and Technology, 2017:28(1), pp. 015012, DOI:10.1088/1361-6501/28/1/015012

14. Próchniewicz, D., R. Szpunar & A. Brzeziński (2016) Network-Based Stochastic Model for instantaneous GNSS real-time kinematic positioning. Journal of Surveying Engineering, 2016:142(4), pp. 05016004, DOI:10.1061/(ASCE)SU.1943-5428.0000188
15. Rajner, M., Brzeziński A. (2017). Free Core Nutation Period Inferred from the Gravity Measurements at Józefosław. Studia Geophysica et Geodaetica, nr 61, 2017, ss. 639-656, DOI:10.1007/s11200-016-0174-4
16. Rajner, M., T. Liwosz (2017) Analysis of seasonal position variation for selected GNSS sites in Poland using loading modelling and GRACE data. Geodesy and Geodynamics, 8 (4), 253 – 259, doi:http://dx.doi.org/10.1016/j.geog.2017.04.001.
17. Ryczywolski, M., T. Liwosz (2015) The EUREF Poland 2015 Campaign. Presentation given at EUREF 2015 Symposium, Leipzig, Germany, 3-5 June.
18. Szabo, V., M. Barlik (2018) Analiza zgodności zmian przyspieszenia siły ciężkości obserwowanych metodą satelitarną z cyklicznymi pomiarami absolutnymi prowadzonymi w Józefosławiu. In: Monografia Działalność Laboratorium Grawimetrycznego w Obserwatorium Astronomiczno-Geodezyjnym w Józefosławiu. Politechnika Warszawska 2018 (in Polish)
19. Tercjak, M., Brzeziński A. (2017) On the influence of known diurnal and subdiurnal signals in polar motion and UT1 on ring laser gyroscope observations, Pure and Applied Geophysics, vol. 174, nr 7, 2017, ss. 2719-2731, DOI:10.1007/s00024-017-1552-8
20. Zygmunt, M., M. Rajner, T. Liwosz (2016) Assessment of continental hydrosphere loading using GNSS measurements. Reports on Geodesy and Geoinformatics. Volume 101, Issue 1, pp 36–53, DOI: 10.1515/rgg-2016-0020, July 2016

2

REMOTE SENSING

THE EARTH OBSERVATION DEPARTMENT

The Earth Observation Department (ZOZ) at Space Research Centre (CBK PAN) specializes in remote sensing and geographic information systems (GIS). The Department has been active in the European projects, ESA programs and in domestic research programs. ZOZ handles with developing innovative applications, software and algorithms as well.

AF3 - Advanced Forest Fire Fighting

Duration: 01.05.2014 – 31.07.2017
Forest fires are the natural phenomenons which cause major economic, social and environmental damages at the global, regional and local scale. AF3 – Advanced Forest Fire Fighting project aims to bring and integrate the newest technologies for fire prevention, detection, extinction and post-fire assessment into one system. The system is developed for the management of large scale forest fires, which are especially difficult to control and are very destructive due to their intensity. The AF3 project is fund by European Commission in the 7th Framework Programme. The project involves 19 partners from 10 countries. The Space Research Centre is responsible for the satellite remote sensing. The institute develops algorithms and software for mapping of strategic infrastructures, fuel types and burnt areas, as well as, forest fire risk estimation.
In 2016 we devised method for automatic detection of burnt areas. The mapping of historical and current burnt areas allows understanding of fire regime, which helps in fire protection organisation. It is also very important to evaluate the impact of forest fires on land cover, terrestrial ecosystems, climate and other fields. Optical satellite images are the main source of data for burnt areas mapping at local regional and global scales. Due to the big amount of available data the development of fully automatic algorithms for burnt area detection is needed. The Earth Observation Group proposed a fully automatic method for burnt area mapping based on high resolution Landsat satellite images. The method uses object oriented approach and consists of two steps: "core" burnt area detection and its growing. The "core" areas are mapped on

the base of spectral differences between pre- and post- fire images, as well as, the differences in indices: NDVI (Normalised Difference Vegetation Index) and NBR (Normalised Burn Ratio). The "core" areas are detected using thresholds, which separate burnt and unburnt areas. Thresholds are automatically adjusted to an image dataset. Next, neighbourhood analysis is performed, it allows the classification of objects that have not been classified so far but their spatial and spectral distances suggest that they may be parts of the burnt areas. Although, automatic mapping of burnt areas has proved to be a challenging task, due to the wide diversity of vegetation cover worldwide and the heterogeneous nature of fires themselves the attempt of global mapping of regional fires was done. We tested our algorithm in various areas all over the world (around 70 scene were tested) e.g. Spain, Greece, Israel, Siberia, Canada, California, Brazil, Bolivia, Australia, Papua New Guinea, Zambia, Angola, South Africa. We succeeded applying our method in different geographic zones and and on different optical images (Landsat and Sentinel-2) without any modification or recalibration of our algorithm for burnt areas mapping. Comparison with the manual interpretation shows high accuracy of burnt areas maps (80-100% overall accuracy depending on the images dataset) while maintaining full automaton of the classification process.

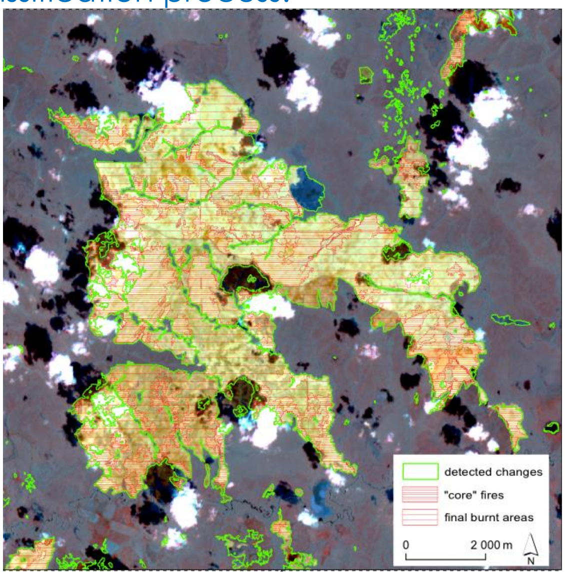

Fig. 2. 1. Burnt area mapping using Sentinel-2 images, e.g. Colombia

We also developed the algorithm for fuel type classification. This characterizes fuel in terms of live and dead, load and fuel bed depth. It also determines the characteristics of fire behaviour, such as the flaming front, postfrontal combustion, fuel consumption, smoke production and crown fire. The algorithm makes it possible to map fuel type models according to the inputs described in the fire spread model presented in Rothermel (1972) and the description offered by Anderson (1982). Fuels are grouped into four main classes: grass, shrub, timber litter and slash, and then divided into 13 subclasses. The product has been developed from geospatial data and satellite images: the CORINE Land Cover database, Landsat and Sentinel-2 images, Sentinel-1 SAR images, the ASTER Global Digital Elevation Model and the Fire History Map.
2017 was a final year of the project so all subsystems were developed, integrated and tested. The Space Research Centre created a subsystem which provided information derived from satellite images to other subsystems, such as, fire risk evaluation subsystem, fire spread simulator, etc. Our subsystem delivered, among others, maps of strategic infrastructures, fuel types and burnt areas, as well as, forest fire risk estimation. All technologies were successfully tested during trials which took places in Greece, Spain and Israel.

S2GLC - Sentinel-2 Global Land Cover Classification

Duration: 1 February 2016 – 31 January 2018

2. REMOTE SENSING

The goal of the ESA SEOM Sentinel-2 Global Land Cover (S2GLC) project was to develop a land cover classification algorithm capable of producing automatically a global fine spatial resolution map based on Copernicus Sentinel-2 Earth Observation imagery. The proposed processing model is fully automated so that the land cover map can be continuously updated and take advantage of the Sentinel-2 temporal and spatial resolution to produce the first global land cover (GLC) map with a resolution of 10 m.

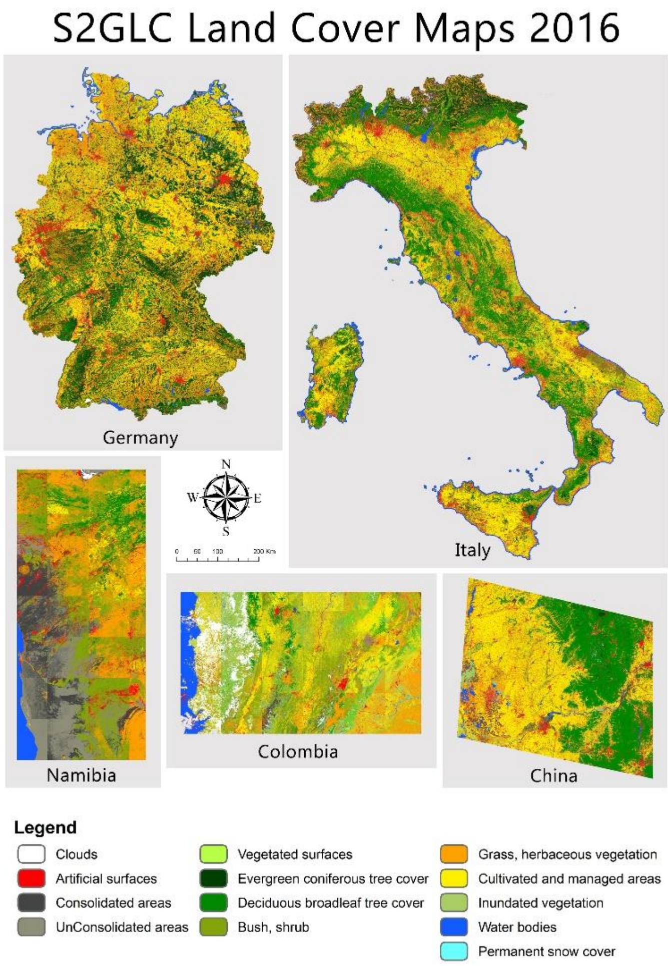

Fig. 2. 2. Final classifications produced by S2GLC

The S2GLC classification legend was defined based on existing legends used within global land cover databases. Land cover classes representing complex structures were not included because of the improved spatial resolution of the Sentinel-2 imagery. The S2GLC map legend identifies the basic land cover classes as well as cultivated areas. Although the agriculture-related class represents land use rather than land cover, it was included due to its importance and existence across all other global land cover databases. The structure of the legend is hierarchical with the third and most detailed level consisting of 15 classes.

Taking into account the spatial resolution of Sentinel-2 data (10 m) and the need to fully automate the classification process, one of the most important and challenging components of the methodology was generating the required training points dataset. For global mapping, the training points can only be selected based on existing databases. Current detailed and reliable open GLC databases are only available at spatial resolutions of 300 m and coarser. The project departed from a common assumption that high accuracy land cover classification results could be obtained solely based on highly precise reference data. However, it was demonstrated that even with the lower uncertainty inherent from the application of coarser reference data, it is still possible to produce high overall land cover accuracy. Therefore, the existing databases were used as the primary source of identifying training reference data for the developed Sentinel-2 classification methodology. Our experiments indicated that the most accurate classification results were obtained when no filtering was applied to the reference data derived from the GLC databases. Additional tests showed that the designed data selection method provides better data than either those collected through innovative data collection strategies such as crowdsourced databases or Sentinel-1 based mask identifying pre-selected land cover classes.

A variety of land cover classification techniques were investigated during the course of the project including object-based and pixel-based, supervised and unsupervised methods. A supervised pixel-based approach was selected because it provided the best results based on classification accuracy, preservation of class details and processing efficiency. Among the supervised methods tested, the Random Forest algorithm outperformed the other classifiers in our tests. The experiments also indicated that the best results were obtained if the classifier training was carried out based on a large number of training samples: between 500 to 1000 pixels per land cover class, per tile. The adopted tile-wise processing approach in part was due to the need for atmospheric correction using the Sen2Cor processor. For each individual Sentinel-2 tile, the potential locations of land cover classes were defined using existing coarser GLC databases. For each class, a thematic mask was defined and then an independent set of randomly designated training points was selected. It was shown that the use of more than one reference land cover database significantly improves the results.

During the course of testing the classification process, it was observed that in many cases the agreement between individual land cover classes from global databases was low. It was also observed that this agreement was correlated to the final classification accuracy. These observations led to the development of a linear model for predicting classification accuracy based only on the agreement of classification results obtained using different global databases as training sources (without any additional validation data). Consequently, for cases where the Sentinel-2 tiles level of the accuracy was predicted to be low, two alternative approaches were developed: (1) the inclusion of local databases and (2) a semi-automatic process for reference data collection with limited human intervention. The following GLC databases were analysed for all testing areas: CCI LC, GlobCover, GLCNMO, MCD12Q1 (MCD). The regional databases available for the analysed test sites (e.g. CORINE LC, Land Cover Classification for Africa by IIASA, Coberturas de la Tierra) were also tested and used as reference data in the final classification approach.

Dedicated functions were applied to analyse the distribution of pixel values in the images from a time series over the analysed period of time. The attempts that were made showed that this type of approach was not the optimal solution due to cloud cover differences across images in a time series. Therefore, the final solution works on each image separately within a time series based on a different set of training data originating from different databases. In the final stage of the classification process, all the results of individually classified Sentinel-2 tiles are aggregated to produce the final output. The proposed aggregation method considers both information on the frequency of a given thematic class occurrence and the value of the prediction score resulting from Random Forest classification. The classification completed over the testing areas confirms the validity of the adopted assumption. Positive final results are obtained even when the image time series is composed of numerous cloudy scenes.

Within the context of the S2GLC project, an additional semi-automatic approach was proposed that could be applied when the results obtained from the automatic method do not produce satisfactory results. Only three to five seed training points per land cover class need to be identified by an operator which minimises his workload. Based on these few seed points, masks with thousands of pixels are automatically generated for selected land cover classes as the training dataset. From these masks the final training samples are randomly selected for the Random Forest classification. Compared to traditional procedures, the proposed solution can significantly reduce the amount of manual intervention. The main automated classification and the class aggregation are then performed in exactly the same manner as described above.

The proposed workflow includes a post-processing procedure to minimise basic classification errors. The initial classification is changed only in the case of pixels classified with low prediction scores and pixels meeting specifically defined neighbourhood conditions. Our approach differs from the commonly used "salt and pepper" smoothing technique and maintains a high degree of spatial details.

The developed classification workflow was applied to Sentinel-2 images acquired throughout 2016 for five test countries located across four continents: Germany – 360 000 km^2 and Italy – 300 000 km^2 (Europe), an area of 200 000 km^2 in China (Asia), an area of 200 000 km^2 in Colombia (South America) and area of 220 000 km^2 in Namibia (Africa). Depending on the test site, between 12 and 13 classes were identified. A summary of the inputs and results is presented in **Błąd! Nieprawidłowy odsyłacz do zakładki: wskazuje na nią samą.** for the test sites.

2. REMOTE SENSING

Table 2. 1. Sentinel-2 images and existing databases used for classification

Prototype Site	Area km²	Sentinel-2 tiles	Available images (2016)	Classified images per tile	Databases used for training	Overall accuracy
Germany	357 375	56	1956	10	2 global, 1 regional	85.2%
Italy	301 230	63	2182	10	2 global, 1 regional	72.5%
China	200 750	31	551	6-10	3 global	72.0%
Namibia	235 345	32	1228	10	1 global, 1 regional	56.1%
Colombia	211 705	30	846	3-10	2 global, 1 regional	52.5%
Summary:	*1 306 405*	*212*	*6763*			

A land cover map validation was performed on an image tile basis. Initial sampling for the map validation followed a probability-based, stratified random sampling approach to identify at least ten representative sites. This covered approximately 1 000 Sentinel-2 pixels per tile and per class. Among this initial sampling, validation points were reviewed and manually selected. The applied land cover map validation approach followed the ISO Standards 19157 and 2859-1 for samplings strategies.

The best S2GLC classification results were achieved for the German and Italian test sites: 85.2% and 72.5% overall accuracy (OA) respectively. These results are in-line with both German and Italian CORINE LC 2012 database validations based on LUCAS points (82.8% and 76.0% of OA respectively) even though the S2GLC classification approach is completely different from the one used to produce the CORINE LC database. The accuracy of the results from the Chinese test site was 72% OA and is also considered relatively high accuracy and characterized with a high degree of details. The results obtained for the test sites in Namibia and Columbia produced lower OA at 56.1% and 52.5%

respectively. Disagreement between the existing GLC databases in these areas resulted in having to apply lower quality reference data (compared to Europe) and hampered the collection of reliable training samples. This is considered to be the primary reasons for the obtained lower classification accuracies. Additional problems in the case of the Columbian site are related to difficulties in obtaining cloud free images, high elevation differences producing different lighting conditions within the test area and no seasonal changes in vegetation cover during the year. The latter decreases the usefulness of multi-temporal data because of the lack of change in vegetation throughout the year. The lower results obtained for the Namibian site could be explained by the severe drought occurring in this part of Africa in recent years (2014 - 2016). This contributed to abnormal water regime, i.e. drying up of water bodies and changes in vegetation cover compared to the classes found in the coarse GLC databases. Furthermore, in many areas the difficulty was identifying a clear distinction of the class boundaries, e.g. un-consolidated – grasses, grasses – bush and shrubs, bush and shrubs – tree cover. These areas are transitional zones between the classes and represent a mixture of their components. Another identified issue related to the distinction between non-irrigated areas used for agricultural purposes that closely resemble other classes such as shrubs or grassland.

The essential part of the developed S2GLC classification algorithm is the application of existing low resolution GLC databases to automatically generate training points to produce high spatial resolution land cover maps. The proposed S2GLC solution applies the Radom Forest classifier, a supervised pixel-based approach. Automating the entire land cover classification process makes it possible to map the globe through batch processing. Our uniquely applied solution includes the aggregation procedure which combines results of single tile classifications from multiple dates into a final map product.

The entire classification procedure, including pre- and post-processing are deployed as a dedicated software developed by CBK PAN. The quality of the land cover classification results depends on the training data quality and can be improved by access to regional and local reference datasets.

The solutions and tools developed within the S2GLC project, with adjustments required for specific geographical zones, are able to produce a unique and accurate global land cover database.

The project consortium included research institutes and companies with experience in global, pan-European and regional land cover classification. The consortium was led by CBK PAN and included IABG GmbH, Friedrich Schiller University Jena, and EOXPLORE UG.
Project website: http://s2glc.cbk.waw.pl/

ADEMOS - An improved automated procedure for informal and temporary dwellings detection and enumeration, using mathematical morphology operators on VHR satellite data

Duration: 01.09.2015 – 28.02.2017

The goals of ADEMOS project are: (i) to improve the methodology for the detection of dwellings; and (ii) to develop an operational stand-alone application that provides reliable and consistent results, independent of the imaging sensor type and environmental conditions.

The main focus is the improvement and automation of pre-processing, feature extraction algorithm and verification of results. The work is designed to be applied in emergency response decision support, for the European Commission and United Nations' bodies, and humanitarian aid agencies.

This project is funded from Norway Grants in the Polish-Norwegian Research Programme operated by the National Centre for Research and Development.

The proposed approach consists of several steps and starts with data class evaluation, data fusion and border camp delineation (Figure 3). By performing this part of analysis the successive steps focus only on the area of interest and take advantage of both the spatial and spectral information. This study demonstrated that with dataset limited to the panchromatic VHR satellite images the typical classes of dwellings could be correctly extracted. The added-value of additional spectral band, blue range, occurred in Ifo, Hagadera and Lukole camps, where the most frequent type of structures are

tents and other structures which are covered by a highly reflecting material.
The results obtained by mathematical morphology technique show that algorithm overestimates extracted structures, mainly due to the incorrectly selection of the NDVI threshold. Final errors consist of small bushes or shadows of large trees.

This study demonstrated that applying the hit-or-miss transform enable to indicate more precisely the dwellings with a spectral response similar to the bare soil, by making use of additional information as dwellings' shadows and fences. The difficulties occurred in a camp's area where the spatial location of dwellings within one single household is very compact and dense, leaving a space in the middle which is incorrectly extracted as a bright dwelling casting shadow.
Nevertheless, the method proved to be easily adapted to different environmental conditions, mainly due to its simplicity and limited number of dwellings descriptors that are taken into account in the information extraction process.

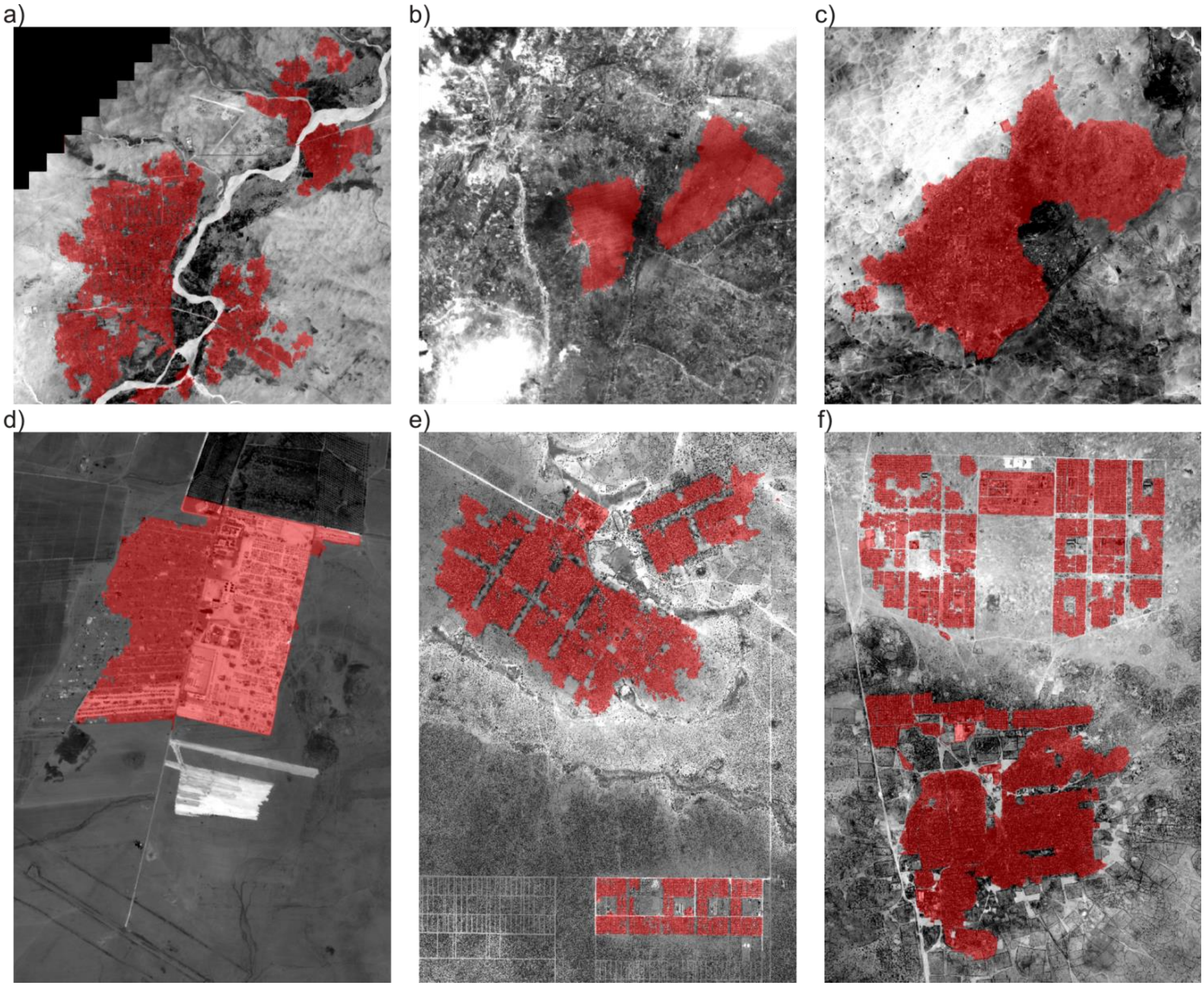

Fig. 2. 3. The camp area detection results, red – merged objects, distinguished in the classification process as High Texture. a) Al Geneina camp (GeoEye-1); b) Lukole camp (Ikonos); c) Al Salam camp (QuickBird-2); d) Al Mafraq (WorldView-2); e) Hagadera camp (Pléiades 1B); f) Ifo camp (Pléiades 1A).

The final task of the project was mainly focused on the development and testing of the stand-alone application that provides reliable and consistent results, independent of the imaging sensor type and environmental conditions.

This task consists of the following activities:

1. Development of detailed workflow, based on testing stage and processing steps developed in previous tasks (WP 1 - 5);
2. Development of MATLAB/IDL/OS application for automatic dwellings detection and enumeration, using mathematical morphology operators on VHR satellite data;

This tasks during the entire duration of the project were carried out in close collaboration with the experts from Joint Research Centre EC (JRC).

Ad. 1 Development of detailed workflow

At this stage the successive steps developed and tested in the previous WPs was applied on the selected dataset. The analysis was done one by one with the utilization of calculation machine Lenovo, and with a commercial remote sensing software: Erdas Imagine and Envi (funded from project funding) and in available commercial software: eCognition Definiens, Arc GIS (not funded from project funding). Figure 4 shows the detailed processing workflow designed within this WP.

Ad.2 Development of MATLAB application

The detailed workflow has been later translated into the scripting language with support of Graphical User Interface (GUI) implemented in MATLAB software.
The stand-alone application consists of four main bookmarks, which refer to the four main stages of the analysis.
First bookmark is **INPUT DATA** selection (Figure 5a). There user has a possibility to choose optical or SAR data (note: test carried on for SAR data includes data processing steps only until the camp mask calculation, no further test with use of this type of data were proceed). From the optical data set, user may upload Multispectral dataset (MS) or/and Pan-sharpened dataset (PS, results of the data fusion analysis) and Panchromatic imagery (PAN). Within this specific bookmark user has the possibility to classify dataset in a frame of data parametrisation task.
Second bookmark is **PREPROCESSING** of selected data. The most important step in the data preparation for further analysis is to calculate the image texture (Figure 5b), thus the camp mask and the vegetation mask (Figure 5c). The first

one will enable to limit the analysis to the camp area and the second will enable to eliminate vegetation form the results.
Third one is **PROCESSING** of selected data. This part consists of the automatic dwellings' characterization based on the selected camp sample (Figure 5d), i.e. dwellings size distribution (5e) and dwellings spectral response (Figure 5f). Next the user has a possibility to verify automated derived parameters and implement them in the process of semi-automated dwellings extraction (Figure 5g).
Last bookmark is **RESULTS VERIFICATION**. The tools designed in this part enable the visual verification of results mask (Figure 5h), randomly selection of camp samples and visual interpretation of image content (reference data collection) (Figure 5i) and the statistical measures calculation (results of the comparison analysis) (Figure 5j).
The main features of the stand-alone application can be presented as follows:

1. Automatic assignment of an image class in a data hierarchy tree;
2. Manually change of threshold for "high-texture" class in camp border delineation procedure;
3. Manually change of threshold for "vegetation" class in vegetation mask calculation procedure;
4. Automatic calculation of dwellings size by applying the granulometry, i.e. structures size distribution;
5. Automatic calculation of intensity threshold by verifying the cross section of structures and their surrounding on satellite imagery;
6. Manually selection of Structural Element for containment criterion;
7. Manually selection of area size (amount of randomly selected samples) to be verified in results quality assessment;
8. Interface for visual interpretation;
9. Calculation of correlation coefficient and main statistics.

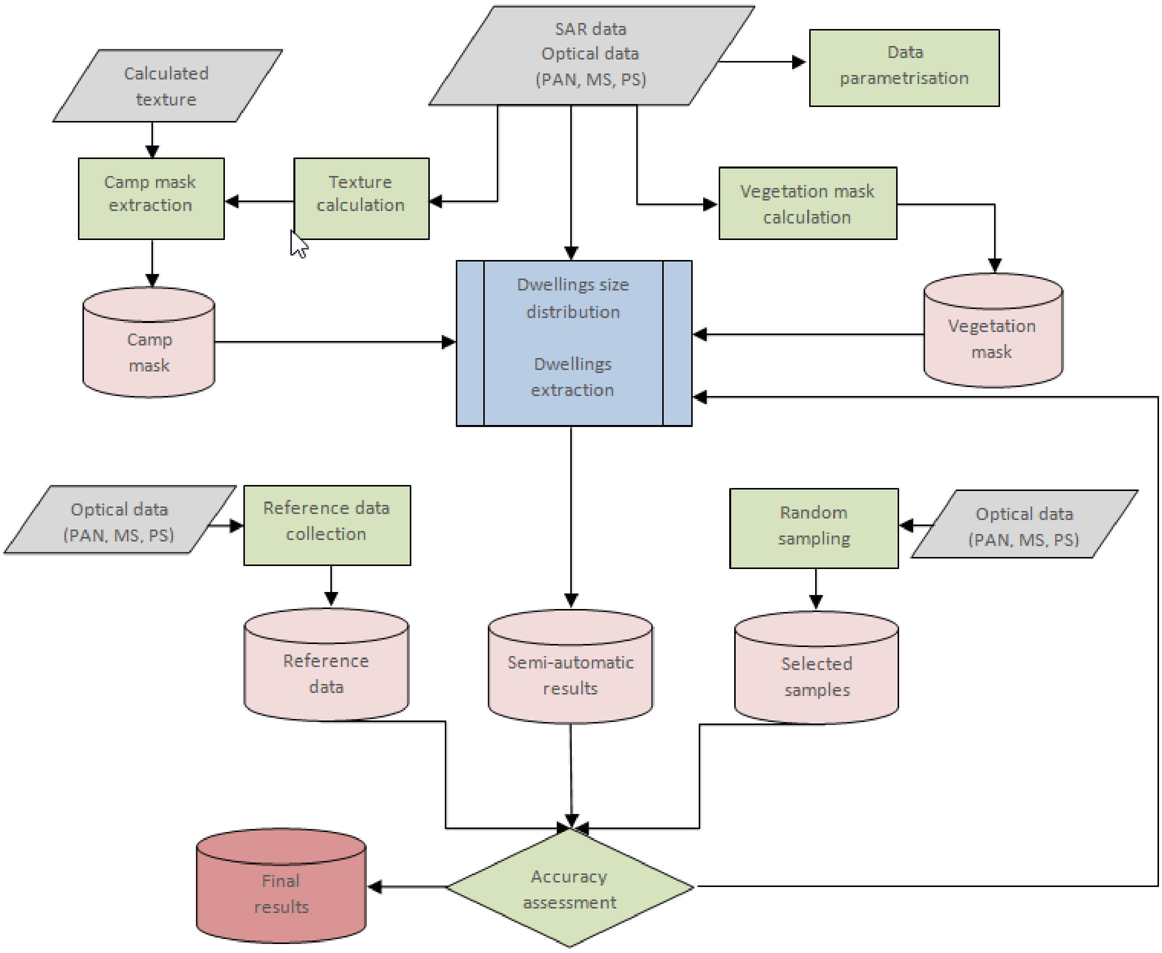

Fig. 2. 4. Processing workflow

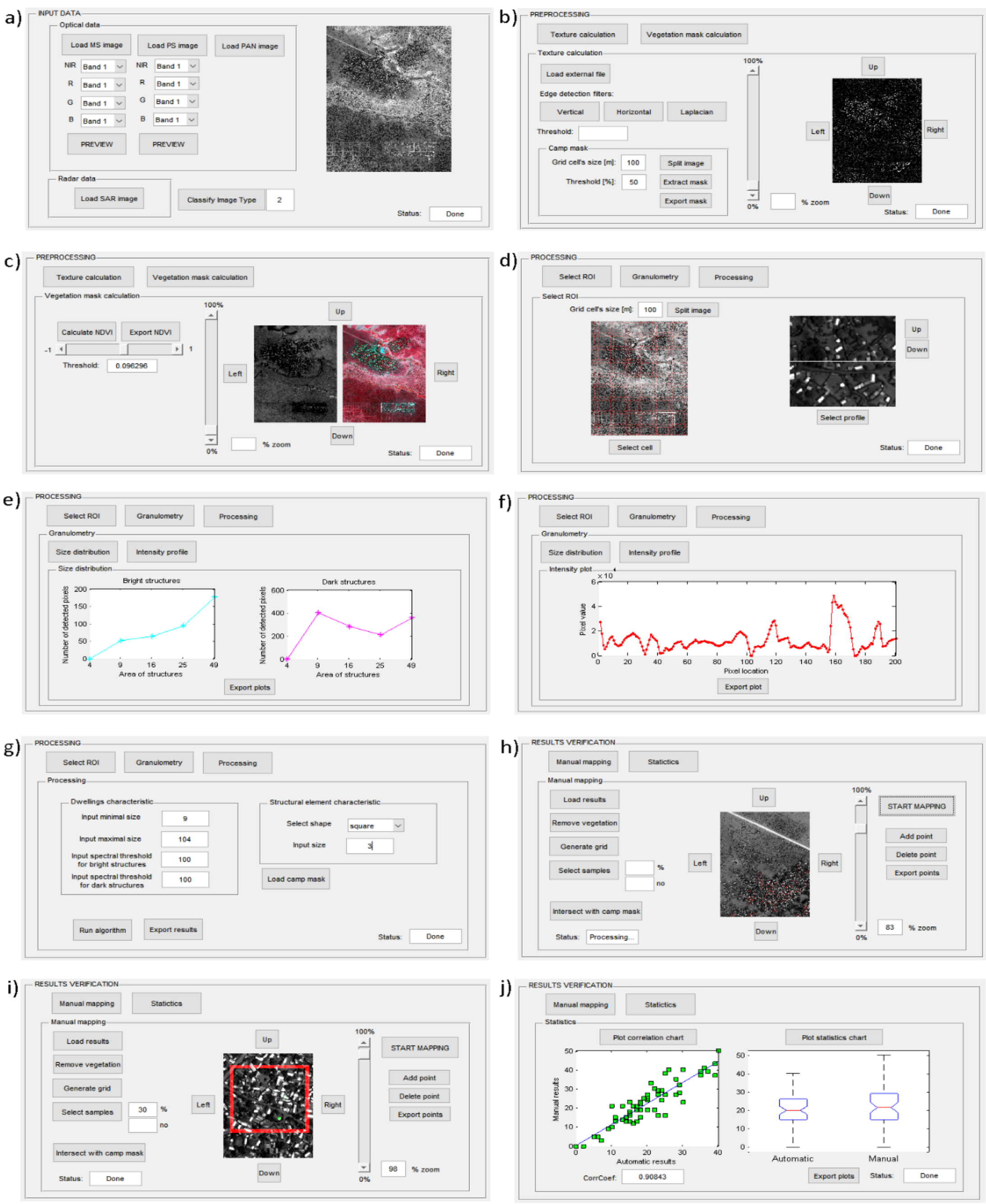

Fig. 2. 5. An example of developed application use

Multi-sensor satellite and aerial data fusion for illicit crops detection
Duration: 1 November 2015 - 30 April 2017
Within the project, CBK PAN and Planetek Italia developed and validated algorithms for illicit crops detection using satellite imagery analysis. CBK PAN was responsible for poppy plantations identification in Poland and Birma, and Planetek Italia worked on cannabis detection in Netherlands. CBK PAN has developed two approaches to identify poppy plantations. One is designed to utilize commercial Very High Resolution satellite images from RapidEye. The second one is based on multitemporal analysis of freely available High Resolution images from Sentinel-2 and Landsat satellites. Moreover CBK PAN has developed the map of locations invisible for observers travelling by car or trains or located within urban areas where illegal plantations could be placed.
Project was founded by ESA.

Fig. 2. 6. Growth of the poppy monitored within the project.

Artificial Impervious Surfaces detection with Snow-featured satellite imagery
Snow cover, similarly to clouds, has been seen as an obstacle to impervious surface detection based on optical remote sensing. As a consequence, satellite images acquired winter-time (when snow is present) are rejected from further analysis. On the other hand, snow increases the spectral contrast between impermeable surfaces and other land use types. The question rises if the presence of snow does actually degrade data quality? If so, how significant is the decrees in impervious surface detection?
That hypothesis has been addressed with the following study. Six locations worldwide were selected: three urban (Winnipeg, Canada; Kiev, Ukraine; Changchun, China), three rural (Eagle Grove, USA; Straubing, Germany; Shuangcheng, China). For each location a pair of Landsat data was acquired, with one image representing summer conditions, and second one – winter conditions (Fig. 7). Next, all data were classified. In order to minimize subjectivity,

a machine learning AdaBoost method has been applied, and human intervention was limited only to indication of reference (training and validation) points. The points were common for classification of summer and winter data. Summer data served as reference classification.

The research revealed that presence of snow had no significant impact on accuracy of impervious surface detection. For most locations, the overall accuracy of the classification was 91–94% (kappa 81–93%), which was only 1–3% less than for summer (92–98%, kappa 86–95%). Importantly, this difference was not statistically significant. There was no difference in accuracy between dense urban fabric and rural regions. The findings were also true for bi-temporal analysis, when summer and winter data were merged prior to classification. In that case accuracy was by approximately 1–3% higher than for summer data alone, and the difference was statistically significant.

Location of the impervious surfaces can be also detected with the use of night-time imagery. A study of Berlin (Fig. 8) looked at the use of high resolution (~10 m/pixel) night-time photography from the International Space Station (ISS). Results were interpreted in the context of the Operational Linescan System (OLS) data, which has been used to detect impervious surfaces for the past two decades.

Our ISS-based classification was 85% accurate for both user and producer measures. Impervious surfaces omitted by ISS photography were mainly transit roads and airport runways, while green areas and water bodies within the city were falsely identified. An analysis based on ISS imagery classified 55.7% of the study area as impervious, which is only 3.9% less than ground truth (while the OLS-based estimate was 40% higher than ground truth). ISS imagery failed to provide reliable information about the degree of imperviousness for individual pixels (±20% errors); nevertheless it accurately estimated the spatially-averaged degree of imperviousness for the whole study area (30.2% vs. the reference value of 30.1%). These results show that ISS photography is an important source of nighttime imagery for mapping the extent of impervious surfaces, and represents a considerable improvement over OLS capabilities.

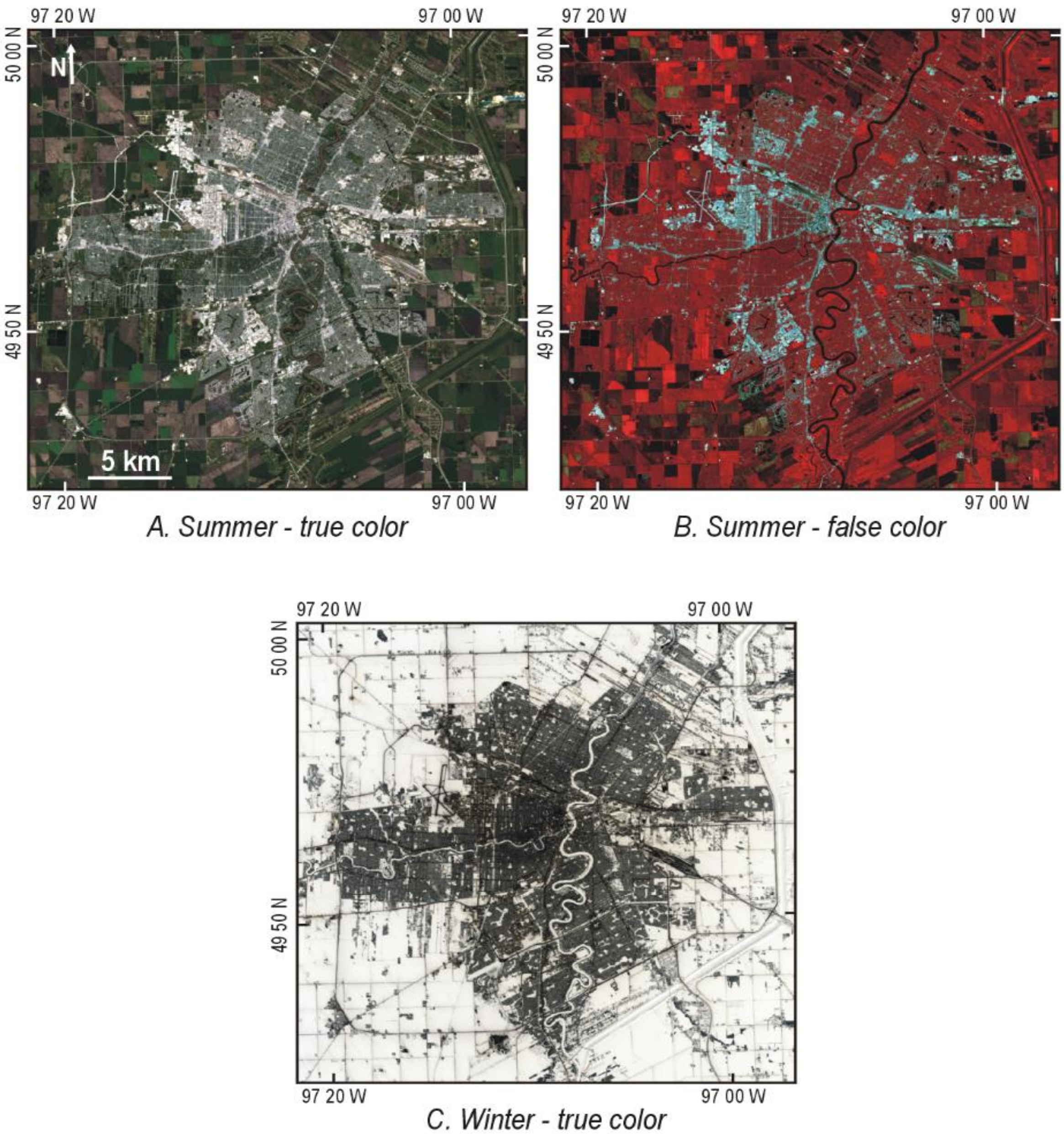

Fig. 2. 7. The city of Winnipeg (Canada), imaged by Landsat-8/OLI in summer (a, b) and winter (c).

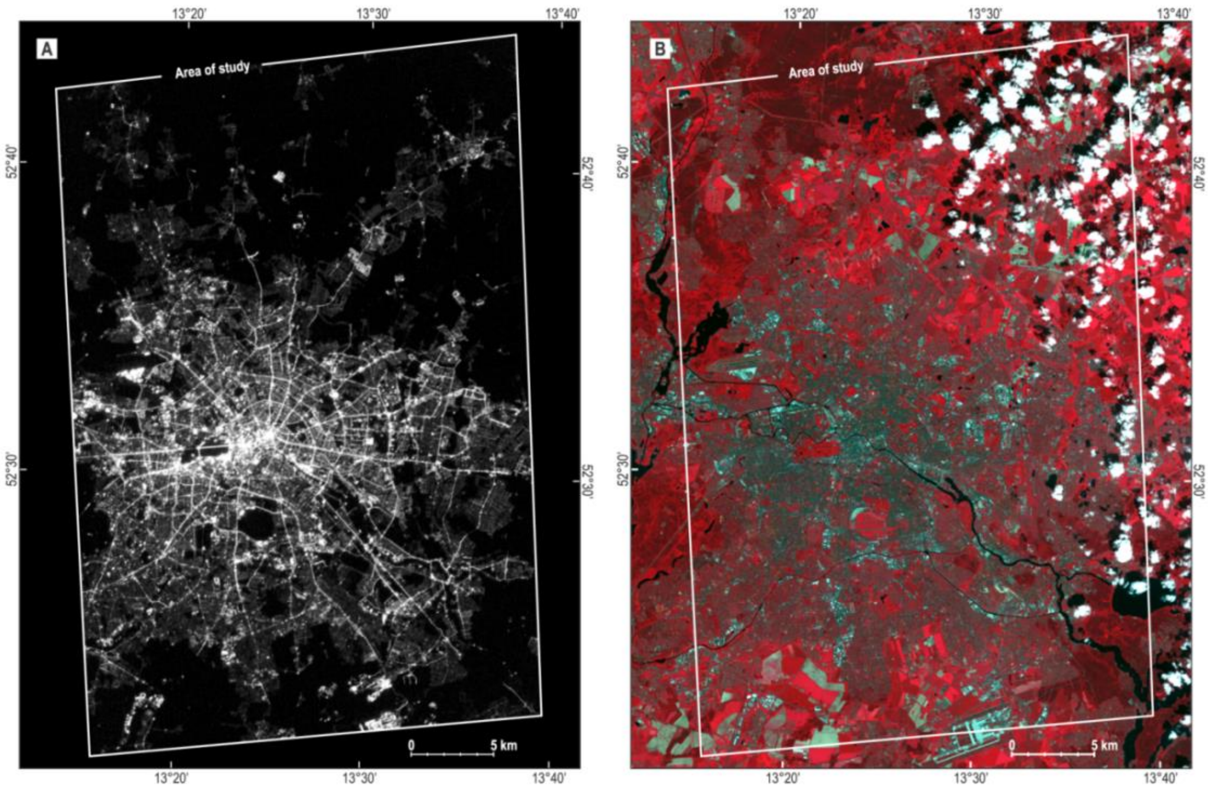

Fig. 2. 8. Landsat 8 daytime imagery of Berlin (right) and night-time (left). Digital photography taken by an astronaut onboard the International Space Station on April 6, 2013, 22:37 UTC.

Sentinel-1 FEasibility Study of Land Cover Classification Based on SAR Sentinel-1 Images

Duration: 3 February 2014–31 January 2016

This work concerned a feasibility study of land cover classification based on SAR Sentinel-1 images. The project is part of the European Space Agency's pre-accession Plan for European Cooperating States (PECS). The aim of the study was to evaluate how much higher potential for land cover classification have multi-temporal dual-polarization SAR Sentinel-1 images processed using polarimetric methods than a time series of backscatter images. The testes were performed using object-oriented classification approach. To fulfill the main objective the influence of several factors on the classification results were tested:

Which input dataset has the highest potential for classification?

- a time series of 13 dual polarization backscatter image;
- a time series of 13 of dual polarization Coherence Matrix;
- a multi-temporal one polarization Coherence Matrix VH and VV;
- a multi-temporal dual polarization Coherence Matrix VHVV;
- entropy/alpha/lambda derived from Multi-temporal Coherence Matrices: VHVV, VV and VH;
- 13 maps of scatter zone;
- scatter zone temporal stability map.

- Which classifier gives better classification results?
  - K-Nearest Neighbour; o Support Vector Machine;
  - Decision Tree;
  - Random Forests.
- How does segments' size influence on classification results?

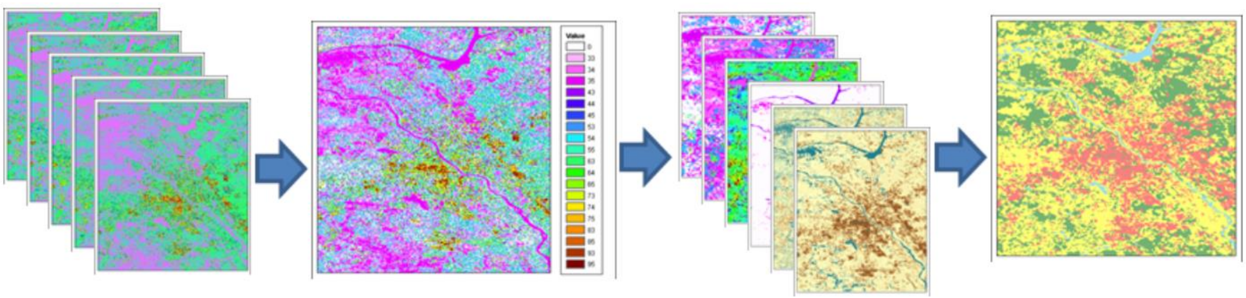

Fig. 2. 9. Overview of the approach based on multi-temporal Wishart classification of scatter zones: time series of scatter zones; pixel-level temporal analysis of scatter recurrence; spatial distribution of scatter; classification (Decision Tree algorithm)

The best classification result was obtained with the use of the dataset formed by scatter zone temporal stability map and 13 maps of scatter zone. For 4 basic land cover classes (urban, agricultural, forest, water bodies) the overall accuracy was 93.17% and the increase of the overall accuracy in comparison to reference classification, realized on the time series of backscatter images, was 4.45%. For 6 land cover classes (urban, fields, grasslands, coniferous and deciduous forests and water bodies) the overall accuracy was 3.77% better than in the case of backscatter images and reached 88.44%. The most suitable classifier resulted to be Support Vector Machine. The study revealed that the use of very small segments (mean segment size 9.4 ha) causes significant decrease of the classification accuracy (around 15%) in comparison to the best segment size (mean segment size 16.3 ha). Obtained results prove that polarimetric processing of series of radar Sentinel-1 images brings better classification result than the time series of backscattering images. The use of the proposed method can improve the accuracy of land cover classification based on radar images, what is important, especially in the cloudy regions.

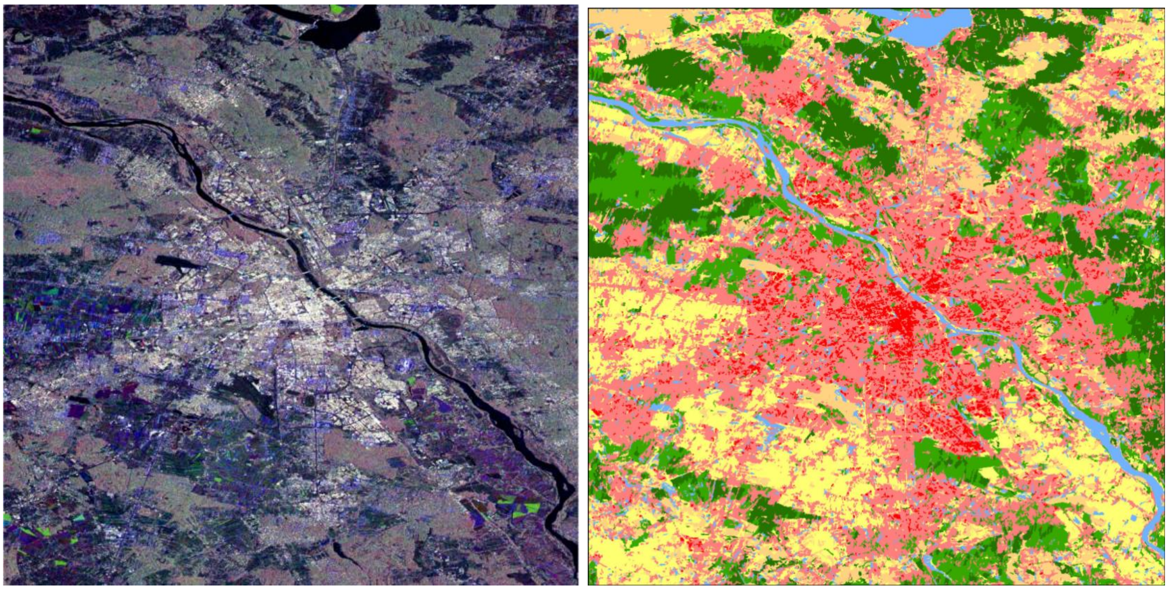

Figure 2. 10. Sentinel-1 multi-temporal coherence matrix (left), classification of land cover based on Sentinel-1 multi-temporal co

Publications:

1. Woźniak, E., Kofman, W., Lewiński, S., Wajer, P., Rybicki, M., Aleksandrowicz, S., Włodarkiewicz, A.(2018,), Multi-temporal polarimetry in land cover classification. International Journal of Remote Sensing
2. Kotarba A.Z., Nowakowski A. (2018), Impact of snow cover on impervious surface detection. International Journal of Remote Sensing, doi:10.1080/01431161.2018.1475775
3. Kotarba A.Z. (2018) Vertical profile of cloud amount over Poland: variability and uncertainty based on CloudSat-CALIPSO observations. International Journal of Climatology, doi:10.1002/joc.5558
4. Kulczyk S., Woźniak, E., Derek, M. (2018) Landscape, facilities and visitors: An integrated model of recreational ecosystem services, Ecosystem Services, doi: 10.1016/j.ecoser.2018.02.016
5. Woźniak E., Kulczyk S., Derek M. (2018) From intrinsic to service potential: An approach to assess tourism landscape potential, Landscape and Urban Planning, 170, 209-220, doi: 10.1016/j.landurbplan.2017.10.006
6. Wajer P., Woźniak E., Kofman W., Rybicki M., Lewiński S. (2018) Simulation of SAR images of urban areas by using the ray tracing method with measured values of backscatter coefficients, International Journal of Remote Sensing, 39:9, 2671-2689, doi: 10.1080/01431161.2018.1430396

7. Kukawska E., Lewiński S., Krupiński M., Malinowski R., Nowakowski A., Rybicki M., Kotarba A. (2017) Multitemporal Sentinel-2 data – remarks and observations. 9th International Workshop on the Analysis of Multitemporal Remote Sensing Images (MultiTemp), Brugge, 2017, pp. 1-4, doi: 10.1109/Multi-Temp.2017.8035212
8. Lewiński S., Nowakowski A., Malinowski R., Rybicki M., Kukawska E., Krupiński M. (2017) Aggregation of Sentinel-2 time series classifications as a solution for multitemporal analysis. In Proc. SPIE 10427, Image and Signal Processing for Remote Sensing XXIII, 104270B doi: 10.1117/12.2277976
9. Angelidis I., Levin G., Díaz-Varela R. A., Malinowski R. (2017) Assessment of changes in formations of non-forest woody vegetation in southern Denmark based on airborne LiDAR. Environmental Monitoring and Assessment, 189(9), 437, doi: 10.1007/s10661-017-6119-8
10. Derek M., Woźniak E., Kulczyk S. (2017) Tourism in a nature-based destination: the human versus the ecological perspectives, Tourism Geographies, 10.1080/14616688.2017.1314545
11. Malinowski, R., Groom, G.B., Heckrath, G. (2017) Do Remote Sensing Mapping Practices Adequately Address Localized Flooding? A Critical Overview, et al. Springer Science Reviews, doi: 10.1007/s40362-017-0043-8
12. Kotarba A.Z. (2017) Inconsistency of surface-based (SYNOP) and satellite-based (MODIS) cloud amount estimations due to the interpretation of cloud detection results. International Journal of Climatology, 37, 4092-4104, doi:10.1002/joc.5011

2. REMOTE SENSING

13. Kotarba A.Z., Aleksandrowicz S. (2016) Impervious surface detection with nighttime photography from the International Space Station. Remote Sensing of Environment Volume 176, April 2016, Pages 295-307, doi: 10.1016/j.rse.2016.02.009
14. Woźniak E., Kofman W., Wajer P., Lewiński S., Nowakowski A. (2016) The influence of filtration and decomposition window size on the thresholdvalue and accuracy of land-cover classification of polarimetric SAR images, International Journal of Remote Sensing, 37:1, 212-228, doi: 10.1080/01431161.2015.1125548
15. Aleksandrowicz, S.; Wawrzaszek, A.; Drzewiecki, W.; Krupiński, M. (2016) Change Detection Using Global and Local Multifractal Description, IEEE Geoscience and Remote Sensing Letters, Volume: 13, Issue: 8, Aug. 2016, doi: 10.1109/LGRS.2016.2574940
16. Kotarba A.Z. (2016) Comparison of Differences Between MODIS 250 m and 1 km Cloud Masks. Atmospheric Research, 181, 54-62, doi:10.1016/j.atmosres.2016.06.014
17. Kulczyk S., Woźniak E., Derek M., Kowalczyk M. (2016) How much is the "wonder of nature" worth? The valuation of tourism in the Great Masurian Lakes using travel cost method, Ekonomia i Środowisko, V.4 Nr.59
18. Drzewiecki W., Wawrzaszek A., Krupiński M., Aleksandrowicz S., Bernat K. (2016) Applicability of multifractal features as global characteristics of WorldView-2 panchromatic satellite images, European Journal of Remote Sensing, 49:1, 809-834, doi: 10.5721/EuJRS20164943
19. Peng Y., Kheir R.B., Adhikari K., Malinowski R., Greve M.B., Knadel M., Greve, M.H. (2016) Digital Mapping of Toxic Metals in Qatari Soils Using Remote Sensing and Ancillary Data. Remote Sensing, 8, 1003, doi:10.3390/rs8121003
20. Malinowski R., Höfle B., Koenig K., Groom G., Schwanghart W., Heckrath G. (2016) Local-scale flood mapping on vegetated floodplains from radiometrically calibrated airborne LiDAR data. ISPRS Journal of Photogrammetry and Remote Sensing 2016, 119, 267-279, doi: 10.1016/j.isprsjprs.2016.06.009
21. Jenerowicz M., Kemper T. (2016) An improved automated procedure for informal and temporary dwellings detection and enumeration, using mathematical morphology operators on VHR satellite data, Remote Sensing Technologies and Applications in Urban Environments, doi: 10.1117/12.2254808
22. Kotarba A.Z. (2016) Regional high-resolution cloud climatology based on MODIS cloud detection data, Volume 36, Issue 8 30 June 2016 Pages 3105–3115, doi: 10.1002/joc.4539

3

SPACE PHYSICS

3. SPACE PHYSICS

Compiled by Jan Błęcki and Małgorzata Michalska

Solar Physics

DIOGENESS B. Sylwester, J. Sylwester

The Diogeness (DIOG) soft X-ray spectrometer operated aboard the Russian CO-RONAS-F satellite in 2001. The instrument collected hundreds of high resolution spectra from a period of high solar activity, including the X5.3 flare on 25 August 2001. This flare was also observed by the COES X-ray monitor and the Yohkoh JAXA/NASA satellite.

During 2017, a complete re-analysis of DIOG spectra was performed, including investigation of possible effects from fluorescence arising from instrument structure and diffracting crystals in particular. Example spectral scans are shown in Figure 3.1.

Theoretical calculations of the line and continuum in the spectral range covered by DIOG, available from CHIANTI Code (SolarSoft), have been supplemented with hundreds of new satellite lines calculated using Robert Cowan's code for calculating atomic energy levels (https://www.tcd.ie/Physics/people/Cormac. McGuinness/Cowan/Code/Lanl/RCGWriteup.pdf). This work was performed in close collaboration with Prof. Kenneth J.H. Phillips from the Museum of Natural History, London. The new approach made it possible to identify new line structures in the vicinity of Ca XIX forbidden lines, representing the first progress in this spectral region in more than 40 years (see Figure 3. 2).

A paper describing the results of DIOG spectra interpretation is under preparation.

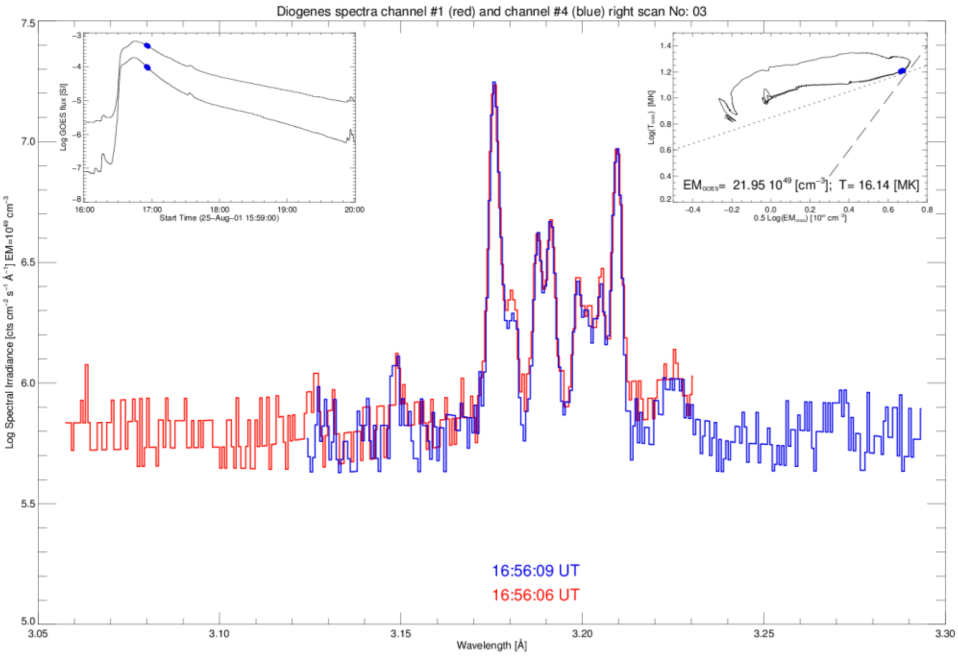

Fig. 3. 1. DIOG spectra obtained from scans executed shortly after the maximum of the X5.3 flare. Time of scans is indicated by blue dots in the upper left insert, which shows the GOES X-ray fluxes in 1-8 Å band (upper curve) and 0.5-4 Å band (lower curve). The right insert is a so-called diagnostic diagram, obtained from isothermal interpretation of GOES measurements. Again, the blue dot represents the instant of spectra registration, showing the values of plasma temperature and emission measures at that moment. In the main graph, the times below the spectra correspond to registration of maximum Ca XIX resonance line emission at 3.179 Å for DIOG spectral channels No. 1 and 4 (red and blue respectively). Good agreement was observed between the spectra recorded in the two channels.

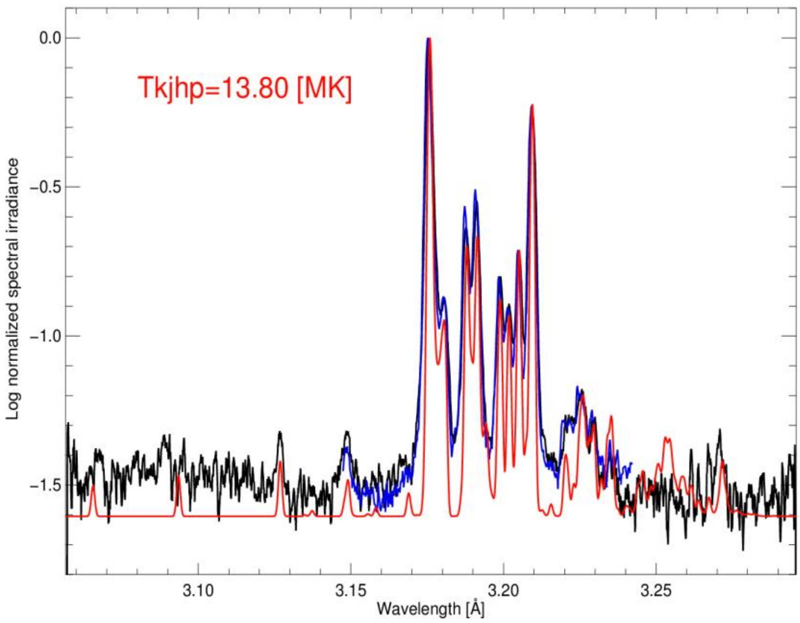

Fig. 3. 2. Comparison of average spectrum for the X5.3 flare of 25 August (in black) with theoretical spectra obtained using Cowan's atomic code (in red). The blue line represents the spectrum recorded from P78 satellite (Seely and Doschek, 1989; see their Figure 2 for line identifications). The derived average plasma temperature is shown.

RESIK A. Kępa

In 2017, spectral analysis using the RESIK spectrometer was continued. RESIK was created at the Solar Physics Division of the CBK PAN and was used to observe the Sun between 2001 and 2003, providing measurements of high resolution X-ray solar spectra in the wavelength range 3.3 - 6.1 Å. This data has contributed among othersto studies of the thermal structure of the solar corona, and to calculations of the differential emission measure (DEM).
Multi-temperature analysis was performed for the SOL2003-01-09T01:27 flare (C9.8 GOES class, maximum ~01:27 UT; see Figure 3), which occurred in NOAA Active Region 10242, located at S08W36. Time evolution data of the flux, provided by the Geostationary Operational Environmental Satellite (GOES), show that the flare consists of a number of successive individual events, in which two maxima are clearly visible.
In order to determine the differential emission measure (DEM) distributions for

individual brightening, we employed the Withbroe-Sylwester algorithm (Sylwester et al., 1980) and seventeen fluxes integrated in selected RESIK lines.

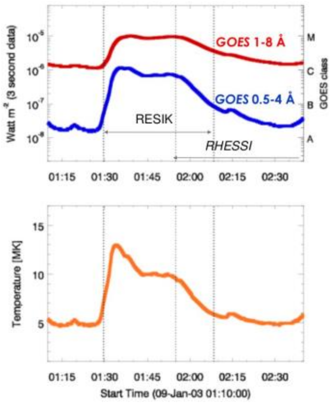

Fig. 3. 3. GOES light curves (top panel) and temperature variations over time (bottom panel) were calculated using an isothermal approximation for the SOL2003-01-09T01:27 flare. Vertical lines show RHESSI and RESIK observation intervals.

We applied the methology presented by Gryciuk et al. (2017) for determining an elementary flare time profile to the RESIK data. Seventeen RESIK light curves were selected for calculation of DEM distributions; they were decomposed into a number of elementary events with overlapping time profiles. This process provides new possibilities for diagnosing flaring plasma, such as analysing DEM distributions of individual flare components.

In Figure 3. 4, we present examples of decomposed RESIK light curves comprising two, three and four elementary flare profiles. We regard these elementary flares as the individual brightenings and/or the distinctive heating episodes taking part within the flaring region.

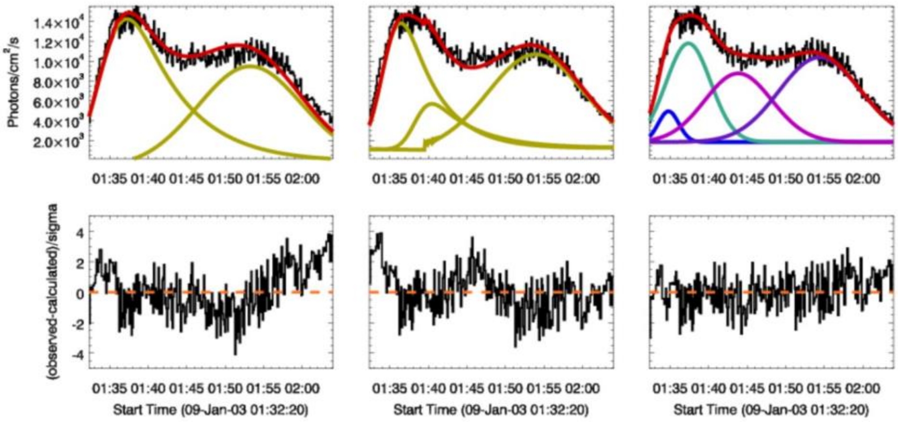

Fig. 3. 4. Top: RESIK light curves for one of the spectral bands recorded during the 9 January 2003 flare, showing the decomposition into two, three, and four elementary flare profiles respectively. In each case, the red line indicates the summed profile. Residuals obtained after subtracting the summed profiles from the observed are shown in lower panels.

Results of the DEM calculations are presented in Figure 3. 5.

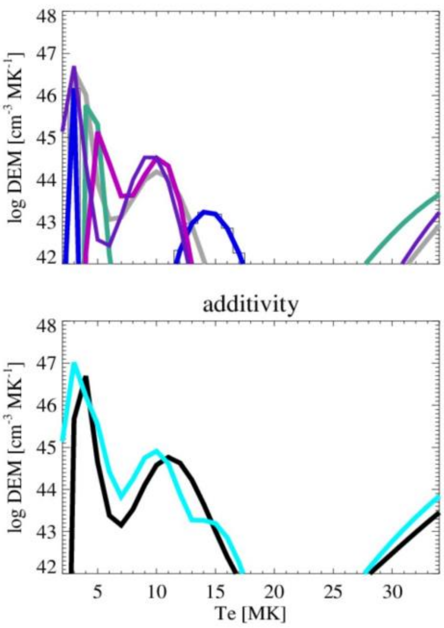

Fig. 3. 5. Top panel: DEM distributions for four flares obtained by decomposition of RESIK light curves to elementary flare profiles. The colors correspond to the profiles in Figure 2. Lower panel: The black line indicates the DEM distribution obtained for the non-decomposed data, for the flare of January 9, 2003. The blue line represents the sum of DEM distributions obtained for four individual flares, for comparison.

The results of this work are being prepared for submission to the Journal of Atmospheric and Solar-Terrestrial Physics.

SMM BCS B. Sylwester, J. Sylwester

In 2017, we continued reduction of astrophysical spectra in the range covered by the Bent Crystal Spectrometer (BCS) aboard the NASA Solar Maximum Mission satellitedata, but still the best. This work was performed in collaboration with Prof. Chris Rapley (UCL) and Prof. Ken Phillips (London). We revised instrument characteristics, taking into account ageing effects. The BCS was part of the X-ray Polychromator, which observed numerous flares and bright active regions from February 1980 until November of the same year, when operation was suspended as a result of the failure of the spacecraft fine pointing system. Observations resumed following the Space Shuttle SMM Repair Mission in April 1984 and continued until November 1989.

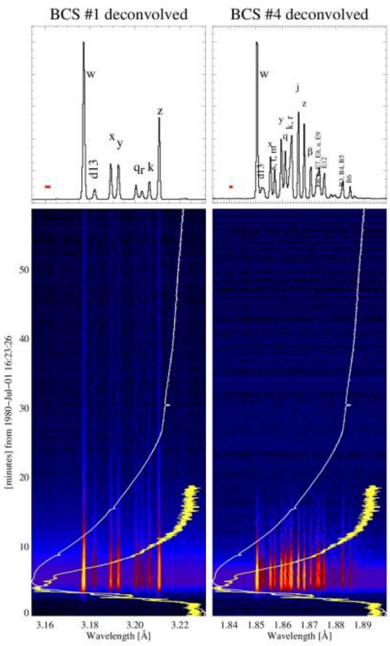

Fig. 3. 6. Example of deconvolved stacked spectra (lower panels) in two (out of eight) BCS spectral channels. In channel No.1 (left column), spectra in the vicinity of Ca XIX He-like ion triplet are displayed, similar to those observed by Diogeness; in the right column, spectra in the vicinity of Fe XXV He-like triplet (see Beiersdorfer et al., 1993) are shown. Upper panels show the spectra averaged for the flare considered, with line identifications provided. The white and yellow lines represent flare X-ray emissions: soft emissions measured by GOES (white line, channel 1-8 Å) and hard emissions measured by HXRBS, another SMM instrument (yellow, 20-300 keV). The vertical axis shows the time in minutes from the start of the observation sequence. The relative intensity and shape of the selected spectral lines depends strongly on plasma conditions in the hot flare kernel.

Results of the instrument calibration work have been described in a dedicated paper (Rapley et al., 2017). Improved estimates of instrument parameters enabled us to deconvolve the instrumental broadening of spectral lines. An example is presented in Figure 3. 6, for two of the eight BCS spectral channels.

Ongoing analysis of SMM BCS data will proceed thanks to a three-year NCN grant obtained by Barbara Sylwester, who will lead the team of five people. The analysis will use modern tools, including spectral deconvolution. Results are expected to reveal physical conditions in flaring plasmas, and possibly indicate the presence of non-equilibrium and non-stationary effects.

Such effects have previously been studied in detail by a team of scientists at the International Space Science Institute (ISSI; project: Non-Equilibrium Processes in the Solar Corona and their Connection to the Solar Wind, http://www.issibern.ch/ teams/scsolwind/), who have shown that depending on the shape of electron distribution function in the source, relative line intensities may change substantially (see Figure 3. 7). This dependence has been discussed in detail in an invited review article (Dudik et al., 2017).

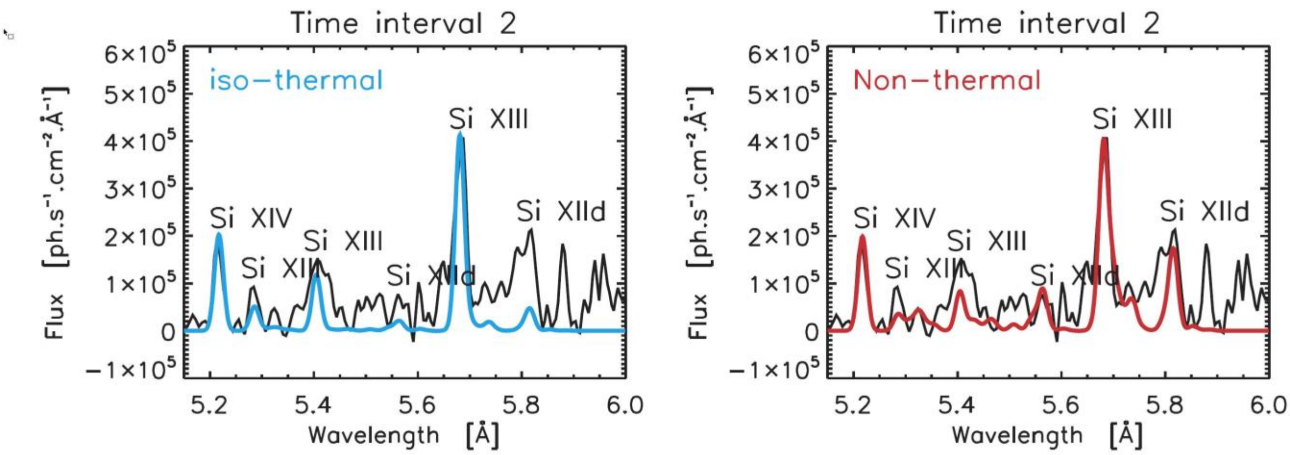

Fig. 3. 7. Comparison of the observed spectrum in the RESIK channel 4 with synthetic spectra for the Maxwellian distribution (left) and n-distribution with n = 11 (right). (Dzifcáková et al.et al., 2008, Astron. Astrophys. 488, 311).

The Optical path equipment for SOLPEX Ż. Szaforz, Z. Kordylewski

Theoretical simulations of reflection parameters for SOLPEX crystals.

Solar X-ray spectra are a source of information about the composition of solar coronal plasma, plasma temperatures and densities, and also plasma velocities. In order to reveal the X-ray spectra, an X-ray spectrometer must be well-calibrated and use high quality crystals. X-ray spectrometers operate based on the Bragg law, utilising the specific arrangement of atoms in the crystal lattice. Correct interpretation of the observed spectra requires understanding of the instrumental function. It is necessary to know the parameters of all elements located in the optical path of the instrument, between the radiation source and the detector.

Crystals are a particularly important element. The amount of radiation that undergoes effective diffraction on the crystal can be determined theoretically using specialised software (assuming that we are dealing with so-called ”perfect” crystals). The Solar Physics Division at CBK PAN is currently involved in preparations for two future missions requiring crystals: ChemiX and SOLPEX (B-POL and RDS). Theoretical simulations of the reflection parameters of these crystals have been conducted, using XOP software (Xcrystal and Xcrystal_bent) and GID_SL (Sergey Stepanov’s X-ray Server) to carry out the calculations. The crystal reflection functions deter-mined in this way, combined with other instrument parameters (such as filter permeability and sensitivity of detectors), make it possible to simulate the spectra that will be observed with the X-ray spectrometers (Figure 8).

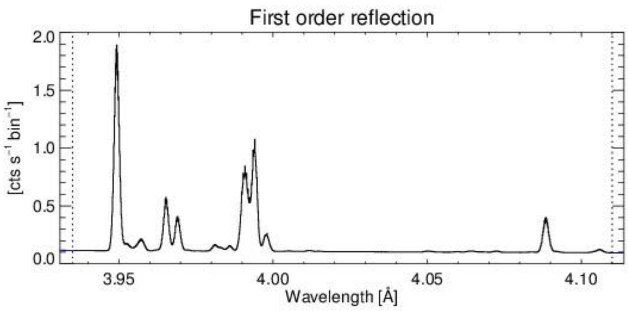

Fig. 3. 8. Simulation of the solar spectrum to be observed with the SOLPEX (B-POL) instrument during the GOES M5 class solar flare.

X-ray collimators

A field method was developed for the construction of X-ray collimators from capillary plates. The principle is illustrated in Figure 3. 9, in which x represents a position on the input plate and y a position on the output plate. Using these (x, y) coordinates, Figure 3. 10 shows “transmission fields”, labelled C, which are loci of coordinate pairs where radiation would be transmitted by the collimator in the absence of the intermediate plate; and “blackout fields”, labelled P, where radiation is extinguished by the intermediate plate. Software based on IDL (Interactive Data Language) can then be used to select intermediate plates that completely eliminate unwanted side radiation.

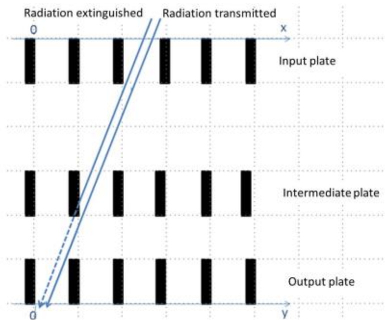

Fig. 3. 9. Capillary collimator.

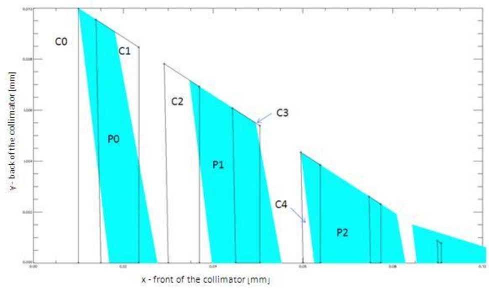

Fig. 3. 10. Transmission and blackout fields.

The X-ray characterisation of Bragg crystal spectrometer

A method was developed for X-ray characterisation of a Bragg crystal spectrometer equipped with a bent monocrystalline wafer.

Procedures were written for digital instruments to measure small rotations or movements precisely. The instruments were built in the Solar Physics Division. A procedure for precisely calculating the area for the hole in a pinhole camera was also written. Experimental procedures for X-ray characterisation of bent and flat monocrystalline wafers were continued.

SPHINX Sz. Gburek, M. Gryciuk, M. Siarkowski

Basic research on coronal and photospheric activity during SphinX mission

In 2017, research continued on the link between photospheric and coronal structures during very low solar activity observed in 2009. The research is based on measurements from the Polish Solar Photometer in X-rays (SphinX), the X-Ray Telescope (XRT) operating on the Hinode satellite, and sunspot data from various sources. The principal focus this year was analysis of the XRT Synoptic Composite Image Archive (SCIA), which is a source of X-ray full-disk solar images obtained from the XRT Telescope. The SCIA solar images provide a calibrated track of solar activity for studies of the X-ray corona. The images were rotated and shifted to bring them to a common reference frame, so that they could be superimposed for investigations of coronal activity and its evolution on short and long time scales. An example showing X-ray activity signatures over the entire duration of the SphinX instrument mission is presented in Figure 3. 11. Further work will compare the SCIA images with images of sunspot locations from Debrecen Photoheliographic Data (DPD) and SOHO/MDISunspot Data (SDD) catalogues, which are the most comprehensive and suitable for this research.

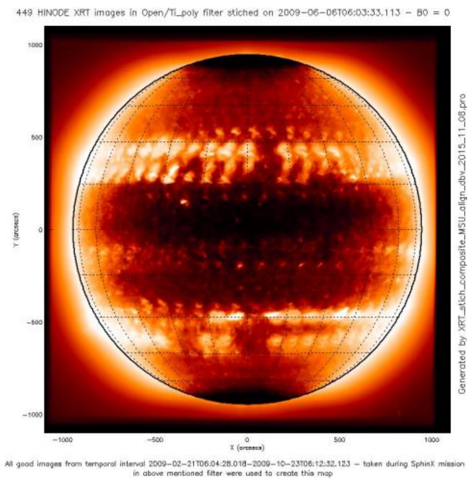

Fig. 3. 11. Composite image of 449 SCIA X-ray expositions from the XRT telescope taken during the SphinX mission(2009-02-20—-11-30).

SphinX data analysis

In 2017, analysis of SphinX data continued, principally focussing on SphinX flares.

One of the tasks was analysis and interpretation of common SphinX and GOES observations. For both instruments, the temperatures and emission measures were obtained based on flux ratio in two spectral bands. For GOES, these bands are 1-8 A and 0.5-4 A. For SphinX, the first band is nearly identical: 0.82-8.2 A; but the second one lies on the opposite side of the wavelength axis: 8.2-10.7 A (see Figure 12). The different energy channels produced different measurements of temperatures and emission measures by the two instruments.

SphinX data was also used as a basis for estimating expected STIX fluxes. In order to evaluate expected flux observed by STIX detectors during deep solar minimum activity, we selected a time period in which the SphinX spectrophotometer had recorded X-ray emissions of B1 class intensity, according to the standard GOES classification. Results obtained for a quiet Sun with two non-flaring active regions suggest that STIX will be able to register only ~15 counts per second in a single detector, in the energy range 4 to 15 keV. This suggests that higher solar emissions may be required for efficient imaging. These results were presented during the Second VarSITI General Symposium (Russia).

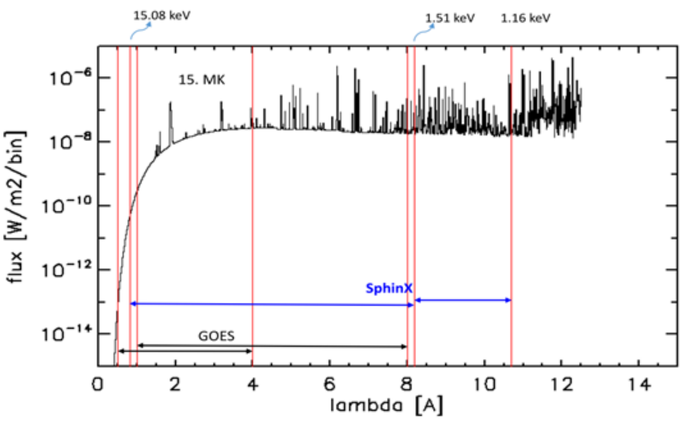

Fig. 3. 12. Example of solar flux with SphinX and GOES wavelength channels ranges superimposed.

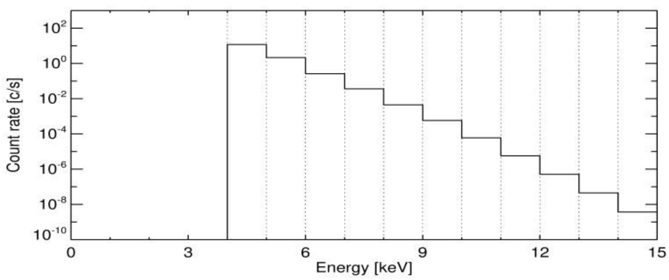

Fig. 3. 13. Estimated count rates in individual STIX energy bins for input solar flux of GOES B1 class intensity.

3. SPACE PHYSICS

The Spectrometer Telescope for Imaging X-rays (STIX) A. Barylak, J. Barylak, T. Mrozek

Image reconstruction —simulations and modelling

The Spectrometer Telescope for Imaging X-rays (STIX) is an X-ray spectroscopic imager, which will be installed on board the Solar Orbiter. It is a typical coded-aperture instrument with several important improvements over previous instruments of this type, such as YOHKOH/ HXT or RHESSI. The overall concept of the imaging method is well-defined, but in-orbit behaviour will be influenced by several crucial issues, including cross-calibration of detectors and collimators, particle background, and fluorescence from instrument parts. Therefore, we are developing simulations (software and hardware) that will allow better understanding of the performance of the instrument. Within the general framework of image reconstruction and simulations of spectra, we have developed a new method for image restoration from STIX data.

In the first step, we analysed and modelled the process of image formation on the detector.

The STIX imaging module consists of 30 pairs of sub-collimators and detectors. Each subcollimator consists of two distant parallel grids with slightly different pitches and orientations, with the result that incoming photons from the Sun form characteristic Moire patterns on the detector plane. This modulation pattern is recorded in four rectangle subpixels (named A, B, C and D —see Figure 14).

It can be shown that each subcollimator measures one Fourier component of the source image, and photons counted in four subpixels can be used to calculate the amplitude and phase of these components (i.e. the real and imaginary parts of the visibility function). The 30 Fourier components will be used to restore the source image in conjunction with a variety of imaging algorithms, such as back projection, CLEAN, forward fit, MEM, Pixon, etc..

We have started testing a restoration method that uses a vector of count rate values recorded in all 120 subpixels. This is an iterative method based on the maximum likelihood principle. Similar methods have been used by us for many years for deconvolution of images and spectra. The first attempts are promising: Figure 15 illustrates an example of assumed and restored source.

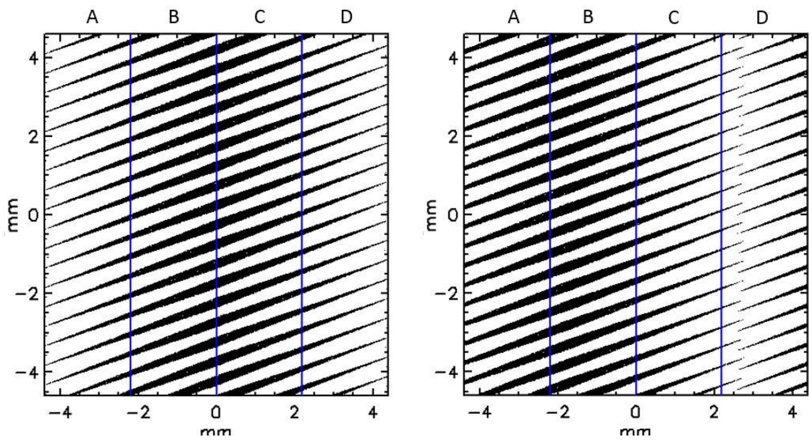

Fig. 3. 14. Images of incoming photons (black), forming a Moire pattern on the detector plane. Photons are counted in four large vertical subpixels denoted as A, B, C and D. Left: on-axis distant source. Right: off-axis source (shifted about one arc minute from the collimator axis in the northwest direction).

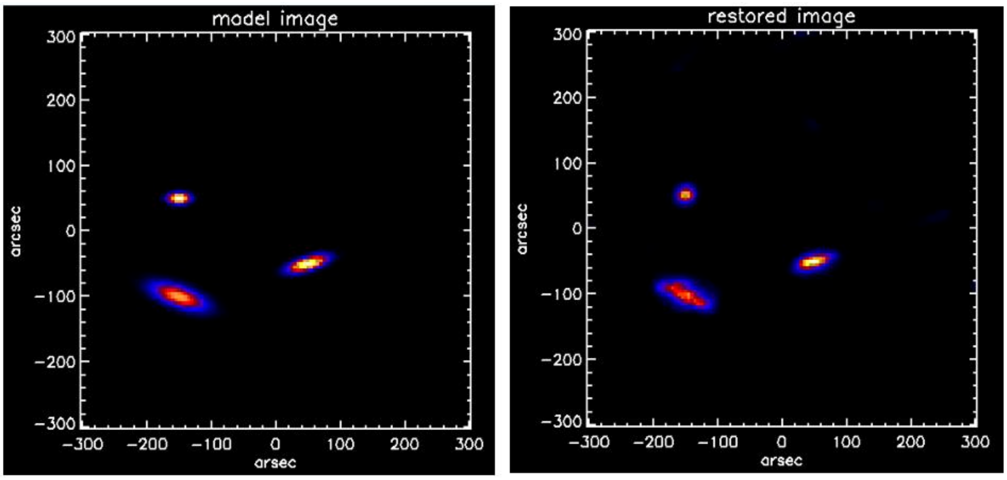

Fig. 3. 15. An example of assumed (left) and restored (right) photon sources distribution.

Moreover, in collaboration with several European institutes under the leadership of Switzerland's FHNW, we are developing software for analysis of STIX scientific data. To date we have completed the overall threat for simulation of transmission of solar photons through grids, and image reconstruction with two algorithms (Backprojection and CLEAN).

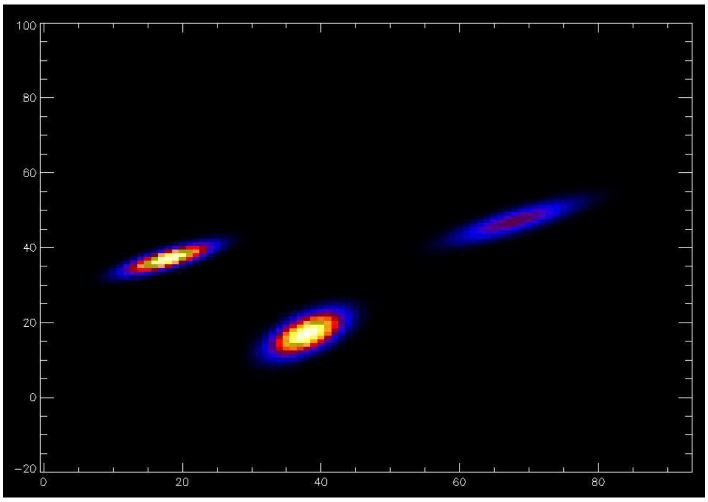

Fig. 3.16. An example of assumed photon source distribution used for software analysis of STIX scientific data. Due to current limitations, sources must be confined within an area having diameter less than 120 arcsec.

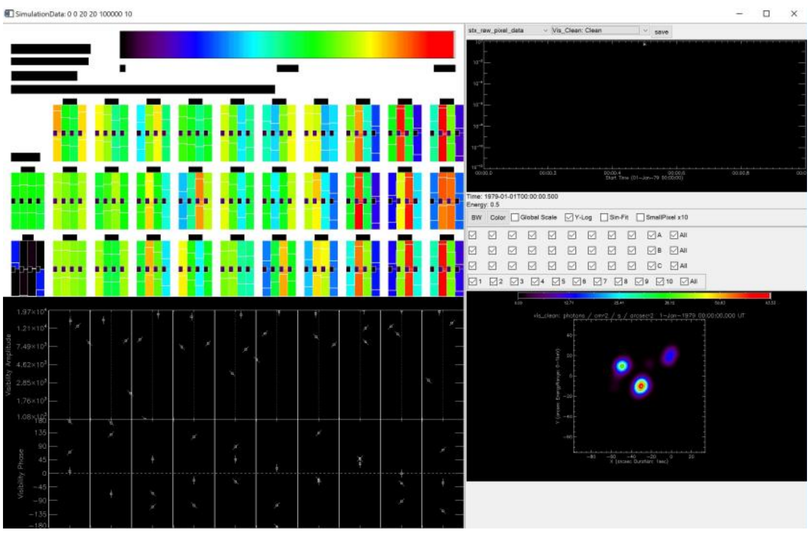

Fig. 3. 17. The main window of the STIX scientific data analysis software interface. The map in the lower left corner shows an image reconstruction of the distribution presented in Figure 16, using the CLEAN algorithm.

Grid transmittance

The imaging concept is based on subcollimators, which modulate and measure incoming X-ray photons. Each subcollimator is a pair of grids behind which is

placed a pixelated CdTe detector. STIX is equipped with 30 pairs of grids of various pitches and orientations.
Each pair of grids produces a Moiré pattern whose phase is dependent on the inclination of the incoming radiation. Each detector is divided into four sectors, each consisting of three pixels. This geometry allows exact measurement of the phase and amplitude of the Moiré pattern. The values obtained will be used to reconstruct the spatial distribution (image) of X-rays. The final image quality depends strongly on the calculated transmission of the pair of grids.
Transmission was modelled for pairs of grids using Geant4. Figure 18 presents result of the simulation for two energies (4 keV and 150 keV) for the same inclination of incoming photons. It is clear that at 4 keV, the Moiré pattern can be measured very precisely, but at 150 keV the information is blurred because the slats are partially transparent to such high energy photons. Therefore, additional uncertainty is introduced into the measurement of modulation, which may affect the reconstructed image.

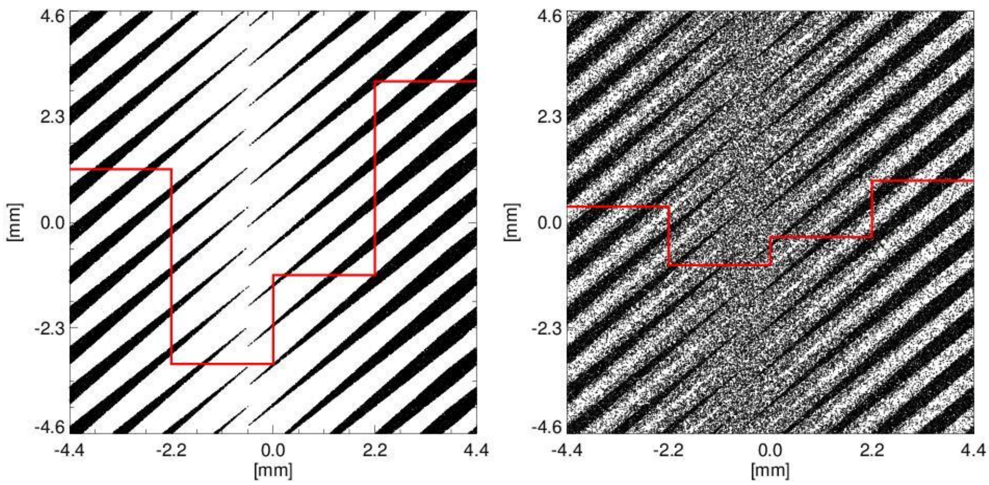

Fig. 3. 18. Results of Geant4 simulations for photons of energy 4 keV (left) and 150 keV (right). Red lines correspond to levels of total signal measured in detector sectors.

We further investigated the energy dependence of transmission for a pair of grids, as shown in Figure 20. It can be seen that for energies below 40 keV, the grids are effectively opaque. Above 40 keV, transmission increases until 69.5 keV, where it abruptly decreases to base level due to the absorption edge of tungsten. For higher energies, transmission increases monotonically, resulting in increasingly poor quality of the modulation pattern.

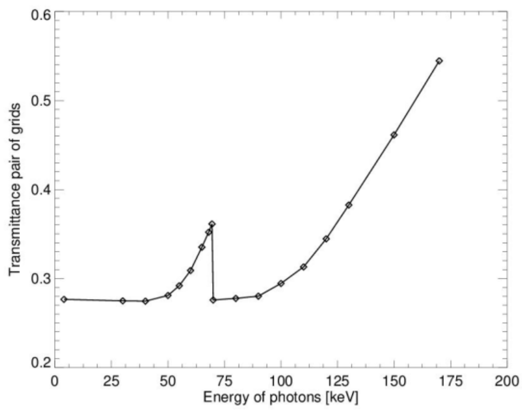

Fig. 3. 19. Energy dependence of transmission for a pair of grids.

The Solar Energetic Particle background in STIX detectors

One of ten instruments to be installed on board the Solar Orbiter, STIX will use a set of 32 pixelised CdTe detectors to provide spectroscopy of solar thermal and non-thermal X-ray emissions from 4 to 150 keV. A potentially significant source of background in the detectors will come from impacts from Solar Energetic Particles (SEP), especially when the satellite is close to the perihelion, which will be as short as 0.3 AU. The STIX detector consists of a CdTe sensor and dedicated front-end electronics. The CdTe sensor is divided into eight large and four small pixels, whose effective areas are 9.7 mm2 and 1.0 mm2, respectively. The attenuators and special observational modes will decrease the signal measured by one detector to 20 000 counts per second. The Geant4 package is a tool for Monte Carlo simulations of particle interactions with matter. When performing Ge-ant4 simulations, it is necessary to define the geo-metrical model of the instrument and the input spectrum of particles. The package contains a broad suite of physical models (including electromagnetic, hadronic and optical) covering a wide range of energies from ~250 eV up to several TeV, which can be freely selected while running the package.

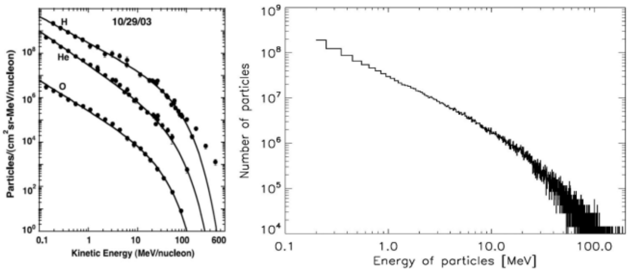

Fig. 3. 20. Left panel: results of SEP event measurements from Mewaldt et al. (2005). Right panel: input spectrum for GEANT4 simulation constructed on the basis of results presented in the left panel.

Scenario 1: direct particle hit.

First, we investigated the case where the front side of the detector (Figure 3. 21, left panel) is hit directly by particles. Based on the event of 29-Oct-2003, we might expect up to 2000 counts/keV. Usually SEPs last several hours at least, thus the influence of such background is expected to be quite weak. Moreover, the front side of instrument is equipped with a thermal baffle, which should stop the majority of particles.

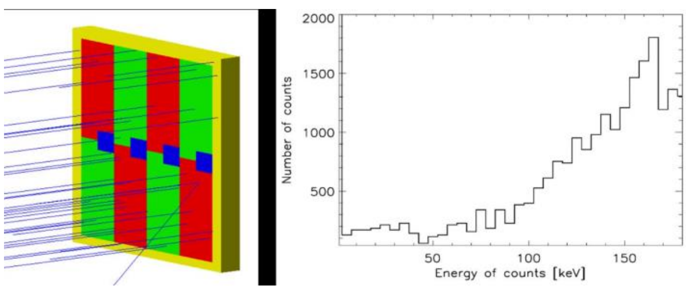

Fig. 3. 21. Left panel: front side of a Caliste-SO detector hit by particles. Right panel: the expected count spectrum from particles (integrated over the whole event).

Scenario 2: secondary emission from constructional parts.

In this exercise we used a simplified model of the Solar Orbiter, taking into account aluminum only. Figure 3. 22 presents numbers of particles (electrons, protons, photons) predicted to escape from the aluminum parts of the instrument when it is hit by an SEP similar to the 29-Oct-2003 event. The expected background from these secondary emissions is 10-100 more severe than from direct hits. The combined effect arising from SEP may be as high as 1000 counts/second/detector, which may significantly affect spectra and images obtained by the STIX.

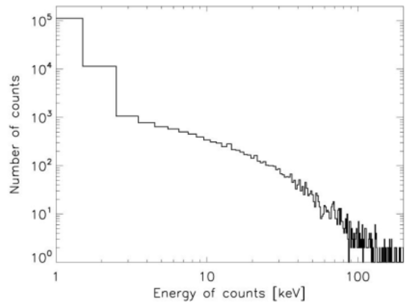

Fig. 3. 22. The count spectrum of secondary emissions from aluminum parts.

Heliospheric physics M. Bzowski

The hypersonic, ionized solar wind carves out a cavity in the interstellar matter, called the heliosphere. Its size is determined by a balance between the pressures of the magnetized solar wind and the interstellar gas, which is also magnetized. The heliosphere is bounded by a contact discontinuity layer called the heliopause, which separates the solar wind and interstellar plasmas. While the interstellar plasma is deflected and flows past the heliopause, the neutral component, mainly hydrogen and helium, penetrates freely into the heliosphere, where it can be directly observed. An artist's impression of the heliosphere is shown in Fig. 3. 23.

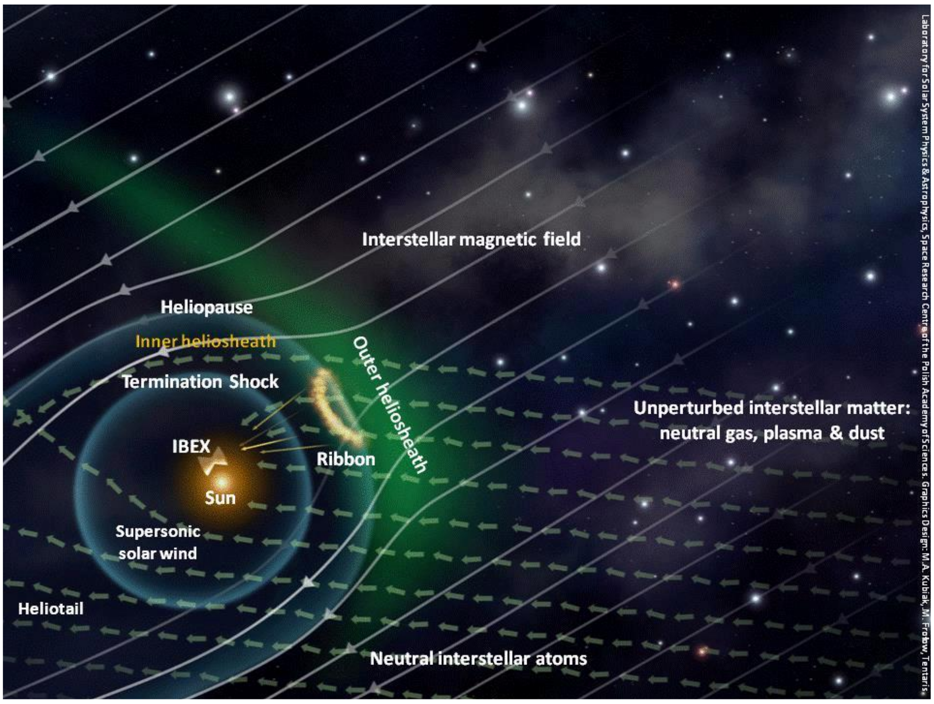

Fig. 3. 23. Artist's impression of the heliosphere and its nearest Galactic neighbourhood as it emerges based on the analysis of recent IBEX observations and several years of research carried out in the Laboratory for Solar System Physics and Astrophysics. Graphics design: Marzena A. Kubiak, Maciej Frołow, Tentaris.

The figure shows the Sun embedded in the local cloud of interstellar matter composed of ionized and neutral atoms and dust grains of various sizes. It is one of many similar clouds within the Local Interstellar Medium, which is a ~200 pc remnant of a series of Supernova explosions that happened a few million years ago. The Sun moves through the cloud from right to left, emitting the solar windever-evolving, omnidirectional, latitudinally-structured, hypersonic outflow of solar plasma. Subjected to the ram pressure of the ambient interstellar matter, the solar wind slows down through a shock wavesolar wind termination shockeventually flows down-stream, forming a contact discontinuity surface called the heliopause, which separates the solar and interstellar plasmas, and an elongated heliotail (bottom-left corner of Fig. 3. 23). The heliopause, inpenetrable for charged particles except for cosmic rays, is transparent for neutral atoms. Energetic neutral atoms (ENAs) form everywhere in the heliosphere due to the charge exchange reaction between the ions from local

plasma and neutral interstellar atoms.
Charge exchange operates both in the supersonic solar wind and in the inner heliosheath (centre-left in Fig. 24), i.e., in the region between the termination shock and the heliopause. Some of those atoms freely escape from the heliosphere and, due to eventual collisions, slightly modify the inflowing interstellar gas.
Others run in the opposite direction and reach detectors located in the Earth's orbit (in Fig. 3. 23, schematically drawn close to the Sun). Neutral atoms from the interstellar matter (whose stream-lines are marked by the short arrows in Fig. 3. 23) typically have energies of between a few dozen, and about 150 eV, and freely enter the heliosphere, where some of them are detected by space-borne detectors. Due to interaction between the heliosphere and the interstellar medium, a disturbed region called the outer heliosheath (the green haze in the figure) forms in front of the heliosphere. In this region, the flows of interstellar plasma and interstellar neutral gas decouple. This leads to the formation of another population of neutral atoms (former outer heliosheath ions) through charge exchange reactions. Some of these atoms also enter the heliosphere and are detected as the socalled secondary population of neutral interstellar gas. Together with all the other populations of neutral atoms, they provide an important means for analysing the physical state of the distant regions that they originated from.
During recent years, a very important insight into the heliosphere, local interstellar medium and processes responsible for the coupling of these astrophysical objects was obtained based on observations by the NASA space probe Interstellar Boundary Explorer (IBEX). This mission was developed, and is being led by the Southwest Rese-arch Institute in San Antonio, TX under the NA SA Small Explorers program. It is managed by the Goddard Space Flight Center for the NASA Science Mission Directorate in Washington, DC. Research is carried out by the IBEX Science Team of researchers from the United States, Poland, Switzerland, Germany, and Russia. The Centrum Badań Kosmicznych Polskiej Akademii Nauk (CBK PAN) has participated in the IBEX effort, since the planning phase, at the Co-Investigator level.

Shortly after the start of IBEX observations, an arc-like, almost circular region of enhanced neutral atom emission was unexpectedly discovered in the sky. This was subsequently called the IBEX Ribbon. It appears that the IBEX Ribbon is formed somewhere close to the heliopause, probably in the outer heliosheath, where IBEX looks perpendicularly to the local direction of the interstellar magnetic field lines (marked by the long arrows neighbouring the heliopause in Fig. 3. 23). Currently, the most probable hypothesis is that the centre of the IBEX Ribbon approximately points towards the direction of the interstellar magnetic field. The action of the interstellar magnetic field distorts the heliosphere from axial symmetry and probably pushes the heliotail to the side. Depending on the magnetic field strength and direction, and the relative speed between the Sun and the interstellar gas, the outer heliosheath at the upwind side may or may not be terminated by a shock wave called the bow shock. Assuming the interstellar gas velocity as obtained from the recent IBEX measurement, the character of the wave-like structures in front of the heliosphere is much more complex than previously thought.

Among the most important results obtained by scientists from the Laboratory of Solar System Physics and Astrophysics (LSSPA) of CBK PAN in 2017 is an understanding of the nature of the heliospheric Warm Breeze. The Warm Breeze, discovered by scientists from LSSPA in 2012, is an inflow of neutral helium into the heliosphere, which is different from the well-known inflow of interstellar neutral helium. When projected on the sky, the location of the Warm Breeze partly overlaps with the location of neutral interstellar gas. The region in the sky where the Warm Breeze and neutral interstellar gas are observed is shown in Fig. 25.

In earlier studies, scientists from LSSPA had determined the apparent direction and inflow speed of the Warm Breeze. A comparison of the inflow direction of the interstellar neutral gas and the lo-cation of the centre of the IBEX Ribbon (Fig. 3. 24) suggested that the Warm Breeze is the secondary population of interstellar neutral gas, created in the outer heliosheath (shown previously in Fig. 3. 23), which is due to charge exchange between the unperturbed interstellar helium and the compressed, heated and slowed-down He+ plasma flo-wing in the outer heliosheath past the heliopause.

The constituents of the neutral atom flux (Fig. 3. 24) are mostly helium, and at a distance of 1 astronomical unit (i.e., at Earth's orbit) they run at ~50 km/s relative to the Sun and ~70 km/s relative to the IBEX spacecraft. Observed in this energy band, most of the sky is empty (shown in black in Figure 3. 24). The blue, yellow and red colours in Figure 3. 24 correspond to a sequence of increasing intensities of the low-energy helium atoms observed by the IBEX-Lo sensor. The region corresponding to interstellar neutral (helium) atoms (ISN) lies inside the yellow contour. The region occupied by the Warm Breeze lies inside the white contour.

The ISN and Warm Breeze regions partly overlap. The directions of inflow of ISN and Warm Breeze beyond the heliopause are marked by the yellow and white dots, respectively. The offsets of the centroids of the ISN and Warm Breeze regions from the unperturbed directions of ISN and Warm Breeze are due to the bending of the atom trajectories by the solar gravity force (the gravitational lensing effect).

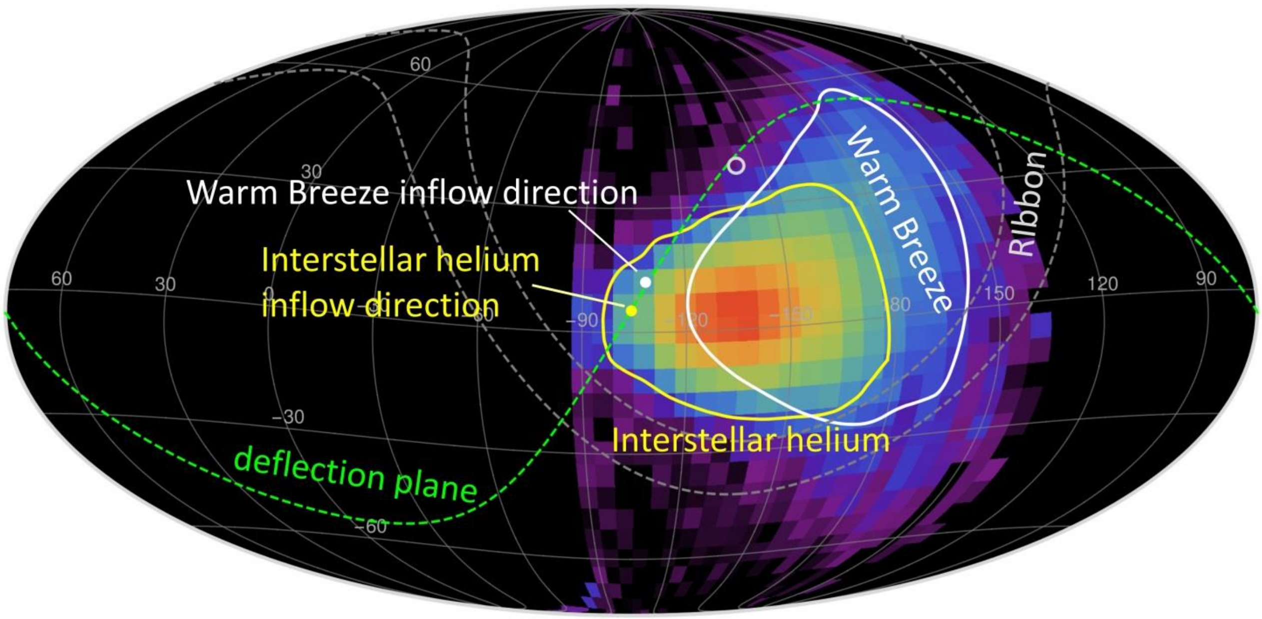

Fig. 3. 24. Sky map of the neutral atom flux, observed by the IBEX-Lo sensor.

The green dashed line (bottom-left in Fig. 3. 24) is a projection on the sky of the plane of deflection of the secondary populations of neutral interstellar gas. The grey arcs mark the location of the IBEX Ribbon in the sky. Note that the centre of the IBEX Ribbon, marked by the small white circle (right of centre in Fig. 25), lies within this plane.

During 2017, scientists from LSSPA (M. Bzowski, M. A. Kubiak, A. Czechowski, and J. Grygorczuk) verified the hypothesis that the Warm Breeze is the secondary population of interstellar neutral gas, by reproducing the observed signal through simulations, starting from first principles. The process of charge exchange between the plasma and neutral gas in the outer heliosheath was simulated along the orbits of the atoms that enter the IBEX-Lo detector by solving the atom gains and loss balance equation along the atom orbits. The plasma in the outer heliosheath was simulated using a magnetohydodynamics (MHD) model developed previously; the signal-synthesis portion of the simulation suite was also based on earlier work that had determined Warm Breeze parameters. Scientists from LSSPA demonstrated that: (1) in the absence of the assumed perturbation of the plasma in the outer heliosheath the Warm Breeze signal is not created; (2) the Warm Breeze signal appears whenever one assumes a perturbation for the plasma flow characteristic for the outer heliosheath; (3) characteristic discrepancies between observation and simulation results arise when the simulated outer heliosheath is axially symmetric, as expected in the absence of the interstellar magnetic field, and; (4) when the strength and direction of the interstellar magnetic field that are similar to those obtained from the analysis of the IBEX Ribbon are included in the background MHD modelling of the plasma, the simulated Warm Breeze qualitatively signal agrees with observations (see Fig. 3. 25). This strongly suggests that the Warm Breeze is, in fact, the secondary population of interstellar neutral gas, and since details of this signal seem to depend on the assumed magnetic field and plasma parameters in front of the heliosphere, studying the Warm Breeze will likely bring important insights into both the physics of the outer heliosheath, and the physical state of the matter in the Local Interstellar Cloud.

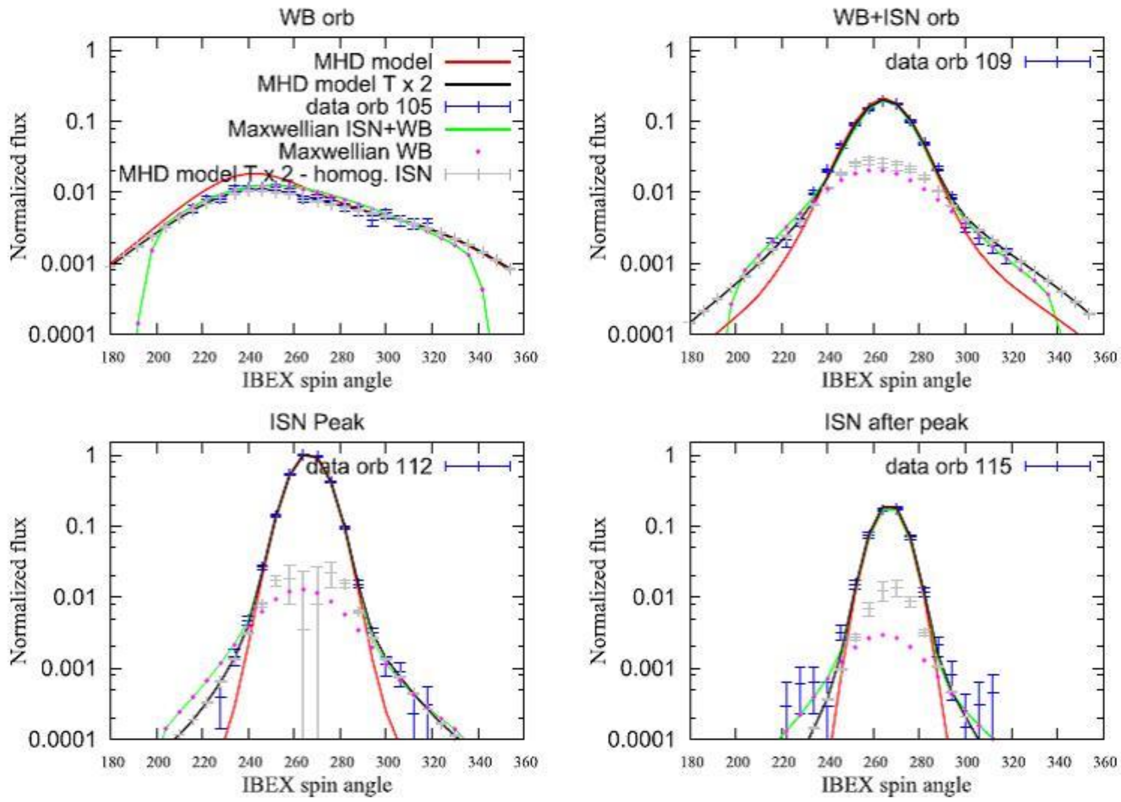

Fig. 3. 25. Comparison of observations of neutral He by IBEX-Lo in selected orbits (105, 109, 112, and 115; blue dots with error bars) with models (solid lines). The green line represents a simplified model of two independent populations of neutral He, fitted in an earlier analysis. The red line illustrates the present model, where the signal is composed of a mixture of atoms penetrating the outer heliosheath without any interaction with the ambient plasma and those created in the outer heliosheath due to the charge exchange reaction between He atoms from interstellar gas and He+ ions from the compressed interstellar plasma flowing past the heliopause. The grey and purple dots represent the secondary population of interstellar gas, i.e., atoms originating from the outer heliosheath, obtained in the present model and the previous, simplified, approach. Simulated fluxes are normalized to the maximum of simulated flux for Orbit 112 and shown as a function of the IBEX spin angle, i.e., an angle in a plane close to perpendicular to the ecliptic plane (source: Kubiak et al., Ap. J. 845:15, 2017).

As a contribution to the debate on the shape of the heliosphere, A. Czechowski and J. Grygorczuk (J. Phys. CS 900, 012004, 2017) considered a model of an astrosphere surrounded by a partly ionized interstellar medium permeated by a magnetic field with intensities varying from the values typical for the Local Interstellar Cloud (~2 microgauss) up to a much stronger value of (20 microgauss). In addition to the plasma flow in the simulated astrospheres and their global shapes, they also simulated the expected sky distribution of the

ENAs created due to charge exchange between neutral interstellar hydrogen and the plasma. They found that, in accordance with expectations, for the weak field, a comet-like heliosphere appears in the simulation, and its tail is not visible in the ENA signal because the lines of sight directed towards the tail are populated mostly by atoms that are created close to the termination shock, which obscure a much weaker signal from the ENAs created in the tail region. In contrast, for the strongest magnetic field considered, an astrosphere with two jets evacuating the stellar wind plasma appears, in agreement with predictions of the analytical model by Parker. When a moderate-velocity motion of the astrosphere through the interstellar medium is allowed for, the two jets are deflected backward, forming a splittail phenomenon. For the case of a strong magnetic field and a splittail, a strong ENA signal is expected from these regions in the sky because of the ENAs that are injected due to neutralization of energetic ions in the forward and flank parts of the termination shock and subsequently advected with the plasma evacuated through the tail. However, the observed distribution of ENAs in the sky would look qualitatively different under the two aforementioned hypotheses, as illustrated in Figure 3. 26.

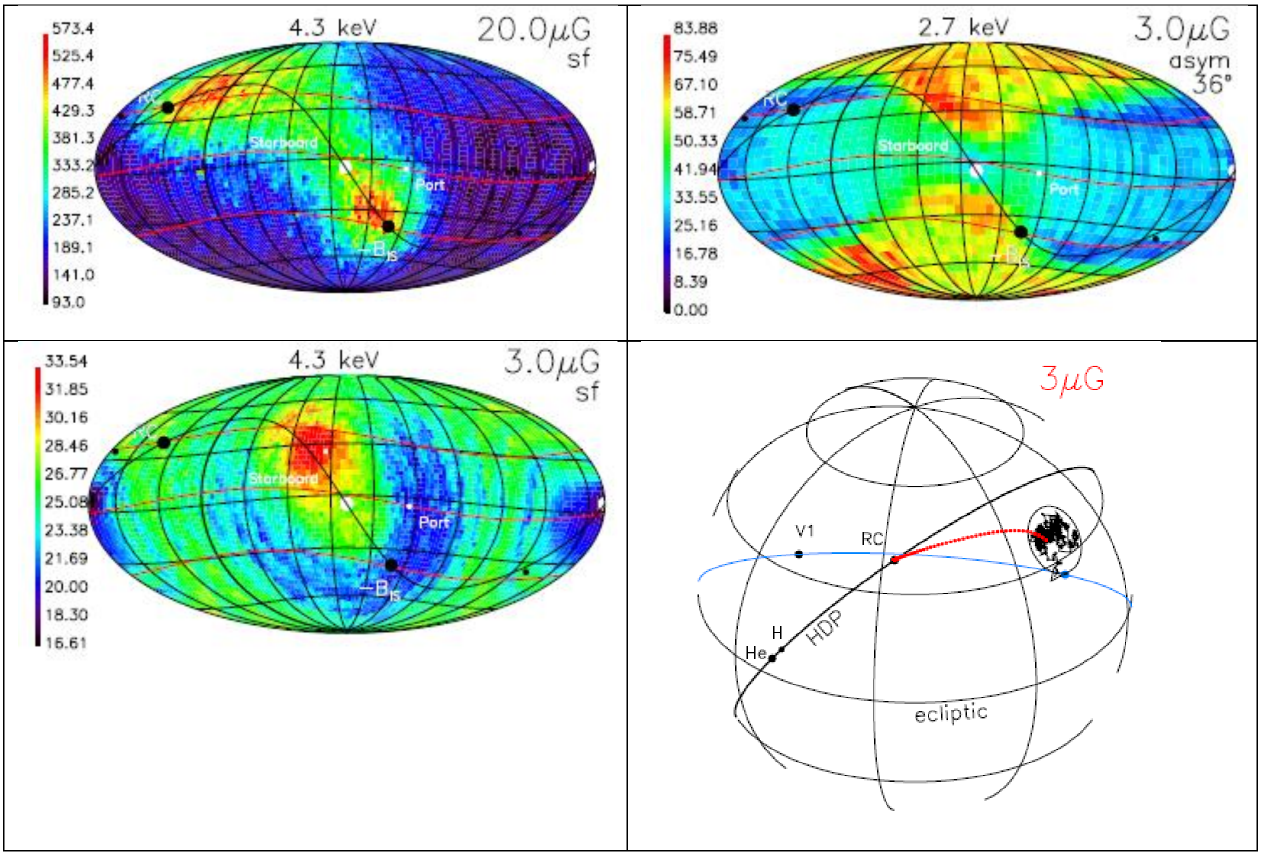

Fig. 3. 26. Comparison of the intensity distribution of H ENAs for a strong interstellar magnetic field of 20 microgauss (upper-left) with that simulated for a low field strength equal to 3 microgauss (lower-left), for a spherically symmetric solar wind. Note the profound differences between these two maps. The upper-right panel illustrates the role of the latitudinal structure of the solar wind in the creation of the global distribution of H ENAs for the realistic case of a 3 microgauss interstellar field. The lower-right panel shows the unfolding direction of the interstellar magnetic field in the outer heliosheath (red line) from the unperturbed direction towards the IBEX Ribbon centre and in situ observations from Voyager 1 for parameters corresponding to those used in the simulation shown in the upper-right panel (adapted from Czechowski & Grygorczuk, J. Phys. CS 900, 012004, 2017).

In the split-tail scenario with a strong magnetic field, the location of the tail regions in the sky should be marked with local maxima of the flux, and not by flux depletion regions, as suggested by researchers who believe that the heliosphere is a croissant shape. The distribution of the ENA flux in the sky, as shown by Czechowski & Grygorczuk (see Fig. 3. 26), depends on the strength and direction of the interstellar magnetic field as well as the latitudinal structure of the solar wind. Since the solar wind is latitudinally structured, with higher-energy flow in the polar regions, the ENA flux distribution for the energies that are chara-cteristic of polar flows (3 keV and larger) is expected to be larger in the polar regions, in line with the observed data. The simulation for the low-strength interstellar magnetic field directed to-wards the IBEX Ribbon centre, and the latitudinally-structured solar wind predicts a draping of the magnetic field in the outer heliosheath, increasing with the decrease in solar distance. This means that for the geometric location of the Voyager 1 spacecraft, this direction and field strength agree with those observed, as shown in the lower-right panel in Fig. 3. 26.

To date, most observations of ENAs have only considered hydrogen. P. Swaczyna, S. Grzędzielski, and M. Bzowski from LSSPA, however, have been investigating the observation of He ENAs and ENAs of selected heavier elements, including N, Ne, and O. For He, ENA fluxes resulting from neutralization of solar wind alpha particles and He+ pickup ions in the inner heliosheath were calculated, as well as ENAs originating in the outer heliosheath in the secondary-ENA emission mechanism, which is most likely responsible for the creation of the IBEX Ribbon. It was found that the dominant source of He ENAs in the heliosphere should be the inner heliosheath, and the magnitudes of the simulated spectra suggest that He ENA will be observable by NASA's planned Interstellar Mapping and Acceleration Probe. The most promising energy band is from a few to a few dozen keV/nucleon. Due to the long integration path, the largest signal is expected from the heliospheric tail. This means that observations of He ENA could be an important tool for diagnosing the global shape of the heliosphere, and help to resolve the ongoing debate about whether the heliosphere is comet-like, croissant-like, or bubble-like. It is hard to use existing H ENA ob-servations for this purpose because energetic pro-tons, which provide the seed population for H ENAs, become neutralized before they progress deeper in the heliospheric tail and consequently it is not possible to see the heliospheric tail (or two tails, in the croissant hypothesis). The sky image simulated for selected energies of He ENAs is shown in Fig. 3. 27. These results were published in Swaczyna et al., Ap. J. 840:75, 2017.

Analysis of the expected fluxes of Ne, N, and O ENA by P. Swaczyna and M. Bzowski (Ap. J. 846:128, 2017) are a continuation of the He ENA study. The treatment of these species had to be simplified because of a much larger number of charge exchange reactions involved. Atoms of heavy species are much less abundant than H and He, so expected fluxes are much lower than these of H and He, and detection is much more challenging (see Fig. 3. 28). Potentially, however, heavy ENAs may help in understand the details of the processes operating in different regions of the heliosphere. This is because they have different charge exchange cross sections across species, and consequently different extinction lengths. This means that they contain information from different distances from the Sun.

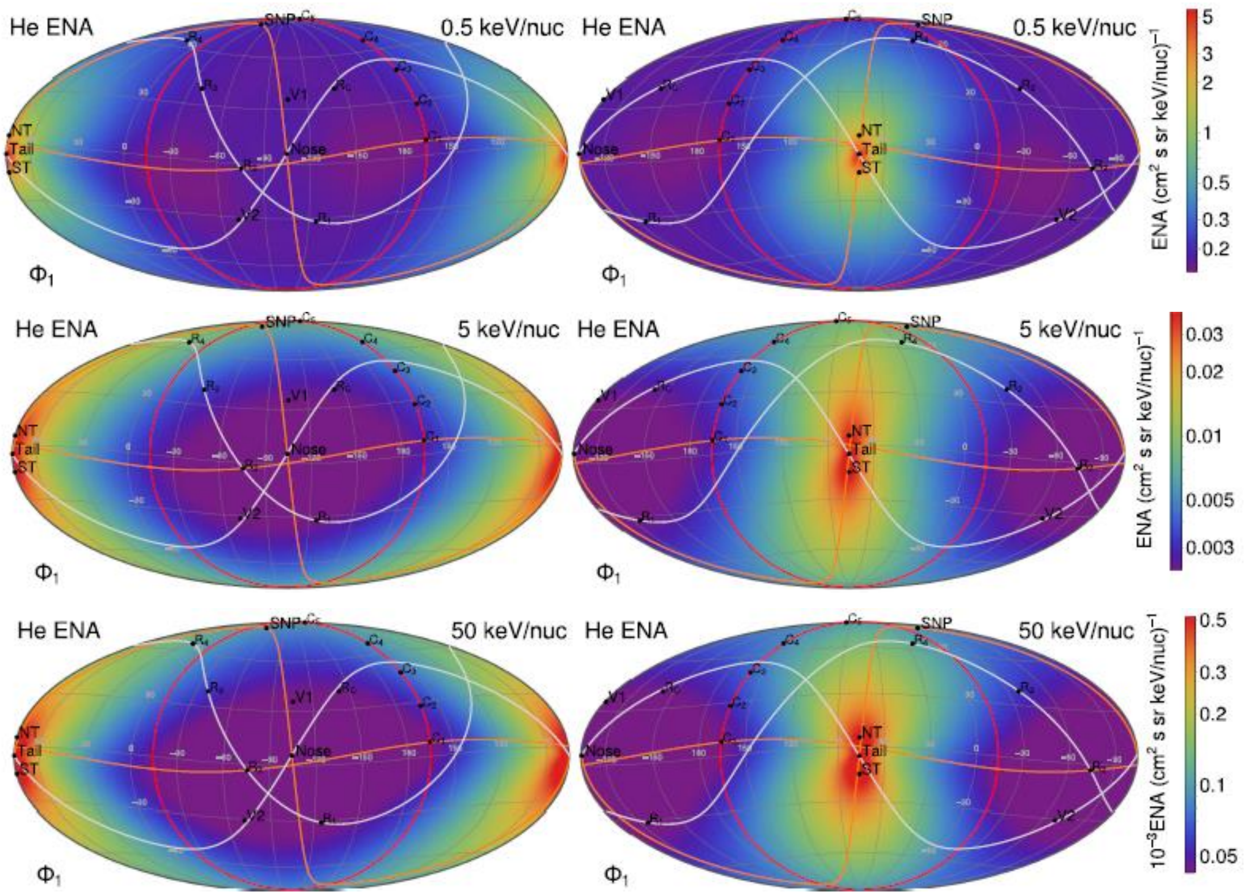

Fig. 3. 27. Maps of the flux of He ENAs for selected energy bands 0.5, 5, and 50 keV/nuc, simulated using potential-flow models of the heliosphere and latitudinally-structured solar wind. The left-hand column shows the sky centred at the heliospheric nose (in the middle for the plots), and the right-hand column the same flux distribution in a projection centred at the heliospheric tail direction. The grey lines represent the IBEX Ribbon centreline (the R1line) and the neutral gas deflection plane. The red circles represent the crosswind plane (i.e., the plane perpendicular to the direction of motion of the Sun through the Local Interstellar Cloud), and the plane perpendicular to the latter (adapted from Swaczyna et al. Ap. J. 840:75, 2017).

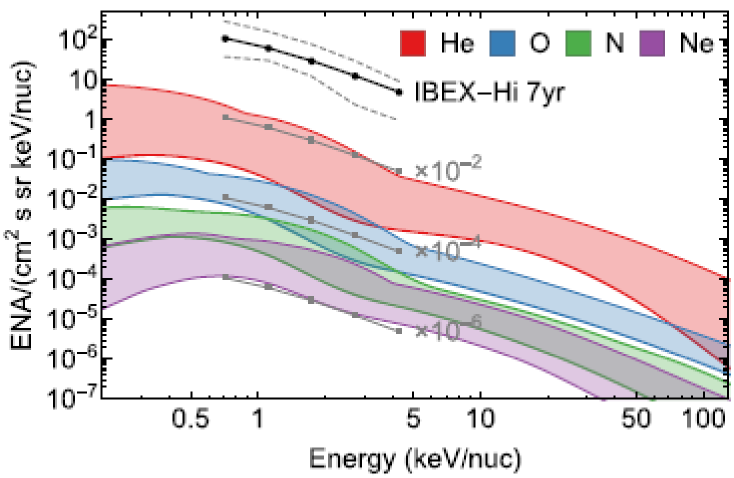

Fig. 3. 28. The range of simulated ENA intensities of He, O, N, and Ne, marked with the colours shown in the panel. Intensity ranges are compared with the mean spectrum of H ENAs observed by IBEX (black dotted lines). The grey lines are eye-guides and represent the IBEX spectrum scaled down by the factors indicated at the respective guidelines (adapted from Swaczyna & Bzowski, Ap. J. 846:128, 2017).

Nanodust grainstiniest grains of interplanetary dustcomposed of just hundreds or thousands of atoms. Stationary models of the dynamics of nanodust grains inside the Earth's orbit suggest that these grains hover unrealistically long in their orbits, which should lead to a build-up of their density distribution; however, this is not supported by observations. Based on extensive modelling by A. Czechowski from LSSPA and J. Kleimann, the key to resolving this enigma is momentum transfer (drag force) from plasma particles to nanodust grains during coronal mass ejections (CMEs). CMEs are strongly dynamic, transient phenomena that involve eruptions of high-speed, high-density plasma from the solar corona that propagate away from the Sun in the solar wind. The momentum imparted to nanodust grains by CME ions creates an effective force that results in a reduction in the aphelia of dust grain orbits. Eventually, this brings nanodust particles close to the Sun for sufficiently long to sublime. The evolution of the distance of a nanodust grain from the Sun in the absence and in the presence of a CME is illustrated in Fig. 30. CMEs appear to be responsible for elimination of nanodust particles from their bound orbits inside 1 AU (astronomical unit), which probably prevents an excessive build-up of their density.

Turbulence is a complex phenomenon and the driving mechanisms are still not clearly understood. It appears naturally in astrophysical plasmas, including planetary and interstellar shocks.

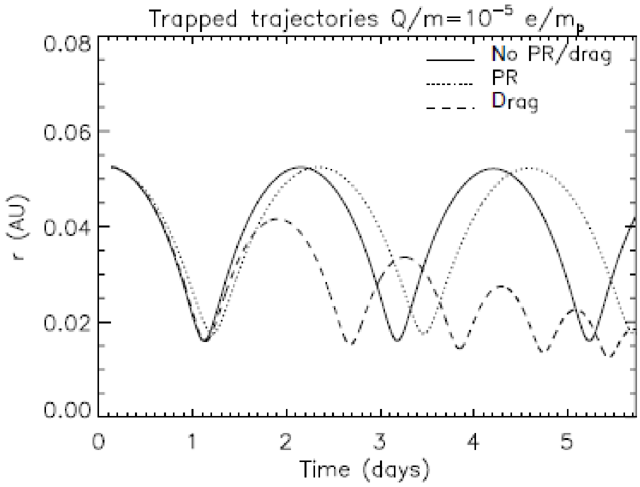

Fig. 3. 29. Comparison of the evolution of the distance from the Sun of a nanodust grain with no drag effects (solid line, stable orbit), under the influence of Poyntingdrag (dotted line, very ineffective decay of the perihelion), and under drag due to momentum transfer from CME plasma (broken line), which results in a rapid decay of the perihelion, eventually leading to the loss of the grain in the heat of the Sun (source: Czechowski & Kleimann, Ann. Geophys. Vol. 35, pp. 1033—, 2017).

The shocks in astrophysical plasmas are usually collisionless due to the very low density of the medium, and differ from those observed in fluids because they often result from the interaction of nonlinear structures. Investigating collisionless shocks and weakly collisional plasma is difficult under laboratory conditions, but given the plethra of past and current space missions, the solar wind appears to offer a natural laboratory for investigating these phenomena. Based on plasma measurements from several space probes within the THEMIS mission, W. M. Macek and A. Wawrzaszek from LSSPA, in collaboration with researchers from other Polish and American institutions, have shown that the plasma dynamics within the magnetosheath (i.e., behind the Earth's bow shock, when looking from the Sun) is intermittent, and turbulence is strongly anisotropic. More particularly, for very strong shock waves (i.e., for flow speeds much larger than the Alfven speed, which is the speed of sound in a magnetized medium) fluctuations in plasma parameters in the direction perpendicular to the local magnetic field strongly differ from the normal distribution. However, for the direction parallel to the local magnetic field, the plasma is close to equilibrium, i.e., normally distributed. This result, published in Macek et al., Ap. J. Lett. 851: L42, 2017, is potentially important for the development of a theory of turbulence.

Line-preserving flows in magnetized fluids are those where any fluid element on a given external field line remains on that line. The case of inviscid and incompressible fluids was described by Helmholtz in 1858. His description was later extended to barotropic compressible fluids by Thomson in 1869 and Nanson in 1874. In this same area, P. Figura from LSSPA has recently investigated the stability of line-preserving flows against certain perturbations introduced to the flow itself, and to the external field. He defined the deviation vector that describes a departure of a given system from the line-preserving regime. Examination of this vector will facilitate investi-gating departures of this given system from the line-preserving regime. These results, published in Figura, Geophys. Astophys. Fluid Dynamics 111, 508, 2017, offer a new view on magnetic re-connection processes.

In addition to leading several projects, researchers from LSSPA have also collaborated with international colleagues on several studies of the heliosphere. A. Czechowski contributed to a large-scale review paper (Pogorelov et al., Sp. Sci. Rev. 212, 193, 2017) on processes operating in the outer heliosheath.

J. M. Sokół and M. Bzowski assisted in the first analysis of observations of interstellar pickup ions in the solar wind, carried out during the cruise of the NASA New Horizons mission to Pluto (McComas et al., Ap. J. S. 238:18, 2017). They also formed part of the international team of scientists involved in identifying plasma wave signatures of the process of pickup of newly-injected ions due to ionization of interstellar atoms in the inner heliosphere. This ongoing, comprehensive research programme involves measurements taken at 1 AU from the Sun and outward. Results obtained so far were published by Argall et al. in Ap. J. 849:61, 2017, and by Smith et al. in J. Phys. CS 900, 012018, 2017.

M. Bzowski, M. A. Kubiak, and J. M. Sokół provi-ded input to an overview of seven years of global imaging of heliospheric ENAs by IBEX (Mc Comas et al., Ap. J. S. 229:41, 2017), and J. M. So-kół, M. Bzowski, and M. A. Kubiak supported A. Galli and an international team of scientists in the analysis of the lowest-energy ENAs from the downwind hemisphere, i.e., from the tail region. This analysis was challenging on the one hand because the low observation statistics, and on the other hand because time-dependent losses of the observed atoms between the creation and detection sites had to be precisely accounted for. Results were published by Galli et al. in Ap. J. 851:2, 2017.

J. M. Sokół and S. Grzędzielski assisted O. Khabarova's effort to identify and understand evidence from the available observations to support the existence of high-latitude conic current sheets in the solar wind, published in Khabarova et al., Ap. J. 836:108, 2017.

J. M. Sokół helped E. Zirnstein and colleagues to analyse the imprint of the Sun's evolving solar wind on the ENA atoms observed by IBEX; the model of evolution of the latitudinal structure of solar wind (developed by J. M. Sokół, P. Swaczyna and M. Bzowski in 2016 and carefully maintained during 2017) was critical to this study. Results of the ENA study were published by Zirnstein et al. in Ap. J. 846:63, 2017.

Ionospheric and magnetospheric physics

Meteoroid impacts onto the surface of the Moon and dust particle launching
B. tamaniuk, S. I. Popel, A. P. Golub, H. Rothkaehl, E. A. Lisin, Yu. N. Izvekova, G. Dol'nikov, A. V. Zakharov, and L. M. Zelenyi
It is now almost universally accepted that the dust over the lunar surface is a component of a plasma-dust system. The first lunar dust observations were made during the Surveyor and Apollo missions. The analysis of the data obtained by the Surveyor landers led to a conclusion that the dust particles with a diameter of about 5 μm might levitate at a height of about 10 cm above the lunar surface. Some features of dusty plasma system over the Moon are clear. There are unsolved problems concerning its parameters and manifes-tations. In particular, significant uncertainty exists as *to the physical mechanism through which dust particles are released from the surface of the Moon*. Adhesion has been identified as a significant force in the dust particle launching process which should be considered to understand particle launching methods. The problem of the dust particle release from the lunar surface can be solved, for example, by considering meteoroid impacts onto the surface of the Moon. THE FORCE OF ADHESION: The effect of surface roughness results in significant attenuation of the effect of adhesion in comparison with the results. Indeed, the calculation of the force of adhesion between a plane with an asperity of the radius r and a spherical particle of radius a gives.

$$F_{\mathrm{adh}} = \frac{AS^2}{24\Omega^2}\left(\frac{ra}{r+a} + \frac{a}{1 + rS^2/(2\Omega))^2}\right); \quad (1)$$

Where A is the Hamaker's constant, S is the surface cleanliness, and □ = 0.132 nm characterizes the diameter of oxygen ion. The Hamaker's constant characterizes the force which arises due to the Londonder Waals attraction between two spheres and is estimated usually within the range of 10-21 J to 10-18 J, depending on the chemical and mineral compositions. For the lunar regolith, the Hamaker's constant is 4.3·10-20 J. Surface cleanliness varies in the range of 1 to 0 and is calculated for the lunar dayside. Calculations based on Eq. (1) show that the effect of roughness results in two-three orders of magnitude attenuation of the effect of adhesion in com-parison with the case of a smooth particle (see Fig. 3. 30) dated as S = 0.88 .

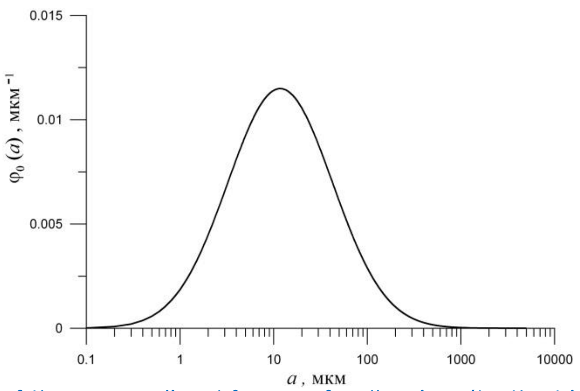

Fig. 3. 30. Dependence of the normalized force of adhesion (to that in the absence of asperity) on asperity size r for the particles with the sizes of 100 nm, 1 μm, and 10 μm under the conditions of the dusty plasma system at the lunar surface.

DUST PARTICLE RELEASE: When a high-speed meteoroid impacts the lunar surface, the substances of the impactor and the target are strongly compressed and heated. As a result of the action of high pressure, strong shock wave is formed. The shock propagates and weakens while moving away from the impact epicenter. Finally, the weakening shock transforms into the linear acoustic wave. The zones (around the impact epicenter) of evaporation of the substance, its melting, destruction of particles constituting lunar regolith, their irreversible deformations are formed due to the propagation of the weakening wave. Beyond the zone of irreversible deformations, the zone of elastic deformation is created which is characterized by the magnitudes of the pressure in the acoustic wave less than dynamic limit of elasticity. Considering the balance between the maximum force of pressure in the blast wave and the sum of the adhesive, electrostatic, and gravitational forces we determine the radius of the zone around the impact epicentre which restricts the region where dust particles are released from the surface of the Moon due to meteoroid impacts. Furthermore, we estimate the speeds of the released particles, find their size-distribution (Fig. 3. 31), and evaluate maximum heights of dust particle rise.

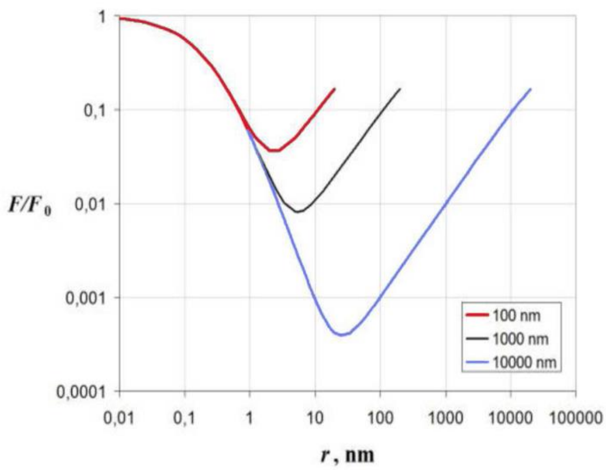

Fig. 3. 31. The size-distribution function of particles released from the lunar surface due to meteoroid impacts.

The normalized distribution function shown in Fig. 3. 31 is valid for various altitudes and indicates the presence of microparticles over the surface of the Moon. This fact distinguishes particles rising over the surface of the Moon owing to impacts of meteoroids from particles usually considered when describing the plasmasystem in which nanoparticles and submicroparticles levitate over the Moon. The consideration of only the processes typical of a dusty plasma (excluding strong perturbations such as impacts of meteoroids) allows for the explanation of the presence of microparticles (with sizes of 2—μm) only over the region of the lunar terminator. In all other cases, the sizes of levitating dust particles are no more than several hundred nanometers.
To summarize, it has been shown that impacts of meteoroids are important for the separation of dust particles from the surface of the Moon. When considering processes significant for the separation of dust particles, it is necessary to take

into account adhesion, whose effect is weakened if the roughness of the surface is taken into account. The number of collisions of meteoroids with unit area of the surface of the Moon per unit time has been determined and the ultimate tensile strength of lunar regolith owing to adhesion has been estimated. Processes occurring at the collision of a fast meteorite with the surface of the Moon have been described. The characteristic parameters of the material evaporation zone, material melting zone, destruction zone of lunar regolith particles, zone of irreversible deformations of particles, and zone of elastic deformations of the regolith material have been determined. It has been shown that most particles leaving the surface of the Moon owing to impacts of meteoroids originate from the zone of elastic deformations of the regolith material. The number of dust particles separated from a unit area of the surface of the Moon per unit time because of impacts of meteoroids has been calculated for various altitudes over the Moon. The size distribution function of these particles has been determined. It has been shown that impacts of meteo-roids constitute an important source of dust microparticles in the plasmasystem over the surface of the Moon.

AKR Cyclotron Maser Instability M. Marek, R. Schreiber

Our paper, titled, "Is the AKR Cyclotron Maser Instability a SelfCriticality System?" was presented at the 8th International Workshop on Planetary, Solar and Heliospheric Radio Emis-sions, and has been accepted for publication in a substantially extended form. The paper presents our analysis of auroral kilometric radiation (AKR) burst frequency as a function of intensity, using data gathered by the POLRAD experiment (part of the Interball-2 mission).

We repeated the analysis for 241 dynamic spectra (vs. 53 analysed in the first paper). This helped to find that it is much better to use Anderson—Darling statistical test, rather than the commonly used Kolmogorovmetric, for estima-ting the distance between the power-law model and our empirical data. The Andersontest produces compact scaling parameters (α), and reduces errors (σ) for single α values (Fig. 3. 32). We compared the fit of our data with three distribu-tions: power-law, exponential and log-normal. This found that the power-law distribution is a better fit than the exponential one; however, the results are inconclusive for the power-law vs. the log-normal distribution. It is possible that our data are not good enough to permit a detailed compa-rison in the latter case.

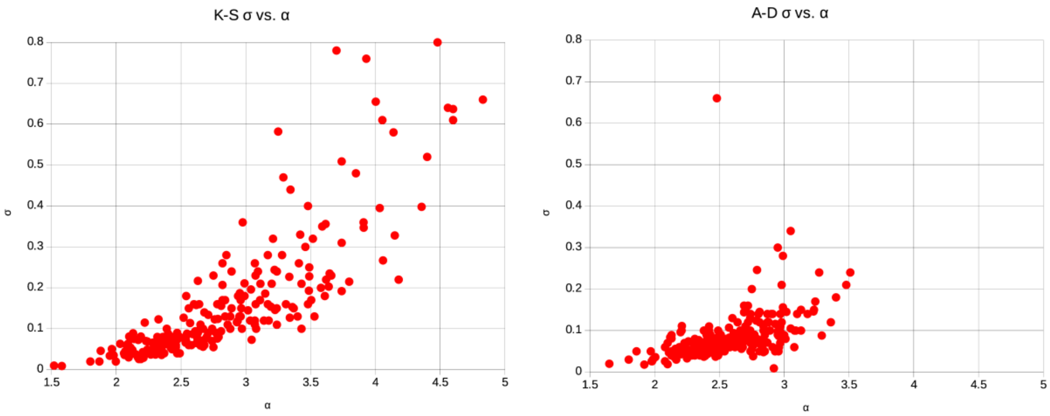

Fig. 3. 32. Scatter plot of σ vs. a values for the Kolmogorovmetric (left), and for the Andersonmetric (right).

A detailed analysis of AKR bursts based on very scarce AKR waveform data collected by the French experiment MEMO onboard the Interball-2 mission (F. Lefeuvre, M. Parrot) shows that, in a 6 ms POLRAD 'window' it is possible to see more than ten AKR bursts. Similar findings, based on a limited time resolution, have been reported for decimetric millisecond spikes in solar bursts (Aschwanden et al., 1998, Ning et al., 2007), and lead to overestimates of the scaling parameter. Based on our 241 dynamic spectra, we found about 80% of scaling parameters to be within the [2.0—.0] interval, with a mode of ~2.5 (Fig. 3. 33).

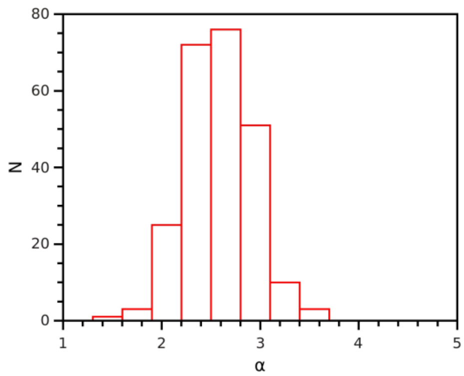

Fig. 3. 33. Histogram of the a scaling parameter based on the Andersonmetric.

Total Electron Content (TEC) and scintillation indices M. Grzesiak

Here we describe a novel, empirical technique for a regional, short-term (seconds to minutes) forecasting of Total Electron Content (TEC) and scintillation indices. The technique is designed to feed mitigation algorithms that aim to improve the accuracy of Global Navigation Satellite Systems positioning techniques under harsh ionospheric conditions. The method exploits a conservative form of the continuity equation, while scintillation forecasting uses the continuity equation with the source term added. The performance of the model has been found to be satisfactory when applied at the equatorial latitudes in Brazil, and post-sunset, when scintillation phenomena are more likely to occur. Model performance is based on an observation of five days affected by the amplitude scintillation, characterized by S4 > 0.7. Average forecasting accuracy, expressed as the standard deviation of the distribution of the difference between the forecast and actual values, is about one order of magnitude for TEC, S4 and σΦ, (amplitude and phase scintillation index, respectively).

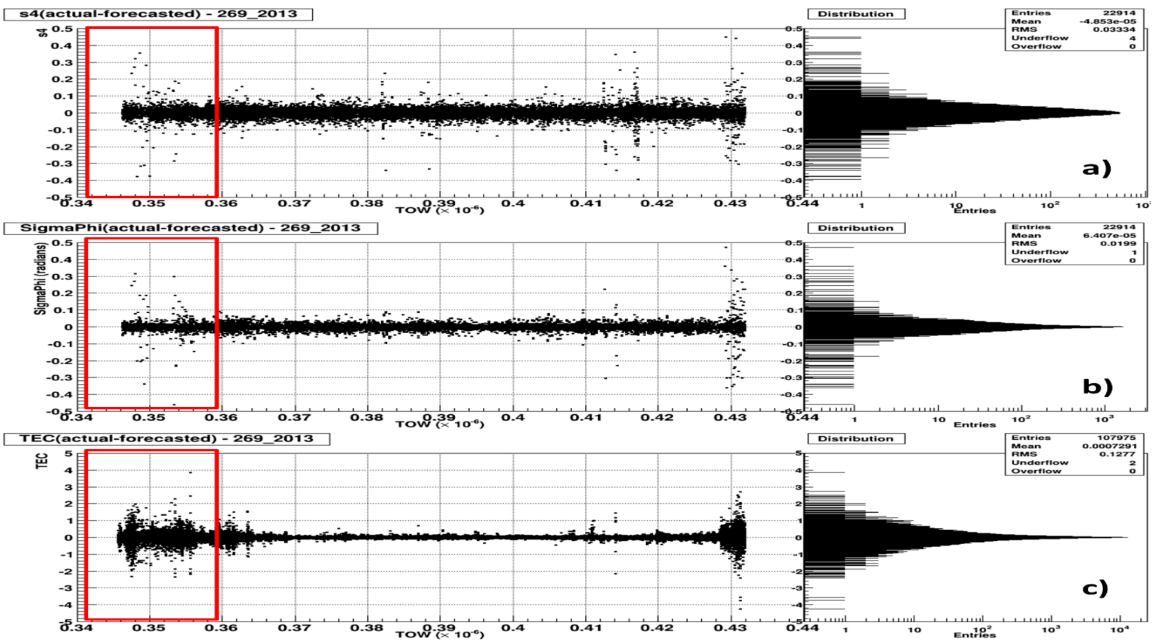

Fig. 3. 34. Time profiles (left plots) and corresponding logarithmic-scale distributions (right plots) of the difference between the actual and forecast values of S4 (a), σΦ (b) and TEC (c) for the day 26 September 2013 for each ionospheric pierce point over the state of São Paulo. The red box indicates the post-sunset hours.

3. SPACE PHYSICS

Global instantaneous ionospheric maps of foF2 critical frequency
O. Rynyshyna - Poliuga

Global instantaneous ionospheric maps of foF2 critical frequency GIM-foF2 and the ionospheric weather W(foF2) maps are produced with the PRIME Kriging technique with a resolution of 1 h, 5° and 2.5° in time, longitude and latitude, respectively, for 1998-2017. The results are obtained, for the first time, for the global super-storm which occurred in March, 1989 and demonstrate a new opportunity for the ionosphere investigations conducted in the past since the 19th solar cycle, at the time when ionosonde network was active but none navigational satellite data existed. The individual ITU-R (CCIR) predicted median foF2 map (left panel), PRIME-foF2 instant map (middle panel) and W(foF2) (right panel) index map are plotted in Figure 1 for the peak of the Dst super-storm (Dst = -589 nT) on 14 March, 1989, at 01:00 h UT. The dominant positive storm on March 14, 1989, at 01:00 h UT is observed (pW = 66%) in W(foF2) map as compared to the negative storm (nW = 12%) at this particular instant. The proposed technique for foF2 map adjustment to the climatological ITU-R predictions appears to be very promising for the investigation of the past ionosphere weather for a few decades of ionosonde observations when none GNSS monitoring of the ionosphere existed. Application of the PRIME-foF2 mapping and W (foF2) mapping to the severe storm of March, 1989, demonstrates that W index captures the increases and decreases in the peak electron density which could amount to 100% global occurrence during the severe space weather storm. A potential of application of the proposed approach appears to be promising because of significant improvements in modeling and forecasting the ionospheric weather.

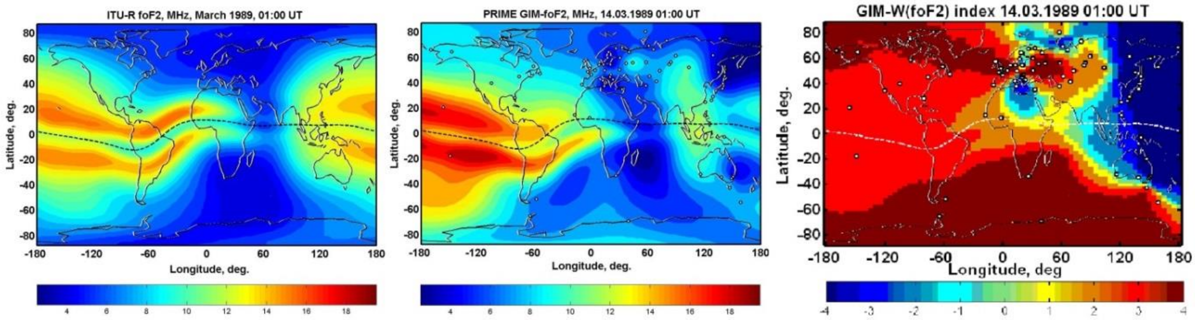

Fig. 3. 35. ITU-R (CCIR) prediction of reference quiet monthly foF2 map (left), instant PRIME GIM-foF2 map (middle) and W(foF2) map (right) at the peak of super-storm of 14 March 1989 at 01 h UT.

Disturbances of the ionosphere over thunderstorm areas observed by DEMETER and Swarm satellites J. Błęcki, J. Słomiński, R. Wronowski, E. Słomińska, A. Kułak, J. Młynarczyk, R. Haagmans

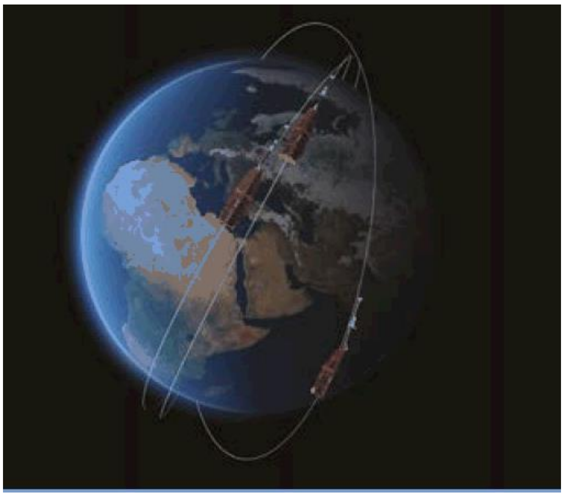

a)

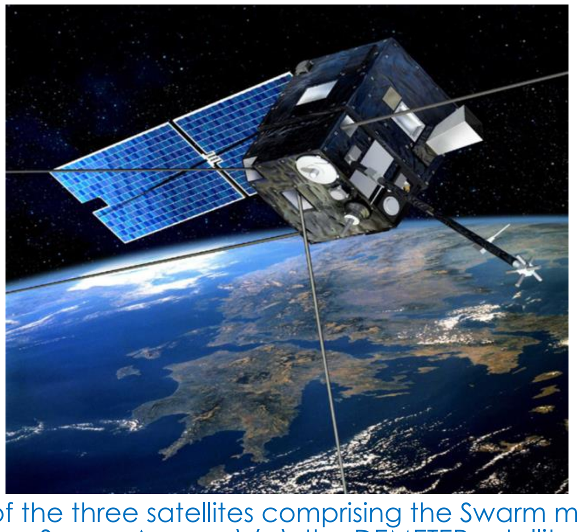

b)

Fig. 3. 36. Configuration of the three satellites comprising the Swarm mission (courtesy of the European Space Agency) (a); the DEMETER satellite (b).

The principal objective of these studies was to seek cross-correlation between data recorded by ground-based instruments and Swarm satellites relating to effects of thunderstorms and transient luminous events (TLE's). 430 very strong lightning discharges, having a charge moment of 1000 [Ckm] or larger, were identified as potential candidates for the cross-analysis. Data from Swarm included measurements of variations of the magnetic field, with sampling frequency 50Hz, and electron density and temperature as measured by the Langmuir probe, with 1Hz sampling. Figure 3. 37 shows disturbances of electron temperature and concentration, recorded during a Swarm Al-pha flight over an African thunderstorm centre. These disturbances were correlated with extremely low frequency (ELF) magnetic field variations.

Data from the DEMETER satellite were also used to study ionospheric disturbances over thunderstorm areas. Figure 3. 38 shows data gathered over a thunderstorm in Poland on 30 June 2009, during which very low frequency (VLF) emissions were recorded throughout the entire flight. The middle panel of Figure 3. 38 shows electron temperature, the bottom panel ion temperature; both were observed to increase during the VLF emissions.

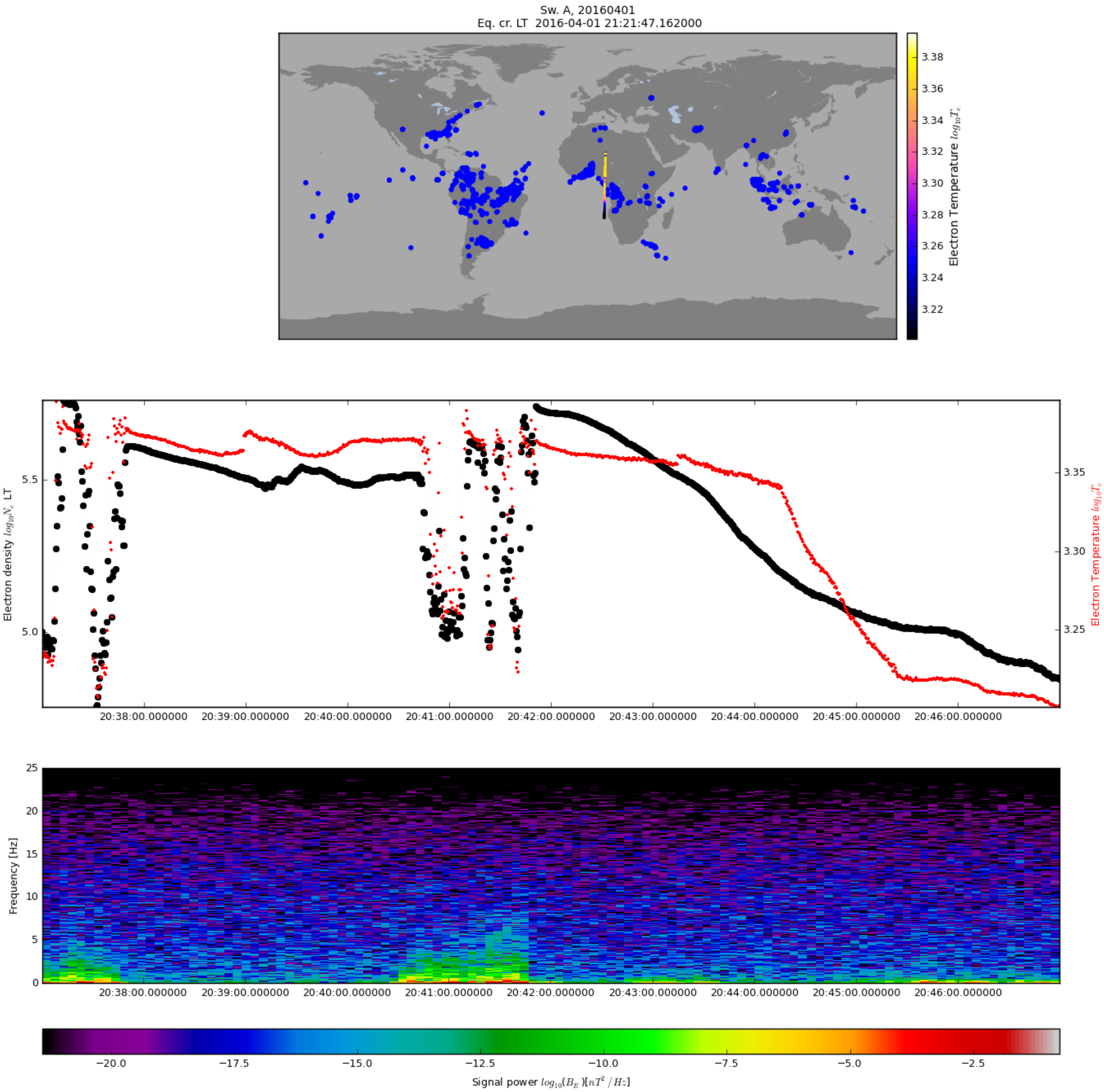

Fig. 3. 37. Swarm Alpha passing over a strong African lightning centre on 01-Apr-2016 20:37:54 - 20:46:12 UT. Upper panel: the part of the Swarm A orbit corresponding to the flight over the African thunderstorm zone. The colour of the dots on the orbit line corresponds to the intensity of magnetic field variations. Middle panel: variations in electron concentration (black line) and temperature (red line). Bottom panel: spectra of the δBE component of magnetic fluctuation.

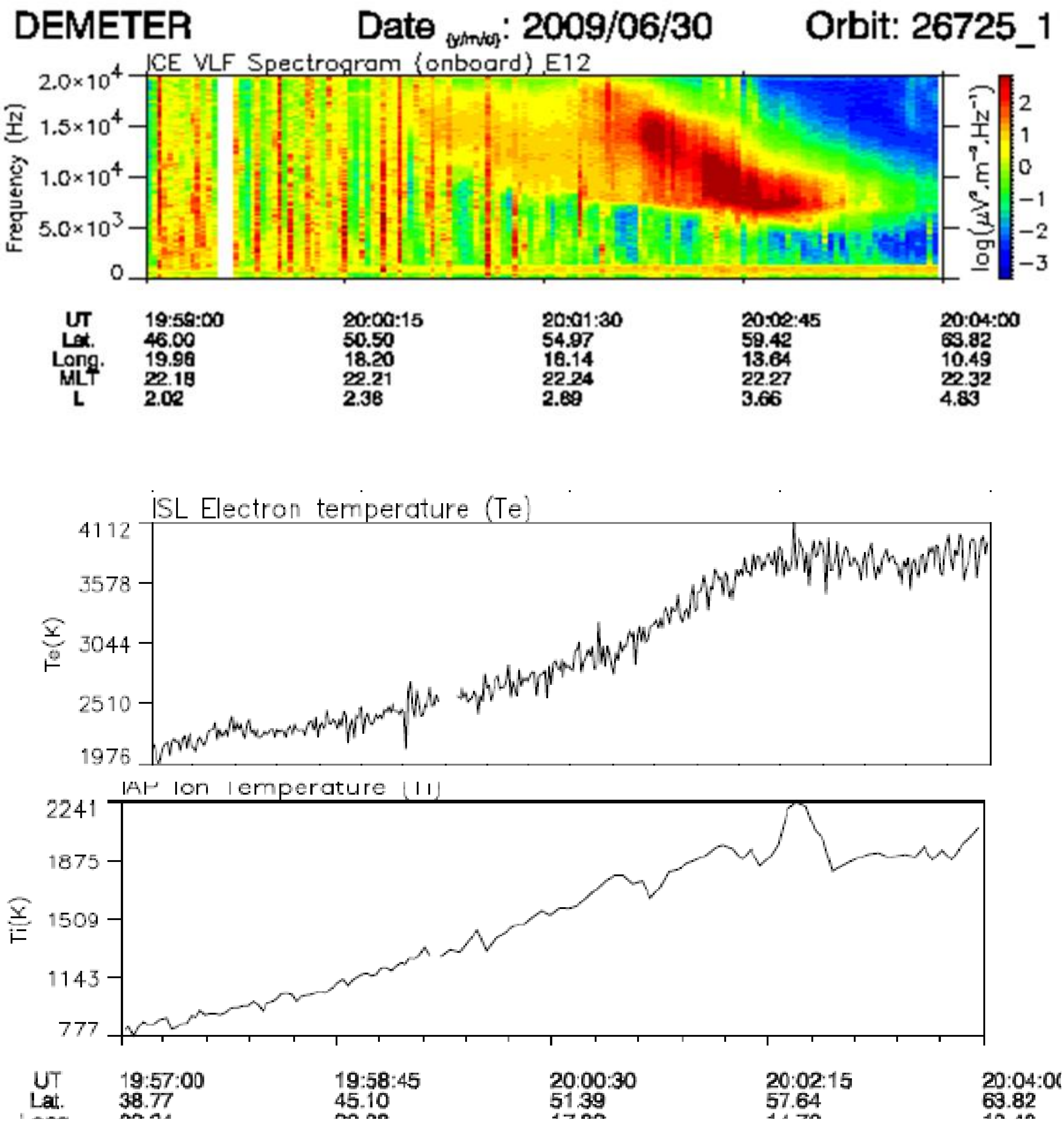

Fig. 3. 38. Recordings of VLF emissions (upper panel), electron temperature (middle panel) and ion temperature (bottom panel) during DEMETER's flight over a thunderstorm area in Poland on 30 June 2009.

Disturbances in the ionosphere above the Vrancea earthquake site observed by Swarm satellites J. Błęcki, J. Słomiński, T. Ernst, W. Jóźwiak, D. A. Stanica, D. Stanica

The relationship between pre-seismic geomagnetic signals and the M5.7 earthquake at Vrancea in September 2016 was explored. The normalised function Bzn was obtained from geomagnetic data recorded in the ultra-low frequency (ULF) range (0.001—.0083Hz), and statistical analyses were performed to identify, on the new Bzn* time series, a preseismic signature related to the M5.7earthquake. Significant anomalous behaviour of Bzn* was identified on September 21, three days prior to the onset of the seismic event. Similar information was provided by Swarm satellite recordings of variations in magnetic field and electron concentration in the ionosphere over the Vrancea zone, four days and one day before the earthquake. Figures 3. 40 and 3. 41 present registrations of ionospheric variation before the earth-quake, seen by the Swarm B satellite.

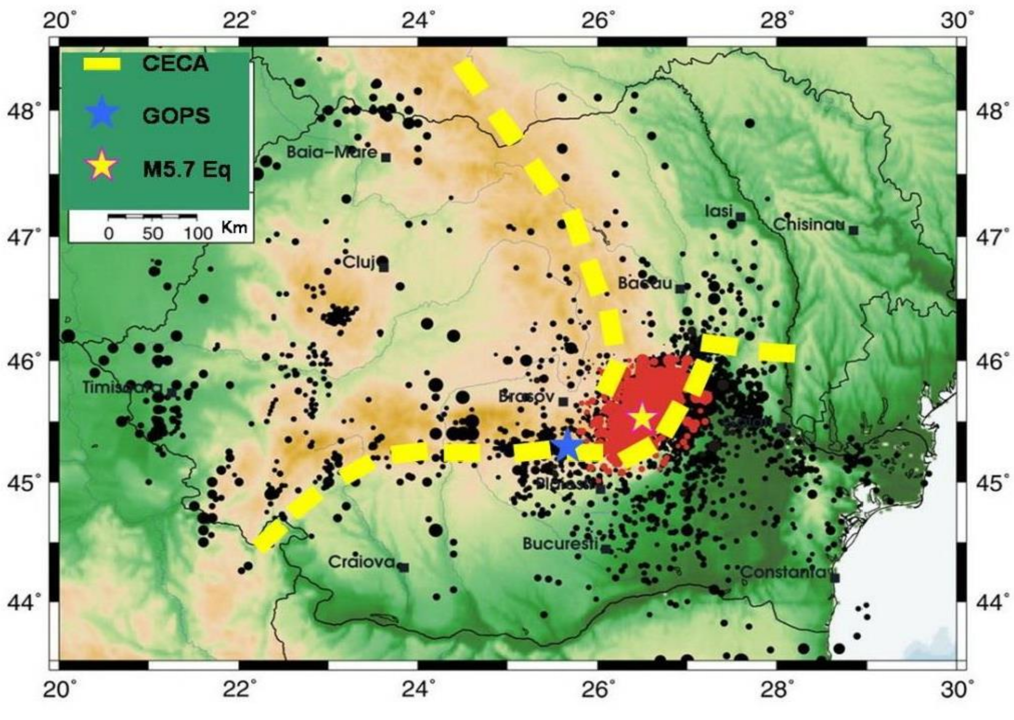

Fig. 3. 39 Map of crustal (black dots) and intermediate (red dots) earthquakes in the Vrancea zone. Yellow dashed line: Carpathian Electrical Conductivity Anomaly (CECA); yellow star: epicentre of the M5.7 earthquake; blue star: GOPS.

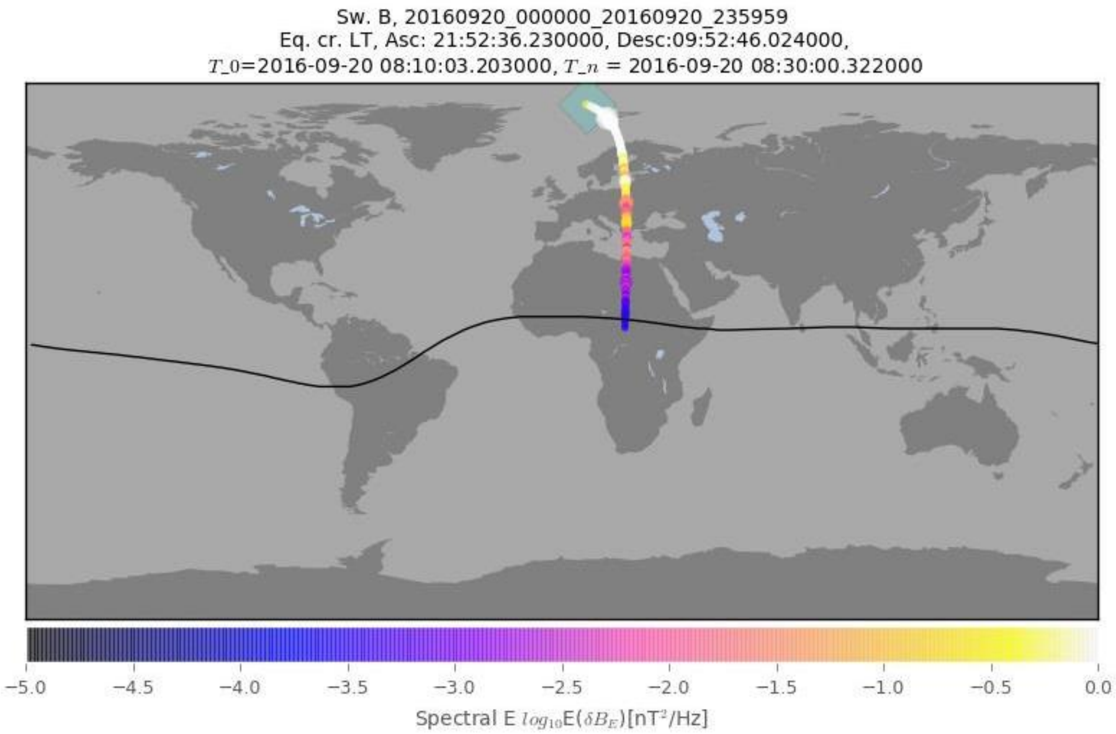

Fig. 3. 40. The section of the Swarm B orbit corresponding to the flight over the Vrancea earthquake zone on 20 September. The colour of the dots on the orbit line corresponds to the intensity of magnetic field variations.

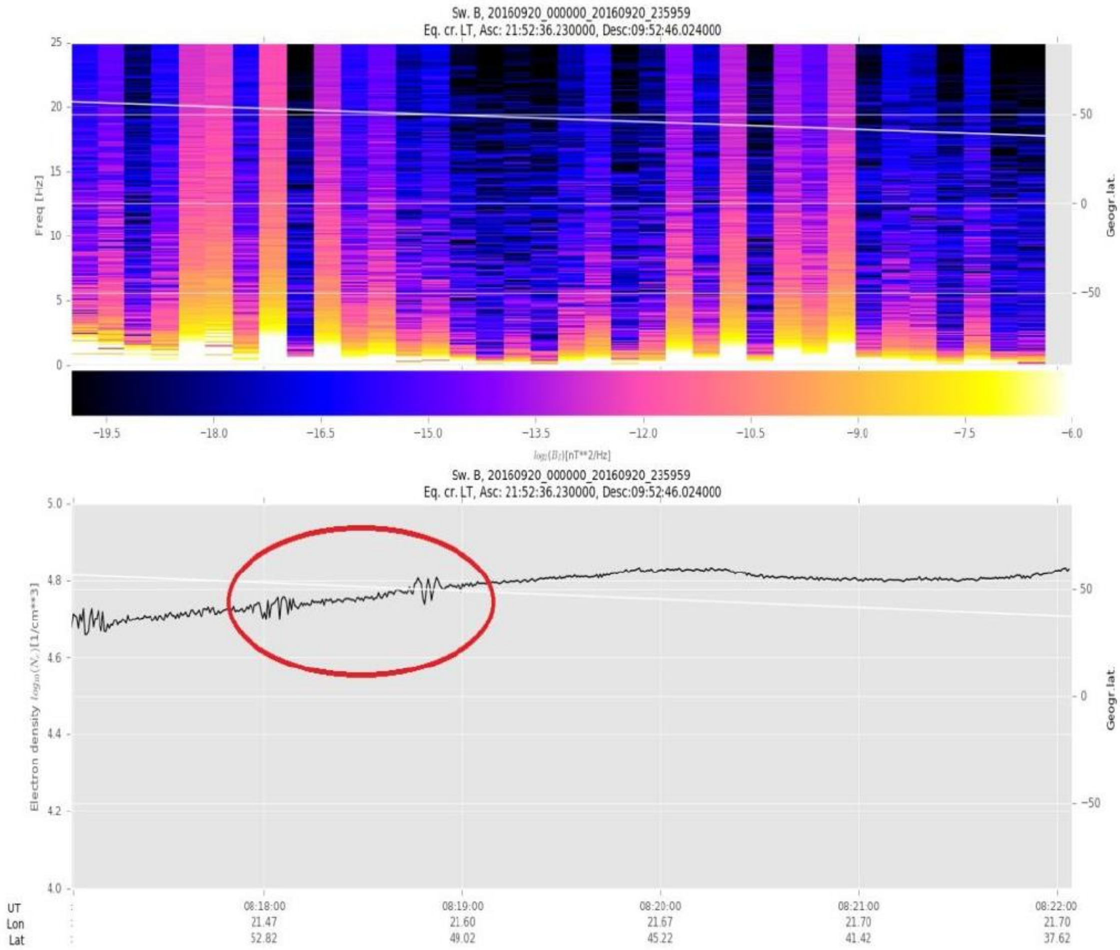

Fig. 3. 41. Spectra of magnetic field variations (upper panel) and electron concentration (lower panel) recorded by the Swarm B satellite in the vicinity of the Vrancea zone on 20 September.

Interaction of the energetic electron fluxes with the plasma in the polar cusp, ionosphere and with upper atmosphere J. Błęcki, J. Słomiński, R. Wronowski, R. Iwański and S. Savin

The satellite Magion 4sub-satellite of Interball 1 in the polar cuspsoccasionally registered extremely high intensity emissions around the electron cyclotron resonance frequency. These waves correlate with strong fluxes of highly energetic electrons that have been observed within the polar cusp by Interball

1 and Magion 4, as well as by Polar and CLUSTER satellites. Similar effects have been registered by the DEMETER satellite at ionospheric altitudes in the polar cusp, and also over thunderstorm regions. In both cases, fluxes of superthermal electrons are likely to be the source of the emissions. Registrations of the ELF/VLF waves and energetic electrons in the polar cusp, ionospheric trough and over thunderstorm areas were studied. Beam instability resulting from interaction of fluxes of electrons having energy up to 200keV with the ionosphere and upper atmosphere is discussed.

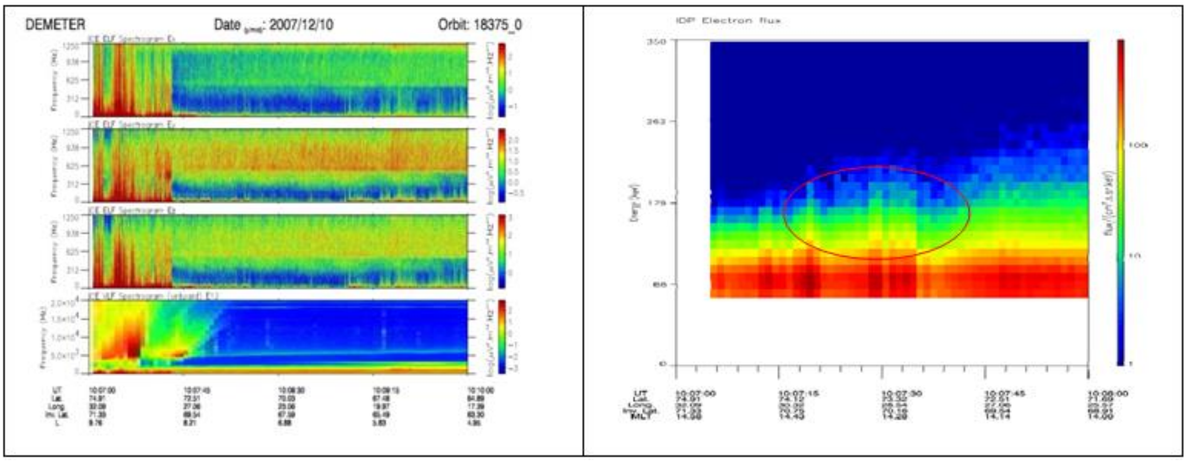

Fig. 3. 42. Up panel: Wave spectra of three components of the electric field in the ELF range and one component in the VLF range. Down panel: energetic electrons spectra recorded by DEMETER in the polar cusp at ionospheric altitude.

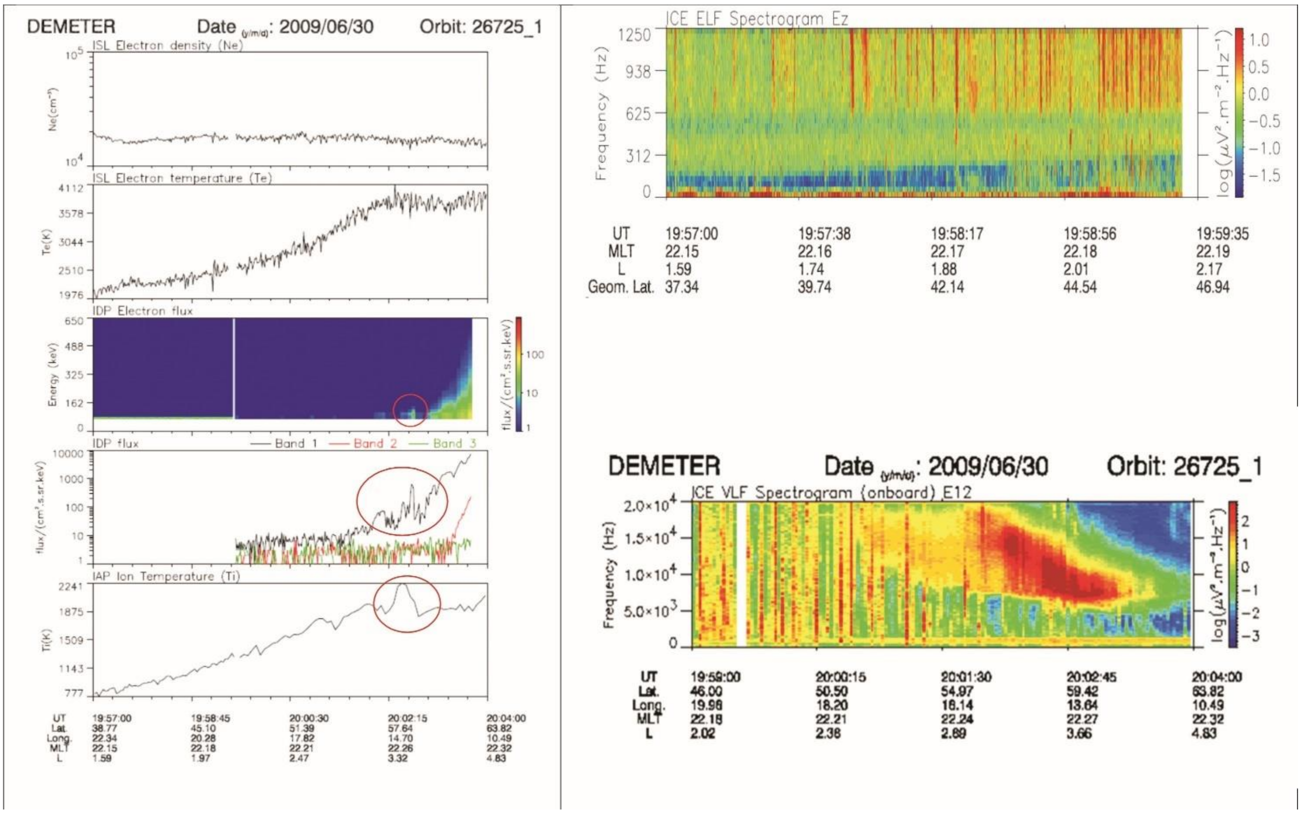

Fig. 3. 43. The presence of the energetic electron fluxes (fourth panel from the top) in the ionospheric trough is associated with strong ELF/VLF/HF emissions (bottom five panels).

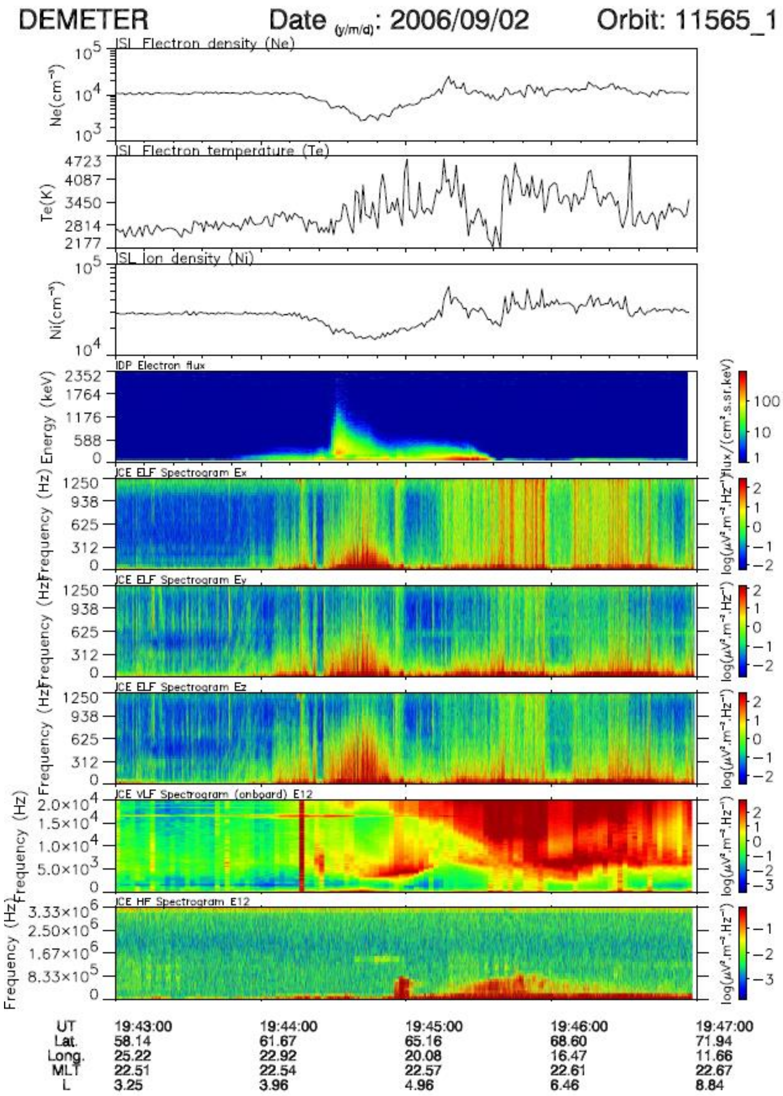

Fig. 3. 44. The registrations of ionospheric parameters (left side figure) from top to bottom- electron concentration and temperature, energetic electrons spectrogram, flux of the energetic electrons, ion temperature together with spectrograms of electric field variations (right side figure) in ELF (upper panel) and VLF (bottom panel) ranges during DEMETER's flight over thunderstorm area.

Observations of the geomagnetic storm on 27—May 2017 with LOFAR Pl610

H. Rothkaehl, M. Pożoga, B. Matyjasiak, R. Wronowski, D. Przepiórka,
K. Budzińska

On 23 May 2017 a coronal mass ejection took place, and it headed toward the Earth and encountered the Earth's magnetic field on 27 May, causing a strong geomagnetic storm of type G3 (Kp index reached the value of 7). A geomagnetic Dst index, during the main phase of the storm reached the value of −125 nT in the early hours of 28 May (about 08:00 UTC). The recovery phase lasted until 31 May. During the time period from 26 May to morning hours of 29 May the LOFAR station PL610 worked in a local mode which allowed for monitoring of signal scintillation caused by turbulent ionosphere.

The LOw Frequency ARray (LOFAR) is designed to study distant astrophysical radio sources, and operates at 10—MHz: this range is particularly suitable for studying the weak scintillation regimes that prevail in the midlatitude ionosphere.

Scintillation monitoring was performed on LBA antennas in the frequency range 5—MHz at a rate of 4 bits per sample. Measured amplitudes of signal from different frequency bands were used to calculate a ionospheric scintillation level. Signal with 1 second resolution is divided by median and then a standard deviation is computed. In Fig. 3. 45 the results are presented. An increase in the scintillation level, obviously correlated with the occurring geomagnetic storm, can be found in the picture. A sudden commencement occurred on 27 May at 15:36 and is marked in Fig. 17a) and 17b) by a vertical red line. From Cassiopea A observations we can identify an amplitude variations increase correlated with this particular event. Cygnus A was not observed due to too low elevation (below 30°). Another clearly visible signature of the storm is a scintillation peak associated with the minimum Dst value, marked by the vertical green line in Fig. 3. 45a. This can also be seen from Cygnus A observations (Fig. 3. 45b).

The analysis of signal scintillations from LOFAR single-station observations can be a complementary tool for monitoring ionosphere local properties. Based on the presented measurements we can conclude that, at times when the Earth's ionosphere is significantly disturbed, scintillations of signal amplitude can be measured. The low-frequency range of the instrument makes it possible to extend ionospheric scintillation studies to frequency bands and sizes of ionospheric irregularities that are not covered with other methods (e.g GPS).

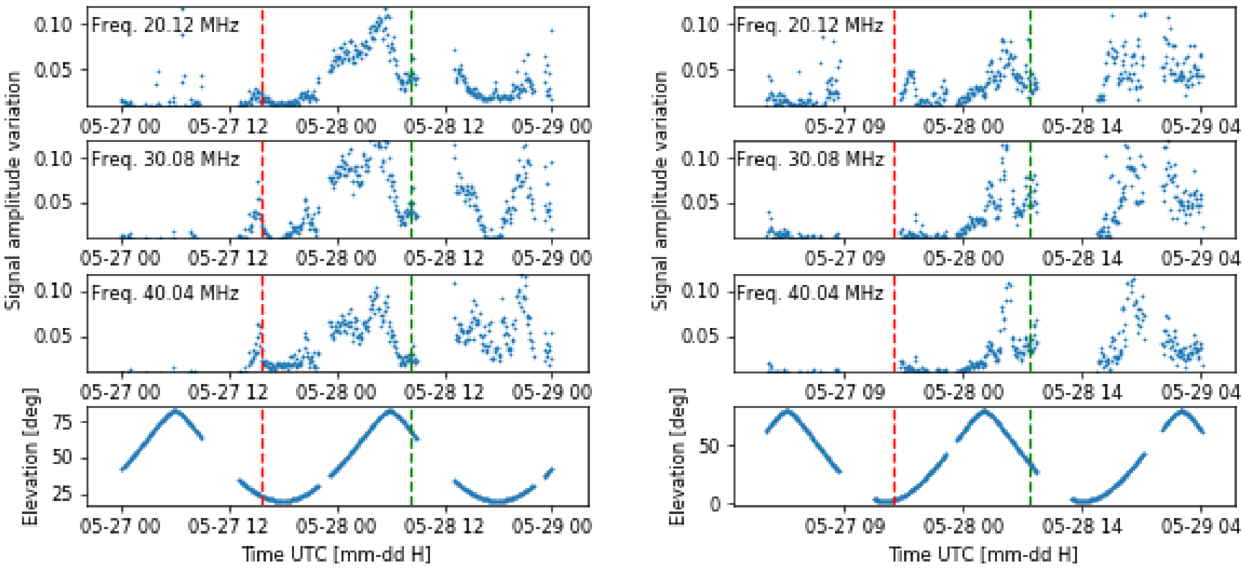

Fig. 3. 45: The signal amplitude variation calculated for 3 different frequencies (3 top panels) of the radio sources Cas A (a) and Cyg A (b) for a time period of 26—May 2017. Bottom panels show the elevation of observed radio sources.

Planetology and Solar System Dynamics

Comet 67P/Churyumov-Gerasimenko from Rosetta mission

Comet 67P outbursts and quiescent coma at 1.3 au from the Sun: dust properties from Ro-setta/VIRTIS-H observations D. Bockelee-Morvan, G. Rinaldi, S. Erard, C. Leyrat, F. Capaccioni, P. Drossart, G. Filacchione, A. Migliorini, E. Quirico, S. Mottola, G. Tozzi, G. Arnold, N. Biver, M. Combes, J. Crovisier, A. Longobardo, M. I. Błęcka, and M.-T. Capria
We present 2—μm spectroscopic observations of the dust coma of 67P/Chobtained with the VIRTIS-H instrument onboard Rosetta during two outbursts that occurred on 2015, 13 September 13.6 h UT and 14 September 18.8 h UT at 1.3 au from the Sun. Scattering and thermal properties measured before the outburst are in the mean of values measured for moderately active comets. The colour temperature excess (or superheat factor) can be attributed to submicrometre-sized particles composed of absorbing material or to porous fractal-like aggregates such as those collected by the Rosetta in situ dust

instruments. The power-law index of the dust size distribution is in the range 2—3. The sudden increase of infrared emission associated with the outbursts is correlated with a large increase of the colour temperature (from 300 to 630 K) and a change of the dust colour at 2—2.5 µm from red to blue colours, revealing the presence of very small grains (≤100 nm) in the outburst material. In addition, the measured large bolometric albedos (~0.7) indicate bright grains in the ejecta, which could either be silicatic grains, implying the thermal degradation of the carbonaceous material, or icy grains. The 3 µm absorption band from water ice is not detected in the spectra acquired during the outbursts, whereas signatures of organic compounds near 3.4 µm are observed in emission. The H2O 2.7 µm and CO2 4.3 µm vibrational bands do not show any enhancement during the outbursts.

Published in the *Monthly Notices of the Royal Astronomical Society* (August 2017). It was necessary to prepare an erratum for this paper (to be published in 2018)

Cosmochemical implications of CONSERT permittivity characterization

A. Herique, W. Kofman, P. Beck, L. Bonal, I. Buttarazzi, E. Heggy, J. Lasue, A. C. Levasseur-Regourd, E. Quirico, and S. Zine

Analysis of the propagation of the Comet Nucleus Sounding Experiment by Radiowave Transmission (CONSERT) signal throughout the small lobe of the 67P/CG nucleus has permitted us to deduce the real part of the permittivity, at a value of 1.27 ±0.05. The first interpretation of this value, using the dielectric properties of mixtures of ices (H_2O, CO_2), refractories (i.e. dust) and porosity, led to the conclusion that the comet porosity lies in the range 75—85 per cent. In addition, the dust-to-ice ratio was found to range between 0.4 and 2.6 and the permittivity of dust (including 30 per cent porosity) was determined to be lower than 2.9. This last value corresponds to a permittivity lower than 4 for a material without any porosity. This article is intended to refine the dust permittivity estimate by taking into account updated values of the nucleus densities and dust/ ice ratio and to provide further insights into the nature of the constituents of comet 67P/CG. We adopted a systematic approach: determination of the dust permittivity as a function of the volume fraction of ice, dust and vacuum (i.e. porosity) and comparison with the permittivity of meteoritic, mineral and organic materials from literature and laboratory measurements. Then different composition models of the nuclei corresponding to cosmochemical end

members of 67P/CG dust are tested. For each of these models, the location in the ice/dust/vacuum ternary diagram is calculated based on available dielectric measurements and confronted to the locus of 67P/CG. The number of compliant models is small and the cosmochemical implications of each of them is discussed, to conclude regarding a preferred model.
Published in the *Monthly Notices of the Royal Astronomical Society* (March 2017).

Laboratory spectral reflectance studies aimed at providing clues to composition of refractory phases of comet 67P/CG's nucleus L. V. Moroz, K. Markus, G. Arnold, D. Henkel, D. Kappel, U. Schade, M. Ciarniello, B. Rousseau, E. Quirico, B. Schmitt, F. Capaccioni, D. Bockelee-Morvan, G. Filacchione, S. Erard, C. Leyrat,

A. Longobardo, And The Virtis-Rosetta Team including M. I. Błęcka

We present 0.3—5 micron reflectance spectra of well-characterized powdered crystalline materials (Fe-sulfides, Mg-silicates), natural complex hydrocarbons and their mixtures that can serve as spectral analogues of comet 67P/CG's refractory phases. We study the ability of Fe-sulfides to suppress absorption bands of other cometary refractory components and to affect spectral slopes and reflectance values of the 67P/CG surface at different wavelengths from the near-UV to the IR. We investigate the evolution of organic absorption bands as a function of sulfide content in the mixtures and the possibility for detection of individual C-H stretching bands in reflectance spectra of 67P/CG. This study was reported during the conference —European Planetary Science Congress 2017 in Riga, Latvia (17—September 2017).

Published in *EPSC Abstracts* (September 2017).

Temporal evolution of comet 67P/Chury-umov-Gerasimenko's surface as observed by VIRTIS-M M. Ciarniello, G. Filacchione, F. Capaccioni, A. Raponi, M. C. De Sanctis, F. Tosi, M. T. Capria, M. Formisano, S. Erard, D. Bockelee-Morvan, C. Leyrat, G. Arnold, M. A. Barucci, E. Quirico, S. Fornasier, D. Kappel, A. Longobardo, B. Rousseau, S. Mottola, and the ViRTIS-Rosetta team including M. I. Błęcka
We report about the seasonal evolution of 67P/Ch-G's surface as inferred from VIRTIS-Rosetta measurements. We analyse observations performed from August

2014, when the comet was at a heliocentric distance of 3.5 AU along the inbound part of the orbit, up to the end of the Rosetta mission in September 2016, when 67P was at 3.8 AU outbound. This study was reported during the European Planetary Science Congress.
Published in *EPSC Abstracts* (September 2017).

The interior of 67P/C-G comet as seen by CONSERT bistatic radar on ROSETTA, key results and implications W. Kofman, A. Henrique, V. Ciarletti, J. Lasue, A. C. Levasseur-Regourd, S. Zine, and D. Plettemeier
The structure of the nucleus is one of the major unknowns in cometary science. The scientific objectives of the Comet Nucleus Sounding Experiment by Radiowave Transmission (CONSERT) aboard ESA's spacecraft Rosetta are to perform an interior characterization of comet 67P/Ch-G nucleus. This is done by means of a bistatic sounding between the lander Philae laying on the comet's surface and the orbiter Rosetta. Current interpretation of the CONSERT signals is consistent with a highly porous carbon rich primitive body. Internal inhomogeneities are not detected at the wavelength scale and are either smaller, or present a low dielectric contrast. Given the high bulk porosity of 75% inside the sounded part of the nucleus, a likely interior model would be obtained by a mixture, at this 3-m size scale, of voids (vacuum) and blobs with material made of ices and dust with porosity larger than 60%. The absence of any pulse spreading due to scattering allows us to exclude heterogeneity with higher contrast (0.25) and larger size (3m) (but smaller than few wavelengths scale, since larger scales would be responsible for multipath propagation). CONSERT is the first successful radar probe to study the sub-surface of a small body. Presented during the European Planetary Science Congress.
Published in *EPSC Abstracts* (September 2017)

Selected spectrometric studies M. I. Błęcka
During 2017 the spectrometric studies (modelling and interpretation of data) in the VIS to IR spec-tral range were continued. Almost all the works were still mostly concentrated on VIRTIS/ Rosetta. Influence of dust on radiance spectra of Comet 67P/C-G and presence of two kinds of ices (H_2O and CO_2) on the cometary surface were again examined but also the first trials of numerical modelling the spectrometric measurements of dark regions of Mercury were started (SYM-BIOSYS project for Bepi-Colombo mission Co-I).

3. SPACE PHYSICS

Imaging of the Rosetta target comet, 67P/ Ch-G H. Rickman together with the OSIRIS-Rosetta Team
Scientific results based on observations from OSIRIS camera on board Rosetta were published in 24 papers from 2017. Of these, 4 appeared in *Astronomy & Astrophysics*, 17 in *Monthly Notices of the Royal Astronomical Society*, and one each in the *Science, Nature Astronomy*, and *Planetary and Space Science*.

Internal structure of comets

Imaging the interior of a comet from bistatic microwave measurements: Case of a scale comet model C. Eyraud, A. Hrique, J.-M. Geffrin, W. Kofman
Imaging the internal structure of comets and asteroids is an important way to provide information about their formation process. In this paper, we investigate the possibility to image the interior of such structures with electromagnetic waves in the microwave domain (radar system) using an inverse algorithm adapted to take advantage of a bistatic configuration, considering the polarization effects, and which presents low memory requirement. To this end, a scale model of a comet/asteroid was built and was used for an experimental simulation. The scattered fields of this scale model were measured in a perfectly controlled environment, in an anechoic chamber, to avoid measurement disturbances and to focus this study only on which structural information can be obtained with such measurements. To profit from the spatial diversity of information, a vectorial-induced current reconstruction algorithm was used. Two configurations were tested and analyzed including one with very few measurements. From the qualitative reconstructed maps, we have shown that it is possible to detect the presence of a core in both cases.

Published in *Advances in Space Research* (October 2017)

Model of a cometary atmosphere

Two-dimensional molecular line transfer for a cometary coma S. Szutowicz
Cometary comae exhibit anisotropic density distribution of gas and dust. The main volatile constituent of cometary nucleus ices is water. In the proposed outgassing model, enhanced water emission is related to the discrete active area accompanied by a lower and more uniform emission from the rest nucleus surface. It is assumed an axisymmetric distribution of the gas density that depends on the distance to the nucleus, r, and the angular distance from the

outgassing axis. For radiative transfer calculations the cometary coma is discretized into cells according to spherical coordinate system (r, β) where β is the latitude. A model of excitation of the cometary water molecule includes collisional excitation and infrared pumping by solar radiation. The fractional populations of water rotational levels are derived as simultaneously solution of equations of statistical equilibrium and the equation of radiative transfer in the iterative process. Three methods for treating radiative transfer in the cometary coma are adopted: the Large Velocity Gradient (LVG), Accelerated Lambda Iteration (ALI) and Accelerated Monte Carlo (AMC). In the LVG method, the radiative transfer is solved locally, and in the ALI and AMC methods the radiative energy is transported from one region to the next. Both ALI and AMC methods are based on the Lambda Iteration scheme. In contrast with AMC method, in ALI the sampling of the radiation field is not random and is based on a fixed set of directions and frequencies. ALI and AMC agree very well but computational cost of the ALI code is much more lower than AMC. The results of simulations for two-dimensional density structures (e.g. the population distribution of water rotational levels as a function of distance to nucleus, synthetic line profiles —see Figure 46) were compared and presented during the European Planetary Science Congress.

Published in *EPSC Abstracts* (September 2017)

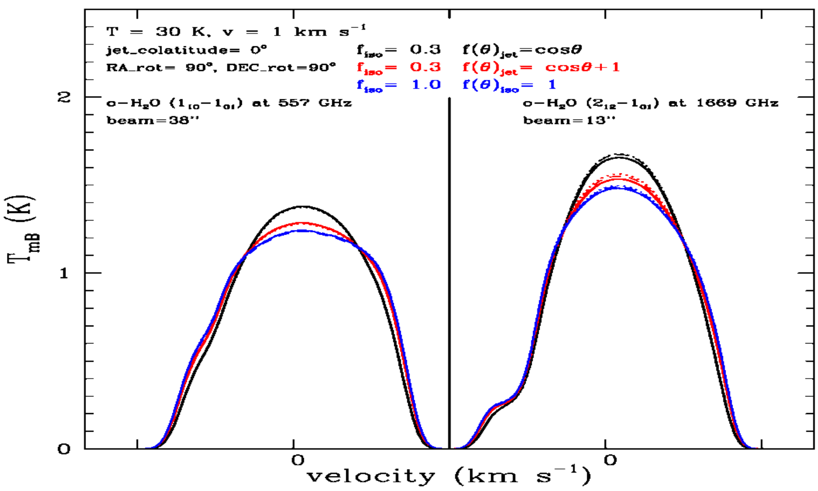

Fig. 3. 45. Synthetic line profiles for water transitions o-H2O at 557 GHz and o-H2O at 1669 GHz from ALI (solid), AMC (dashed) and LVG (dotted) method for axisymmetric and isotropic (blue) density distribution. Difference of average integrated line intensities between anisotropic and isotropic case is up to 7%. For the axisymmetric gas distribution two different form of the angular density function are employed (black and red curves).

3. SPACE PHYSICS

Oort Cloud Comets —Observations and Simulations

Oort spike comets with large perihelion distances M. Królikowska and P. A. Dybczyński
The complete sample of large-perihelion nearly-parabolic comets discovered during the period 1901—is studied starting from their orbit determination. Next, an orbital evolution that includes three perihelion passages (previous-observed-next) is investigated where a full model of Galactic perturbations and perturbations from passing stars have been incorporated.
We show that the distribution of planetary perturbations suffered by actual large-perihelion comets during their passage through the Solar system has a deep, unexpected minimum around zero which indicates a lack of "almost unperturbed" comets (see Annual Report 2016). By a series of simulations we show that this deep well is moderately resistant to some diffusion of orbital elements of analysed comets. It seems reasonable to state that the observed stream of these large-perihelion comets experienced a series of specific planetary configurations when passing through the planetary zone.
An analysis of the past dynamics of these comets clearly shows that dynamically new comets may appear only when their original semimajor axes are greater than 20 000 au. However, only for semi-major axes longer than 40 000 au dynamically old comets are completely not present. We demonstrated that the observed 1/aori-distribution exhibits a local minimum separating dynamically new from dynamically old comets, see Figure 3. 46. This figure suggests that the local minimum in the 1/aprev distribution might be explained with a more distant threshold value than this assumed in the paper, and corresponding to the outer planetary zone radius of 35 au.
Long-term dynamical studies reveal a large variety of orbital behaviour. Several interesting examples of action of passing stars are also described, in particular the impact of Gliese 710 which will pass close to the Sun in the future. However, none of the obtained stellar perturbations is sufficient to change the dynamical status of analysed comets.
Published in the *Monthly Notices of the Royal Astronomical Society* (December 2017), see also the Catalogue of near-parabolic comets at: ssdp.cbk. waw. pl/LPCs.

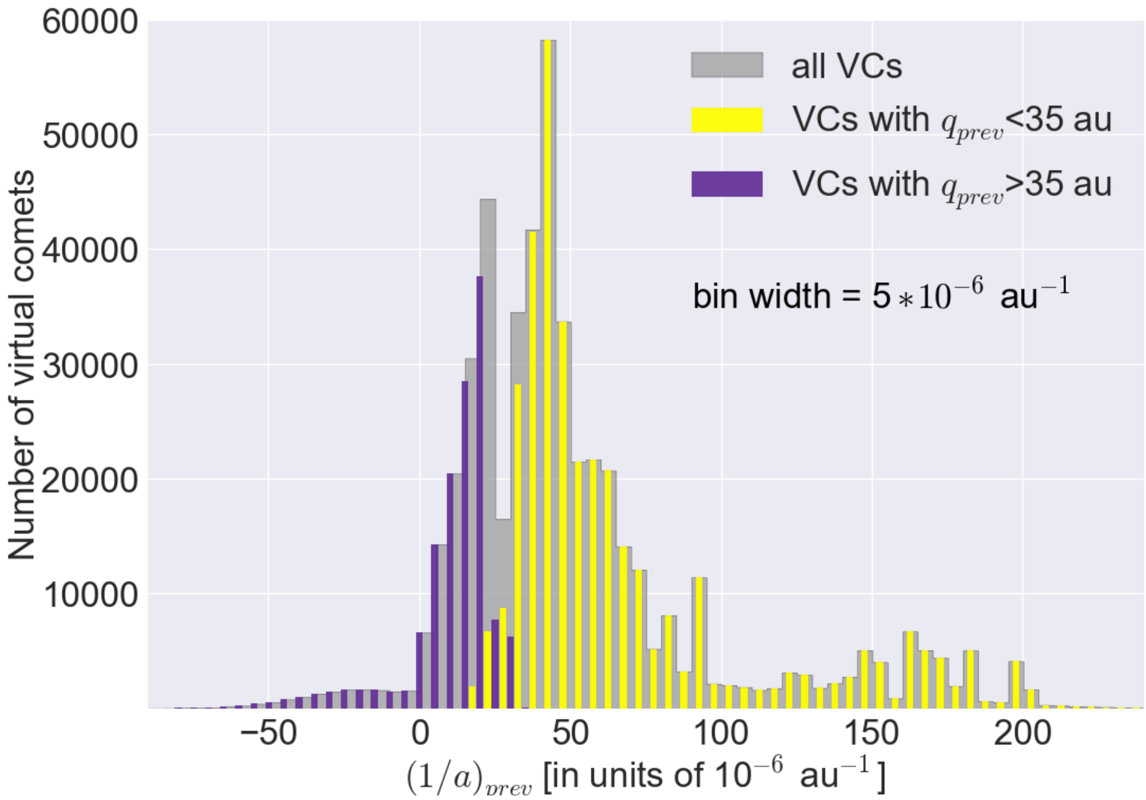

Fig. 3. 46. Distribution of dynamically new (violet histogram) and dynamically old (yellow histogram) of all VCs representing actual comets under consideration, where a value of 35 au was assumed for a previous perihelion border between dynamically old and dynamically new comets. The overall distribution of 1/aprev is shown by a grey histogram in all panels. Dividing numbers given in the vertical scale by 5001 we obtain numbers of comets in bins.

Catalogue of One-apparition Comets

New Catalogue of One-Apparition Comets discovered in the years 1901-1950. Part II: LPCs outside Oort spike M. Królikowska, S. Szutowicz, R. Gabryszewski, H. Rickman, K. Ziołkowski and E. M. Pittich

Marsden and Williams Catalogue of Cometary Orbits (2008, hereafter MWC08) listed 38 Oort spike comets recalculated by us in Part I of this Catalogue (Królikowska et al., 2014, see also the Catalogue of near-parabolic comets at: ssdp.cbk. waw.pl/LPCs), and 77 long period comets (LPCs, orbital periods greater than 200 yrs) including 34 parabolic comets (orbits are derived assuming e=1). This gives discovery rate of about 23 LPCs per decade in the first half of 20th century. At present, orbital recalculations of these 77 LPCs are performed for about 85% of them, where definitive orbits (e≠1) were obtained for 19 parabolic comets from MWC08, see Figure 3. 47.

The current state of this research was reported during the European Planetary Science Congress. Investigations will continue next year.

Published in *EPSC Abstracts* (September 2017).

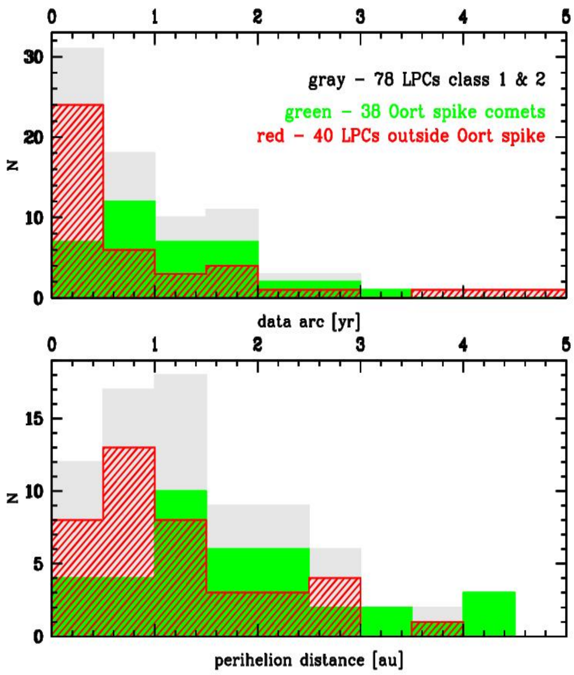

Fig. 3. 47. The analysed sample (red histograms) differs from the sample of Oort spike (green histogram). There are more LPCs of small perihelion distances (smaller than 1 au, lower panel) and short arcs of observations (less than 6 months, upper panel). Subsample of 34 parabolic comets in MWC08 (very short data arcs) and three more LPCs with recalculated orbits of poor quality (worse than 2; in MWC08 are eight such comets) are excluded in this figure.

Asteroids

Orbital bistatic radar observations of asteroid Vesta by the Dawn mission

E. M. Palmer, E. Heggy, W. Kofman

We present orbital bistatic radar observations of a small-body, acquired during occultation by the Dawn spacecraft at asteroid Vesta. The radar forward-scattering properties of different reflection sites are used to assess the textural properties of Vesta's surface at centimeter- todecimeter scales and are compared to subsurface hydrogen concentrations observed by Dawn's Gamma Ray and Neutron Detector to assess potential volatile occurrence in the surface and shallow subsurface. We observe significant differences in surface radar reflectivity, implying substantial spatial variations in centimeter-to-decimeter-scale surface roughness. Our results suggest that unlike the Moon, Vesta's surface roughness variations cannot be explained by cratering processes only. In particular, the occurrence of heightened hydrogen concentrations within large smoother terrains (over hundreds of square kilometers) suggests that potential ground-ice presence may have contributed to the formation of Vesta's current surface texture. Our observations are consistent with geomorphological evidence of transient water flow from Dawn Framing Camera images.

Published in *Nature Communications* (September 2017)

Direct Observations of Asteroid Interior and Regolith Structure: Science Measurement Requirements A. Herique, B. Agnus, E. Asphaug, A. Barucci, P. Beck, J. Bellerose, J. Biele, L. Bonal, P. Bousquet, L. Bruzzone, C. Buck, I. Carnelli, A. Cheng, V. Ciarletti, M. Delbo, J. Du, X. Du, C. Eyraud, W. Fa, J. Gil Fernandez, O. Gassot, R. Granados-Alfaro, S. F. Green, B. Grieger, J. T. Grundmann, J. Grygorczuk, R. Hahnel, E. Heggy, T-M. Ho, O. Karatekin, Y. Kasaba, T. Kobayashi, W. Kofman, C. Krause, A. Kumamoto, M. Küppers, M. Laabs, C. Lange, J. Lasue, A. C. Levasseur- Regourd, A. Mallet, P. Michel, S. Mottola, N. Murdoch, M. Mütze, J. Oberst, R. Orosei, D. Plettemeier, S. Rochat, R. RodriguezSuquet, Y. Rogez, P. Schaffer, C. Snodgrass, J- C. Souyris, M. Tokarz, S. Ulamec, J-E. Wahlund, and S. Zine

Our knowledge of the internal structure of asteroids is, so far, indirect —relying entirely on inferences from remote sensing observations of the surface, and theoretical modeling of formation and evolution. What are the bulk properties of the regolith and deep interior? And what are the physical processes that shape asteroid internal structures? Is the composition and size distribution observed on the surface representative of the bulk? These questions are crucial to understand small bodies' history from accretion in the early Solar System to the present, and direct measurements are needed to answer these questions for the benefit of science as well as for planetary defense or exploration.

3. SPACE PHYSICS

Radar is one of the main instruments capable of sounding asteroids to characterize internal structure from sub-meter to global scale. In this paper, we review the science case for direct observation of the deep internal structure and regolith of a rocky asteroid of kilometer size or smaller. We establish the requirements and model dielectric properties of asteroids to outline a possible instrument suite, and highlight the capabilities of radar instrumentation to achieve these observations. We then review the expected science return including secondary objectives contributing to the determination of the gravitational field, the shape model, and the dynamical state. This work is largely inherited from MarcoPolo-R and AIDA/AIM studies.

Published in *Advances in Space Research* (October 2017)

Interstellar intruder in the Solar System

On the dynamical history of the recently discovered interstellar object ’Oumuamua —where does it come from? P. A. Dybczyński and M. Królikowska

1I/2017 U1 ’Oumuamua is the first interstellar object recorded inside the Solar System. We try to answer the obtrusive question: where does it come from? To this aim we searched for proximities between ’Oumuamua and all nearby stars with known kinematic data during their past motion. We had checked over 200 thousand stars and found just a handful of candidates. If we limit our investigation to within a 60 pc sphere surrounding the Sun, then the most probable candidate for the ’Oumuamua parent stellar habitat is the star UCAC4 535-065571. However, this goes without ruling out GJ 876, as it is also a favorable candidate. Additionally, the origin of ’Oumuamua from a much more distant source is still an open question. An important conclusion is also that the quality of the original orbit of ’Oumuamua is accurate enough for such a study and that none of the checked stars had perturbed its motion significantly.

An article describing these findings was submitted for publication in *Astronomy & Astrophysics Letters*.

Mars

The WISDOM Radar: Unveiling the Subsur-face Beneath the ExoMars Rover and Iden-tifying the Best Locations for Drilling V. Ciarletti, S. Clifford, D. Plettemeier, A. Le Gall, Y. Herv, S. Dorizon, C. Quantin-Nataf, W-S. Benedix, S. Schwenzer, E. ettinelli, E. Heggy, A. Herique, J-J. Berthelier, W. Kofman, J. L. Vago, S- E. Hamran, and the WISDOM Team

The search for evidence of past or present life on Mars is the principal objective of the 2020 ESA-Roscosmos ExoMars Rover mission. If such evidence is to be found anywhere, it will most likely be in the subsurface, where organic molecules are shielded from the destructive effects of ionizing radiation and atmospheric oxidants. For this reason, the ExoMars Rover mission has been optimized to investigate the subsurface to identify, understand, and sample those locations where conditions for the preservation of evidence of past life are most likely to be found. The Water Ice Subsurface Deposit Observation on Mars (WISDOM) ground-penetrating radar has been designed to provide information about the nature of the shallow subsurface over depth ranging from 3 to 10m (with a vertical resolution of up to 3 cm), depending on the dielectric properties of the regolith. This depth range is critical to understanding the geologic evolution stratigraphy and distribution and state of subsurface H_2O, which provide important clues in the search for life and the identification of optimal drilling sites for investigation and sampling by the Rover's 2-m drill. WISDOM will help ensure the safety and success of drilling operations by identification of potential hazards that might interfere with retrieval of subsurface samples.

Published in *Astrobiology* (July 2017)

Global permittivity mapping of the Martian surface from SHARAD L. Castaldo, D. Mège, J. Gurgurewicz, R. Orosei, G. Alberti

SHARAD is a subsurface sounding radar aboard NASA's Mars Reconnaissance Orbiter, capable of detecting dielectric discontinuities in the subsurface caused by compositional and/or structural changes. Echoes coming from the surface contain information on geometric properties at metre scale and on the permittivity of the upper layers of the Martian crust. A model has been developed to estimate the effect of surface roughness on echo power, depending on statistical parameters such as RMS height and topothesy. Such model is based on the assumption that topography can be characterized as a self-affine fractal, and its use allows the estimation of the dielectric properties of the first few metres of the Martian soil. A permittivity map of the surface of Mars is obtained, covering several large regions across the planet surface. The most significant correspondence with geology is observed at the dichotomy boundary (Figure 3. 48), with high dielectric constant on the highlands side (7 to over 10) and lower on the lowlands side (3 to 7). Other geological correlations are discussed.

Published in *Earth and Planetary Science Letters* (January 2017).

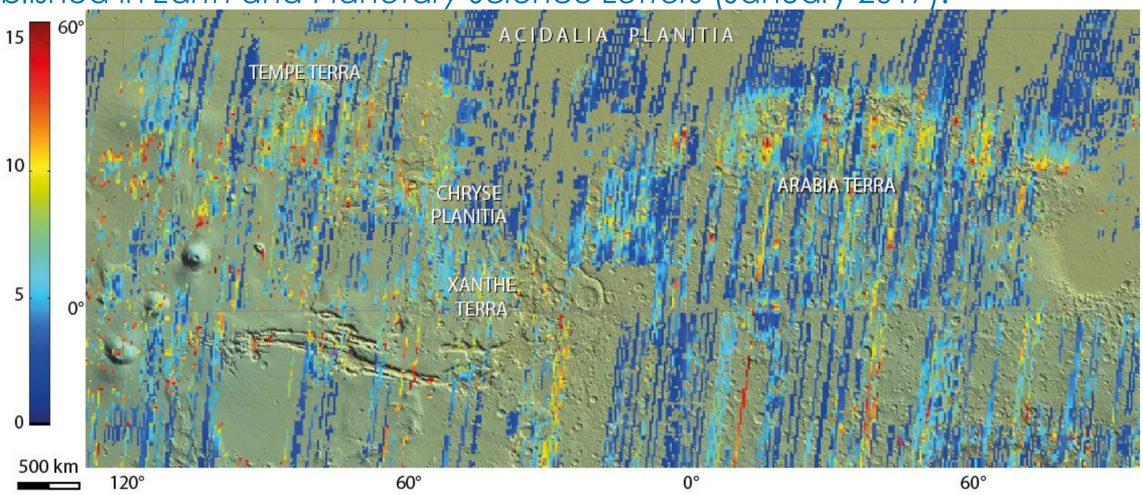

Fig. 3. 48. SHARAD permittivity in the dichotomy boundary area between Tempe Terra and Arabia Terra. The dichotomy boundary is underlined by a moderately high (~6) permittivity strip bordering the highlands (Tempe Terra, Xanthe Terra, Arabia Terra) and lowlands (Chryse Planitia, Acidalia Planitia), of higher and lower permittivity, respectively. The geographic scale is for equatorial regions.

Geomorphology of Ius Chasma, Valles Marineris, Mars K. Dębniak, D. Mege, J. Gurgurewicz

Cartographic products of the Martian trough system, Valles Marineris, are useful to identify the diversity and complexity of geological activity that has occurred there. A huge fraction of the processes that have shaped the surface of Mars are also concentrated there. A geomorphological map of Ius Chasma in western Valles Marineris is presented. The map is published in three sheets at 1:260000. It was drawn on the basis of 100 Mars Reconnaissance Orbiter's

Context Camera images of 12 m/pixel resolution, mosaiced using the USGS ISIS Planetary Image Processing Software, and subsequently mapped and interpreted for geomorphology in ArcGIS. The map displays 52 main geomorphological units of which some are further subdivided. They include both well-established features (e.g. spur-and-gully morphology on trough walls, landslide scars, and deposits), and newly reported landforms (e.g. alluvial fans with dendritic channels, moraines in western Ius Chasma). The proposed classifications of land-slide deposits, glacial landforms, and floor areas are more detailed than on any previous map of Valles Marineris. The Ius Chasma map is the first cartographic product presenting a full inventory of dune fields, impact craters, light-toned out-crops, and mass-wasting features.

Published in *Journal of Maps* (March 2017).

Global Martian volcanism as a new interpretation of geological past of terrestrial bodies and moons in the Solar System N. Zalewska

Many papers and articles have been telling us for years about the (Late) Heavy Bombardment of Earthtype planets including our Moon. Numerous craters on these planets are considered traces of collisions with smaller celestial bodies. This theory has been around for years, since the exploration of space began. Besides, Jupiter's moons have such traces and even characteristic crater chains interpreted exclusively as traces of serial impacts of asteroids after fragmentation above the surface. But when we look at the volcanic cones and the various other volcanic forms on Earth, we also notice that craters, especially those that are inactive for millions of years, are strikingly similar to the conically formed domes and caldera craters on Mars and terrestrial planets, additionally including moons of Jupiter and moons of other large planets as well as our Moon.

The primary basaltic volcanism of hundreds of millions of years ago could produce very broad calderas because of very low viscosity (low Si content of ultramafic rocks: <5% assuming ~ 100 µm grains) which bottom part collapsed in time after cooling, creating something that resembles a crater. Also, the center of volcanic crater, which stagnated last and after solidification formed a cone, which could have been interpreted as the central peak of the impact crater. Ring material from the caldera, instead of being interpreted as the edges of lava flows, is interpreted as ejectamaterial thrown during the impact. Forms that we can compare them to on Earth are, for example: Lake Myvatn with its pseudocraters located in volcanic active part of Iceland, underwater volcanoes in Hudson Bay, Pinacate Peaks in Mexico (Fig. 3. 49a, c), Atlantic volcanism, Aleutian maars (large calderas), Hawaiian volcanoes, Pacific plate volcanoes in San Francisco and Crater Lake in Oregon. Volcanic forms we can observe are: pseudocraters, scoria cones, maars, tuyas, guyots and lava domes. Many of these form under ice cover or at the bottom of the ocean. Similar forms are recognizable on Mars especially on its northern hemisphere. Isidis Planitia (Fig. 3. 49b), Acidalia Planitia, Utopia Planitia and Ama-zonis Planitia (Fig. 3. 49d) are densely dotted with cones and calderas. Latest study of LCP/HCP (low and high calcium pyroxene) from dust-free Mars sites show a relatively recent volcanism on Mars.

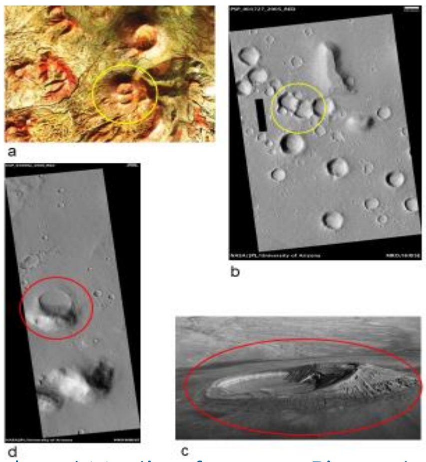

Fig. 3. 49. Comparison of terrestrial and Martian forms. a. Pinacate Mexico, image 2x2 km. The beginning of eruption 4 million years ago. Characteristic double caldera is in the center of the image (yellow circle). 31.756338 N, 113.496827 W. b. HiRISE, PSP 001727_2005, Lat: 20.5 Long: 94.8°. Northern part of Isidis. Characteristic double calderas are in the center of the image. (yellow circle). Calderas in the form of a maars on Isidis are probably not the result of an impact but of extensive volcanism. c. Cerro Colorado volcano Pinacate Crater in Mexico- irregular caldera, diameter 975 m, 31.916360 N, 113.299865 W. d. HiRISE, ESP 046992_1950, Lat: 15° Long: 192.1°, Amazonis Planitia. In the middle of the image an irregular caldera is visible. The calderas are covered with dust. Forms are probably of volcanic origin.

The difference between the impact crater and the volcanic crater on terrestrial bodies can be very difficult to recognize because of close similarity between them, especially in morphology as well as the geometric distortion of images made by spectrometers in the nadir. In this case, the geochemistry and the degree of melting or lack there at the moment of impact must be taken into account. Whether krystobalite, trydymite, stiszovite, shocked varieties of quartz are found in the crater or not, will tell us which phenomenon occurred. This

would require precise on site research using rovers.
Published in *EPSC Abstracts* (September 2017).
This research is ongoing.

Modelling the transport of trace gases in the Martian atmosphere P. Wajer, P. P. Witek, M. Banaszkiewicz and W. Kofman
The European-Russian ExoMars Trace Gas Orbiter (TGO) is set to reach its scientific orbit in the middle of 2018 after the aerobraking campaign. The data returned by the probe will help to understand the origin and evolution of trace gases, especially methane (CH4), in the Martian atmosphere. To analyze the data sent back by the probe we have developed a model of the photochemistry in the atmosphere of Mars. The model follows a few dozen molecules that are present or expected to exist in the atmosphere due to a few hundred considered chemical and photochemical reactions. To properly take into account the radiation fluxes driving the photochemistry at different altitudes above the surface of Mars the model solves the radiative transfer problem. Radiative transfer model is an important part of the model of the Martian atmospheric chemistry. Photolysis rates J(λ) depend on the availability of high-energy radiation at the given level of the atmosphere. We used two-stream approximation to calculate the actinic fluxes in a given wavelength range. The fluxes are calculated with the open source package DISORT (DIScrete Ordinate Radiative Transfer). Optical depths of atmospheric layers due to absorption and scattering are calculated from the optical properties of main atmospheric gases and the properties of Martian dust. The abundant and optically active gases we consider are: CO_2, Ar, N_2, O_2, CO, and H_2O. The optical properties of dust were calculated from Mie theory, with the assumption of log-normal grain size distribution, using Bohren and Huffman's numerical model. The database of photochemical reactions in the atmosphere was expan-ded with quantum yields of considered reactions. We are studying the feasibility of adding hetero-geneous chemistry to our model (i.e. reactions on the surfaces of dust grains and ice clouds).
To verify our numerical modelling we plan to use images obtained from stereoscopic camera CaSSIS, that should give us the mineralogical description of the surface from where the methane originates, and another instruments onboard the TGO orbiter.
Published in *EPSC Abstracts* (September 2017). This research is ongoing.

3. SPACE PHYSICS

Mars and other Solar System bodies

Planetary geology: Endogenic processes E. Hauber, D. Mege, T. Platz, P. Brož

Endogenic processes in geology are a function of a body's internal geodynamic activity. They comprise volcanic, tectonic, and isostatic processes, which shaped the surfaces of all terrestrial planets, the Moon, and basically all other Solar System bodies with solid surfaces that have been observed in some detail. The most recent spacecraft observations have confirmed this notion, and revealed past or present endogenic activity even on bodies where this was not previously expected. The study of endogenic processes and their resulting landforms and landscapes puts important constraints on the internal evolution and the surface history of a geologic body.

As most investigations of planetary endogenic processes are necessarily limited to the analysis of remote sensing data acquired by fly-by or orbital missions, this chapter focusses on larger-scale surface features, typically ranging in size from a few meters to thousands of kilometres (Figure 3. 50). Although rovers and landers can study much smaller features, they are few in numbers and are typically very restricted in their operational range. Whereas their main science goals are typically not oriented towards studying structural geology, they did provide invaluable information on the magmatic evolution of their target bodies. Another important source of information, specifically on the petrology of magmatic rocks, comes from meteorites (e.g., from Mars or asteroids). All such studies need to be complemented by modelling to arrive at a physical understanding of the driving forces and mechanisms.

The study of endogenic processes addresses some of the most fundamental questions in planetary geology, including the bulk composition, the history of accretion and differentiation, the heat generation and transport, and the evolution of planetary atmospheres (via outgassing) and climates (via large-scale tectonic surface changes, e.g., mountain building). As igneous intrusive and extrusive magmatic processes operated or still operate on all terrestrial planets, possibly on larger asteroids or their parent bodies, and on some satellites in the outer Solar System, and tectonic processes left their traces on all observed objects, this chapter necessarily needs to limit its scope to a few major aspects. Here we concentrate on endogenic processes on the terrestrial planets, the Moon, and Io. After a short review of the driving for-ces, we first describe for both tectonism and volcanism main geodynamic settings on the different planets, followed by an overview on the relevant processes. We then present the inventory of respective landforms and techniques for their analysis. Published in Rossi, A. P., and van Gasselt, S. (eds) *Planetary Geology* (November 2017).

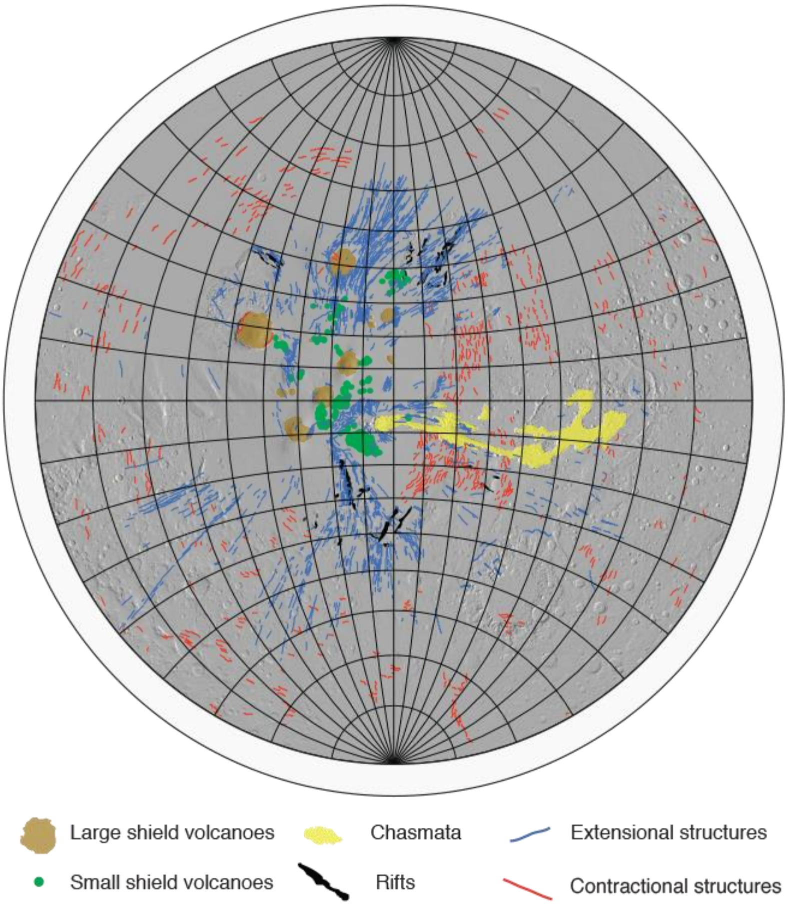

Fig. 3. 50. Tectonic sketch map of Tharsis, the largest volcanic province in theSolar System. The huge topographic bulge dominates the western equatorial hemisphere of Mars. It is characterized by very large shield volcanoes (brownish colours) and hundreds of smaller volcanic vents (lowshield clusters are shown in green), several sets of long and narrow grabens (thin blue lines) that radiate outwards from several centres, and a concentric set of wrinkle ridges (thin red lines). Volcanic loading of the lithosphere is likely responsible for the concentric tensional stress and the radial compressive stress. A few large and complex extensional features (in black) are comparable to terrestrial continental rifts. The 4000 km-long trough system of Valles Marineris (yellow) is controlled by Tharsis-radial trends and was probably formed by a combination of extension and collapse.

3. SPACE PHYSICS

Space Astronomy

Interpretation of the Herschel data: Otsuka, M.; Ueta, T.; van Hoof, P.A.M.; Sahai, R.; Aleman, I.; Zijlstra, A.A.; Chu, Y-H; Villaver, E.; Leal-Ferreira, M.L.; Kastner, J.; Szczerba, R.; Exter, K.M.

We perform a comprehensive analysis of the planetary nebula NGC 6781 to investigate the physical conditions of each of its ionized, atomic, and molecular gas and dust components and the object's evolution, based on panchromatic observational data ranging from UV to radio. Empirical nebular elemental abundances, compared with theoretical predictions via nucleosynthesis models of asymptotic giant branch (AGB) stars, indicate that the progenitor is a solar-metallicity, 2.25-3.0 M⊙ initial-mass star. We derive the best-fit distance of 0.46 kpc by fitting the stellar luminosity (as a function of the distance and effective temperature of the central star) with the adopted post-AGB evolutionary tracks. Our excitation energy diagram analysis indicates high-excitation temperatures in the photodissociation region (PDR) beyond the ionized part of the nebula, suggesting extra heating by shock interactions between the slow AGB wind and the fast PN wind. Through iterative fitting using the Cloudy code with empirically derived constraints, we find the best-fit dusty photoionization model of the object that would inclusively reproduce all of the adopted panchromatic observational data. The estimated total gas mass (0.41 M⊙) corresponds to the mass ejected during the last AGB thermal pulse event predicted for a 2.5 M⊙ initial-mass star. A significant fraction of the total mass (about 70%) is found to exist in the PDR, demonstrating the critical importance of the PDR in planetary nebulae that are generally recognized as the hallmark of ionized/H+ regions.

Herschel/HIFI observations of the circumstellar ammonia lines in IRC+10216 Schmidt, M.R.; He, J.H.; Szczerba, R.; Bujarrabal, V.; Alcolea, J.; Cernicharo, J.; Decin, L.; Justtanont, K.; Teyssier, D.; Menten, K.M.; Neufeld, D.A.; Olofsson, H.; Planesas, P.; Marston, A. P.; Sobolev, A.M.; de Koter, A.; Schöier, F. L.

A discrepancy exists between the abundance of ammonia (NH3) derived previously for the circumstellar envelope of IRC+10216 from far-IR submillimeter rotational lines and that inferred from radio inversion or mid-infrared (MIR) absorption transitions. To address this discrepancy, new high-resolution far-infrared observations of both ortho- and para-NH_3 transitions toward IRC+10216 were obtained with Herschel, with the goal of determining the ammonia abundance and constraining the distribution of NH_3 in the envelope of IRC+10216. For this purpose, we used the Heterodyne Instrument for the Far Infrared (HIFI) on board Herschel to observe all rotational transitions up to the J = 3 level (three ortho- and six para- NH_3 lines). We conducted non-LTE multilevel radiative transfer modelling, including the effects of near-infrared (NIR) radiative pumping through vibrational transitions. The computed emission line profiles are compared with the new HIFI data, the radio inversion transitions, and the MIR absorption lines in the v2 band taken from the literature. We found that NIR pumping is of key importance for understanding the excitation of rotational levels of NH_3. The derived NH_3 abundances relative to molecular hydrogen were $(2.8 \pm 0.5) \times 10^{-8}$ for ortho- NH_3 and for para- NH_3, consistent with an ortho/para ratio of 1. These values are in a rough agreement with abundances derived from the inversion transitions, as well as with the total abundance of NH_3 inferred from the MIR absorption lines. To explain the observed rotational transitions, ammonia must be formed near to the central star at a radius close to the end of the wind acceleration region, but no larger than about 20 stellar radii (1σ confidence level).

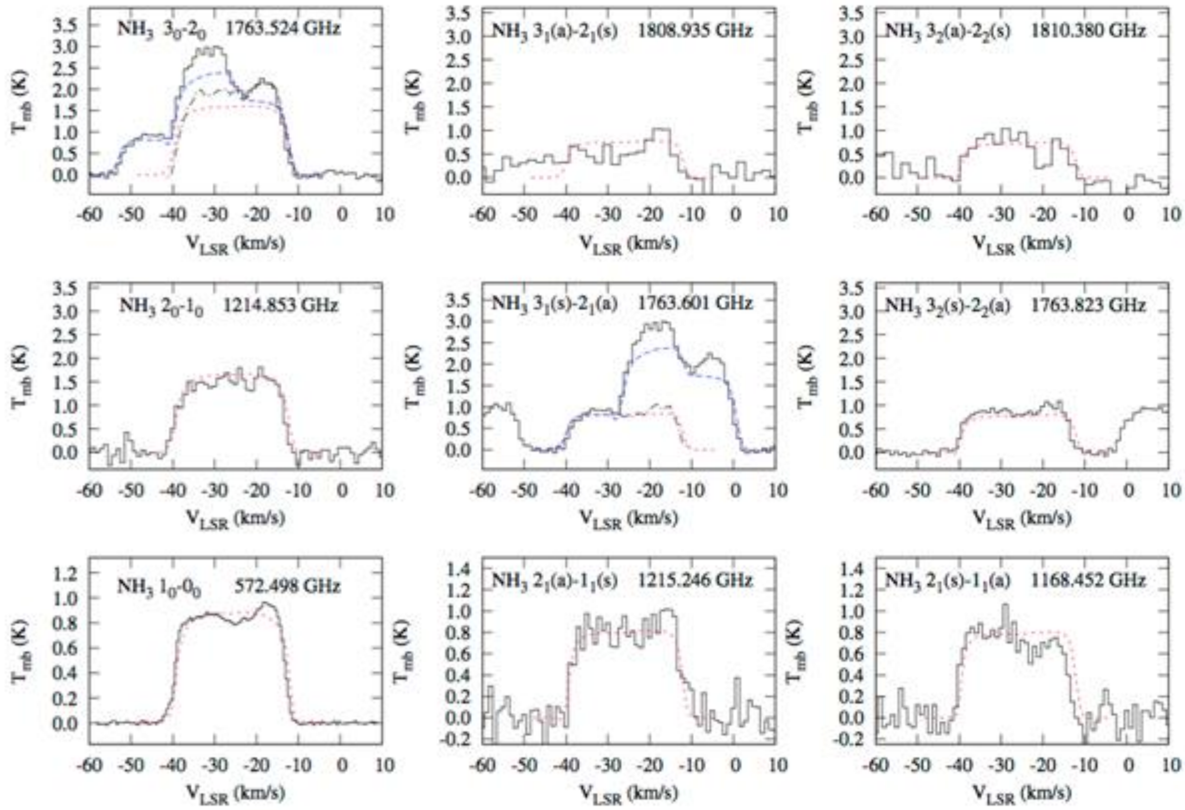

Fig. 3. 51. In the figure 3. 51, the HIFI observations of rotational transitions of ortho-NH3 (left column) and para-NH3 (middle and right columns) are shown by solid lines. Emission profiles are overplotted with theoretical profiles (red dashed lines) from our best fit models computed separately for each ammonia spin isomer. More details can be found in Schmidt et al. (2016).

Interpretation of the Spitzer data: Szczerba, R.; Yung, B.H.K.; Sewiło, M.; Siódmiak, N.; Karska, A,

In this short contribution we presented the results of our search for low- and intermediate mass evolved stars in the outer Galaxy using AllWISE catalogue photometry. We show that the Spitzer [3.4]-[12] vs. [4.6]-[22] colour-colour diagram is most suitable for separating C-rich/O-rich AGB and post-AGB star candidates. We are able to select 2,510 AGB and 24,821 post-AGB star candidates. However, the latter are severely mixed with the known young stellar objects in this diagram.

Comparison between 30 micron sources in different galaxies Gładkowski, M.; Szczerba, R.; Sloan, G. C.; Lagadec, E.; Volk, K.

We present an analysis and comparison of the 30 μm dust feature in the spectra of carbon-rich objects located in the Milky Way, Magellanic Clouds and the Sagittarius dwarf spheroidal galaxy. These spectra were collected by Spitzer Space Telescope. All of these galaxies are characterized by the different metallicities. Our analysis uses the "Manchester method" as a basis of estimating the temperature of dust for the carbon-rich stars and the planetary nebulae in our sample. We used a blackbody function with a single temperature deduced from the Manchester method to approximate the continuum under the 30 μm feature. Our study should allow us to better understand the mass loss process and thus late stages of stellar evolution of carbon-rich stars in these four galaxies.

Stellar evolution in the outer Galaxy Szczerba, R.; Siódmiak, N.; Leśniewska, A.; Karska, A.; Sewiło, M.

We investigated the distribution of different classes of spectroscopically identified sources and theoretical models in the color-color diagrams (CCDs) combining the near-infrared (NIR) and mid-infrared (MIR) data to develop a method to classify Outer Galaxy sources detected with the Spitzer Space Telescope (hereafter Spitzer) SMOG survey in the IRAC 3.6 - 8.0 μm and MIPS 24 μm bands. We supplement the Spitzer data with the data from other satellite and ground-based surveys. The main goal of our study is to discover and characterize the population of intermediate- and low-mass young stellar objects (YSOs) in the Outer Galaxy and use it to study star formation in a significantly different environment than the Galaxy inside the solar circle. Since the YSOs can be confused with evolved stars in the MIR, these classes of objects need to be carefully separated. Here we present the initial results of our analysis using the Ks-[8.0] vs. Ks-[24] CCD as an example.

Summary of activities on ATHENA mission -2016-2018

Since the beginning of 2014, when the first ATHENA kick-off meeting took place in MPE, Munich, I'm coordinating activities of Polish scientists and engineers in design and development four subsystems for ATHENA mission.

ATHENA is an Advance Telescope for High ENergy Astrophysics to explore Hot and Energetic Universe in X-ray band. ATHENA is a second "Large-class" mission selected by ESA in Cosmic Vision plan, with a launch foreseen in 2028.

3. SPACE PHYSICS

With the current technology, the best detection we achieve for photons from a narrow energy range from 0.1 to 10 keV - for those photons we can measure with the high accuracy the photon energy, direction and moment of their arrival. ATHENA telescope will be equipped with the most modern X-ray mirrors inclined in such a way that X-ray photons are grazing over their surface. ATHENA will have two focal plane detectors, which will be used alternatively depending on the observational plan. X-IFU (X-ray Integral Field Unit) is a very innovative detector, in which a single pixel measures extremely small temperature difference caused by X-ray photon that enters into it. The photon energy will be measured with the very high precision as never before. The second detector, WFI (Wide Field Imager) will be built with conventional silicon pixels, but with modern electronics ensures rapid signal readout. ATHENA will provide us an information about the dynamics and the distribution of hot matter in the Universe. Thanks to them we will understand how supermassive black holes (SMBH) grow and how hot gas stabilizes clusters of galaxies. X-rays with energies 0.1-9 keV interact with matter producing emission or absorption from ionized heavy elements. Observations of those lines allow us precisely examine heavy elements content and their chemical evolution of astrophysical objects. With ATHENA we will investigate process of matter falling onto supermassive black hole, in particular its relation with outflowing hot winds (galaxy feedback). Beside more distant objects, ATHENA will be suitable to search for objects from our Galaxy as, X-ray binary systems and their outflows, coronae of hot stars, and our Galactic Center.

PI if this project, dr. hab. Agata Różańska (CAMK PAN), who works on X-ray astronomy since many years. Her specialization is to search warm ionized outflows observed in active galactic nuclei (AGN). Furthermore, she works on X-ray image of Sgr A* in Galactic Center and hot atmospheres of accretion disks and neutron stars.

With the whole Polish ATHENA-PL consortium, we aim to design and manufacture of two mission components: Dewar Door (DD) and Power Distribution Unit (PDU) for X-IFU/ATHENA instrument. The X-IFU will be placed in dewar cylinder, for which door is needed to provide vacuum conditions. The dewar door will be open in space once a suitable out-gassing period will be completed. PDU will be used to distribute power into the given instrument components.Below the proposed DD conceptual model (closed & opened) designed by B. Kędziora from Astronika company who is involved in the project.

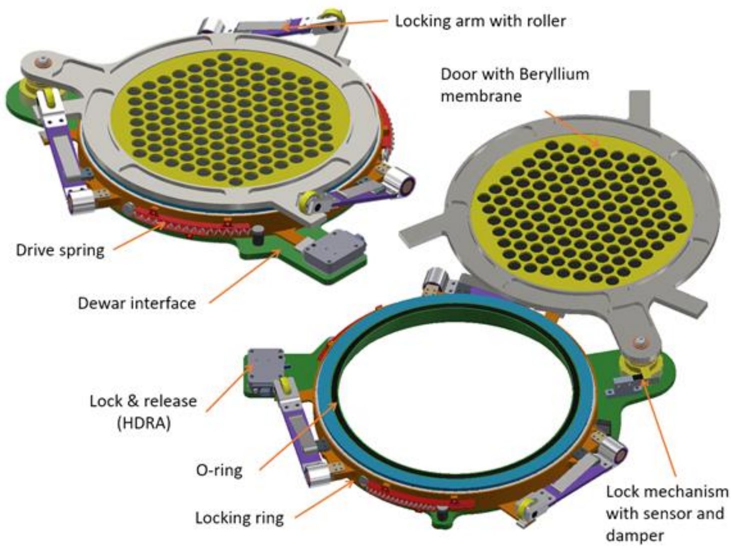

Fig. 3. 52 In addition, we aim to design and manufacture of two subsystems: Filter Wheel Assembly (FWA) and Power Distribution Unit (PDU) for WFI/ATHENA instrument. FWA is a subsystem which allows to change spectral filters and to use calibration source. We are responsible for deliver FWA with filter wheel controller. PDU will be used to distribute power into the given instrument components.Below the proposed scheme of filter wheel housing designed by dr hab. Mirosław Rataj from CBK PAN.

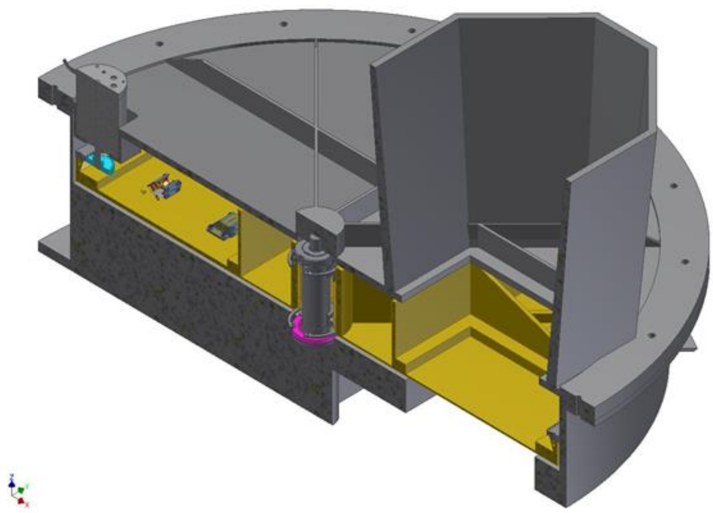

Fig. 3. 53 Currently we are opening the PRODEX founding for both instruments (WFI and X-IFU). We have already achieved Letter of Endorsement form Polish Delegate to start the project.

3. SPACE PHYSICS

Publications:

1. Abdellaoui, G., S. Abe, J. BŁĘCKI, P. ORLEAŃSKI, H. ROTHKAEHL, K. SŁOMIŃSKA and other 400 authors; *Cosmic ray oriented performance studies for the JEM-EUSO first level trigger*; Nuclear Instruments and Methods in Physics Research, Section A: Accelerators, Spectrometers, Detectors and Associated Equipment Volume 866, Pages 150-163, DOI: 10.1016/j.nima.2017.05.043, 2017
2. Abdellaoui, G., J. BŁĘCKI, P. ORLEAŃSKI, H. ROTHKAEHL, K. SŁOMIŃSKA and other 400 authors; *Meteor studies in the framework of the JEM-EUSO program*; Planetary and Space Science, Volume 143, Pages 245-255, DOI: 10.1016/j.pss.2016.12.001, 2017
3. Alfonsi, L., A. W. WERNIK, M. Materassi, L. Spogli; *Modelling ionospheric scintillation under the crest of the equatorial anomaly*; Advances in Space Research, DOI: 10.1016/j.asr.2017.05.021, 2017
4. Agarwal, J., M. F. A'Hearn, J.-B. Vincent, C. Gttler, S. Höfner, H. Sierks, C. Tubiana, C. Barbieri, P. L. Lamy, R. Rodrigo, D. Koschny, H. RICKMAN, M. A. Barucci, J.-L. Bertaux, I. Bertini, S. Boudreault, G. Cremonese, V. Da Deppo, B. Davidsson, S. Debei, M. De Cecco, J. Deller, S. Fornasier, M. Fulle, A. Gicquel, O. Groussin, P. J. Gutiérrez, M. Hofmann, S. F. Hviid, W.-H. Ip, L. Jorda, H. U. Keller, J. Knollenberg, J.-R. Kramm, E. Kührt, M. Küppers, L. M. Lara, M. Lazzarin, J. J. Lopez Moreno, F. Marzari, G. Naletto, N. Oklay, X. Shi, N. Thomas; Acceleration of individual, decimetre-sized aggregates in the lower coma of comet 67P/Churyumov-Gerasimenko; Monthly Notices of the Royal Astronomical Society, Volume 462, 2016, Pages S78-S88, DOI: 10.1093/mnras/ stw2179, 2016
5. Andr, N., M. Grande, N. Achilleos, M. Barthélémy, M. Bouchemit, K. Benson, P.-L. Blelly, E. Budnik, S. Caussarieu, B. Cecconi, T. Cook, V. Génot, P. Guio, A. Goutenoir, B. Grison, R. Hueso, M. Indurain, G. H. Jonesi, J. Lilensten, A. Marchaudon, D. Matthiä, A. Opitz, A. Rouillard, I. STANISŁAWSKA, J. Soucek, C. Tao, Ł. TOMASIK, J. Vaubaillon; *Virtual Planetary Space Weather Services offered by the Europlanet H2020 Research Infrastructure*; Planetary and Space Science, DOI: 10.1016/ j.pss.2017.04.020, 2017
6. Aok, S., Y. Sato, M. Giuranna, P. WOLKENBERG, T. M. Sato, H. Nakagawa, Y. Kasaba; *Mesospheric CO2 ice clouds on Mars observed by Planetary Fourier Spectrometer onboard Mars Express*; Icarus, Volume 302, Pages 175-190, DOI: 10.1016/j.icarus.2017.10.047, 2017
7. Argall Matthew, R., S. J. Hollick, Z. B. Pine, C. W. Smith, C. J. Joyce, P. A. Isenberg, B. J. Vasquez, N. A. Schwadron, J. M. SOKÓŁ, M. BZOWSKI, L. F. Burlaga; *Observation of Magnetic Waves Excited by Newborn Interstellar Pickup He+ Observed by the Voyager 2 Spacecraft at 30 au*; The Astrophysical Journal, Volume 849, Number 1, DOI: 10.3847/1538-4357/ aa8ee2, 2017
8. Auger, A.-T., O. Groussin, L. Jorda, M. R. El-Maarry, S. Bouley, A. Sjourné, R. Gaskell, C. Capanna, B. Davidsson, S. Marchi, S. Höfner, P. L. Lamy, H. Sierks, C. Barbieri, R. Rodrigo, D. Koschny, H. RICKMAN, H. U. Keller, J. Agarwal, M. F. A'Hearn, M. A. Barucci, J.-L. Bertaux, I. Bertini, G. Cremonese, V. Da Dep-po, S. Debei, M. De Cecco, S. Fornasier, M. Fulle, P. J. Gutiérrez, C. Güttler, S. Hviid, W.-H. Ip, J. Knollenberg, J.-R. Kramm, E. Kührt, M. Küppers, L. M. Lara, M. Lazzarin, J. J. Lopez Moreno, F. Marzari, M. Massironi, H. Michalik, G. Naletto, N. Oklay, A. Pommerol, L. Sabau, N. Thomas, C. Tubiana, J.-B. Vincent, K.-P. Wenzel; *Meter-*

scale thermal contraction crack polygons on the nucleus of comet 67P/Churyumov-Gerasimenko; Icarus Volume 301, February 2018, Pages 173-188, DOI: 10.1016/j.icarus.2017.09.037, 2017
9. Baranets, N., Yu. Ruzhin, V. Dokukin, M. Ciobanu, H. ROTHKAEHL, A. KIRAGA, J. Vojta, J. Šmilauerd, K. Kudela; *Injection of 40 kHz-modulated electron beam from the satellite: I. Beam-plasma interaction near the linear stability boundary*; Advances in Space Research, Volume 59, Issue 12, Pages 2951—2968, DOI: 10. 1016/j.asr.2017.03.030, 2017
10. Barret D. et al. (90 coauthors including Różańska A.), The Athena X-ray Integral Field Unit (X-IFU), 2016, Proceedings of the SPIE, Volume 9905, id. 99052F 41 pp.
11. Barta, V., C. Haldoupis, G. Stori, D. Buresova, J. Chum, M. POŻOGA, K. A. Bernyi, J. Bór, M. Popek, Á. Kis, P. Bencze; *Searching for effects caused by thunderstorms in midlatitude sporadic E layers*; Journal of Atmospheric and Solar-Terrestrial Physics, Volume 161, Pages 150-159, DOI: 10.1016/j.jastp.2017. 06.006, 2017
12. Bertini, I., F. La Forgia, C. Tubiana, C. Güttler, M. Fulle, F. Moreno, E. Frattin, G. Kovacs, M. Pajola, H. Sierks, C. Barbieri, P. Lamy, R. Rodrigo, D. Koschny, H. RICKMAN, H. U. Keller, J. Agarwal, M. F. A'Hearn, M. A. Barucci, J.-L. Bertaux, D. Bodewits, G. Cremonese, V. Da Deppo, B. Davidsson, S. Debei, M. De Cecco, E. Drolshagen, S. Ferrari, F. Ferri, S. Fornasier, A. Gicquel, O. Groussin, P. J. Gu-tierrez, P. H. Hasselmann, S. F. Hviid, W.-H. Ip, L. Jorda, J. Knollenberg, J. R. Kramm, E. Kührt, M. Küppers, L. M. Lara, M. Lazzarin, Z.-Y. Lin, J. J. Lopez Moreno, A. Lucchetti, F. Marzari, M. Massironi, S. Mottola, G. Naletto, N. Oklay, T. Ott, L. Penasa, N. Thomas, J.-B. Vincent; *The scattering phase function of comet 67P/Churyumov-Gerasimenko coma as seen from the Rosetta/OSIRIS instrument*; Monthly Notices of the Royal Astronomical Society Volume 469, 2017, Pages S404-S415; DOI: 10.1093/ mnras/stx1850, 2017
13. Blecki J., M. Parrot, J. Słomiński , M.Kościesza, R.Wronowski, S. Savin, Evolution of the ionospheric Plasma Turbulence over Seismic and Thunderstorm Areas, Journal of Environmental Science and Engineering A 6 (2016) 277-285, doi:10.17265/2162-5298/2016.06.001
14. Bockele-Morvan, D., G. Rinaldi, S. Erard, C. Leyrat, F. Capaccioni, P. Drossart G., Filacchione, A. Migliorini, E. Quirico, S. Mottola, G. Tozzi, G. Arnold, N. Biver, M. Combes, J. Crovisier, A. Longobardo, M. BŁĘCKA, M.-T. Capria; *Comet 67P outbursts and quiescent coma at 1.3 au from the Sun: dust properties from Rosetta/VIRTIS-H observations*; Monthly Notices of the Royal Astronomical Society, Volume 469, Issue Suppl_2, Pages S443—S458, doi: 10.1093/mnras/stx1950, 2017
15. Bogomolov, V. V., M. I. Panasyuk, S. I. Svertilov, V. Bogomolov, G. K. Garipov, A. F. Iyudin, P. A. Klimov, S. I. Klimov, T. M. Mishieva, P. Yu. Minaev, V. S. Morozenko, O. V. Morozov, A. S. Posanenko, A. V. Prokhorov, H. ROTHKAEHL; *Observation of Terrestrial gamma-ray flashes in the RELEC space experiment on the Vernov satellite*; Cosmic Research, Volume 55, Issue 3, pp 159—168, DOI:10.1134/S001095 2517030017, 2017
16. BZOWSKI, M., M. A. KUBIAK, A. CZECHOWSKI, J. GRYGORCZUK; *The Helium Warm Breeze in IBEX Observations As a Result of Charge-exchange Collisions in the Outer Heliosheath*; The Astrophysical Journal, Volume 845, Number 1; DOI: 10.3847/1538-4357/aa 7ed5, 2017

17. Castaldoa, L., D. MGE, J. GURGUREWICZ, R. Orosei, G. Alberti; *Global permittivity mapping of the Martian surface from SHARAD*; Earth and Planetary Science Letters, Volume 462, Pages 55—65, DOI: 10.1016./j.epsl.2017. 01.012, 2017
18. Ciarletti, V., A. Herique, J. Lasue, A.-C. Levasseur-Regourd, D. Plettemeier, F. Lemmonier, C. Guiffaut, P. Pasquero, W. KOFMAN; *CONSERT constrains the internal structure of 67P at a few-metre size scale*; Monthly Notices of the Royal Astronomical Society, stx3132, DOI: 10.1093/mnras/stx3132, 2017
19. Ciarletti, V., S. Clifford, D. Plettemeier, A. Le Gall, Y. Herve, S. Dorizon, C. Quantin-Nataf, W.-S. Benedix, S. Schwenzer, E. Pettinelli, E. Heggy, A. Herique, J.-J. Berthelier, W. KOF-MAN, J. L. Vago, S.-E. Hamran and the WIS-DOM team; *The WISDOM Radar: Unveiling the Subsurface Beneath the ExoMars Rover and Identifying the Best Locations for Drilling*; ASTROBIOLOGY, Volume 17, Numbers 6 and 7, DOI: 10.1089/ast.2016.1532, 2017
20. CZECHOWSKI, A., J. Kleimann; *Nanodust dynamics during a coronal mass ejection*; Annales Geophysicae, 35, 1033—, DOI: 10.5194/ angeo-35-1033-2017, 2017
21. CZECHOWSKI, A., J. GRYGORCZUK; Heliosphere in a strong interstellar magnetic field; Journal of Physics: Conference Series 900 (2017), 012004, DOI:10.1088/1742-6596/900/1/012004, 2017
22. de Angelis, A., V. Tatischeff, M. Tavani, U. Oberlack, I. Grenier, L. Hanlon, R. Walter, A. Argan, P. von Ballmoos, A. Bulgarelli, I. Donnarumma, M. Hernanz, I. Kuvvetli, M. Pearce, A. Zdziarski, A. Aboudan, M. Ajello, G. Ambrosi, D. Bernard, E. Bernardini, V. Bonvicini, A. Brogna, M. Branchesi, C. Budtz-Jorgensen, A. Bykov, R. Campana, M. Cardillo, P. Coppi, D. de Martino, R. Diehl, M. Doro, V. Fioretti, S. Funk, G. Ghisellini, E. Grove, C. Hamadache, D. Hartmann, M. Hayashida, J. Isern, G. Kanbach, J. Kiener, J. Knödlseder, C. La banti, P. Laurent, O. Limousin, F. Longo, K. Mannheim, M. Marisaldi, M. Martinez, M. N. Mazziotta, J. McEnery, S. Mereghetti, G. Minervini, A. Moiseev, A. Morselli, K. Nakazawa, P. ORLEAŃSKI, J. M. Paredes, B. Patricelli, J. Peyr, G. Piano, M. Pohl, H. Ramarijaona, R. Rando, I. Reichardt, M. Roncadelli, R. Silva, F. Tavecchio, D. J. Thompson, R. Turolla, A. Ulyanov, A. Vacchi, X. Wu, A. Zoglauer; *The e-ASTROGAM mission: Exploring the extreme Universe with gamma rays in the MeV —GeV range*; Experimental Astronomy, Pages 1-58, DOI: 10.1007/s10686-017-9533-6, 2017
23. Dębniak, K., D. MEGE, J. GURGUREWICZ; *Geomorphologic map of Ius Chasma, Valles Marineris, Mars*; Journal of Maps, Volume 13, Issue 2, Pages 260-269, DOI: 10.1080/1744 5647.2017.1296790, 2017
24. Drolshagen, E., T. Ott, D. Koschny, C. Guttler, C. Tubiana, J. Agarwal, H. Sierks, C. Barbieri, P. Lamy, R. Rodrigo, H. RICKMAN, M. F. A'Hearn, M. A. Barucci, J.-L. Bertaux, I. Bertini, G. Cremonese, V. D. Deppo, B. Davidsson, S. Debei, M. D. Cecco, J. Deller, C. Feller, S. Fornasier, M. Fulle, A. Gicquel, O. Groussin, P. J. Gutiérrez, M. Hofmann, S. F. Hviid, W.-H. Ip, L. Jorda, H. U. Keller, J. Knollenberg, J. R. Kramm, E. Kührt, M. Küppers, L. M. Lara, M. Lazzarin, J. J. L. Moreno, F. Marzari, G. Naletto, N. Oklay, X. Shi, N. Thomas, B. Poppe; *Distance determination method of dust particles using Rosetta OSIRIS NAC and WAC data*; Planetary and Space Science, Volume 143, Pages 256-264 DOI: 10.1016/ j.pss.2017.04.018, 2017
25. Dudík, J., E. Dzifčková, N. Meyer-Vernet, G. Del Zanna, P. R. Young, A. Giunta, B. SYLWESTER, J. SYLWESTER, M. Oka, H. E. Mason, C. Vocks, L. Matteini, S. Krucker, D. R. Williams, Š.

Mackovjak; *Nonequilibrium Processes in the Solar Corona, Transition Region, Flares, and Solar Wind (Invited Review)*; Solar Physics, Volume 292, Issue 8, Article number 100, DOI: 10.1007/s11207-017-1125-0, 2017

26. Eyraud, C., A. Hrique, J.-M. Geffrin, W. KOFMAN; *Imaging the interior of a comet from bistatic microwave measurements: Case of a scale comet model*; Advances in Space Research, DOI: 10.1016/j.asr.2017.10.012, 2017
27. Feller, C., S. Fornasier, P. H. Hasselmann, A. Barucci, F. Preusker, F. Scholten, L. Jorda, A. Pommerol, B. Jost, O. Poch, M. R. El-Maary, N. Thomas, I. Belskaya, M. Pajola, H. Sierks, C. Barbieri, P. L. Lamy, D. Koschny, H. RICKMAN, R. Rodrigo, J. Agarwa, M. A'Hearn, J.-L. Bertaux, I. Bertini, S. Boudreault, G. Cremonese, V. Da Deppo, B. J. R. Davidsson, S. Debei, M. De Cecco, J. Deller, M. Fulle, A. Giquel, O. Groussin, P. J. Gutierrez, C. Guttler, M. Hofmann, S. F. Hviid, H. Keller, W.-H. Ip, J. Knollenberg, G. Kovacs, J.-R. Kramm, E. Kuhrt, M. Kuppers, M. L. Lara, M. Lazzarin, C. Leyrat, J. J. Lopez Moreno, F. Marzari, N. Masoumzadeh, S. Mottola, G. Naletto, D. Perna, N. Oklay, X. Shi, C. Tubiana, J.-B. Vincent; Decimetre-scaled spectrophotometric properties of the nucleus of comet 67P/Churyumov-Gerasimenko from OSIRIS observations; Monthly Notices of the Royal Astronomical Society, Volume 462, Pages S287-S303, DOI: 10.1093/mnras/stw2511, 2016
28. FIGURA, P.; *Stability of the line preserving flows*; Geophysical & Astrophysical Fluid Dynamics, Volume 111, Issue 6, p. 508-526, DOI: 10.1080/03091929.2017.1365363, 2017
29. Fornasier, S., C. Feller, J.-C. Lee, S. Ferrari, M. Massironi, P. H. Hasselmann, J. D. P. Deshapriya, M. A. Barucci, M. R. El-Maarry, L. Giacomini, S. Mottola, H. U. Keller, W.-H. Ip, Z.-Y. Lin, H. Sierks, C. Barbieri, P. L. Lamy, R. Rodrigo, D. Koschny, H. RICKMAN, J. Agarwal, M. A'Hearn, J.-L. Bertaux,I. Bertini, G. Cremonese, V. Da Deppo, B. Davidsson, S. Debei, M. De Cecco, J. Deller, M. Fulle, O. Groussin, P. J. Gutierrez, C. Güttler, M. Hofmann, S. F. Hviid, L. Jorda, J. Knollenberg, G. Kovacs, R. Kramm, E. Kührt, M. Küppers, M. L. Lara, M. Lazzarin,J. J. L. Moreno, F. Marzari, G. Naletto, N. Oklay, M. Pajola, X. Shi, N. Thomas, I. Toth, C. Tubiana, J.-B. Vincent; *The highly active Anhur-Bes regions in the 67P/ Churyumov- Gerasimenko comet: Results from OSIRIS/ROSETTA observations*; Monthly Notices of the Royal Astronomical Society Volume 469, Pages S93-S107; 2017
30. Fouchard, M., H. RICKMAN, Ch. Froeschlé, G. B. Valsecchi; *Distribution of long-period comets: comparison between simulations and observations*; Astronomy and Astrophysics, Volume 604, Article Number A24 (9pp), DOI: 10.1051/ 0004-6361/201630343, 2017
31. Fouchard, M., H. RICKMAN, Ch. Froeschlé, G. B. Valsecchie; *On the present shape of the Oort cloud and the flux of "new" comets*; Icarus, Volume 292, Pages 218-233, DOI: 10.1016/ j.icarus.2017.01.013, 2017
32. Frattin, E., G. Cremonese, E. Simioni, I. Bertini, M. Lazzarin, T. Ott, E. Drolshagen, F. La Forgia, H. Sierks, C. Barbieri, P. Lamy, R. Rodrigo, D. Koschny, H. RICKMAN, H. U. Keller, J. Agarwal, M. F. A'Hearn, M. A. Barucci, J.-L. Bertaux, V. Da Deppo, B. Davidsson, S. Debei, M. De Cecco, J. Deller, S. Ferrari, F. Ferri, S. Fornasier, M. Fulle, A. Gicquel, O. Groussin, P. J. Gutierrez, C. Gttler, M. Hofmann, S. F. Hviid, W.-H. Ip, L. Jorda, J. Knollenberg, J.-R. Kramm, E. Kührt, M. Küppers, L. M. Lara, J. J. Lopez Moreno, A. Lucchetti, F. Marzari, M. Massironi, S. Mottola, G. Naletto, N. Oklay, M. Pajola, L. Penasa, X. Shi, N. Thomas, C. Tubiana, J.-B. Vincent; *Post-perihelion photometry of dust grains in the coma of 67P Churyumov-*

Gerasimenko; Monthly Notices of the Royal Astronomical Society, Volume 469, Pages S195-S203, 2017

33. Galli, A., P. Wurz, N. Schwadron, H. Kucharek, E. Möbius, M. BZOWSKI, J. M. SOKÓŁ, M. A. KUBIAK, S. A. Fuselier, H. O. Funsten, D. J. McComas, *The downwind hemisphere as seen with IBEX-Lo during 8 years*; ASTROPHYSICAL JOURNAL, Vol. 851:1, 16pp, DOI: 10.3847/1538-4357/aa988f, 2017
34. Giacomini, L., M. Massironi, M. R. El-Maarry, L. Penasa, M. Pajola, N. Thomas, S. C. Lowry, C. Barbieri, G. Cremonese, F. Ferri, G. Naletto, I. Bertini, F. La Forgia, M. Lazzarin, F. Marzari, H. Sierks, P. L. Lamy, R. Rodrigo, H. RICKMAN, D. Koschny, H. U. Keller, J. Agarwal, M. F. A'Hearn, A.-T. Auger, M. A. Barucci, J.-L. Bertaux, S. Besse, D. Bodewits, V. Da Deppo, B. Davidsson, M. De Cecco, S. Debei, S. Fornasier, M. Fulle, O. Groussin, P. J. Gutierrez, C. Gttler, S. F. Hviid, W.-H. Ip, L. Jorda, J. Knollenberg, G. Kovacs, J.-R. Kramm, E. Kührt, M. Küppers, L. M. Lara, J. J. Lopez Moreno, S. Magrin, H. Michalik, N. Oklay, A. Pommerol, F. Preusker, F. Scholten, C. Tubiana, J.-B. Vincent; Geologic mapping of the Comet 67P/Churyumov-Gerasimenko's Northern hemisphere; Monthly Notices of the Royal Astrono-mical Society, Volume 462, 2016, Pages S352-S367; DOI: 10.1093/mnras/stw2848, 2016
35. Gicquel, A., M. Rose, J.-B. Vincent, B. Davidsson, D. Bodewits, M. F. A'Hearn, J. Agarwal, N. Fougere, H. Sierks, I. Bertini, Z.-Y. Lin, C. Barbieri, P. L. Lamy, R. Rodrigo, D. Koschny, H. RICKMAN, H. U. Keller, M. A. Barucci, J.-L. Bertaux, S. Besse, S. Boudreault, G. Cremonese, V. Da Deppo, S. Debei, J. Deller, M. De Cecco, E. Frattin, M. R. El-Maarry, S. Fornasier, M. Fulle, O. Groussin, P. J. Gutirrez, P. Gutiérrez-Marquez, C. Güttler, S. Höfner, M. Hofmann, X. Hu, S. F. Hviid, W.-H. Ip, L. Jorda, J. Knollenberg, G. Kovacs, J.-R. Kramm, E. Kührt, M. Küppers, L. M. Lara, M. Lazzarin, J. J. L. Moreno, S. Lowry, F. Marzari, N. Masoumzadeh, M. Massironi, F. Moreno, S. Mottola, G. Naletto, N. Oklay, M. Pajola, F. Preusker, F. Scholten, X. Shi, N. Thomas, I. Toth, C. Tubiana; *Modelling of the outburst on 2015 July 29 observed with OSIRIS cameras in the Southern hemisphere of comet 67P/ Churyumov-Gerasimenko*; Monthly Notices of the Royal Astronomical Society, Volume 469, Pages S178-S185, 2017
36. Gicquel, A., J.-B. Vincent, J. Agarwal, M. F. A'Hearn, I. Bertini, D. Bodewits, H. Sierks, Z.-Y. Lin, C. Barbieri, P. L. Lamy, R. Rodrigo, D. Koschny, H. RICKMAN, H. U. Keller, M. A. Barucci, J.-L. Bertaux, S. Besse, G. Cremonese, V. Da Deppo, B. Davidsson, S. Debei, J. Deller, M. De Cecco, E. Frattin, M. R. El-Maarry, S. Fornasier, M. Fulle, O. Groussin, P. J. Gutíerrez, P. Gutíerrez-Marquez, C. Guttler, S. Hofner, M. Hofmann, X. Hu, S. F. Hviid, W.-H. Ip, L. Jorda, J. Knollenberg, G. Kovacs, J.-R. Kramm, E. Kuhrt, M. Kuppers, L. M. Lara, M. Lazzarin, J. J. Lopez Moreno, S. Lowry, F. Marzari, N. Masoumzadeh, M. Massironi, F. Moreno, S. Mottola, G. Naletto, N. Oklay, M. Pajola, A. Pommero, F. Preusker, F. Scholten, X. Shi, N. Thomas, I. Toth, C. Tubiana; Sublimation of icy aggregates in the coma of comet 67p/ churyumov-gerasimenko detected with the osiris cameras on board rosetta; Monthly Notices of the Royal Astronomical Society Volume 462, 2016, Pages S57-S66, DOI: 10.1093/mnras/stw 2117, 2016
37. Gładkowski, M.; Szczerba, R.; Sloan, G. C.; Lagadec, E.; Volk, K. Comparison between 30 micron sources in different galaxies, 2016, Journal of Physics: Conference Series, Volume 728, Issue 6, article id. 062007
38. Stellar evolution in the outer Galaxy

39. Grün, E., J. Agarwal, N. Altobelli, K. Altwegg, M. S. Bentley, N. Biver, V. Della Corte, N. Edberg, P. D. Feldman, M. Galand, B. Geiger, C. Götz, B. Grieger, C. Güttler, P. Henri, M. Hofstadter, M. Horanyi, E. Jehin, H. Krüger, S. Lee, T. Mannel, E. Morales, O. Mousis, M. Müller, C. Opitom, A. Rotundi, R. Schmied, F. Schmidt, H. Sierks, C. Snodgrass, R. H. Soja, M. Sommer, R. Srama, C.-Y. Tzou, J.-B. Vincent, P. Yanamandra-Fisher, M. F. A'Hearn, A. Erikson, C. Barbieri, M. A. Barucci, J.-L. Bertaux, I. Bertini, J. Burch, L. Colangeli, G. Cremonese, V. Da Deppo, B. Davidsson, S. Debei, M. De Cecco, J. Deller, L. M. Feaga, M. Ferrari, S. Fornasier, M. Fulle, A. Gicquel, M. Gillon, S. F. Green, O. Groussin, P. J. Gutiérrez, M. Hofmann, S. F. Hviid, W.-H. Ip, S. Ivanovski, L. Jorda, H. U. Keller, M. M. Knight, J. Knollenberg, D. Koschny, J.-R. Kramm, E. Kührt, M. Küppers, P. L. Lamy, L. M. Lara, M. Lazzarin, J. J. Lòpez-Moreno, J. Manfroid, E. Mazzotta Epifani, F. Marzari, G. Naletto, N. Oklay, P. Palumbo, J. Wm. Parker, H. RICKMAN, R. Rodrigo, J. Rodrìguez, E. Schindhelm, X. Shi, R. Sordini, A. J. Steffl, S. A. Stern, N. Thomas, C. Tubiana, H. A. Weaver, P. Weissman, V. V. Zakharov, M. G. G. T. Taylor; The 2016 Feb 19 outburst of comet 67P/CG: An ESA rosetta multi-instrument study; Monthly Notices of the Royal Astronomical Society, Volume 462, Pages S220-S234, DOI: 10.1093/mnras/stw2088, 2016
40. GRYCIUK, M., M. SIARKOWSKI, J. SYLWESTER, S. GBUREK, P. PODGÓRSKI, A. KĘPA, B. SYLWESTER, T. Mrozek; *Flare Characteristics from X-ray Light Curves*; Solar Physics, Volume 292, Issue 6, Article number 77, DOI: 10.1007/s11207-017-1101-8, 2017
41. Gulyaeva, T.L., F. Arikan, I. STANISŁAWSKA; *Earthquake aftereffects in the Equatorial Ionization Anomaly region under geomagnetic quiet and storm conditions*; Advances in Space Rese-arch, Volume 60, Issue 2, Pages 406-418 (13 pp), DOI: 10.1016/j.asr.2017.03.039, 2017
42. Gttler, C., P. H. Hasselmann, Y. Li, M. Fulle, C. Tubiana, G. Kovacs, J. Agarwal, H. Sierks, S. Fornasier, M. Hofmann, P. Gutiérrez Marqués, T. Ott, E. Drolshagen, I. Bertini, C. Barbieri, P. L. Lamy, R. Rodrigo, D. Koschn, H. RICKMAN, M. F. A'Hearn, M. A. Barucci, D. Bodewits, J.-L. Bertaux, S. Boudreault, G. Cremonese, V. Da Deppo, B. Davidsson, S. Debei, M. De Cecco, J. Deller, B. Geiger, O. Groussin, P. J. Gutiérrez, S. F. Hviid, W.-H. Ip, L. Jorda, H. U. Keller, J. Knollenberg, J. R. Kramm, E. Kührt, M. Küppers, L. M. Lara, M. Lazzarin, J. J. López-Moreno, F. Marzari, S. Mottola, G. Naletto, N. Oklay, M. Pajola, X. Shi, N. Thomas, J.-B. Vincent; *Characterization of dust aggregates in the vicinity of the Rosetta spacecraft*; Monthly Notices of the Royal Astronomical Society, Volume 469, Pages S312-S320, doi:10.1093/mnras/stx1692 2017
43. Heller, M., E. J. Schioppa, A. Porcelli, I. T. Pujadas, K. Ziętara, D. D. Volpe, T. Montaruli, F. Cadoux, Y. Favre, J. A. Aguilar, A. Christov, E. Prandini, P. Rajda, M. Rameez, W. Bilnik, J. Błocki, L. Bogacz, J. Borkowski, T. Bulik, A. Frankowski, M. Grudzińska, B. Idźkowski, M. Jamrozy, M. Janiak, J. Kasperek, K. Lalik, E. Lyard, E. Mach, D. Mandat, A. Marszałek, L. D. M. Miranda, J. Michałowski, R. Moderski, A. Neronov, J. Niemiec, M. Ostrowski, P. PAŚKO, M. Pech, P. Schovanek, K. SEWERYN, V. Sliusar, K. Skowron, Ł. Stawarz, M. Stodulska, M. Stodulski, R. Walter, M. Więcek, A. Zagdański; *An innovative silicon photomultiplier digitizing camera for gamma-ray astronomy*; European Physical Journal C, Volume 77, Issue 1, Article number 47, DOI: 10.1140/epjc/s100 52-017-4609-z, 2017
44. Herique, A., W. KOFMAN, P. Beck, L. Bonal, I. Buttarazzi, E. Heggy, J. Lasue, A. C. Levasseur-Regourd, E. Quirico, S. Zine; Cosmochemical implications of CONSERT permittivity

characterization of 67P/CG; Monthly Notices of the Royal Astronomical Society Volume 462, 2016, Pages S516-S532, DOI: 10.1093/ mnras/stx040, 2016

45. Herique, A., B. Agnus, E. Asphaug, A. Barucci, P. Beck, J. Bellerose, J. Biele, L. Bonal, P. Bousquet, L. Bruzzone, C. Buck, I. Carnelli, A. Cheng, V. Ciarletti, M. Delbo, J. Du, X. Du, C. Eyraud, W. Fa, J. Gil Fernandez, O. Gassot, R. Granados-Alfaro, S. F. Green, B. Grieger, J. T. Grundmann, J. Grygorczuk, R. Hahnel, E. Heggy, T-M. Ho, O. Karatekin, Y. Kasabaw, T. Kobayashi, W. KOFMAN, C. Krause, A. Kumamoto, M. Kppers, M. Laabs, C. Lange, J. Lasueza, A. C. Levasseur-Regourda, A. Mallet, P. Michel, S. Mottola, N. Murdoch, M. Mütze, J. Oberst, R. Orosei, D. Plettemeier, S. Rochat, R. Rodriguez Suquet, Y. Rogez, P. Schaffer, C. Snodgrass, J-C. Souyris, M. Tokarz, S. Ulamec, J-E. Wahlund, S. Zinea; *Direct observations of asteroid interior and regolith structure: Science measurement requirements*; Advances in Space Research, DOI: 10.1016/j.asr. 2017.10.020, 2017
46. Jones, G. H., M. M. Knight, K. Battams, D. C. Boice, J. Brown, S. Giordano, J. Raymond, C. Snodgrass, J. K. Steckloff, P. Weissman, A. Fitzsimmons, C. Lisse, C. Opitom, K. S. Birkett, M. BZOWSKI, A. Decock, I. Mann, Y. Ramanjooloo, P. McCauley; *The Science of Sungrazers, Sunskirters, and Other Near-Sun Comets*; Space Science Reviews, Volume 214, Issue 1, Article number 20, 2017
47. Keller, H. U., S. Mottola, S. F. Hviid, J. Agarwal, E. Kührt, Y. Skorov, K. Otto, J.-B. Vincent, N. Oklay, S. E. Schröder, B. Davidsson, M. Pajola, X. Shi, D. Bodewits, I. Toth, F. Preusker., F. Scholten, H. Sierks, C. Barbieri, P. Lamy, R. Rodrigo, D. Koschny, H. RICKMAN, M. F. A'Hearn, M. A. Barucci, J.-L. Bertaux, I. Bertini, G. Cremonese, V. Da Deppo, S. Debei, M. De Cecco, J. Deller, S. Fornasier, M. Fulle, O. Groussin, P. J. Gutiérrez, C. Güttler, M. Hofmann, W.-H. Ip, L. Jorda, J. Knollenberg, J. R. Kramm, M. Küppers, L.-M. Lara, M. Lazzarin, J. J. Lopez-Moreno, F. Marzari, G. Naletto, C. Tubiana, N. Thomas; *Seasonal mass transfer on the nucleus of comet 67P/ Chuyumov-Gerasimenko*; Monthly Notices of the Royal Astronomical Society, Volume 469, Pages S357-S371, 2017
48. Khabarova, O., H. V. Malova, R. A. Kislov, L. M. Zelenyi, V. N. Obridko, A. F. Kharshiladze, T. Munetoshi, J. M. SOKÓŁ, S. GRZĘDZIELSKI, F. Kenichi; *High-latitude Conic Current Sheets in the Solar Wind*; Astrophysical Journal, Volume 836, Issue 1, Article number 108, DOI: 10.3847/1538-4357/836/1/108, 2017
49. KRÓLIKOWSKA, M., P. A. Dybczyński; *Oort spike comets with large perihelion distances*; Monthly Notices of the Royal Astronomical Society, Volume 472, Issue 4, Pages 4634—4658, DOI: 10.1093/mnras/ stx2157, 2017
50. KRÓLIKOWSKA, M.; S. SZUTOWICZ, R. GABRYSZEWSKI, H. RICKMAN, K. ZIOŁKOWSKI, E. M. Pittich; New Catalogue of One-Apparition Comets discovered in the years 1901-1950. Part II; European Planetary Science Congress 2017, held 17-22 September, 2017 in Riga Latvia, id. EPSC2017-79, 2017
51. Lai, I.-L., W.-H. Ip, C.-C. Su, J.-S. Wu, J.-C. Lee, Z.-Y. Lin, Y. Liao, N. Thomas, H. Sierks, C. Barbieri, P. Lamy, R. Rodrigo, D. Koschny, H. RICKMAN, H. U. Keller, J. Agarwal, M. F. A'Hearn, M. A. Barucci, J.-L. Bertaux, I. Bertini, S. Boudreault, G. Cremonese, V. Da Deppo, B. Davidsson, S. Debei, M. De Cecco, J. Deller, S. Fornasier, M. Fulle, O. Groussin, P. J. Gutiérrez, C. Güttler, M. Hofmann, S. F. Hviid, L. Jorda, J. Knollenberg, G. Kovacs, J.-R. Kramm, E. Kührt, M. Küppers, L. M. Lara, M. Lazzarin, J. J. L. Moreno, F. Marzari, G. Naletto, N. Oklay, X. Shi, C. Tubiana, J.-B. Vincent; Gas outflow and dust transport of comet

67P/Churyumov-Gerasimenko; Monthly Notices of the Royal Astronomical SocietyVolume 462, 2016, Pages S533-S546, DOI: 10.1093/ mnras/stx332, 2016

52. Lee, J.-C., M. Massironi, W.-H. Ip, L. Giacomini, S. Ferrari, L. Penasa, M. R. El-Maarry, M. Pajola, I.-L. Lai, Z.-Y. Lin, F. Ferri, H. Sierks, C. Barbieri, P. Lamy, R. Rodrigo, D. Koschny, H. RICKMAN, H. U. Keller, J. Agarwal, M. F. A'Hearn, M. A. Barucci, J.-L. Bertaux, I. Bertini, G. Cremonese, V. D. Deppo, B. Davidsson, S. Debei, M. De Cecco, J. Deller, S. Fornasier, M. Fulle, O. Groussin, P. J. Gutiérrez,C. Güttler, M. Hofmann, S. F. Hviid, L. Jorda, J. Knollenberg, G. Kovacs, J.-R. Kramm, E. Kührt, M. Küppers, L. M. Lara, M. Lazzarin, F. Marzari, J. J. L. Moreno, G. Naletto, N. Oklay, X. Shi, N. Thomas, C. Tubiana, J.-B. Vincent; Geomorphological mapping of comet 67P/Churyumov-Gerasimenko's Southern hemisphere; Monthly Notices of the Royal Astronomical Society Volume 462, 2016, Pages S573-S592, DOI: 10.1093/mnras/ stx450, 2016
53. Lucchetti, A., M. Pajola, S. Fornasier, S. Mottola, L. Penasa, L. Jorda, G. Cremonese, C. Feller, P. H. Hasselmann, M. Massironi, S. Ferrari, G. Naletto, N. Oklay, H. Sierks, C. Barbieri, P. L. Lamy, R. Rodrigo, D. Koschny, H. RICKMAN, H. U. Keller, J. Agarwal, M. F. A'Hearn, M. A. Barucci, J. L. Bertaux, I. Bertini, S. Boudreault, V. Da Deppo, B. Davidsson, S. Debei, M. De Cecco, J. Deller, M. Fulle, O. Groussin, P. J. Gutierrez, C. Gttler, M. Hoffman, S. F. Hviid, W. H. Ip, J. Knollenberg, J. R. Kramm, E. Kührt, M. Küppers, L. M. Lara, M. Lazzarin, F. La Forgia, L. Z. Lin, J. J. Lopez Moreno, F. Marzari, F. Preusker, F. Scholten, X. Shi, N. Thomas, C. Tubiana, J. B. Vincent; *Geomorphological and spectro-photometric analysis of Seth's circular niches on comet 67P/Churyumov-Gerasimenko using OSIRIS images*; Monthly Notices of the Royal Astronomical Society, Volume 469, Pages S238-S251, 2017
54. Macek, W. M., A. WAWRZASZEK, B. Kucharuk, D. G. Sibeck; *Intermittent Anisotropic Turbulence Detected by THEMIS in the Magnetosheath*; The Astrophysical Journal Letters, Volume 851, Number 2, DOI: 10.3847/2041-8213/aa9ed4, 2017
55. Masoumzadeh, N., N. Oklay, L. Kolokolova, H. Sierks, S. Fornasier, M. A. Barucci, J.-B. Vincent, C. Tubiana, C. Güttler, F. Preusker, F. Scholten, S. Mottola, P. H. Hasselmann, C. Feller, C. Barbieri, P. L. Lamy, R. Rodrigo, D. Koschny, H. RICKMAN, M. F. A'Hearn, J.-L. Bertaux, I. Bertini, G. Cremonese, V. Da Dep-po, B. J. R. Davidsson, S. Debei, M. De Cecco, M. Fulle, A. Gicquel, O. Groussin, P. J. Gutiérrez, I. Hall, M. Hofmann, S. F. Hviid, W.-H. Ip, L. Jorda, H. U. Keller, J. Knollenberg, G. Kovacs, J.-R. Kramm, E. Kührt, M. Küppers, L. M. Lara, M. Lazzarin, J. J. Lopez Moreno, F. Marzari, G. Naletto, X. Shi, N. Thomas; *Opposition effect on comet 67P/Churyumov-Gerasimenko using Rosetta-OSIRIS images*; Astronomy and Astrophysics, Volume 599, Article number A11, DOI: 10.1051/0004-6361/ 201629734, 2017
56. McComas, D. J., E. J. Zirnstein, M. BZOWSKI, H. A. Elliott, B. Randol, N. A. Schwadron, J. M. SOKÓŁ, J. R. Szalay, C. Olkin, J. Spencer, A. Stern, H. Weaver; *Interstellar Pickup Ion Observations to 38 au*; Astrophysical Journal, Supplement Series, Volume 233, Issue 1, Article number 8, DOI: 10.3847/1538-4365/ aa91d2, 2017
57. McComas, D. J., E. J. Zirnstein, M. BZOWSKI, M. A. Dayeh, H. O. Funsten, S. A. Fuselier, P. H. Janzen, M. A. KUBIAK, H. Kucharek, E. Mbius, D. B. Reisenfeld, N. A. Schwadron, J. M. SOKÓŁ, J. R. Szalay, M. Tokumaru; *Seven Years of Imaging the Global Heliosphere with IBEX*; Astrophysical Journal, Supplement Series Volume 229, Issue 2, Article num-ber 41, DOI: 10.3847/1538-4365/aa66d8, 2017

3. SPACE PHYSICS

58. Nordlander, T., H. RICKMAN, B. Gustafsson; *The destruction of an Oort Cloud in a rich stellar cluster*; Astronomy and Astrophysics, Volume 603, Article number A112, DOI: 10.1051/0004-6361/201630342, 2017
59. Oklay N., J. M. Sunshine, M. Pajola, A. Pommerol, J.-B. Vincent, S. Mottola, H. Sierks, S. Fornasier, M. A. Barucci, F. Preusker, F. Scholten, L. M. Lara, C. Barbieri, P. L. Lamy, R. Rodrigo, D. Koschny, H. RICKMAN; M. F. A'Hearn; J.-L. Bertaux; I. Bertini; D. Bodewits; G. Cremonese; V. Da Deppo; B. J. R. Davidsson; S. Debei; M. De Cecco; J. Deller; M. Fulle; A. Gicquel; O. Groussin; P. J. Gutirrez; C. Güttler; I. Hall; M. Hofmann; S. F. Hviid; W.-H. Ip; L. Jorda; H. U. Keller; J. Knollenberg; G. Kovacs; J.-R. Kramm; E. Kührt; M. Küppers; M. Lazzarin; Z.-Y. Lin; J. J. Lopez Moreno; F. Marzari; G. Naletto; X. Shi; N. Thomas; C. Tubiana; *Comparative study of water ice exposures on cometary nuclei using multispectral imaging data;* Monthly Notices of the Royal Astronomical Society, Volume 462, Pages S394-S414, DOI: 10.1093/mnras/ stw2918, 2017
60. Oklay, N., S. Mottola, J.-B. Vincent, M. Pajola, S. Fornasier, S. F. Hviid, D. Kappel, E. Kührt, H. U. Keller, M. A. Barucci, C. Feller, F. Preusker, F. Scholten, I. Hall, H. Sierks, C. Barbieri, P. L. Lamy, R. Rodrigo, D. Koschny, H. RICKMAN, M. F. A'Hearn, J.-L. Bertaux, I. Bertini, D. Bodewits, G. Cremonese, V. Da Deppo, B. J. R. Davidsson, S. Debei, M. De Cecco, J. Deller, J. D. P. Deshapriya, M. Fulle, A. Gicquel, O. Groussin, P. J. Gutiérrez, C. Güttler, P. H. Hasselmann, M. Hofmann, W.-H. Ip, L. Jorda, J. Knollenberg, G. Kovacs, J.-R. Kramm, M. Küppers, L. M. Lara, M. Lazzarin, Z.-Y. Lin, J. J. Lopez Moreno, A. Lucchetti, F. Marzari, N. Masoumzadeh, G. Naletto, A. Pommerol, X. Shi, N. Thomas, C. Tubiana; *Long-term survival of surface water ice on comet 67P*; Monthly Notices of the Royal Astronomical Society Volume 469, 2017, Pages S582-S597, DOI: 10.1093/mnras/ stx2298, 2017
61. Olech, A., P. Żołądek, M. Wiśniewski, Z. Tymiński, M. Stolarz, M. Bęben, D. Dorosz, T. Fajfer, K. Fietkiewicz, M. Gawroński, M. Gozdalski, M. Kałużny, M. Krasnowski, H. Krygiel, T. Krzyżanowski, M. Kwinta, T. Łojek, M. Maciejewski, S. Miernicki, M. Myszkiewicz, P. Nowak, K. Polak, K. Polakowski, J. Laskowski, M. Szlagor, G. Tissler, T. SUCHODOLSKI, W. Węgrzyk, P. Woźniak, P. Zaręba; *Enhanced activity of the Southern Taurids in 2005 and 2015*; Monthly Notices of the Royal Astronomical Society, Volume 469, Issue 2, p.2077-2088, 10.1093/mnras/stx716, 2017
62. Otsuka, M.; Ueta, T.; van Hoof, P.A.M.; Sahai, R.; Aleman, I.; Zijlstra, A.A.; Chu, Y-H; Villaver, E.; Leal-Ferreira, M.L.; Kastner, J.; Szczerba, R.; Exter, K.M., The Herschel Planetary Nebula Survey (HerPlaNS): A Comprehensive Dusty Photoionization Model of NGC6781" 2017, ApJS, 231, 220
63. Ott, T., E. Drolshagen, D. Koschny, C. Gttler, C. Tubiana, E. Frattin, J. Agarwal, H. Sierks, I. Bertini, C. Barbieri, P. I. Lamy, R. Rodrigo, H. RICKMAN, M. F. A'Hearn, M. A. Barucci, J.-L. Bertaux, S. Boudreault, G. Cremonese, V. Da Deppo, B. Davidsson, S. Debei, M. De Cecco, J. Deller, C. Feller, S. Fornasier, M. Fulle, B. Geiger, A. Gicquel, O. Groussin, P. J. Gutiérrez, M. Hofmann, S. F. Hviid, W.-H. Ip, L. Jorda, H. U. Keller, J. Knollenberg, G. Kovacs, J. R. Kramm, E. Kührt, M. Küppers, L. M. Lara, M. Lazzarin, Z.-Y. Lin, J. J. López-Moreno, F. Marzari, S. Mottola, G. Naletto, N. Oklay, M. Pajola, X. Shi, N. Tho-mas, J.-B. Vincent, B. Poppe; *Dust mass distribution around comet 67P/Churyumov-Gerasimenko determined via parallax measurements using Ro-setta's OSIRIS cameras*; Monthly Notices of the Royal Astronomical Society, Volume 469, Pa-ges S276-S284, DOI: 10.1093/mnras/stx 1419, 2017

64. Pajola, M., A. Lucchetti, M. Fulle, S. Mottola, M. Hamm, V. Da Deppo, L. Penasa, G. Kovacs, M. Massironi, X. Shi, C. Tubiana, C. Güttler, N. Oklay, J. B. Vincent, I. Toth, B. Davidsson, G. Naletto, H. Sierks, C. Barbieri, P. L. Lamy, R. Rodrigo, D. Koschny, H. RICKMAN, H. U. Keller, J. Agarwal, M. F. A'Hearn, M. A. Barucci, J. L. Bertaux, I. Bertini, G. Cremonese, S. Debei, M. De Cecco, J. Deller, M. R. El Maarry, S. Fornasier, E. Frattin, A. Gicquel, O. Groussin, P. J. Gutierrez, S. Höfner, M. Hofmann, S. F. Hviid, W. H. Ip, L. Jorda, J. Knollenberg, J. R. Kramm, E. Kührt, M. Küppers, L. M. Lara, M. Lazzarin, J. J. Lopez Moreno, F. Marzari, H. Michalik, F. Preusker, F. Scholten, N. Thomas; *The pebbles/boulders size distributions on Sais: Rosetta's final landing site on comet 67P/Churyumov*; Monthly Notices of the Royal Astronomical Society, Volume 469, Issue Suppl_2, Pages S636—S645, doi.: 10.1093/mnras/stx1620, 2017
65. Pajot F., Barret D., Lam-Trong T., et al. (20 coauthors including Różańska A.), The Athena X-ray Integral Field Unit (X-IFU), 2018, Journal of Low Temperature Physics, accepted for publication.
66. Palmer, E. M., E. Heggy, W. KOFMAN; *Orbital bistatic radar observations of asteroid Vesta by the Dawn mission*; Nature Communications 8, Article number: 409, DOI:10.1038/s41467-017-00434-6, 2017
67. Perna, D., M. Fulchignoni, M. A. Barucci, S. Fornasier, C. Feller, J. D. P. Deshapriya, P. H. Hasselmann, H. Sierks, C. Barbieri, P. L. Lamy, R. Rodrigo, D. Koschny, H. RICKMAN, M. A'Hearn, J.-L. Bertaux, I. Bertini, G. Cremonese, V. Da Deppo, B. Davidsson, S. Debei, J. Deller, M. De Cecco, M. R. El-Maarry, M. Fulle, O. Groussin, P. J. Gutierrez, C. Güttler, M. Hofmann, S. F. Hviid, W.-H. Ip, L. Jorda, H. U. Keller, J. Knollenberg, R. Kramm, E. Kührt, M. Küppers, L. M. Lara, M. Lazzarin, J. J. Lopez Moreno, F. Marzari, G. Naletto, N. Oklay, N. Thomas, C. Tubiana and J.-B. Vincent; *Multivariate statistical analysis of OSIRIS/ Rosetta spectrophotometric data of comet 67P/ Churyumov-Gerasimenko*; ASTRONOMY & ASTROPHYSICS, Volume 600, Article Number A115 (9pp), DOI: 10.1051/0004-6361/201630015, 2017
68. Plattner M., Albrecht S., et al. (+16 coauthors including Skup K.), WFI electronics and on-board data processing, 2016, Proceedings of the SPIE, Volume 9905, id. 99052D 9 pp.
69. Pogorelov, N.V., H. Fichtner, A. CZECHOWSKI, A. Lazarian, B. Lembege, J. A. Le Roux, M. S. Potgieter, K. Scherer, E. C. Stone, R. D. Strauss, T. Wiengarten, P. Wurz, G. P. Zank, M. Zhang; *Heliosheath Processes and the Structure of the Heliopause: Modeling Energetic Particles, Cosmic Rays, and Magnetic Fields*; Space Science Reviews, 56pp, DOI: 10.1007/s11214-017-0354-8, 2017
70. Popowicz, A., A. Pigulski, K. Bernacki, R. Kuschnig, H. Pablo, T. Ramiaramanantsoa, E. Zocłońska, D. Baade, G. Handler, A. F. J. Moffat, G. A. Wade, C. Neiner, S. M. Ruciński, W. W. Weiss, O. Koudelka, P. ORLEAŃSKI, A. Schwarzenberg-Czerny, K. Zwintz; *BRITE Constellation: Data processing and photometry*; Astronomy and Astrophysics, Volume 605, Article number A26, DOI: 10.1051/0004-6361/201730806, 2017
71. Preusker, F., F. Scholten, K.-D. Matz, T. Roatsch, S. F. Hviid, S. Mottola, J. Knollenberg, E. Khrt, M. Pajola, N. Oklay, J.-B. Vincent, B. Davidsson, M. F. A'Hearn, J. Agarwal, C. Barbieri, M. A. Barucci, J.-L. Bertaux, I. Bertini, G. Cremonese, V. Da Deppo, S. Debei, M. De Cecco, S. Fornasier, M. Fulle, O. Groussin, P. J. Gutiérrez, C. Güttler, W.-H. Ip, L. Jorda, H. U. Keller, D. Koschny, J. R. Kramm, M. Küppers, P. Lamy, L. M. Lara, M. Lazzarin, J. J. Lopez Moreno, F. Marzari, M. Massironi, G. Naletto, H. RICKMAN, R. Ro-drigo, H. Sierks, N. Thomas, C. Tubiana;

The global meter-level shape model of comet 67P/ Churyumov-Gerasimenko; Astronomy and Astrophysics, Volume 607, Article number L1, DOI: 10.1051/0004-6361/201731798, 2017

72. El-Maarry, M. R., O. Groussin, N. Thomas, M. Pajola, A.-T. Auger, B. Davidsson, X. Hu, S. F. Hviid, J. Knollenberg, C. Güttler, C. Tubiana, S. Fornasier, C. Feller, P. Hasselmann, J.-B. Vincent, H. Sierks, C. Barbieri, P. Lamy, R. Rodrigo, D. Koschny, H. U. Keller, H. RICKMAN, M. F. A'Hearn, M. A. Barucci, J.-L. Bertaux, I. Bertini, S. Besse, D. Bodewits, G. Cremonese, V. Da Deppo, S. Debei, M. De Cecco, J. Deller, J. D. P. Deshapriya, M. Fulle, P. J. Gutierrez, M. Hofmann, W.-H. Ip, L. Jorda, G. Kovacs, J.-R. Kramm, E. Kührt, M. Küppers, L. M. Lara, M. Lazzarin, Z.-Yi Lin, J. J. Lopez Moreno, S. Marchi, F. Marzari, S. Mottola, G. Naletto, N. Oklay, A. Pommerol, F. Preusker, F. Scholten, X. Shi; *Surface changes on comet 67P/Churyumov-Gerasimenko suggest a more active past*; Science Volume 355, Issue 6332, Article number aak9384, DOI: 10.1126/science. aak9384, 2017
73. Rapley, C. G., J. SYLWESTER, K. J. H. Phillips; *New Results from the Solar Maximum Mission/Bent Crystal Spectrometer*; SOLAR PHYSICS, Volume: 292, Issue: 4, Article Number: 50, DOI: 10.1007/s11207-017-1070-y, 2017
74. Rau A., Nandra K., et al. (15 coauthors including Różańska A.), Athena Wide Field Imager key science drivers, 2016, Proceedings of the SPIE, Volume 9905, id. 99052B 11 pp.
75. RICKMAN, H., T. WIŚNIOWSKI, R. GABRYSZEWSKI, P. WAJER, K. Wójcikowski, S. SZUTOWICZ, G. B. Valsecchi, A. Morbidelli; *Cometary impact rates on the Moon and planets during the late heavy bombardment*; Astronomy and Astrophysics Volume 598, Article number A67, DOI: 10.1051/0004-6361/201629376, 2017
76. Savin, S. P., V. V. Lyahov, V. M. Neshchadim, E. Amata, J. L. Rauch, V. P. Silin, V. Y. Popov, V. P. Budaev, S. I. Klimov, A. A. Skalsky, L. A. Legen, J. BŁĘCKI; *Magnetopause charging and transfer of momentum and energy into magnetosphere*; Bulletin of the Lebedev Physics Institute, Volume 44, Issue 4, Pages 99-105, DOI: 10.3103/S1068335617040030, 2017
77. Schmitt, M. I., C. Tubiana, C. Guttler, H. Sierks, J.-B. Vincent, M. R. El-Maarry, D. Bodewits, S. Mottola, S. Fornasier, M. Hofmann, C. Barbieri, P. L. Lamy, R. Rodrigo, D. Koschny, H. RICKMAN, M. F. A'Hearn, J. Agarwal, M. A. Barucci, J.-L. Bertaux, I. Bertini, G. Cremonese, V. Da Deppo, B. Davidsson, S. Debei, M. De Cecco, J. Deller, M. Fulle, A. Gicquel, O. Groussin, P. J. Gutierrez, S. F. Hviid, W.-H. Ip, L. Jorda, H. U. Keller, J. Knollenberg, J. R. Kramm, E. Kuhrt, M. Kuppers, L. M. Lara, M. Lazzarin, J. J. Lopez-Moreno, F. Marzari, G. Naletto, N. Oklay, M. Pajola, D. Prasanna, X. Shi, F. Scholten, I. Toth and N. Thomas; *Long-term monitoring of comet 67P/Churyumov—Gerasimenko's jets with OSIRIS onboard Rosetta*; MNRAS 469, S380, doi:10.1093/ mnras/stx1780, 2017
78. Smith, Ch. W., P. Aggarwal, M. R. Argall, L. F. Burlaga, M. BZOWSKI, B. E. Cannon, S. P. Gary, M. K. Fisher, J. A. Gilbert, S. J. Hollick; Observations of Low-Frequency Magnetic Waves due to Newborn Interstellar Pickup Ions Using ACE, Ulysses, and Voyager Data; Journal of Physics: Conference Series, Volume 900, Number 1, Art no 012018, DOI:10.1088/1742-6596/ 900/1/012018, 2017
79. Snodgrass, C., G. H. Jones, H. Boehnhardt, A. Gibbings, M. Homeister, N. Andre, P. Beck, M. S. Bentley, I. Bertini, N. Bowles, M. T. Capria, C. Carr, M. Ceriotti, A. J. Coates, V. Della Corte, K. L. Donaldson Hanna, A. Fitzsimmons, P. J. Gutiérrez, O. R. Hainaut, A. Herique, M. Hilchenbach, H. H. Hsieh, E. Jehin, O. Karatekin, W. KOFMAN, L. M. Lara, K. Laudan, J.

Licandro, S. C. Lowry, F. Marzari, A. Masters, K. J. Meech, F. Moreno, A. Morse, R. Orosei, A. Pack, D. Plettemeier, D. Prialnik, A. Rotundi, M. Rubin, J. P. Sánchez, S. Sheridan, M. Trieloffa, A. Winterboer; *The Castalia mission to Main Belt Comet 133P/Elst-Pizarro*; Advances in Space Research, DOI: 10.1016/ j.asr.2017.09.011, 2017
80. Soffitta, P., S. GBUREK, M. KOWALIŃSKI and 450 others; XIPE: The X-ray imaging polarimetry explorer; Proceedings of SPIE - The International Society for Optical Engineering Volume 9905, 2016, Article number 990515, 2016
81. Schmidt, M.R.; He, J.H.; Szczerba, R.; Bujarrabal, V.; Alcolea, J.; Cernicharo, J.; Decin, L.; Justtanont, K.; Teyssier, D.; Menten, K.M.; Neufeld, D.A.; Olofsson, H.; Planesas, P.; Marston, A. P.; Sobolev, A.M.; de Koter, A.; Schöier, F. L., Herschel/HIFI observations of the circumstellar ammonia lines in IRC+10216"
82. 2016, A&A, 592, 131
83. STANICA D.A., STANICA D., BŁĘCKI J, ERNST T, JÓŹWIAK W., SŁOMIŃSKI J., Pre-seismic geomagnetic and ionosphere signatures related to the Mw5.7 earthquake occurred in Vrancea zone on September 24, 2016 Acta Geophysica 2018, https://doi.org/10.1007/s11600-018-0115-4
84. STANISŁAWSKA, I., T. L. Gulyaeva, O. GRYNYSHYNA-POLIUGA, L.V. Pustovalova; Instantaneous global maps of ionospheric critical frequency GIM-foF2 for evaluation of the ionospheric weather; General Assembly and Scientific Symposium of the International Union of Radio Science (URSI GASS), 2017 XXXIInd, DOI: 10.23919/URSIGASS. 2017.8105427, 2017
85. STANISŁAWSKA, I., Reflections on a Career in Radio Science; The Radio Science Bulletin, No.362, 104-105, 2017
86. SWACZYNA, P., M. BZOWSKI; *Modeling Emission of Heavy Energetic Neutral Atoms from the Heliosphere*; The Astrophysical Journal, 846:128 (12pp), DOI: 10.3847/1538-4357/aa862b, 2017
87. SWACZYNA, P., S. GRZĘDZIELSKI, M. BZOWSKI; *Helium Energetic Neutral Atoms from the Heliosphere: Perspectives for Future Observations*; The Astrophysical Journal, Volume 840, Number 2, DOI: 10.3847/1538-4357/aa6d5b, 2017
88. Szczerba, R.; Yung, B.H.K.; Sewiło, M.; Siódmiak, N.; Karska, A, AGB and post-AGB objects in the outer Galaxy, 2017, in Planetary Nebulae: Multi-Wavelength Probes of Stellar and Galactic Evolution, Proceedings of the International Astronomical Union, IAU Symposium, Volume 323, pp. 369-370
89. Szczerba, R.; Siódmiak, N.; Leśniewska, A.; Karska, A.; Sewiło, M. Stellar evolution in the outer Galaxy,
90. 2016, Journal of Physics: Conference Series, Volume 728, Issue 4, article id. 042004
91. Thomas, N., G. Cremonese, R. Ziethe, M. Gerber, M. Brndli, G. Bruno, M. Erismann, L. Gambicorti, T. Gerber, K. Ghose, M. Gruber, P. Gubler, H. Mischler, J. Jost, D. Piazza, A. Pommerol, M. Rieder, V. Roloff, A. Servonet, W. Trottmann, T. Uthaicharoenpong, C. Zimmermann, D, Vernani, M. Johnson, E. Pelò, T. Weigel, J. Viertl, N. de Roux, P. Lochmatter, G. Sutter, A. Casciello, T. Hausner, I. Ficai Veltroni, V. da Deppo, P. ORLEAŃSKI, W. NOWOSIELSKI, T. ZAWISTOWSKI, S. Szalai, B. Sodor, S. Tulyakov, G. Troznai, M. BANASZKIEWICZ, J. C. Bridges, S. Byrne, S. Debei, M. R. El-Maarry, E. Hauber, C. J. Hansen, A. Ivanov, L. Keszthelyi, R. Kirk, R. Kuzmin, N. Mangold, L. Marinangeli, W. J. Markiewicz, M.

Massironi, A. S. McEwen, C. Okubo, L. L. Tornabene, P. WAJER, J. J. Wray; *The Colour and Stereo Surface Imaging System (CaSSIS) for the ExoMars Trace Gas Orbiter*; Space Science Reviews, Volume 212, Issue 3—4, pp 1897—1944, DOI: 10.1007/s11214-017-0421-1, 2017

92. Vincent, J.-B., M. F. A'Hearn, Z.-Y. Lin, M. R. El-Maarry, M. Pajola, H. Sierks, C. Barbieri, P. L. Lamy, R. Rodrigo, D. Koschny, H. RICKMAN, H. U. Keller, J. Agarwal, M. A. Barucci, J.-L. Bertaux, I. Bertini, S. Besse, D. Bodewits, G. Cremonese, V. Da Deppo, B. Davidsson, S. Debei, M. De Cecco, J. Deller, S. Fornasier, M. Fulle, A. Gicquel, O. Groussin, P. J. Gutirrez, P. Gutiérrez-Marquez, C. Güttler, S. Höfner, M. Hofmann, S. F. Hviid, W.-H. Ip, L. Jorda, J. Knollenberg, G. Kovacs, J.-R. Kramm, E. Kührt, M. Küppers, L. M. Lara, M. Lazzarin, J. J. Lopez Moreno, F. Marzari, M. Massironi, S. Mottola, G. Naletto, N. Oklay, F. Preusker, F. Scholten, X. Shi, N. Thomas, I. Toth, C. Tubiana; Summer fireworks on comet 67P; Monthly Notices of the Royal Astronomical Society, Volume 462, Pages S184-S194, DOI: 10.1093/mnras/stw2409, 2016
93. Vincent, J.-B., S. F. Hviid, S. Mottola, E. Kuehrt, F. Preusker, F. Scholten, H. U. Keller, N. Oklay, D. de Niem, B. Davidsson, M. Fulle, M. Pajola, M. Hofmann, X. Hu, H. RICKMAN, Z.-Y. Lin, C. Feller, A. Gicquel, S. Boudreault, H. Sierks, C. Barbieri, P. L. Lamy, R. Rodrigo, D. Koschny, M. F. A'Hearn, M. A. Barucci, J.-L. Bertaux, I. Bertini, G. Cremonese, V. Da Deppo, S. Debei, M. De Cecco, J. Deller, S. Fornasier, O. Groussin, P. J. Gutiérrez, P. Gutiérrez-Marquez, C. Güttler, W.-H. Ip, L. Jorda, J. Knollenberg, G. Kovacs, J.-R. Kramm, M. Küppers, L. M. Lara, M. Lazzarin, J. J. L. Moreno, F. Marzari, G. Naletto, L. Penasa, X. Shi, N. Thomas, I. Toth, C. Tubiana; *Constraints on cometary surface evolution derived from a statistical analysis of 67P's topography;* Monthly Notices of the Royal Astronomical Society, Volume 469, Pages S329-S338, DOI: 10. 1093/mnras/stx1691, 2017
94. WAJER, P., P. WITEK, M. BANASZKIEWICZ, W. KOFMAN, A. Pommerol, P. WOLKENBERG; Modelling the transport of trace gases in the Martian atmosphere; European Planetary Science Congress, Vol.1, 2017
95. WOLKENBERG, P., M. Giuranna, D. Grassi, A. Aronica, S. Aoki, D. Scaccabarozzi, B. Saggin; *Characterization of dust activity on Mars from MY27 to MY32 by PFS-MEX observations*; Icarus, DOI: 10.1016/j.icarus.2017.10.045, 2017
96. WOŹNIAK, E., S. Kulczyk, M. Derek; *From intrinsic to service potential: an approach to assess tourism landscape potential*; Landscape and Urban Planning 170, p. 209-220, DOI: 10.1016/ j.landurbplan.2017.10.006, 2017
97. Zirnstein, E.J., M. A. Dayeh, D. J. McComas, J. M. SOKÓŁ; *Imprint of the Sun's Evolving Polar Winds on IBEX Energetic Neutral Atom All-sky Observations of the Heliosphere*; Astrophysical Journal, Volume 846, Issue 1, Article number 63, DOI: 10.3847/1538-4357/aa850b, 2017

4

ASTRONAUTICS AND SPACE TECHNOLOGIES

4. ASTRONAUTICS AND SPACE TECHNOLOGIES

Compiled by Piotr Orleański

During the last two years (2016-2017) the activities in Poland in the domain of astronautics and space technologies have been seriously intensified. Poland joined ESA (2012), the understanding of the importance of space activities has been commonly accepted in Poland. Such important steps gave the engineering, organizational and financial support for many of Polish entities, especially, and a first time in Polish space activities, for industrial ones. In 2016 and 2017 the results expected thanks to the access to ESA became really serious. It should be stated: many of Polish companies are currently involved in different space projects in downstream applications, upstream technologies or space missions. This chapter summarises the most important activities in up-stream (and up-stream support).

The most spectacular result was the launch of CaSSIS (Colour and Stereo Surface Imaging System) onboard TGO/ExoMars orbiter.

ESA Science: ExoMars, SIM, Solar Orbiter, EUCLID, JUICE, ATHENA, THOR and ARIEL

ExoMars (ESA mission) has to investigate the Martian environment and to demonstrate new technologies paving the way for a future Mars sample return mission in the 2020's. The ExoMars programme takes place in the context of broader international cooperation related to the Mars mission that will unfold over the coming decades. Two missions are anticipated coinciding with launch opportunities in 2016 and 2018. The 2016 mission was led by the European Space Agency and concerned the launch by a Roscosmos-supplied Proton rocket. The European Space Agency supplied the Trace Gas Orbiter (TGO).
The Colour and Stereo Surface Imaging System (CaSSIS) instrument, the part of the TGO scientific payload, was designed in Switzerland to provide images of the surface of Mars in support of the search for, and localization of methane sources. CBK PAN was responsible to deliver to University of Bern a power supply

system for the camera. The Polish industry – Creotech Instr. SA, as CBK sub-contractor, performed the assembly of the Flight Model of the unit. The CASSIS instrument was delivered to the satellite integration site in mid-November 2015. In March 2016 the TGO was launched, then, a few weeks later the CaSSIS commissioning on the orbit was successfully performed. The correct results of CaSSIS work on Martian orbit in 2016 and 2017 confirmed, in relation to Polish contingency to the instrument, that the marriage between Polish scientific institute and Polish industry can be really fruitful.

In the same TGO/ExoMars mission SENER Poland, as the contractor responsible for production of the Umbilical Release Mechanism (URM), has to connect the Martian rover with the transport vehicle and provide power supply during the process of robot activation on the Mars surface. Besides, the main role of devoted technology is to support the umbilical harness under environment conditions. The URM remains connected whilst the rover deploys its wheels and lifts itself up from the lander platform. In sequence, the mechanism released on command and the lander side of the URM is collapsed down onto the lander platform to ensure the rover egression and stabilization on the planet surface.

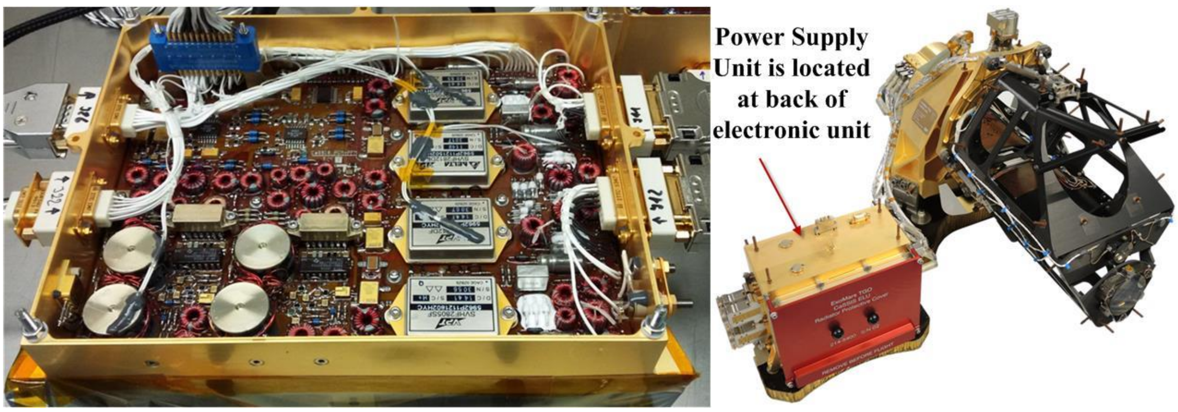

Figure 4. 1. Flight Model of PCM, designed in CBK and assembled in Creotech Instr. SA (left). ©CBK PAN, The whole CaSSIS integrated in Bern (right). © UBE

4. ASTRONAUTICS AND SPACE TECHNOLOGIES

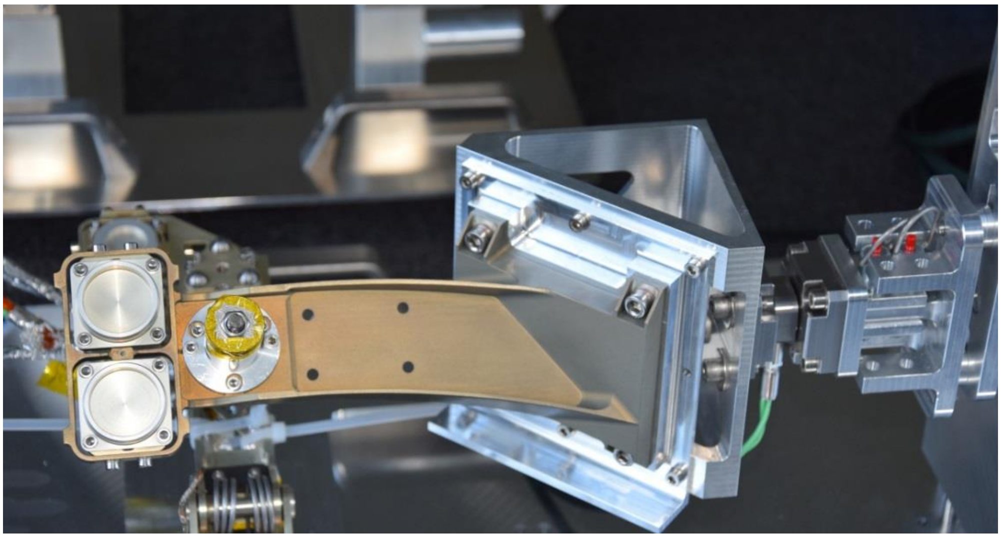

Figure 4. 1. Umbillical Release Mechanism. ©SENER

A few other spectacular results have been achieved in ESA scientific projects (ASIM, SolarOrbiter and EUCLID), CNES, Chinese and Russian projects and finally in ESA and Polish technological projects.

The aim of the **Atmosphere-Space Interactions Monitor (ASIM)** onboard the International Space Station is to study high-altitude optical emissions from the stratosphere and mesosphere related to thunderstorms. One of the two main ASIM instruments is the Miniature-X and Gamma-ray Sensor designed by the University of Bergen and the University of Valencia in cooperation with the CBK PAN. CBK PAN is responsible for the design and manufacture of the Power Supply Unit and its autonomous (FPGA-based) Housekeeping System. In 2016 and 2017 the FM model of the DCDC block was integrated and tested within the whole ASIM and delivered to SPACE-X. Launch is scheduled in April 2018. MXGS/ASIM PSU was one of the two instruments built in Poland in cooperation of scientific institute (CBK PAN) and Polish industry (Creotech Instr. SA).

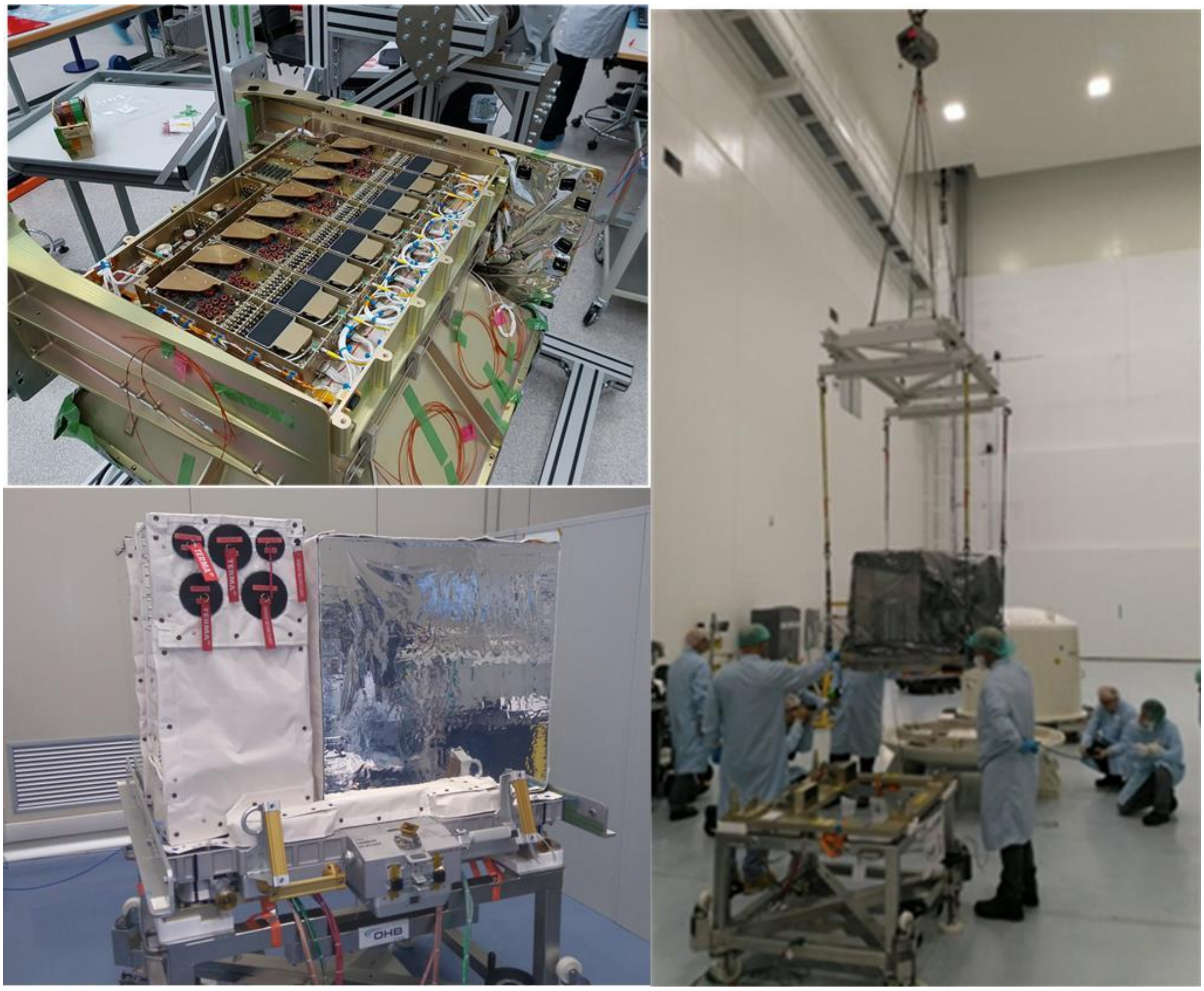

Figure 4. 2. Powert Supply Unit for MXGS/ASIM integrated with the rest of MXGS electronics (top left), whole ASIM integrated (bottom left). both photos © INTA. ASIM delivered to Kennedy Space Center. © ASIM

The **Solar Orbiter (SOLO) ESA mission** will perform observations of the Sun, the inner heliosphere and solar wind. SOLO will fly towards the Sun and will approach the star closer than any other previously launched spacecraft. X-ray Spectrometer/Telescope Instrument (STIX), one of 6 remote sensing instruments on-board SOLO, provides imaging spectroscopy of solar thermal and non-thermal X-ray emission. STIX will provide quantitative information on the timing, location, intensity, and spectra of accelerated electrons as well as of high temperature thermal plasmas, mostly associated with flares and/or microflares.

The Polish participation in STIX consists of the following work-packages: a) participation in STIX scientific program and in data reduction and archiving, b) Instrument Data Processing Unit (IDPU) including IDPU hardware, low level flight software and mechanical frame, c) thermal modeling of the instrument and its subsystems and d) Instrument EGSE including STIX Detector Simulator. In 2017 all activities for Flight Unit have been finished and the instrument was delivered to Airbus UK for satellite integration and tests.

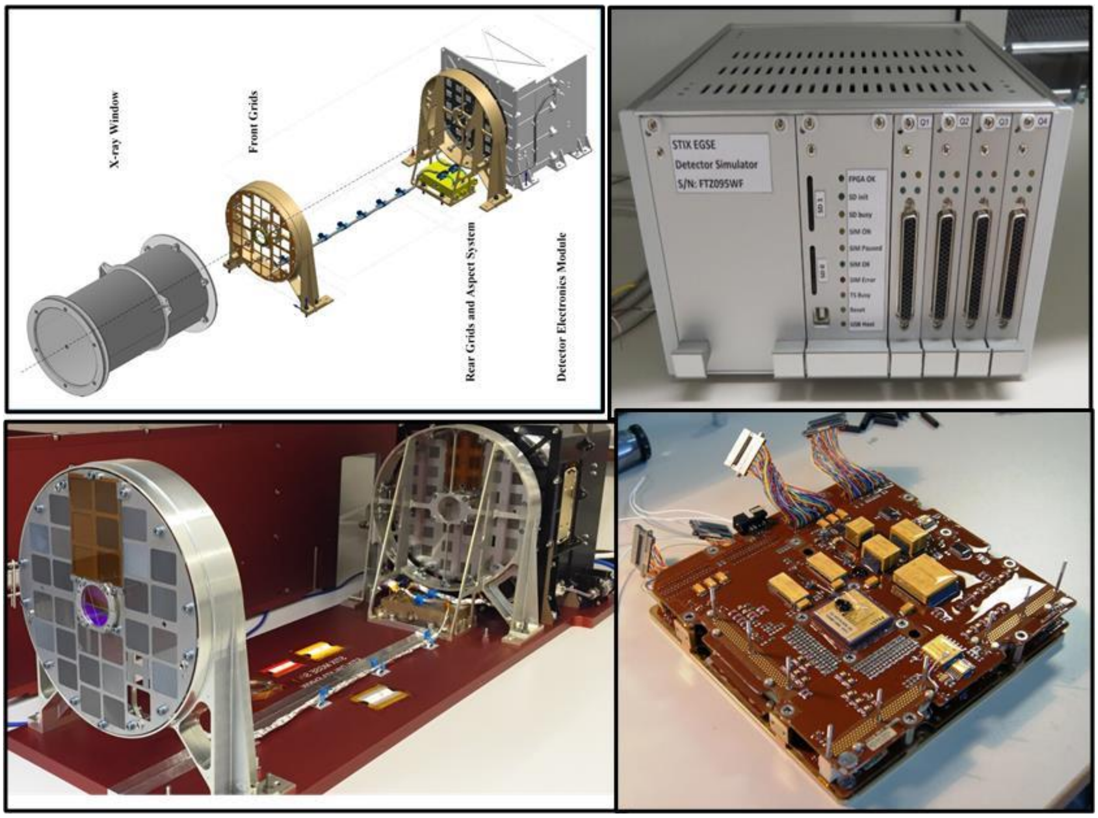

Figure 3. 4. STIX instrument for Solar Orbiter: the skech (top left) and the final assembly of Flight Model (bottom left), both photos © STIX. The STIX Detector Simulator (top right) and Flight Model of STIX DPU (bottom right), both photos © CBK PAN

Euclid (ESA mission) dedicated to map the geometry of the dark Universe and to investigate the distance-redshift relationship and the evolution of cosmic structures as shapes and redshifts of galaxies and clusters of galaxies out to redshifts. SENER Poland was responsible (project ends on 2018) for design, manufacturing, integration and testing of a set of 13 mechanical ground support equipment (MGSE) devices supporting the process of satellite assembly. The most complex and crucial functions are performed by Horizontal Lifting Device (HLD) used to move the satellite in horizontal position in different S/C configurations.

Figure 4. 4. EUCLID MGSE - Horizontal Lifting Device. © SENER

One of the crucial subassembly of the lifting devices is a Centre of Gravity Adjustment Module (CGAM) which is used to perform an adjustment of the lifting point regarding the S/C position Centre of Gravity. Another noteworthy devices are the Actuators for Antenna Deployment and the Panel Support Tilting Stands (PSS) used to mate, demate and tilt the lateral panels of the Euclid service module. For this purpose, the PSS contains a 6 degree of freedom adjustment mechanism for panels of up to 150 kg.

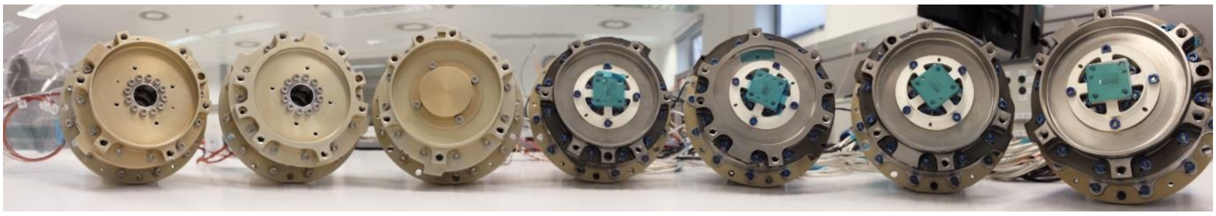

Figure 4. 5. Euclid ADPM - Actuators EM/QM Models. ©SENER

The initial activities (at requirements, first breadboards, simulations and analysis levels) have been performed in other important ESA science missions: **JUICE** (RPWI and SWI), **ATHENA** (X-IFU and WFI), **THOR** (FWP/PSU, EFI/HFA) and **ARIEL** (FGS). CBK PAN, CAMK PAN and the representatives of Polish industry: Astronika, Solaris Optics, SENER PL are involved in this missions.

NASA science: InSight

Astronika has conducted a redesign and integration of Hammering Mechanism for HP3 project - an experiment developed by the German Aerospace Center (DLR) for NASA's InSight mission to Mars to be launched in 2018. The Hammering Mechanism provides a main drive of the HP3 penetrator ensuring delivery of HP3 heat probe up to 5m below the surface of Mars to conduct thermal measurements of Martian soil.

In years 2014-2017 Astronika, together with CBK PAN, under DLR contract developed eight models, all in flight standard, keeping the average integration rate of five months per model.

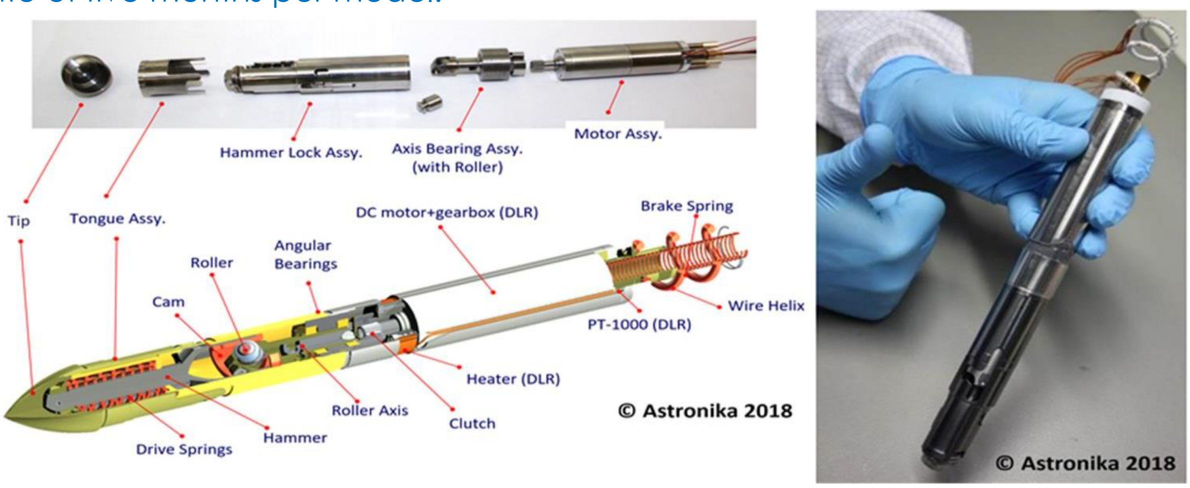

Figure 4. 6. Hammering Mechanism overview (left), one of the assembled mechanisms (Flight Spare model, right). ©Astronika

CNES science: TARANIS

TARANIS is CNES low-altitude microsatellite mission that will provide a set of unprecedented and complementary measurements of physical events associated with TLEs (Transient Luminous Events) and TGFs (Terrestrial Gamma ray Flashes). The MEXIC Power Units (development in CBK PAN) are two blocks (MPU1 and MPU2) of electronics that will be responsible for the conversion, distribution and management of electrical power for the entire scientific payload on board the TARANIS satellite. In 2017, the flight models (FM) of MPU modules for the TARANIS satellite payload were integrated with other payload instruments and tested in flight configuration.

Figure 4. 7. Assembled flight models of MEXIC1 and MEXIC2 modules. The MPUs developed by the CBK PAN are located at the bottom of each stack. © LPC2E

Chinese science: Chang'E4

The Chang'E-4 DSL-P (Discovering the Sky at Longest wavelengths) mission is a pathfinder for future higher-resolution, higher-sensitivity ultra-long wavelength radio diagnostic missions. In 2017 the QM and two Flight Model(FM) of electronic modules and 3D electric antenna system were shipping to National Space Science Center in China for on-board test. The launch is planned for Summer 2018.

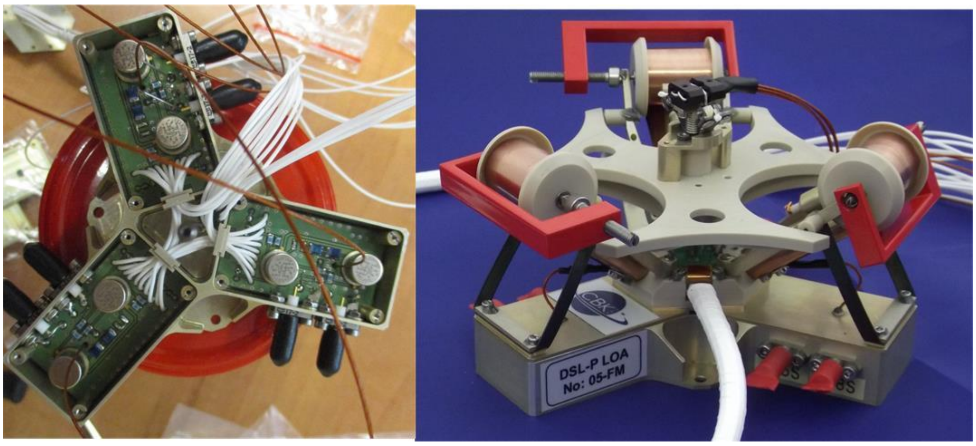

Figure 4. 8. The electronic block (left) and antenna system (right) for DSL-P. © CBK PAN

RKA science: JONOSOND

In order to diagnose top-side ionosphere the four spacecraft mission JONOSOND leading by Russian Space Agency was proposed. The four identical satellites will be located at the polar circular orbit at the altitude 600 km and 800 km. In May 2017 CBK PAN delivered the first two sets of FM-models of scientific instrument LAERT to be used for active probing the ionosphere layers. The delivery was done under the contract with the Russian company Radioexport – Moscow. Another two sets of the instrument are to be delivered in 2018.

Figure 4. 9. Two sets of Flight Model of LAERT instruments for JONOSONDE mission. © CBK PAN

DLR science: DESIS

The DESIS (DLR Earth Sensing Imaging Spectrometer) is hosted on the Earth

Observation Platform, as part of the EXPRESS Logistics Carrier on the International Space Station (ISS). It consists of a hyperspectral imaging spectrometer that covers the visible and near-infrared spectral range, in combination with separate power and instrument control units. The Pointing Unit (CBK PAN responsibility) is the part of the imaging spectrometer that allows the instrument's line of sight (LOS) to be steered under different in-track viewing angles, and to provide views of the in-flight calibration units. The main part of the unit is the mirror, which is rotated by a stepper motor.

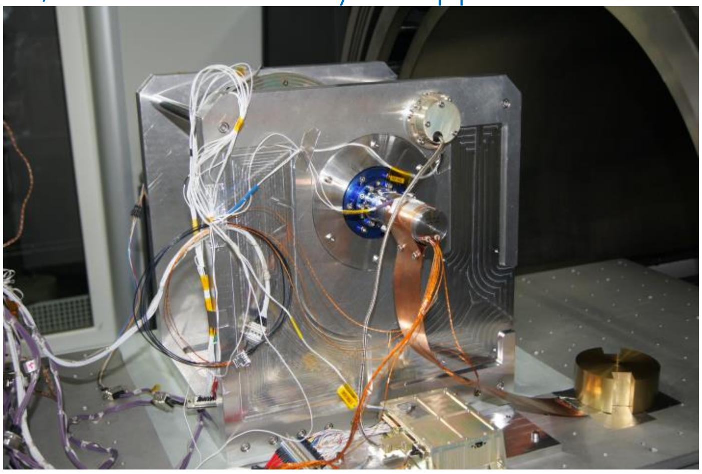

Figure 4. 10. Qualification Model of Pointing Unit during thermal tests. © CBK PAN

In 2017, the Flight Model of Pointing Unit was designed, manufactured and tested, and a new version of the control software was designed, implemented and tested. The FM was delivered to DLR Berlin.

ESA Flight Software and Mission Analysis

GMV Poland is responsible for all the classic mission analysis tasks: orbit maintenance strategy, acquisition, duty cycle, contact with the stations, etc. Last years GMV Poland was responsible as a sole contractor for design of autonomous guidance, navigation and control system (GNC) for descent and landing operations of Phobos Sample Return mission, where feedback was provided by landing camera and radar altimeter. Within the project, the whole subsystem has been prototyped up to Processor in the loop tests. Within AIM mission (consolidation phase) GMV Poland a subcontractor supported GNC

/AOCS subsystem development and performed autocoding and mission analysis. In engineering support and mission analysis domain GMV Poland performed several projects as for instance Galileo 2nd Generation Space Segment Phase A/B1 (G2G) project. The objective of this project was to perform specific study for Galileo 2nd Generation. The mission concept contained several non-standard features that require particular attention from a mission analysis point of view. Within this project GMV Poland was responsible of the mission requirements analysis, G2G mission analysis aspects for different orbits (MEO, IGSO) and different deployment strategies, support mission and operations analysis, satellite control and navigation mission operations concept. GMV Poland has also delivered mission analysis for BIOMASS mission Phase B1 and is providing the same task for Phase C/D.

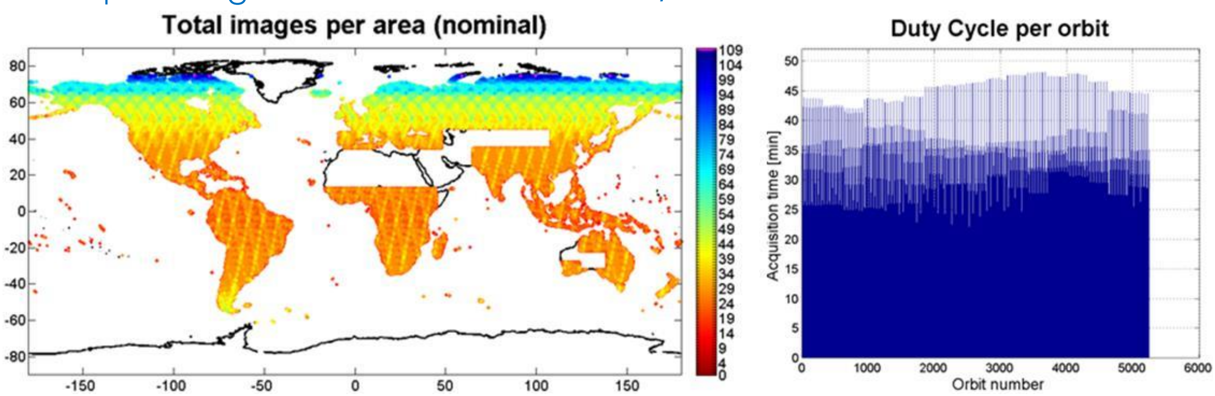

Figure 4. 11. BIOMASS phase B1 Mission Analysis. Coverage build-up for the TOM primary objectives. ©GMV

ESA technology: PROBA3 and OP-SAT

PROBA-3 is the 3rd mission of the PROBA (Project for Onboard Autonomy) line. It is an experimental mission devoted to the in-orbit demonstration of formation flying techniques and technologies. The mission will be implemented with a pair of small spacecraft, which together form a coronagraph. One spacecraft will carry the Coronagraph Instrument and auxiliary units while the second spacecraft will carry the occulter disk. Each spacecraft will be able to maneuver itself. The typical separation distance between the spacecraft will be about 150 m. CBK PAN is responsible for delivery of important blocks of

Coronograph: Filter Wheel Assembly and Coronograph Control Box

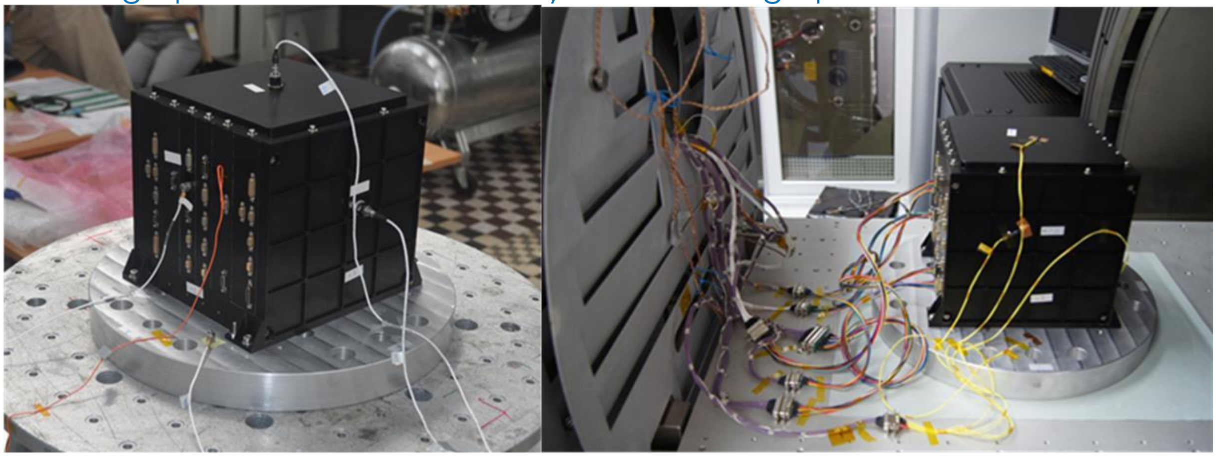

Figure 4. 12. PROBA3 Coronograph Control Box Structure and Thermal model under mechanical (left) and thermal (right) tests. © CBK PAN

OPS-SAT (3U CubeSat) will be a safe, hardware/ software laboratory, flying in a LEO orbit, reconfigurable at every layer from channel coding upwards. This European Space Agency mission aims to provide powerful, in-orbit tools to an emerging experimenter's community that is keen to demonstrate advanced concepts for future space applications, such as: an in-orbit testbed for onboard software applications; advanced communication protocols; compression techniques; demonstrations of advanced software-defined radio concepts for communication purposes; and others.

CBK PAN (with Creotech Instruments S.A. as subcontractor, responsible for FPGA firmware delivery) is responsible for developing the hardware for the CCSDS Engine (the satellite's communication protocol converter). In 2017 the project went to the final phase – the whole Engineering Model of OP-SAT (including Polish CCSDS EM1) has been tested in ESTEC, the other models of CCSDS EM2 have been delivered for tests in Graz and ESA.

4. ASTRONAUTICS AND SPACE TECHNOLOGIES

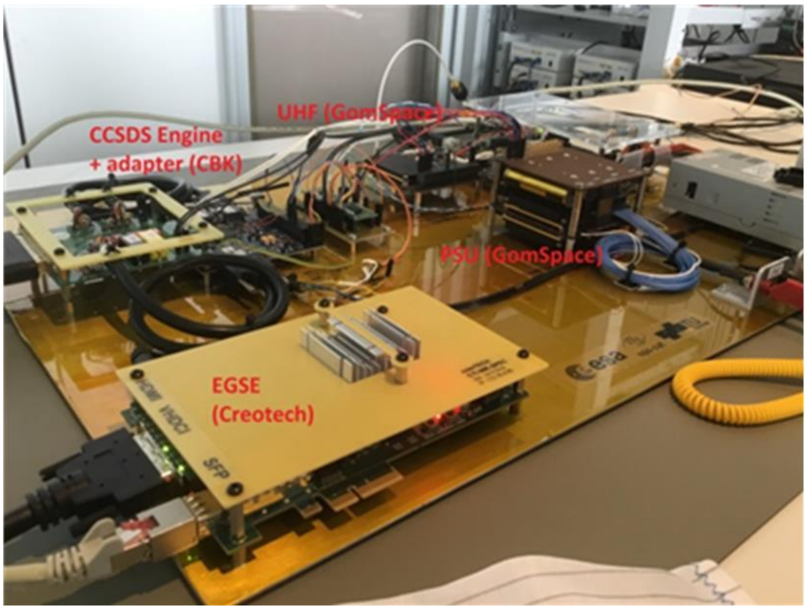

Figure 4. 13. The engineering model of OP-SAT gets connected in ESTEC to an innovative ground control system for the first time (© ESA)

ESA and National technological projects in robotics

ESA is currently studying an active debris removal mission, aiming to remove the defunct ENVISAT from its orbit. CBK PAN is part of a consortium working on this e.deorbit mission. Within the project, CBK PAN is responsible for: simulations of a robotic gripper, in order to develop and evaluate a concept design, including defining the location for sensors; testing a gripper mock-up in microgravity conditions.

The PACKMOON project is focused on developing an entirely new, innovative sample acquisition system. This device consists of two spherical jaws that are inserted into regolith by means of highly dynamic rotary hammering action. PACKMOON is a power-efficient solution that has minimal effect on the lander, allowing for fast sampling of relatively hard material (up to 5-7 MPa) and assuring small thermal and mechanical interactions with the sample (making it more valuable for further scientific investigations). In 2017, the PACKMOON device, based on its innovative rotary hammering concept, was successfully developed. Tests proved the usefulness of the device in simulated low-gravity conditions. The device does not disturb the stability of the lander during sampling (ESA SAMPLER project). All requirements of the ESA Phobos Sample Return Mission were met.

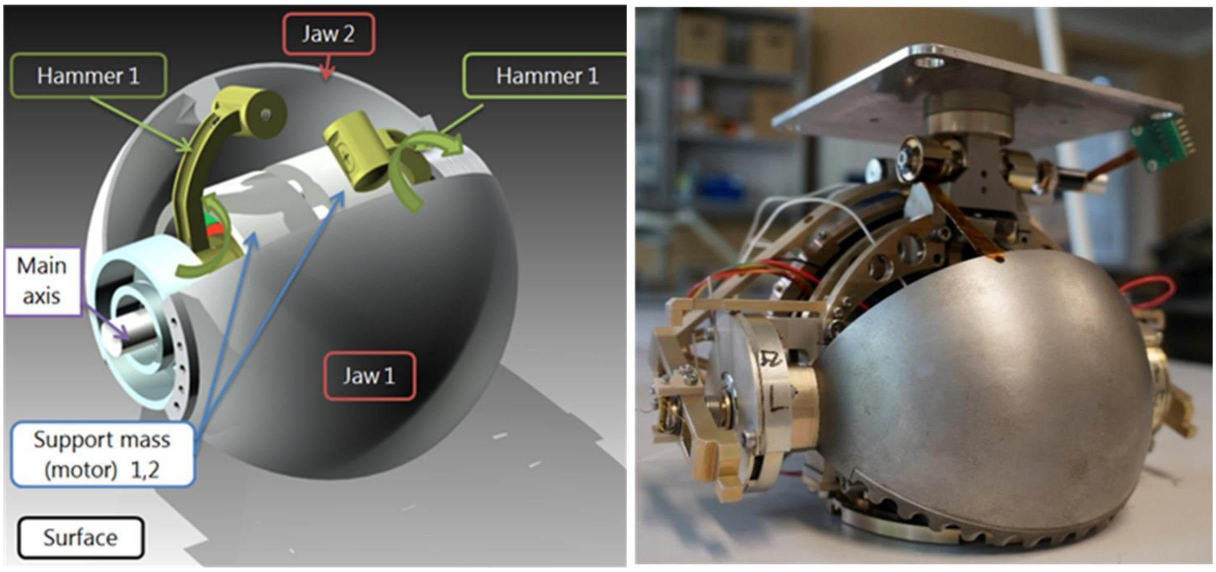

Figure 4. 14. PACKMOON: the sampling mechanism concept – two spherical jaws accelerated by two hammers, sketch (left) and real realization (right).© CBK PAN

Recent research on satellite and rocket propulsion in Poland

Institute of Aviation is now the regional leader in spacecraft and rocket technologies, having a dedicated team with over 30 engineers devoted strictly to rocket propulsion.

At Warsaw University of Technology development of small rocket propulsion systems for satellite applications is carried out. Attitude Control rocket propulsion systems such as "cold gas", "resistojet" as well as monopropellant thrusters utilizing highly concentrated hydrogen peroxide are studied. A Very effective heaters, integrated with the resistojet thruster, allow to improve performance by 30% as compared to cold gas thrusters. Performance of cold gas thrusters has been already successfully demonstrated on a specially adopted table at the CBK for testing propulsion for robotic arms of future satellite manipulators. Also research on thermal as well as catalytic decomposition of highly concentrated hydrogen peroxide has been initiated. On this bases a monopropellant thruster with high performance was developed and tested. This thruster is close to real applications on satellites and only needs long time/cycle endurance tests.

Figure 4. 15. Small monopropellant rocket engines (working on 98% H2O2) developed at the Institute of Aviation and at Institute of Heat Engineering of the Warsaw University of Technology. © WUT

At Institute of Aviation several projects in the domain of space transportation and satellite propulsion are ongoing (15 in total, resources: ESA, NCBiR, FP7, H2020). Apart from several small launch vehicle feasibility studies, extensive work is done in the field of suborbital flight and sounding rocket development.
The ILR-33 "Amber" sounding rocket became in late 2017 the first rocket in the world to use 98%+ hydrogen peroxide as oxidizer in flight. It reached an altitude of 15 km (limited due to the firing range size limitation), while it can achieve altitudes up to 100 km with 150 seconds of 0.001 gravity.

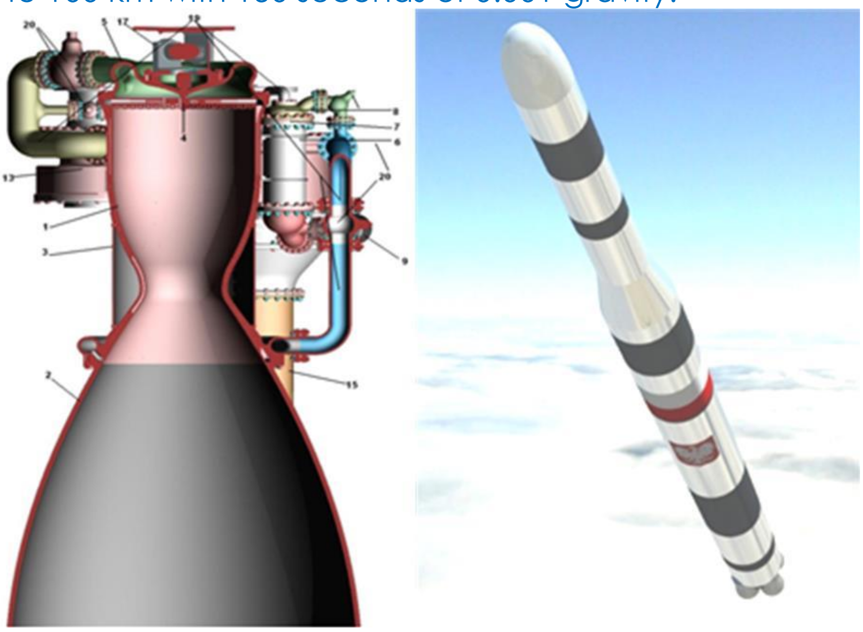

Figure 4. 16. Results of small launch vehicle feasibility studies. © Inst. of Aviation

Research includes experimental studies of modern fuels and oxidizers for space propulsion, development of small thrusters for satellite applications and development of larger propulsion systems. Work on solid, hybrid and liquid propellants is ongoing. Systems with thrust up to 60 000 N are under development. Especially green propulsion is of interest. This is due to the unique technology of producing hydrogen peroxide (up to 99.99% concentrations with high purity), which was invented at Institute of Aviation in 2012 (EPO Patent). Advanced thrusters using novel catalyst beds have been tested for applications in the range of 1-200 N. Development is focused on international programs and filling up European technology gaps. This includes the development of solid rocket motor deorbitation (SMR) systems for end-of-life satellite orbital removal.

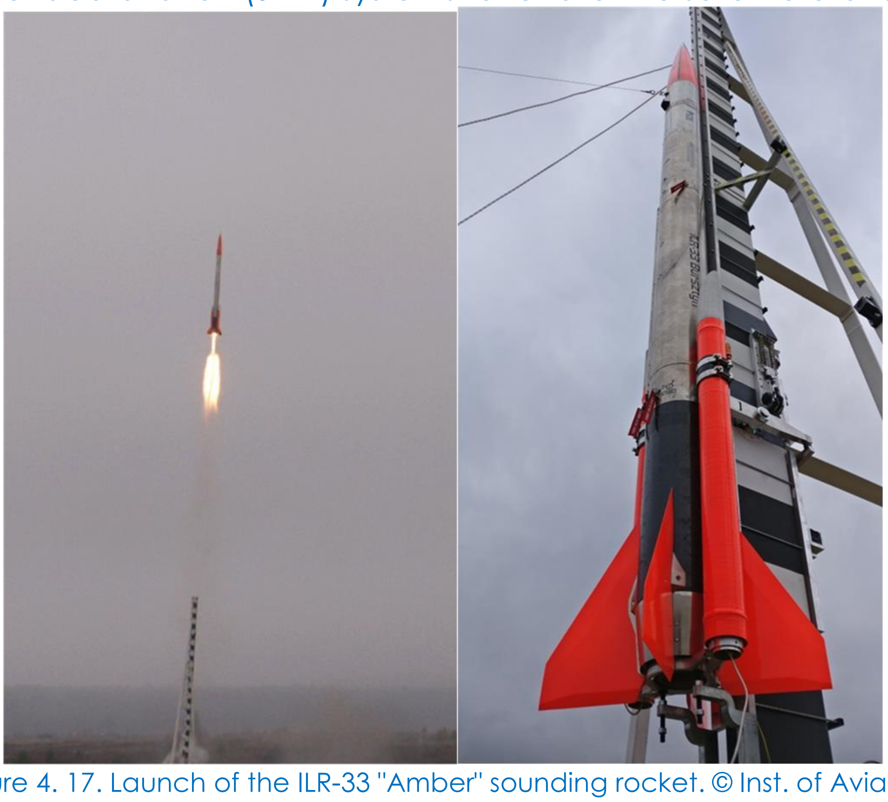

Figure 4. 17. Launch of the ILR-33 "Amber" sounding rocket. © Inst. of Aviation

4. ASTRONAUTICS AND SPACE TECHNOLOGIES

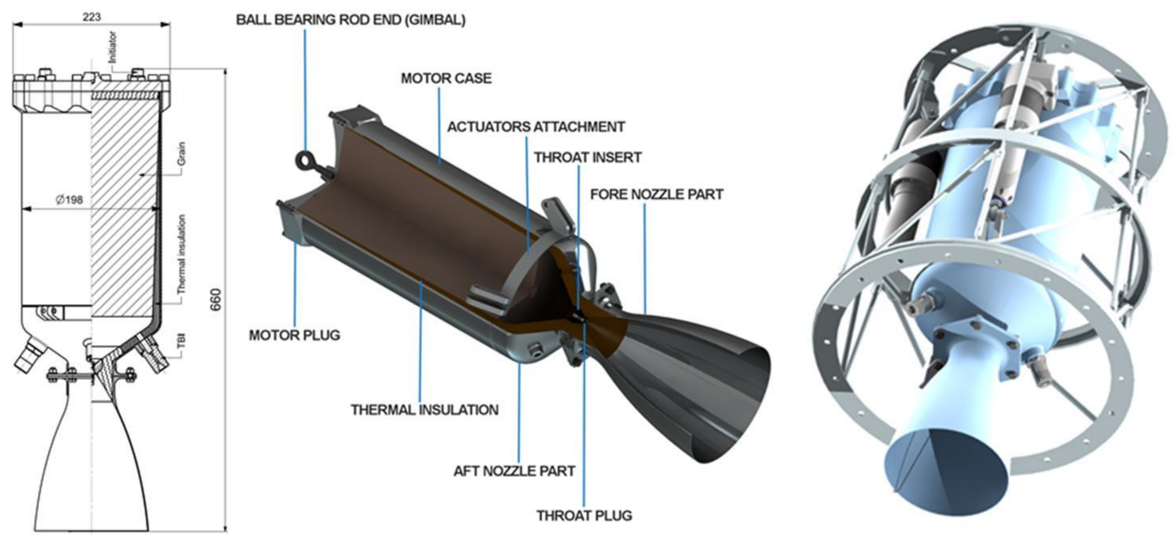

Figure 4. 18. Early designs of SRM and their subsystems for deorbiting S/C. © Inst. of Aviation

The new testing infrastructure in Poland
Institute of Aviation has the most modern facilities in the region, enabling to work with **propulsion systems including spacecraft thrusters and larger engines for space transportation**.

Figure 4. 19. Modern research facilities for rocket propulsion development. © Inst. of Aviation

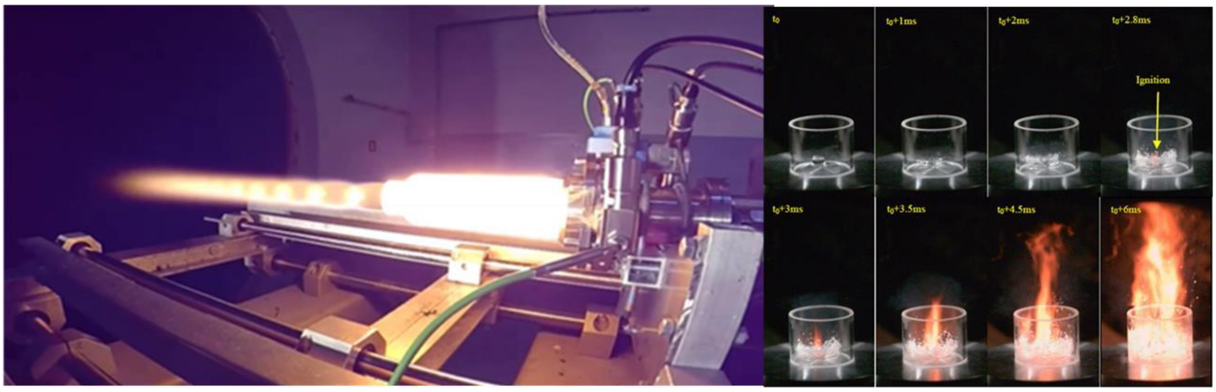

Figure 4. 20. Hydrogen peroxide bipropellants tests. © Inst. of Aviation

The **clean-rooms and fully equipped assembly line** let the company to Creotech Instruments S.A is the first Polish industrial company investing the significant resources for space related infrastructure manufacture space electronics. Within ESA GSTP program, and supported by CBK PAN, Creotech Instruments S.A. received ESA certificates for assembling of space qualified electronics. The line was already used for assembling the electronic boxes for ASIM and CaSSIS missions.

Figure 4. 21. ESA certified assembly line for flight electronics in Creotech Instr. SA. © CTI

The Space Research Centre of the Polish Academy of Sciences (CBK PAN) possesses a **planar air bearing microgravity simulator** that is used for the testing of advanced control algorithms of space robots and conducting different experiments related to space robotics. This facility is in use since 2012. Major upgrade was performed at the 2015/2016. This test bed consists of a granite table which is 2 [m] x 3 [m] wide and a space robot that can move freely on the surface of the table using air bearings. The space robot consists of a base with attached 2 DoF manipulator. The base is equipped with a set of thrusters which allow its motion in the plane. This test bed also consists of a vision system that provides the information about the position and orientation of the robot's parts and is used by the control system for the closed loop control.

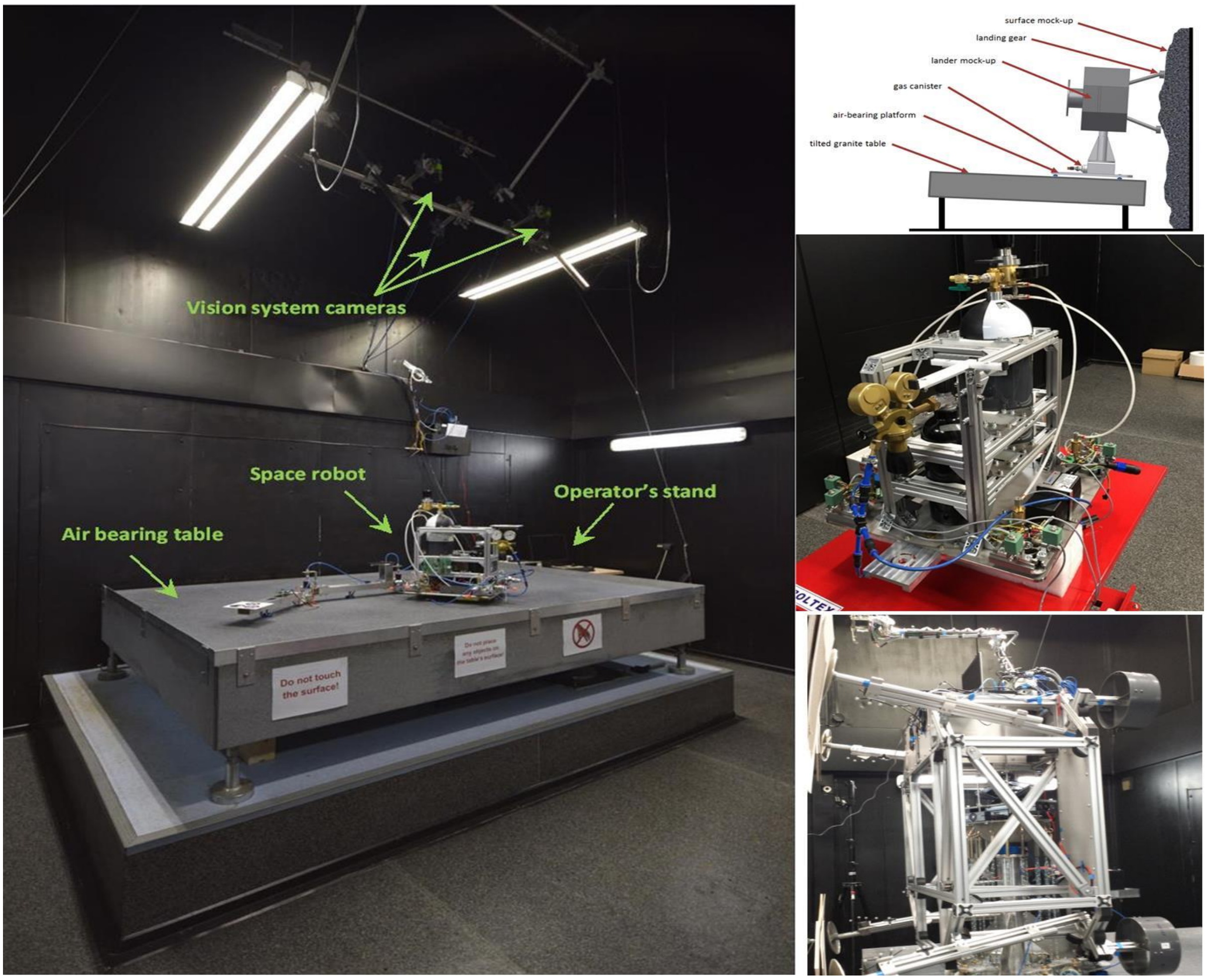

Figure 4. 22. The planar air bearing table in CBK PAN, general view (left), test set-up for lander with a manipulator mock-up during the sampling process on a mock-up of the Phobos surface (top right), the robot equipped with 8 gas thrusters (middle right) and the tests on air-bearing table, showing a lander equipped with manipulator arm with PACKMOON emulator on top. © CBK PAN

Student's activities

At many universities students scientific groups are actively involved in development of rocket propulsion for educational proposes. Students from the Students' Space Association from Warsaw University of Technology already developed and successfully tested many single and two stage solid propulsion rockets, some of which reach altitudes of about 8 km and speeds up to 2.7M. Other activities include tests of rockets deploying CanSats at altitudes of a few km. Initial work on propulsion is also carried out by students from Cracow University of Science and Technology. Other educational research related to space technology is carried out by students at different universities in Poland are related to rockets, space robotics, Mars Rovers, balloons etc. More on student's Astronautical activities at the Warsaw University of Technology can be find on http://ska.pw.edu.pl/

Figure 4. 23. Recent test of the student's rocket. ©SSA WUT

PW-Sat2 is a student satellite project started in 2013 at Warsaw University of Technology by the Students Space Association members. Its main technical goal is to test new deorbit technology in form of a large deorbit sail whereas the project purpose is to educate a group of new space engineers. In February 2018 PW-Sat2 became fully integrated and was being prepared to the launch into orbit planned for the second half of 2018.

4. ASTRONAUTICS AND SPACE TECHNOLOGIES

There are three main experiments and couple of other small projects that were developed by the students of Students Space Association and will be tested on board PW-Sat2.

The first one is large square-shaped deorbit sail that will dramatically decrease a life-time of the satellite. In 2016 the detailed analyses of effectiveness were conducted and the design of the sail was awarded the second prize in Deorbit Device Competition held by UNISEC-Global. The prototypes of the deorbit sail were manufactured in 2016 and 2017 and the final flight configuration units were successfully tested at the Drop Tower in Bremen in November 2017. At the end of 2017 the deorbit sail unit was integrated with the main satellite structure. Second of the payload experiments is the Sun Sensor. It will provide an orientation data which will be compared with the commercial system readings. It is made out of four sets of ambient light sensors (ALS) placed at specific angles and a microcontroller managing the acquisition and analysis of data. In years 2016-2017 the final prototypes and flight model were tested and developed.

PW-Sat2 is equipped with two deployable solar arrays in order to increase the energy gathering area. Arrays' hinges are a subject of one of the members' Engineering Thesis. Both panels have size of approximately 10 x 20 cm and are arranged symmetrically. PW-Sat2 has custom Electrical Power System. It is responsible for power supply to all the subsystems and experiments of the satellite. In case of any subsystem failure it is capable of carrying out the main part of our mission on its own. On board there are also two VGA cameras with aim to observe a process of the deorbit sail deployment.

The integration of PW-Sat2 took place in CBK PAN (clean-room" and Warsaw University of Technology laboratory CEZAMAT PW. Innovative Space Logistics B.V. (Netherlands) became the launch provider after agreement signing on October 26th, 2016. PW-Sat2 will be launched on board Falcon 9 from Vandenberg in the second half of 2018.

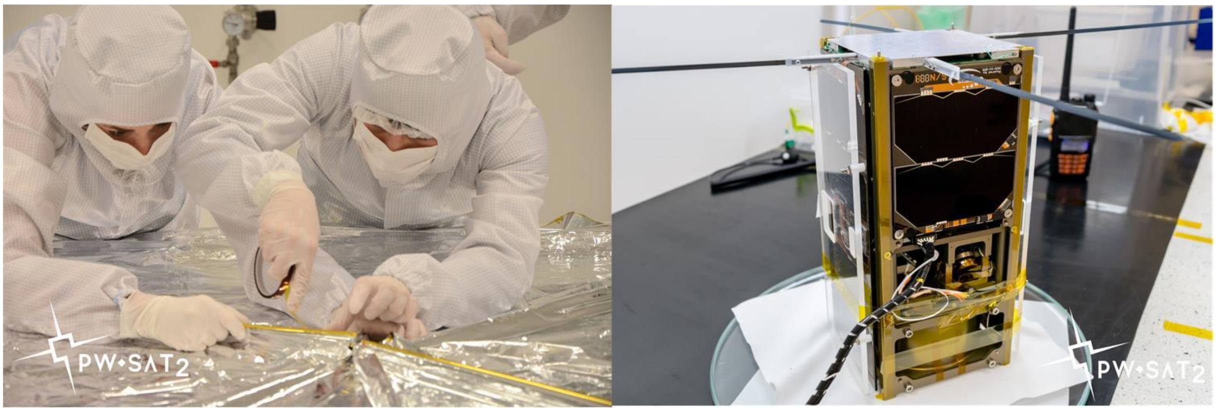

Figure 4. 24. PW-Sat2 deorbit sail during development in CEZAMAT PW in August 2017 (left) and PW-Sat2 Flight Model fully integrated (right). Credit: PW-Sat2/Students Space Association/Warsaw University of Technology, (CC BY-SA 2.0)

5

LAW AND THE SPACE POLITICS

The Members of the Section of Law and Space Policy of the Committee on Space and Satellite Research affiliated with Presidium of the Polish Academy of Sciences participated in the initiative of establishing the Polish Center for Space Law of Manfred Lachs (PCSL). The formal establishment of this cooperation platform took place on 29 May 2017 at the Warsaw University. Its purpose is to propagate knowledge about space activities, in particular space law. The Polish Centre for Space Law is going to apply to the European Centre for Space Law to serve as its National Point of Contact in Poland. Representatives of the Ministry of Science and Higher Education, Ministry of Economic Development, Ministry of Foreign Affairs, Ministry of National Defense, Ministry of the Interior and Administration and the Polish Space Agency took part in the ceremony.

The PCSL is organised under the auspices of the University of Warsaw. At the moment it comprises the following institutions: the Committee on Space and Satellite Research affiliated with Presidium of the Polish Academy of Sciences, the University of Warsaw, the Cardinal Stefan Wyszyński University, the Warsaw School of Economics, the University of Rzeszow, the University of Gdansk, the University of Wrocław, the Cracow University of Economics, the University of Silesia, The mentioned Universities will hold the 1-year presidency of the PCSL on the rotating basis.

On 1st of December 2017 the Members of the Section of Law and Space Policy of the Committee on Space and Satellite Research participated in the conference "*Satellite Navigation - World, Europe, Poland*" organized in connection with the Department of International Aviation and Space Law of the Institute of International Law of the Warsaw University.

Table of Contents